EARTHQUAKE MOTION PREDICTION, MICROZONATION, AND BURIED PIPE RESPONSE FOR URBAN SEISMIC DAMAGE ASSESSMENT

by

Masata SUGITO

School of Civil Engineering

Kyoto University

October, 1986

EARTHQUAKE MOTION PREDICTION, MICROZONATION, AND BURIED PIPE RESPONSE FOR URBAN SEISMIC DAMAGE ASSESSMENT

by

Masata SUGITO

School of Civil Engineering
Kyoto University
October, 1986

SUMMARY

This dissertation is devoted to development of comprehensive earthquake motion prediction models, related methodology for earthquake microzonation, and response characteristic of buried pipelines for urban seismic risk assessment.

The significance of earthquake motion prediction on rock surface level is demonstrated for earthquake engineering. For this objectives the modified strong motion dataset on rock surface is arranged using soil surface ground motion records. In this procedure the simplified technique for separating body and surface wave motion in strong motion accelerograms is used to eliminate the contribution of the surface wave motion. On the basis of the modified rock surface strong motion dataset, two prediction models for nonstationary earthquake motion on rock surface are proposed: one is the EMP-IB model for a given earthquake magnitude and epicentral distance, and the other is the EMP-IIB model for a given fault geometry including fault size, seismic moment, rupture velocity, and rupture pattern. For engineering use, the estimation formulas for peak ground motion, acceleration response spectra, and ground motion duration on rock surface are also proposed on the basis of the simulated rock surface motion by the EMP-IB model.

For use for earthquake microzonation, the simple conversion factor β between earthquake motion on rock surface and soil surface is proposed with consideration for the nonlinear amplification effect of soil layers over bedrock. The conversion factor, β, defined for peak acceleration, peak velocity, acceleration response spectra, and evolutionary power spectra, is modeled as a function of the simple soil parameters S_n, d_p, and the ground motion intensity at the rock surface level.

In this thesis the earthquake response analysis of joint-connected buried pipelines are discussed focusing on the response behavior of typical pipe formations generally used in actual systems. Two representative models are selected for response analysis based upon a detailed survey of the structural characteristics of buried pipelines in the Kyoto City water supply system. From the results of response analysis the simplified formulas are

proposed for estimating joint displacement, axial strain of pipes, and bending strain of pipes at concrete-embedded sections, as a function of input ground strain amplitude and apparent wave length in the longitudinal direction of pipes.

ACKNOWLEDGMENTS

The author wishes to express his sincere gratitude to Professor Hiroyuki Kameda of Urban Earthquake Hazard Research Center of Kyoto University for his supervision, guidance, heartily support, and continuous encouragement during the course of this study. Special appreciation is extended to Professor Hisao Goto of Kyoto University for his heartily support and encouragement on completing this dissertation. Thanks are due to Professor Yoshikazu Yamada of Kyoto University and Professor Kenzo Toki of Disaster Prevention Research Institute of Kyoto University for their critical reading of manuscript and continuous criticism. Professor Takashi Akiyoshi of Kumamoto University, Professor Masaru Kitaura of Kanazawa University, Professor Shiro Takada of Kobe University, Professor Hirokazu Iemura of Kyoto University, Professor Tadanobu Sato of Disaster Prevention Research Institute of Kyoto University, Professor Fusao Oka of Gifu University are acknowledged for their sincere discussions and continuous criticism. Dr. Zoran Milutinovic of Institute of Earthquake Engineering and Engineering Seismology, University "Kiril and Metodij", Skopje, Dr.Helmut Pradlwarter of University of Innsbruck, Lecturer Tsutomu Sawada of Tokushima University, Professor Fusanori Miura of Yamaguchi University, and Mr.shigeru Noda of Kyoto University are also acknowledged for their discussions and encouragement.

Besides these professors and colleagues, the author wishes to express his sincere gratitude to the staffs of the Port and Harbor Research Institute, Ministry of Transport and the Public Works Research Institute, Ministry of Construction for Their sincere cooperation on strong ground motion records and relevant data which have been used in this study.

TABLE OF CONTENTS

1 INTRODUCTION

1.1 General Remarks

It is one of the fundamental and significant subjects in earthquake engineering to estimate the severity of ground motion for the hypothetical earthquakes. For this objectives the great effort was directed toward developing the empirical relationship between peak acceleration of ground motion and earthquake magnitude and source-to-site distance from 1960's(Ref.13). These works were improved with increse in valuable strong motion records obtained from major earthquakes occured after 1940's. Since a peak acceleration is not enough information for earthquake registant design of structures, specially for longer period structures, the empirical estimation formulas for acceleration response spectra have been proposed on the basis of the strong motion records after 1970's(Refs.14,18,24). These works give the significant information to the on-going earthquake registant design procedures in which the acceleration response spectra are used as the seismic load to the structures. The extended work for evaluation of inelastic structural response has been done by Milutinovic and Kameda(Ref.15) in which the equivalent peak acceleration difined by a peak acceleration and strong motion duration was related to the inelastic structual response of bi-linear systems.

On the other hand the dynamic response analysis of structures is one of the important methodology for design of significant structures. For this objectives the input ground motion time history is indespensable. In this point of view it is an essential subject to develop a prediction model for earthquake motion time history for given earthquake magnitude and source-to-site distance. Since the structural responses, specially nonlinear responses, are affected not only by a peak acceleration but by a ground motion duration and nonstationarity of spectral characteristic, the prediction model should include these information on ground motion precisely.

For the development of a prediction model for ground motion time history, the following two significant steps may be completed.

[1] development of a comprehensive simulation model which can simulate the significant engineering characteristic of recorded ground motion.

[2] development of a prediction model on the basis of the statistical regression analysis of the model parameters, which are obtained from the simulation of each ground motion records, on earthquake magnitude and source-to-site distance.

In the past 15 years many works have been done for the first step (Refs.1,2,4,6,7,10,20,22,23). However, the work which is extended to the second step have been scarcely performed (Refs.8,12). Considering from such a viewpoint, this study has been done for development of comprehensive earthquake motion prediction model.

It can be observed in the past earthquake damage data that the ground motion intensity depends strongly on the local site conditions. Therefore, the evaluation of effect of local site conditions on ground motion is a significant subject in earthquake engineering. This is generally called as the microzonation technique for earthquake motion, and is effective tool for estimation of distribution of ground motion intensity for some wide areas such as urban regions. This study deals with the comprehensive method for earthquake microzonation.

The lifeline earthquake engineering has been characterized as one of the major fields in earthquake engineering after the middle of 1970's. In this field, because of its speciality in structural forms, the great effort was directed to evaluation of response characteristic of buried pipes during earthquakes as well as the development of a methodology for system reliability. Some of the results from these works have been characterized in the design code (Ref.9), however, there still remain the problems to be solved for earthquake resistant design of systems, since a system generally consists of variable structural forms. These typical structural characteristic should be analysed one by one for development of a comprehensive seismic risk assessment of systems.

1.2 Review of Previous Studies on Earthquake Motion Prediction and Response

Analysis of Buried Pipelines

1.2.1 Simulation of Acceleration Time History and Its Application

Since the pioneer work was done by Housner (Ref.6), the simulation model for ground motion properties have been improved with increase in the strong motion records as well as the great advance of computer technology. The simulation models are classified into the following three groups according to the engineering characteristic of the simulated motion.

(1) the stationary model [Housner(1955)]

(2) the stationary model with time-varying envelope functions [Tajimi(1960), Shinozuka(1967), Toki(1968), Amin & Ang(1968), Kameda(1977)]

(3) the nonstationary model with varying frequency characteristic [Beaudet(1970), Saragoni & Hart(1974), Goto & Kitaura(1975), Kameda(1977), Hoshiya & Isoyama(1978)]

As for the nonstationary model, which represent actual ground motion most clearly, Beaudet(Ref.2) proposed the simulation technique in which the nonstationary analog filter was used to represent the nonstationarity of ground motion caused by underground explosions. Saragoni and Hart (Ref.20) and Goto and Kitaura (Ref.4) evaluated the power spectrum for each interval of ground motion time history and modeled them as the time dependent power spectrum density. Hoshiya and Isoyama (Ref.7) treated the model for the multi-dimensional earthquake motion by using the typical spectrum parameters for the modeling of spectral characteristic in frequency domain. These simulation models have some common aspect : the spectral characteristic is modeled by using some functions. On the other hand, Kameda(Ref.10) suggested that the spectral characteristic should not be modeled by using such simple functions because the structural response are affected strongly by spectral intensities. From this point of view, the simulation model, which deals with the modeling of evolutionary power spectrum only on time axis, has been proposed(Ref.10), where the simulated motion was compared with corresponding recorded motion as for the inelastic response of structures as well as peak

acceleration and acceleration total power.

In regard to the works extended to the second step, Kameda, Sugito and Asamura(Ref.12) have developed the nonstationary earthquake motion prediction model by using the Japanese soil surface strong motion records, in which the typical three model parameters to control the evolutionary power spectrum were scaled for magnitude and epicentral distance. Izutani(Ref.8) also proposed a statistical model for given dynamic fault parameters such as average value of stress drop and root mean-square of stress drop, by which the characteristic frequency for acceleration spectral density of ground motion is controlled.

These prediction models give significant information on ground motion time history for hypothetical earthquakes. However, for a prediction of ground motion for severe earthquakes, such as large magnitude and short distance, it is very important to incorporate nonlinear soil amplification effect into ground motion time history, as well as the effect of rupture direction and successive faulting. In this point of view, this study has been done for development of the comprehensive earthquake motion prediction models, which can incorporate the nonlinear soil amplification effect of surface layers over bedrocks as well as the effect of fault geometry and successive faulting.

1.2.2 Response Analysis and Damage Estimation for Buried Pipelines

The major subjects of the earthquake engineering are generally consist of the following three steps.

[1] the assessment of the earthquakes which will occur and bring some damages on lifelines systems during their life time, and the estimation for distribution of ground motion intensity over the area where the systems are established.

[2] the estimation of damages of pipes and other related structures from the ground motion intensity for each section.

[3] the assessment of the system reliability based on the results in [2].

The works on earthquake engineering started with the field observation for pipe behavior during earthquakes (Ref.19). In the comparison between works for this field in Japan and in U.S.A., the great effort has been directed toward development of analytical and experimental study on earthquake response of buried pipes in Japan. On the other hand, relatively a lot of works have been done for development of the methodology for assessment of system reliability and serviceability in U.S.A. These historical review is discussed in Chapter 6.

As for the response characteristic of buried pipes both the experimental and analytical study have been done extensively from 1970's (Refs.3,7,17) and the results from these studies have been used effectively in the seismic design code of pipes (Ref.9). However, in the actual systems, there exist a lot of complicated structural formations which are not treated in the design code. For example, in the case of the joint-connected buried pipes which are usually used for water supply systems, the concrete-fixed form is generally used where the pipelines change its directions. These typical forms should be analysed individually for evaluation of response behaviors.

1.3 Layout of Present Thesis

In the view of the problems stated previously, this thesis deals with (1) the comprehensive methodology for earthquake motion prediction and microzonation and, (2) the response characteristic of joint-connected buried pipelines, the type of which have been used in the actual water supply systems.

In Chapter 2, the rock surface strong motion dataset termed MSMD-R (Modified Strong Motion Dataset on Rock Surface) is arranged for development of earthquake motion prediction models. The numerical database termed SERM-II (Seismic Risk and Microzonation-II) is briefly introduced and, the MSMD-R dataset is obtained by using the strong motion records and soil profile data for observation stations stored in SERM-II database. The MSMD-R dataset is consists of the three types of acceleration time histories : (a) rock surface

ground motion estimated from the accelerograms recorded on alluvial and diluvial sites, (b) rock surface ground motion modified from bedrock ground motion, and (c) ground motion recorded on rock surface. In the procedure of the conversion from soil surface to rock surface motion, the earthquake surface wave motion is eliminated from the soil surface motion by using the separation technique proposed in Chapter 3.

In Chapter 3, a simplified separation technique of body and surface waves in strong motion accelerograms is proposed. The evolutionary power spectrum (Ref.11) is used to identify the dispersion characteristic of surface wave components. The three separation parameters in frequency and time domain are characterized to be used for separation of body and surface waves by using FFT technique. The significance of the separation technique is demonstrated in the comparison of evaluation of ground strain caused by surface wave propagation.

In Chapter 4, the nonstationary earthquake motion prediction models on rock surface are proposed. Herein the two typical models are demonstrated : one, the prediction model for given earthquake magnitude and epicentral distance (EMP-IB), and the other, the model for given fault geometry including fault size, seismic moment, rupture velocity, and rupture pattern (EMP-IIB). The second model EMP-IIB is developed for the case that the fault parameters are available and the specific site is located near the hypothetical fault where the ground motion are affected strongly by the direction of fault rupture and rupture velocity in successive faulting. For the engineering use, the estimation formulas for peak ground motion, acceleration response spectra, and ground motion duration on rock surface are also proposed on the basis of the simulated rock surface motion by EMP-IB model.

In Chapter 5, for use of earthquake microzonation, the conversion factor between earthquake motion on rock surface and soil surface is proposed with consideration on nonlinear soil amplification effect of soils overlaid bedrocks. The conversion factor β, defined for peak acceleration, peak velocity, acceleration response spectra, and evolutionary power spectra is modeled as the function of the simple soil parameters S_n, d_p and the ground

motion intensity on rock surface level.

In Chapter 6, the earthquake response analysis of joint-connected buried pipelines are carried out. The two representative models, which have been used in the actual water supply systems, are analysed : the model I for a straight part of pipelines and, the model II for a straight part with concrete-fixed section which is used in actual systems where the route of pipelines changes its direction or crosses with other lines. On the basis of the results of response analysis, the simplified estimation formulas are proposed for joint displacement, axial strain of pipes , and bending strain of pipes at concrete-fixed section, as the function of input ground strain amplitude in longitudinal and transverse direction and the apparent wave length in longitudinal direction.

Finally, in Chapter 7, the summary of the thesis is mentioned, and the significance of this study and the further recommendation are given.

References

1) Amin,M., and Ang,A.H-S.(1968), "Nonstationary Stochastic Model of Earthquake Motion," Proc., ASCE, Vol.94, No.EM2, pp.559-583.
2) Beaudet,P.R.(1970), "Synthesis of Nonstationary Seismic Signals, BSSA, Vol.60, No.5, pp.1615-1624.
3) Bouwkamp,J.G. and Stephen,R.M. (1973), "Large Diameter Pipe Under Combined Loading," Proc. ASCE, TE3, pp.521-536.
4) Goto,H. and Kitaura,M.(1975), "Time Varying Power Spectral Densities of Earthquake Motions and Their Mathematical Representation," Proc. of JSCE, No.236, pp.47-58.
5) Goto,H.,Sugito,M.,Kameda,H., and Ishikawa,Y.(1982), "Seismic Response Analysis of Joint-Connected Buried Pipelines Including Bent Sections," Memoirs of the Faculty of Engineering, Kyoto University, Vol.XLIV, Part 1, pp.182-221.
6) Housner,G.W.(1955), "Properties of Strong Motion Earthquakes," BSSA, Vol.45, No.3, pp.197-218.
7) Hoshiya,M. and Isoyama,R.(1978), "Simulation of Multi-Dimensional Nonstationary Earthquake Accelerations," Proc. of JSCE, No.269,

pp.41-52.

8) Izutani,Y.(1981) "A Statistical Model for Prediction of Quasi-realistic Strong Ground Motion," Journal of Physics of Earth, 29, pp.537-557.

9) Japan Gas Association(1982), Earthquake Resistant Design Code for Gas Supply Pipes for Trunk Route.

10) Kameda,H.(1977), "Stochastic Process Models of Strong Earthquake Motions for Inelastic Structural Response," U.S.-Southeast Asia Symposium on Engineering for Natural Hazards Protection, Manila, pp.71-85.

11) Kameda,H.(1975), "Evolutionary Spectra of Seismogram by Multifilter," Proc. ASCE, Vol.101, No.EM6, pp.787-801.

12) Kameda,H., Sugito,M., and Asamura,T.(1980), "Simulated Earthquake Motions for Magnitude, Distance, and Local Soil Conditions," Proceedings of the 7th World Conference on Earthquake Engineering, Istanbul, Vol.2, pp.295-302.

13) Kanai,K.(1966), "Empirical equations for earthquake motion intensity," 5th Japan Earthquake Engineering Symposium, pp.1-4. (in Japanese).

14) Katayama,T., Iwasaki,T. and Saeki,T.(1978), "Statistical Analysis of Earthquake Acceleration Response Spectra," Proc., JSCE, No.275, pp.2940 (in Japanese).

15) Milutinovic,Z. and Kameda,H.(1984), "Statistical Model for Estimation of Inelastic Response Spectra," Proc. of JSCE, Structural Eng./Earthquake eng. Vol.1, No.2, pp.105-114.

16) Miyamoto,H., Hojyo,S., and Kosho,K.(1976), "Vibration Tests of Buried Pipes for Estimation of Its Behavior during Earthquakes," Kubota Technical Report, Vol.1, No. 2, Dec. pp. 126-153, (in Japanese).

17) Miyajima,N. and Miyauchi,J.(1975), "Stresses in Buried Pipes during Earthquake Based on Static Friction," Proc. of Symposium on Buried Pipelines, Japan Society of Soil Mechanics and Foundation Engineering, pp.57-60, (in Japanese).

18) McGuire,R.K.(1974), "Seismic Structure Response Risk Analysis," Incorporating Peak Response Regressions on Earthquake Magnitude and Distance," Report No.R74-51, School of Engineering, MIT.

19) Sakurai,A., and Takahashi,T.(1969), "Dynamic Stresses of Underground Pipelines during Earthquakes" Proc. of the 4th World Conference on Earthquake Engineering, Santiago, Vol.II, pp.81-95.

20) Saragoni,G.R. and Hart,G.C.(1974), "Simulation of Artificial

Earthquake," Earthquake Engineering and Structural Dynamics, Vol.2, pp.249-267.

21) Shinozuka,M. and Sato,Y.(1967), "Simulation of Nonstationary Random Process," Journal of ASCE, No.EM1, pp.11-40.

22) Tajimi,M.(1960), "A Statistical Method of Determining the Maximum Response of Building Structure During and Earthquake," Proceeding of the 2nd World Conference on Earthquake Engineering, Vol.II, pp.781-797.

23) Toki,K.(1968), "Simulation of Earthquake Motion and Its Application," Annuals, Disaster Prevention Research Institute, Kyoto University, No.11A, pp.291-303. (in Japanese)

24) Trifunac,M.D. and Anderson,J.G.(1977), "Preliminary Empirical Models for Scaling Absolute Acceleration Spectra," Report No.CE77-03, Department of Civil Engineering, University of Southern California.

2. SELECTION AND MODIFICATION OF ROCK SURFAE EARTHQUAKE MOTION FOR DEVELOPMENT OF STATISTICAL PREDICTION MODELS

2.1 General Remarks

In the field of earthquake engineering the storng motion accelerograms obtained from earthquakes are indispensable data. They have provided increased understanding about the characteristic of strong ground motion and structural responses. Many works concerning the statistical prediction models of earthquake motion have been done by using various types of strong motion datasets. For engineering purposes the data should be examined and be selected regarding the objectives of the analysis, since the statistical characteristic of ground motion depends considerably on a dataset(see Appendix A).

In the development of the statistical prediction models for strong ground motion, consistency of data used for the analysis is of special importance. Not only for this purpose but for related analysis such as seismic risk analysis, the numerical database on strong motion, earthquake occurences, and other corresponding information have been investigated (Ref.15).

In this Chapter, the outline of the numerical database on earthquake engineering is introduced, and on this basis a set of modified rock surface earthquake motion is obtained, which is used for the development of earthquake motion prediction models proposed in Chapter 4. In the following Chapter 2.2 the numerical database termed SERM-II(Seismic Risk and Microzonation-II) developed by Tsunekawa, Kameda, Sugito, and Goto(Ref.15) is introduced focussing on the earthquake motion records and soil profile data for strong motion observation stations. In Chapter 2.3 a dataset of modified rock surface earthquake motion is developed on the basis of the data in SERM-II database.

2.2 Strong Motion and Soil Profile Data in SERM-II Database

2.2.1 Significance of Numerical Database in Earthquake Engineering

A large amount of numerical data on the earthquake occurences, the strong ground motion, and the structural damages, etc. have been accumulated and they have contributed to the study in the various fields such as the seismic hazard analysis, earthquake motion prediction, response analysis of structures, and evaluation of seismic load in earthquake-resistant design, etc. In use of these data for analysis, the completeness of the data arrangement is significant, therefore the development of the numerical database is of special importance.

The Design Seismic Load Research Group(SLG)* have made much effort for the development of the numerical database termed SERM-II, which include the data on the earthquake occurences in Japan, the major Japanese and U.S. strong ground motion, the soil profile data for observation stations, the map data for Japanese urban areas and the entire country, and other corresponding information. The outline of the strong motion and soil profile data in SERM-II Database System are as follows.

2.2.2 Strong Motion Data in SERM-II Database System

The four-hundred of Japanese strong motion accelerograms have been included in the SERM-II Database. Most of them are the data published by the Port and Harbor Research Institute, Minstry of Transport(Ref.10), and by the Public Works Research Institute, Ministry of Construction(Ref.11). These accelerograms have been corrected for baseline and instrument characteristic(Ref.2). The frequency range of the correction filter is fixed for the whole data as between f_l=0.15Hz and f_u=10.0Hz. These data can be accessed from user's programs in a simple way as shown in Fig.2.1. The example for the formation of each component of accelerograms is shown in Fig.2.2.

As shown in Fig.2.2 'TITLE' gives corresponding information for the data such as the original data classification number, title of earthquake,

---

*Staffs in the Laboratory of Structural Problem for Transportation Facilities, School of Civil Engineering, Kyoto University.

```
      DIMENSION A(6000),V(6000),D(6000)
      DIMENSION IC(50),FC(50)
      CHARACTER TITLE(400)*4
           .
           .
      CALL EQOPEN(NEQ,TITLE,IC,FC,A,V,D)
           .
           .
```

```
   NEQ ; record number of strong motion
 TITLE ; title and corresponding information for a component of
         strong motion
    IC ; integer parameters in TITLE
    FC ; floating pt. parameters in TITLE
     A ; acceleration time history
     V ; velocity time history
     D ; displacement time history
```

Fig.2.1 Access Procedure for Strong Motion Time History in Users' Program underSERM-II Database System.

TITLE(heading data)

```
CORRECTED ACCELEROGRAM    S-1567          COMP  EAST    SER. NO. 83-0324     0010
  AKITA-S                                                                    0020
  1983 NIHONKAI CHUBU                                                        0030
EPICENTER    40 21  ON 139  4 48E   MAGNITUDE=7.70                          0040
INSTR PERIOD= 0.1400  SEC DAMPING=1.000                                     0050
SOIL CONDITION =     2                                                      0060
UNITS ARE SEC AND CMS/SEC/SEC                                               0070
BASELINE- AND INSTRUMENT CORRECTED BETWEEN 0.150   AND  10.000  HZ         0080
  6025  INSTRUMENT AND BASELINE CORRECTED DATA                              0090
AT EQUALLY-SPACED INTERVALS OF  0.02  SEC.                                  0100
PEAK ACCELERATION =   -226.448    CMS/SEC/SEC AT    21.300 SEC              0110
PEAK VELOCITY     =     26.467    CMS/SEC     AT    24.300 SEC              0120
PEAK DISPLACEMENT =      7.983    CMS         AT    24.680 SEC              0130
PEAK ACCELERATION OF UNAJUSTED ACCELEROGRAM = 203.197 CMS/SEC/SEC           0140
INITIAL VELOCITY  =      0.674 CMS/SEC     INITIAL DISP =    0.067 CMS     0150
                                                                            0160
                                                                            0170
                                                                            0180
                                                                            0190
                                                                            0200
```

IC(integer parameters)

6025	6025	6025	39	45	0	140	9	0	2
40	21	0	139	4	48	324	21007	0	67
1983	5	26	12	2	0	0	0	0	0
0	0	0	0	0	0	0	0	0	0
0	0	0	0	0	0	0	0	0	0

FC(floating pt. parameters)

0.140	1.000	7.700	14.000	107.000	0.020	0.020	0.020	0.100	0.150
10.000	14.000	0.674	0.067	-226.448	21.300	26.467	24.300	7.983	24.680
203.197	0.0	0.0	0.0	0.0	0.0	0.0	0.0	0.0	0.0
0.0	0.0	0.0	0.0	0.0	0.0	0.0	0.0	0.0	0.0
0.0	0.0	0.0	0.0	0.0	0.0	0.0	0.0	0.0	0.0

Fig.2.2 Example for Heading Data and Relevant Constants of Strong Motion Data

occurence date, and peak ground motion, etc. The corresponding numerals appearing in 'TITLE' are stored in 'IC' and 'FC'. The formation for the corrected accelerograms shown in Fig.2.2 has been proposed refering the strong motion data arrangement developed by Earthquake Engineering Research Rabolatory, California Institute of Technology(Ref.3).

Fig.2.3 shows an example of graphic information for a component of corrected accelerograms. In Fig.2.3 the typical parameters for a component of accelerogram are listed in the left top of the figure. The corrected accelerograms, velocity, and displacement time series are shown in the left. The acceleration Fourier spectrum and response spectrum for a component are shown in the right. The numerical parameters in Fig.2.3 and other corresponding parameters such as station number, soil data number, earthquake number, etc. are stored in the SERM-II Database System. The users can refer the strong motion data by using these parameters.

2.2.3 Soil Profile Data in SERM-II Database

The two types of soil profile data have been included in the SERM-II Database. One is the data for strong motion observation stations, and the other for several sets of the SPT blow count data distributed over Japanese urban areas.

Table 2.1 shows examples for the soil profiles for strong motion observation stations, which have been used in the development of the rock surface strong motion dataset(SMD-R) in Chapter 2.3. They have been published by the Port and Harbor Research Institute, Ministry of Transport(Ref.14), and the Public Works Research Institute, Ministry of Construction. The deeper part for Hachinohe-S, Aomori-S, and Kushiro-S have been obtained on the basis of other research works(Ref.1,9).

In Table 2.1 the estimated value for the shear wave velocity is given by use of the empirical formulas(Ref.13) listed in Table 2.2. The estimated value for the density(weight per unit volume) in Table 2.2 is fixed as ρ=1.5 for clay, 1.4 for silt, 1.8 for sand, 1.9 for gravel, and 2.2 for rock, respectively(Ref.5). These data can be accessed in users' programs as shown

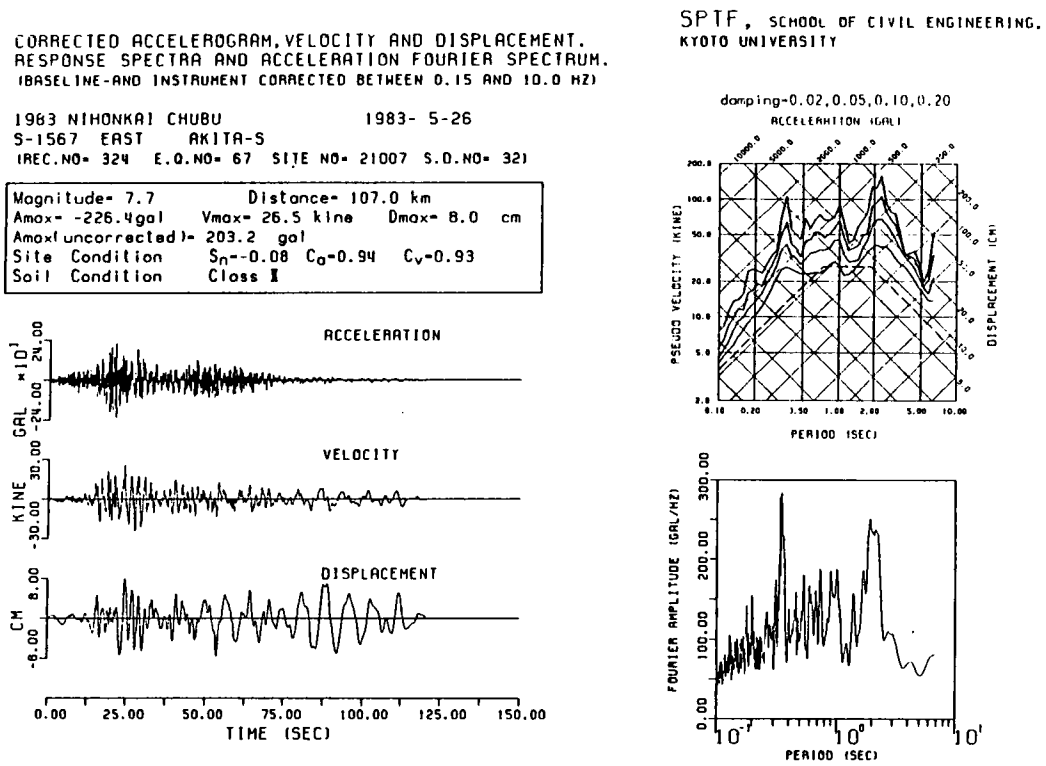

Fig.2.3 Graphic Output of Strong Motion Data

Table 2.1 Site Structure Models for Japanese Strong Motion Observation Stations(Refs.1,9,14).

(a) Muroran-S

layer number	thick-ness (m)	blow-count	shear wave velocity** Vs(m/s)	soil clasifi-cation *	density*** (g/cm³)
1	3.0	2.0	135.9	3	1.8
2	2.4	33.0	182.2	3	1.8
3	1.6	24.5	280.9	4	1.9
4	2.0	17.5	235.3	1	1.5
5	5.5	45.0	303.6	4	1.9
6	100.0	50.0	700.0	5	2.2

* : 1 ; clay 2 ; silt 3 ; sand 4 ; gravel 5 ; rock
** : estimated value
*** : estimated value

(b) Hachinohe-S

layer number	thick-ness (m)	blow-count	shear wave velocity** Vs(m/s)	soil clasifi-cation *	density*** (g/cm³)
1	2.0	8.0	100.0	3	1.8
2	2.0	18.5	160.0	3	1.8
3	5.0	18.0	200.0	4	1.9
4	21.0	50.0	275.0	3	1.7
5	30.0	50.0	320.0	3	1.7
6	15.0	50.0	340.0	3	1.8
7	105.0	50.0	379.0	4	1.9
8	180.0	50.0	690.0	5	2.0
9	20.0	50.0	1100.0	5	2.1
10	100.0	50.0	2800.0	5	2.5

* : 1 ; clay 2 ; silt 3 ; sand 4 ; gravel 5 ; rock

(c) Hososhima-S

layer number	thick-ness (m)	blow-count	shear wave velocity** Vs(m/s)	soil clasifi-cation *	density*** (g/cm³)
1	12.0	15.7	200.4	1	1.5
2	7.5	6.0	174.4	2	1.4
3	3.1	27.5	241.4	3	1.8
4	5.4	10.5	243.0	1	1.5
5	4.3	26.0	359.8	1	1.5
6	5.7	22.0	348.7	1	1.5
7	10.0	10.0	291.4	1	1.5
8	3.0	48.0	566.9	1	1.5
9	100.0	70.0	800.0	5	2.2

* : 1 ; clay 2 ; silt 3 ; sand 4 ; gravel 5 ; rock
** : estimated value
*** : estimated value

(d) Aomori-S

layer number	thick-ness (m)	blow-count	shear wave velocity** Vs(m/s)	soil clasifi-cation *	density*** (g/cm³)
1	8.6	10.0	144.0	3	1.8
2	4.9	10.2	173.0	3	1.7
3	7.75	5.5	152.0	2	1.6
4	2.55	14.5	205.0	3	1.6
5	2.70	10.0	205.0	4	1.6
6	10.95	50.0	260.0	4	1.7
7	3.55	55.0	320.0	4	1.9
8	2.20	25.0	320.0	2	1.9
9	71.85	50.0	320.0	3	1.9
10	100.0	50.0	800.0	5	2.2

* : 1 ; clay 2 ; silt 3 ; sand 4 ; gravel 5 ; rock

Table 2.1 Site Structure Models for Japanese Strong Motion Observation Stations(continued).

(e) Shinagawa－S

layer number	thick-ness (m)	blow-count	shear wave velocity** Vs(m/s)	soil clasifi-cation *	density*** (g/cm³)
1	5.9	0.25	101.8	2	1.4
2	5.4	1.9	132.2	1	1.5
3	3.4	10.0	189.5	3	1.8
4	1.8	10.3	215.2	1	1.5
5	5.95	50.0	317.4	4	1.9
6	4.8	50.0	278.1	3	1.8
7	1.65	50.0	330.9	4	1.9
8	100.0	50.0	600.0	5	2.2

* : 1 ; clay 2 ; silt 3 ; sand 4 ; gravel 5 ; rock
** : estimated value
*** : estimated value

(f) Itajima Bridge

layer number	thick-ness (m)	blow-count	shear wave velocity** Vs(m/s)	soil clasifi-cation *	density*** (g/cm³)
1	3.0	3.0	107.0	1	1.5
2	1.0	3.0	107.0	3	1.5
3	4.0	4.5	125.0	3	1.7
4	5.0	10.2	145.0	2	1.8
5	3.5	6.8	125.0	1	1.8
6	100.0	50.0	480.0	5	2.2

* : 1 ; clay 2 ; silt 3 ; sand 4 ; gravel 5 ; rock

(g) Shiogamakoujou－S

layer number	thick-ness (m)	blow-count	shear wave velocity** Vs(m/s)	soil clasifi-cation *	density*** (g/cm³)
1	4.1	7.0	141.5	3	1.8
2	6.3	0.5	113.3	2	1.4
3	4.1	3.0	178.2	3	1.8
4	2.25	50.0	246.6	5	2.2
5	100.0	50.0	800.0	5	2.2

* : 1 ; clay 2 ; silt 3 ; sand 4 ; gravel 5 ; rock
** : estimated value
*** : estimated value

(h) Onahama-ji－S

layer number	thick-ness (m)	blow-count	shear wave velocity** Vs(m/s)	soil clasifi-cation *	density*** (g/cm³)
1	0.75	4.0	162.0	3	1.8
2	3.2	15.0	162.0	3	1.8
3	1.85	38.0	250.0	3	1.8
4	0.9	35.0	448.0	3	1.8
5	1.6	16.0	448.0	4	1.9
6	100.0	50.0	784.0	5	2.2

* : 1 ; clay 2 ; silt 3 ; sand 4 ; gravel 5 ; rock
*** : estimated value

Table 2.1 Site Structure Models for Japanese Strong Motion Observation Stations(continued).

(i) Yamashita-hen-S

layer number	thick-ness (m)	blow-count	shear wave velocity** Vs(m/s)	soil clasifi-cation *	density*** (g/cm³)
1	3.4	11.0	145.9	3	1.8
2	5.85	3.5	135.0	2	1.4
3	2.55	4.0	174.8	3	1.8
4	6.9	19.5	202.1	3	1.8
5	2.2	34.5	306.4	4	1.9
6	14.1	27.25	360.3	2	1.4
7	100.0	50.0	800.0	5	2.2

* : 1 ; clay 2 ; silt 3 ; sand 4 ; gravel 5 ; rock
** : estimated value
*** : estimated value

(j) Miyako－S

layer number	thick-ness (m)	blow-count	shear wave velocity** Vs(m/s)	soil clasifi-cation *	density*** (g/cm³)
1	2.2	5.0	164.0	3	1.8
2	7.55	30.0	308.0	4	1.9
3	1.85	12.0	164.0	1	1.5
4	100.0	50.0	800.0	5	2.2

* : 1 ; clay 2 ; silt 3 ; sand 4 ; gravel 5 ; rock
** : estimated value
*** : estimated value

(k) Tokachi-M

layer number	thick-ness (m)	blow-count	shear wave velocity** Vs(m/s)	soil clasifi-cation *	density*** (g/cm³)
1	2.0	4.0	125.8	1	1.5
2	4.2	10.0	152.7	3	1.8
3	10.0	50.0	304.6	4	1.9
4	100.0	50.0	800.0	5	2.2

* : 1 ; clay 2 ; silt 3 ; sand 4 ; gravel 5 ; rock
** : estimated value
*** : estimated value

(l) Yamashita-dai 6-S

layer number	thick-ness (m)	blow-count	shear wave velocity** Vs(m/s)	soil clasifi-cation *	density*** (g/cm³)
1	5.5	8.0	142.6	3	1.8
2	1.0	35.0	290.3	4	1.9
3	1.36	8.0	168.3	3	1.8
4	1.0	35.0	293.3	4	1.9
5	6.8	38.0	415.8	2	1.4
6	3.2	50.0	316.4	4	1.9
7	1.36	38.0	439.1	2	1.4
8	100.0	50.0	800.0	5	2.2

* : 1 ; clay 2 ; silt 3 ; sand 4 ; gravel 5 ; rock
** : estimated value
*** : estimated value

Table 2.1 Site Structure Models for Japanese Strong Motion Observation Stations(continued).

(m) Sendai－MB

layer number	thick-ness (m)	blow-count	shear wave velocity** Vs(m/s)	soil clasifi-cation *	density*** (g/cm³)
1	0.6	7.0	130.0	3	1.75
2	3.1	18.0	130.0	3	1.75
3	2.6	27.0	180.0	3	1.85
4	2.0	50.0	820.0	5	2.40
5	100.0	50.0	820.0	5	2.40

(n) Kamaishi－MB

layer number	thick-ness (m)	blow-count	shear wave velocity** Vs(m/s)	soil clasifi-cation *	density*** (g/cm³)
1	2.7		250.0	4	1.9
2	1.6		700.0	4	1.9
3	2.5		1100.0	4	1.9
4	1.2		1100.0	5	2.2
5	2.3		2450.0	5	2.2
6	100.0		2450.0	5	2.2

* : 1 ; clay 2 ; silt 3 ; sand 4 ; gravel 5 ; rock

(o) Kaihoku Bridge

layer number	thick-ness (m)	blow-count	shear wave velocity** Vs(m/s)	soil clasifi-cation *	density*** (g/cm³)
1	5.0	5.0	100.0	3	1.8
2	4.0	50.0	650.0	5	2.2
3	100.0	50.0	1300.0	5	2.2

* : 1 ; clay 2 ; silt 3 ; sand 4 ; gravel 5 ; rock
*** : estimated value

Table 2.2 Estimation Formulas for Shear Wave Velocity(Ref.13).

soil	estimation formula for shear wave velocity (m/sec)
clay	V_S = 100.36 + 6.37 N + 3.35 D
silt	V_S = 99.86 + 7.77 N + 2.33 D
sand	V_S = 133.68 + 1.11 N + 3.96 D
gravel	V_S = 252.31 + 0.89 N + 1.25 D

N:blow-count, D:depth in meters

```
DIMENSION SD(4,30),IS(30)
CHARACTER NS*24
   .
   .
CALL SODM(ID,NL,ISC,NS,SD,IS)
   .
   .
```

```
 IC ; soil data number for a specific site
 NL ; number of soil layers
ISC ; information level on soil profile data
      ISC=1 : blow-count and thickness are given
      ISC=2 : blow-count, thickness, and shear wave velocity
              are given
      ISC=3 : blow-count, thickness, shear wave velocity, and
              density are given
 NS ; site name
 SD ; soil profile data
      SD(1,j) : blow-count
      SD(2,j) : thickness in meters
      SD(3,j) : shear wave velocity in m/sec
      SD(4,j) : density in ton/m
 IS ; classification number of soil
      IS(j)=1 : clay
      IS(j)=2 : silt
      IS(j)=3 : sand
      IS(j)=4 : gravel
      IS(j)=5 : rock
```

Fig.2.4 Access Procedure for Soil Profile Data for Strong Motion Observation Stations.

in Fig.2.4.

Table.2.3 gives the total number of the SPT blow-count data distributed over several Japanese urban areas. They have been stored in the SERM-II Database System. Since the ground motion intensities are effected strongly by local soil conditions near surface, these blow-count data can be used efficiently for earthquake microzonations for urban areas. Fig.2.5 shows the distribution of the soil parameter S_n (Ref.8) obtained from the dataset of SPT blow-count for Kyoto and Sendai City. As discussed in Chapter 5, the soil parameter S_n represents the softness of sites within 15 $\sim$ 20 m from the ground surface. The distribution of S_n in Fig.2.5 gives significant information on distribution of ground motion intensities.

2.3 Selection and Modification of Accelerograms for Development of Earthquake Motion Prediction Model on Rock Surface

2.3.1 Significance of Rock Surface Strong Motion Data

It is well known that the shear modulus and the damping factor of soils depend on its strain level and they change remarkably in case of the large strain level such as $\varepsilon > 10^{-3}$. For the estimation of strong motion on soil surface, therefore, the nonlinear amplification characteristic of soils overlying bedrocks shoud be considered, especially in the cases of severe earthquakes. For this purpose the earthquake motion prediction model based on the rock surface strong motion data is efficient because the soil surface motion can be estimated from the rock surface motion considering the nonlinear amplification effect of soils overlying bedrock. Further the earthquake motion prediction on rock surface level is of special importance for the earthquake registant design for significant structures including nuclear power plants which are usually built on rock sites.

In this engineering point of view, the development of rock surface strong motion dataset is quite important. The ninety-one components of modified rock surface strong motion are explained in the following section.

2.3.2 Development of Rock Surface Earthquake Motion Dataset

(1) Definition of Rock Surface

For engineering purposes rock surface with the shear velocity $v_s \fallingdotseq$ 700 m/sec has been dealt with by Hisada, Ohsaki, Watabe, and Ohta(Ref.6), in which the design spectra for significant structures including nuclear power plants have been proposed. In the present study nearly the same level of rock formations as used in Ref.6 has been dealt with. Fig.2.6 shows a schematic illustration for free rock surface and other related site conditions. Point A represents an imaginal case where overlying deposites are removed, and Point A' is an actual case for free rock surface. For other cases ground motion can be obtained after some appropriate modifications such as response analysis of soil layers(E), of irregular ground(C), and of soil structure interactions(B,D).

(2) Strong Motion Dataset on Free Rock Surface

Strong motion data used in this paper consist of 91 components of accelerograms which have been recorded at 17 stations during 26 Japanese earthquakes. These accelerograms have been corrected for baseline and instrument characteristic(Ref.2). Table 2.4 shows the items of the data which are classified into 3 groups. The data from the group A and B have been modified into rock surface ground motion using soil profile data for strong motion observation stations listed in Table 2.1. The procedure of modifications for each group of the data are as follows.

Elimination of surface wave motion and response analysis of soil-overlying ground (Group A)

The data for group A consists of 77 components of accelerograms recorded on 12 alluvial and diluvial sites. Evolutionary spectra(Ref.7) for these data have been examined as for participation of surface wave motion. In 16 motion of the data in group A, surface wave motion were removed by a simple technique for separation of body and surface waves explained in Chapter 3. The parameters t_d and f_d used for the separation are listed in Table 2.5.

Table 2.3 SPT Blow-count Data for Japanese Urban Areas.

city	No.of data	mesh size
Kyoto (Kyoto Pref.)	672	500x500 m
Sendai (Miyagi Pref.)	330	500x500 m
Noshiro (Akita Pref.)	138	250x250 m

Table 2.4 Classification of Strong Motion Dataset.

contents	No. of record components	No. of sites
A; records on the surface of grounds overlying bed rocks	77	12
B; records at underground bed rocks	8	3
C; records on rock surface	6	2

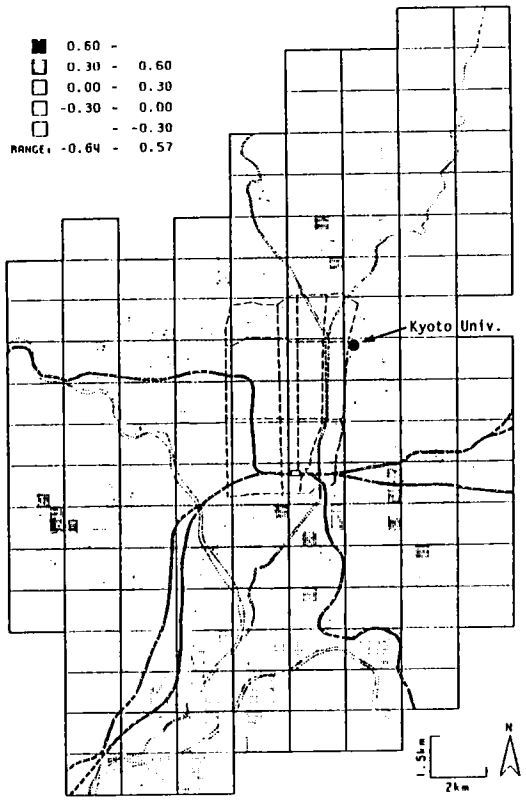

(a) Kyoto City

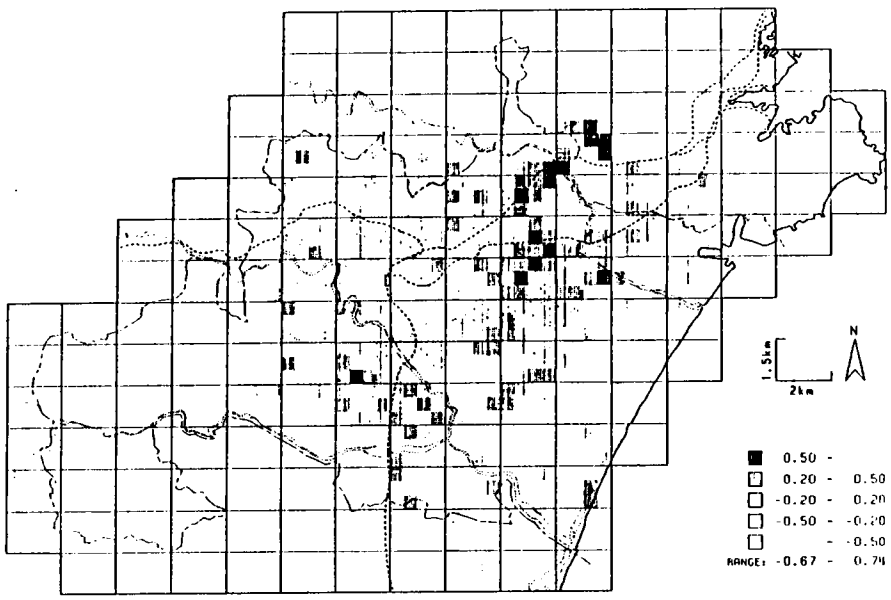

(b) Sendai City

Fig.2.5 Distribution of Soil Parameter S_n for Japanese Urban Areas.

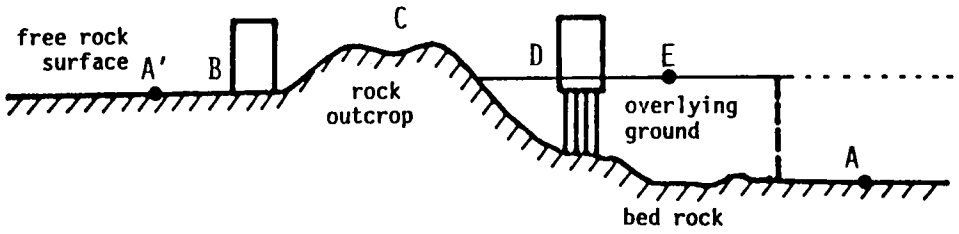

Fig.2.6 Illustration of Bedrock and Free Rock Surface.

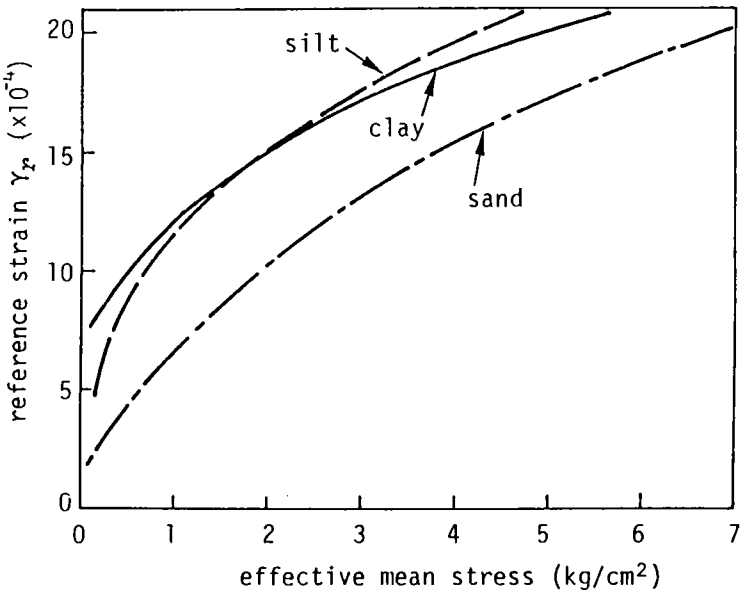

Fig.2.7 Relation between Reference Strain γ_r and Effective Mean Stress for Typical Soils(Ref.4).

Table 2.5 Rock Surface Strong Motion Dataset.

No.	Rec. No.	M	Δ	Comp.	Amax	Amax (free rock)	f_{du}^*	t_d^*	Category**
1	S-213	7.5	110.0	NS	213.4	120.4	-	-	A
2				EW	282.2	174.5	-	-	
3	S-234	7.9	293.0	NS	216.1	175.6	-	-	A
4				EW	245.1	138.0	-	-	
5	S-235	7.9	247.0	NS	252.0	253.2	0.5	25.5	A
6				EW	191.9	165.1	0.5	25.5	
7	S-236	7.9	189.0	NS	167.0	85.3	-	-	A
8				EW	160.3	88.4	-	-	
9	S-241	7.4	196.0	NS	117.4	70.0	-	-	A
10				EW	90.7	61.3	-	-	
11	S-252	7.9	235.0	NS	264.1	181.4	0.5	28.0	A
12				EW	203.3	201.7	0.5	28.0	
13	S-264	7.4	193.0	NS	80.8	57.1	0.7	20.0	A
14				EW	98.6	60.1	0.7	20.0	
15	S-271	7.4	213.0	EW	147.1	67.9	-	-	A
16				NS	121.3	57.2	-	-	
17	S-340	6.1	49.7	NS	87.1	43.1	-	-	A
18				EW	130.9	47.1	-	-	
19	S-453	6.5	52.0	NS	96.5	65.6	-	-	A
20				EW	124.8	90.5	-	-	
21	S-537	5.7	12.0	NS	170.6	82.5	-	-	A
22				EW	152.7	82.3	-	-	
23	S-544	6.7	53.2	NS	145.8	102.0	1.2	7.5	A
24				EW	143.5	147.9	1.2	7.5	
25	605-GR-26	4.8	21.0	NS	-	122.9	-	-	C
26				EW	-	137.5	-	-	
27	308-GR-2	7.5	103.0	LG	194.0	191.2	-	-	A
28				TR	209.3	248.1	-	-	
29	308-GR-8	5.3	18.3	TR	190.6	159.7	-	-	A
30				LG	256.0	264.3	-	-	
31	308-GR-4	6.6	18.7	TR	543.4	491.1	-	-	A
32				LG	600.6	475.6	-	-	
33	S-1204	7.4	166.7	EW	160.6	94.3	-	-	A
34				NS	223.0	123.8	-	-	
35	S-1201	7.4	100.0	NS	316.7	185.8	-	-	A
36				EW	281.7	239.5	-	-	
37	S-1210	7.4	103.0	N41E	-	180.1	-	-	C
38				E41S	-	210.4	-	-	
39	S-1202	7.4	273.0	NS	77.6	47.3	0.62	17.0	A
40				EW	68.7	38.2	0.62	17.0	
41	S-1058	7.0	80.9	E33S	54.3	32.7	0.3	50.0	A
42				S33W	62.7	25.9	0.3	50.0	
43	302-GR-34	6.7	85.8	LG	97.0	111.0	-	-	B
44				TR	170.7	186.6	-	-	
45	302-GR-35	7.4	82.7	LG	315.5	338.0	-	-	B
46				TR	394.4	410.5	-	-	
47	S-1463	5.3	70.0	EW	31.2	23.5	-	-	A
48				NS	48.8	38.0	-	-	
49	S-1470	5.5	57.0	EW	57.4	33.5	-	-	A
50				NS	60.7	23.6	-	-	
51	S-1474	7.1	137.0	NS	159.9	103.4	-	-	A
52				EW	180.5	121.3	-	-	
53	S-1494	6.1	63.0	S15W	-	28.4	-	-	C
54				W15N	-	53.4	-	-	
55	S-1497	6.1	110.0	EW	46.1	23.8	-	-	A
56				NS	53.6	28.4	-	-	
57	S-1505	7.0	124.0	EW	111.8	48.4	-	-	A
58				NS	93.5	49.5	-	-	
59	S-1509	7.0	207.0	E03N	30.4	12.7	-	-	A
60				S03E	29.8	12.1	-	-	
61	S-1514	7.0	251.0	EW	30.5	24.7	-	-	A
62				NS	23.8	18.4	-	-	
63	S-1518	5.7	64.0	W33N	23.3	14.5	-	-	A
64				N33E	42.3	20.0	-	-	
65	S-1519	5.7	64.0	E33S	48.9	20.4	-	-	A
66				S33W	82.4	33.7	-	-	
67	S-1521	5.3	49.0	EW	43.1	27.6	-	-	A
68				NS	34.3	23.0	-	-	
69	S-1526	5.3	79.0	EW	54.5	46.1	-	-	A
70				NS	21.3	16.8	-	-	
71	S-1528	4.8	25.0	EW	62.8	30.2	-	-	A
72				NS	90.9	54.3	-	-	
73	S-1532	5.1	48.0	EW	28.0	13.9	-	-	A
74				NS	34.6	13.3	-	-	
75	S-1571	7.7	270.0	EW	28.6	17.6	-	-	A
76				NS	37.5	18.8	-	-	
77	S-1573	7.7	156.0	EW	149.5	192.3	0.38	31.0	A
78				NS	117.3	96.7	0.33	56.0	
79	S-1592	7.1	160.0	EW	72.7	40.8	0.23	43.0	A
80				NS	59.0	37.3	0.45	55.6	
81	S-1599	7.1	201.0	EW	68.0	36.3	-	-	A
82	M-521	7.1	64.0	NS	143.5	70.9	-	-	A
83				EW	275.6	119.2	-	-	
84	M-522	5.8	59.0	NS	26.9	9.1	-	-	A
85				EW	33.1	13.8	-	-	
86	M-540	5.2	59.0	NS	61.8	25.9	-	-	A
87				EW	64.7	30.5	-	-	
88	M-546	6.1	75.0	N07W	15.0	16.6	-	-	B
89				E07N	13.9	14.9	-	-	
90	M-574	5.3	77.0	NS	11.5	12.6	-	-	B
91				EW	8.4	11.9	-	-	

*separation parameters for elimination of surface wave (Chapter 3)
**corresponds to the contents in Table 2.4

Earthquake motion on bed rock level were calculated using the soil profile data for the stations. Multi-reflection technique and equivalent linear model have been used for the response analysis. It is similar to the SHAKE program developed by Schnabel, Lysmer, and Seed(Ref.12). However, the effect of ground motion duration on the effective shear strain γ_e has been incorporated in the following formula.

$$\gamma_e=0.6(T_d/T_m)^{0.1}\gamma_{max} \tag{2.1}$$

where γ_{max} =maximum shear strain, T_d=ground motion duration defined by Vanmarke and Lai (Ref.16) ($T_d=7.7P_t/A_p^2$, P_t= acceleration total power and A_p= peak acceleration), and T_m= mean value of T_d for the data (herein T_d=6.9 sec). The effective strain γ_e takes $0.5 \sim 0.7\gamma_{max}$ depending on the duration T_d of the strong motion data. The numerals in Eq.(2.1) have been fixed on the basis of the results(Ref.12) where several ground motion records of different duration were analyzed.

For the relation between shear modulus, damping, and strain level, the experimantal formulas proposed by Hardin and Drnevich(Ref.4) have been applied. The shear modulus G and damping h for given shear strain level γ are given as follows.

$$\frac{G}{G_{max}} = \frac{1}{1+\gamma/\gamma_r}, \qquad \frac{h}{h_{max}} = \frac{\gamma/\gamma_r}{1+\gamma/\gamma_r} \tag{2.2}$$

where G_{max}= shear modulus for initial condition, h_{max}= maximum damping factor fixed as $h_{max}\fallingdotseq 30\%$, and γ_r= reference strain which is the function of of the effective mean principal stress. Fig.2.7 shows the values of γ_r for the three types of soils.

After several times of iterative calculation (within 5% error for the maximum shear strain), input motion on rock level were obtained. Then, corresponding rock surface ground motion are given from the input motion by multiplying them by two. The nonlinear amplification characteristic of soil layers are shown in Fig.2.8. In Fig.2.8 the relation between the peak acceleration on rock surface level and the amplification ratio of peak

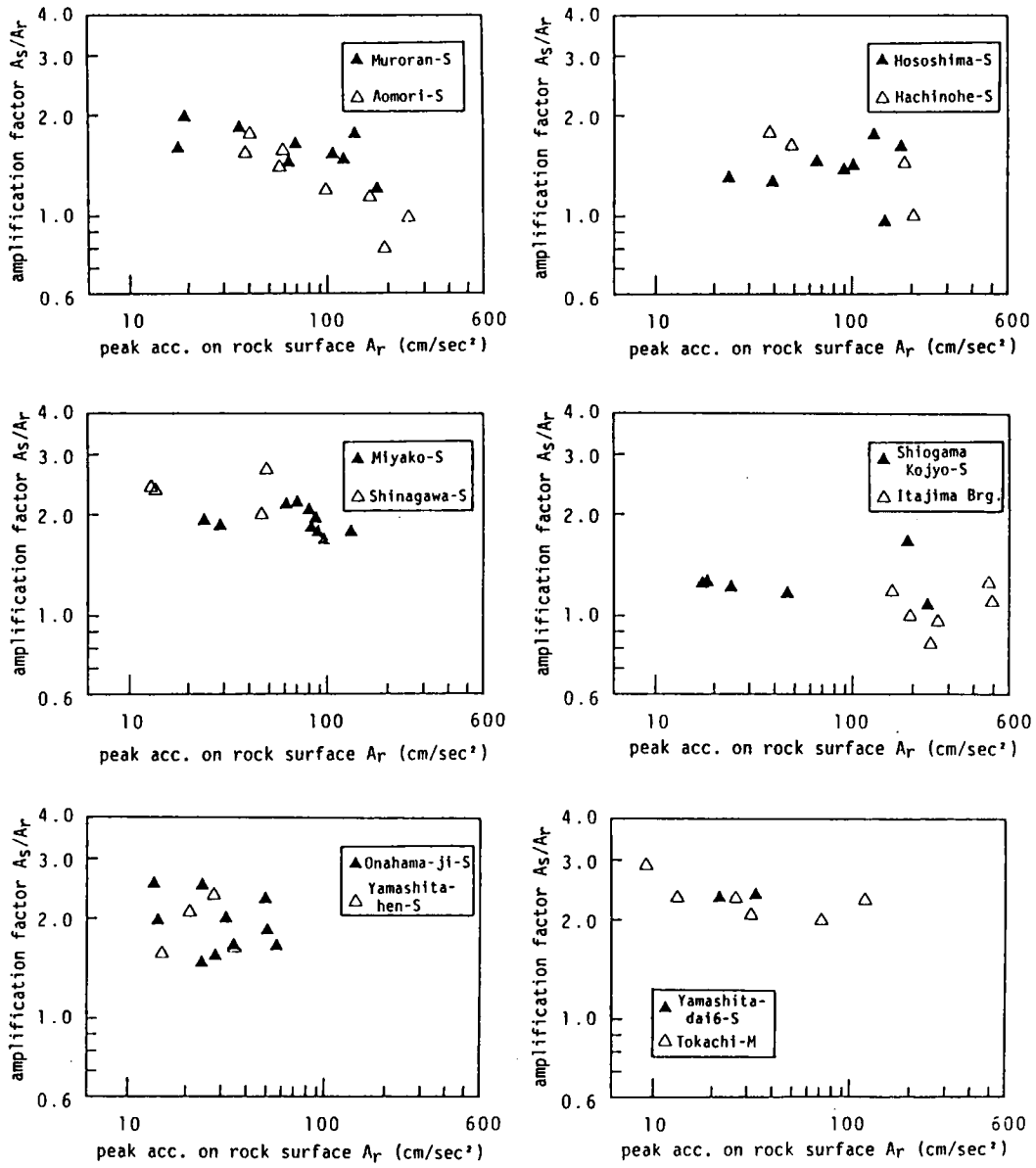

Fig.2.8 Relation between Amplification Factor A_S/A_r and Corresponding Value for Peak Acceleration on Rock Surface A_r.

acceleration between soil surface and rock surface are shown. In the case of the sites which have deep soil deposite or soft surface layers, it is clear that the amplification ratio decreases with increase in the peak acceleration on rock surface level (Aomori-S, Muroran-S sites). On the other hand the nonlinearity of soil amplification is not notable for harder ground and the variation of the amplification ratio is relatively remarkable (Miyako-S, Onahama-ji-S sites).

Response analysis of soil layers for the data recorded at underground bed rock (Group B)

8 components of the data in Group B have been obtained by underground accelerographs at 3 sites during 4 earthquakes. The input amplitudes of bed rock ground motion have been calculated by using the same response analysis procedure as described above. Then corresponding free rock surface motion have been obtained.

Records on rock surface (Group C)

6 components of the data in Group C have been obtained at 2 rock sites during 3 earthquakes. They have been included in the dataset without any modification.

The strong motion dataset on rock surface arranged as described above, are listed in Table 2.5. The scattergram of magnitude and epicentral distance are shown in Fig.2.9. The dashed line in Fig.2.9 shows the boundary of epicentral regions(Ref.7) where the ground motion intensities can be regarded not to depend on the epicentral distance. Fig.2.10 shows the histogram of peak acceleration for the dataset.

2.4 Conclusions

In this chapter, significance of the numerical database in the field of earthquake engineering has been demonstrated. The corrected strong motion accelerograms and soil profile data for strong motion observation stations have been stored in the SERM-II Database System, and they were breifly

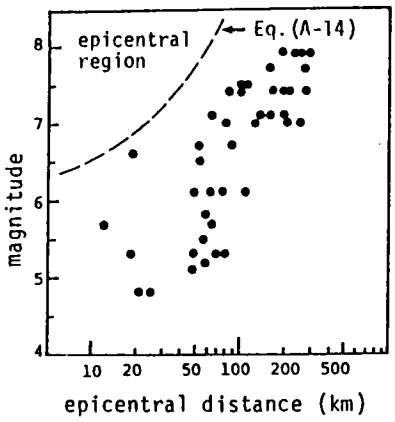

Fig.2.9 Scattergram of Magnitude and Epicentral Distance.

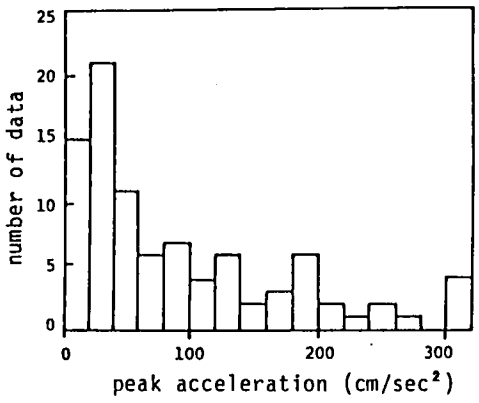

Fig.2:10 Histogram of Peak Acceleration.

introduced.

On this basis the modified acceleration dataset of rock surface motion has been developed, which is used for the development of earthquake motion prediction models in Chapter 4. This dataset is termed Strong Motion Dataset on Rock Surface(SMD-R), and consists of 91 components which are classified into three types : (1) rock surface ground motion estimated from the accelerograms recorded on alluvial and diluvial sites, (2) rock surface ground motion modified from bedrock ground motion, and (3) ground motion recorded on rock surface. In Chapter 4, the dataset SMD-R is used for the development of earthquake motion prediction model on rock surface ground, which include the models for nonstationary earthquake motion as well as the models for the peak ground motion, the ground motion duration, and the response spectra.

References

1) Aoki,T.,Ohta,Y.,Sakai,Y.(1979), "Analysis on Strong Motion Accelerograms Recorded by SMAC Accelerograph in Hokkaido Area," Natural Disaster Data Analysis, No.6.
2) Design Seismic Load Research Group(SLG)(1984), "Corrected and Integrated Earthquake Motion Accelerograms (Graphical Information)," Revised Edition, Research Report, No.84-ST-03, School of Civil Engineering, Kyoto University.
3) Earthquake Engineering Research Laboratory(1974), "Strong Motion Earthquake Accelerograms, Digitized and Plotted Data," California Institute of Technology, Vol.II, Part A-H.
4) Hardin,B.O. and Drnevich,V.P.(1972), "Shear Modulus and Damping in Soils," Proc. ASCE, Vol.98, SM6,7.
5) Goto,H., Kameda,H., Takada,S., and Sugito,M. (1981), "Earthquake Motion Estimation for Buried Lifelines," 2TCLEE, pp.321-334.
6) Hisada,T., Ohsaki,Y., Watabe,M., and Ohta,T.(1978), "Design Spectra for Stiff Structures on Rock," 2nd International Earthquake Microzonation Conference, Vol.III, pp.1178-1198.
7) Kameda,H.(1975), "Evolutionary Spectra of seismogram by Multifilter," Jour. Eng. Mech. Div., ASCE, Vol.101, No.EM6, pp.787-801.

8) Kameda,H., Sugito,M., and Goto,H.(1982), "Microzonaiotion and Simulation of Spatially Correlated Earthquake Motions," Proc. of the 3rd International Earthquake Microzonation Conference, Vol.III, pp.1463-1474.

9) Osawa,Y. et al.(1972), "Analysis on Accelerograms from 1968 Tokachi-oki Earthquake and Soil Structures at Hachinohe Site." Report of Science Research, Ministry of Education(in japanese).

10) Port and Harbour Research Institute, Ministry of Transport(1969-1985), "Technical Note of Port and Harbour Research Institute," Nos.80, 98, 100, 116, 136, 160, 181, 202, 236, 250, 317, 319, 446, 458, 511.

11) Public Works Research Institute, Ministry of Construction(1973-1979), "Technical Note of Public Works Research Institute," Nos.876, 877, 1072.

12) Schnabel,R.B., Lysmer,J., and Seed,H.B.(1972), "SHAKE A Computer Program for Earthquake Response Analysis of Holizontally Layered Sites," EERC, No.72-12.

13) Tajime,T.,Mochizuki,T.,Matsuda,I.(1977), "Site Condition and Earthquake Damage," Maki Book Corporation.

14) Tsuchida,H., Kurata,E., Yamada,T., Ishizaki,T., and Yokoyama,Y. (1967-1980), "Soil Profiles at Strong Motion Stations," Technical Note of the Port and Harbor Research Institute, Ministry of Transport, No.34, 107, 156, 298, 351(in Japanese).

15) Tsunekawa,H., Kameda,H., Sugito,M., and Goto,H.(1985), "Development of a Database for Earthquake Engineering Research(SERM-II) Using a Relational Databese System," Earthquake Engineering Research Report, School of Civil Engineering, Kyoto University, No.85-1.

16) Vanmarke,E.H. and Lai,S-S.P.,(1980), "Strong Motion Duration and RMS Amplitude of Earthquake Records," BSSA, Vol.70, No.4, pp.1293-1307.

3. SIMPLIFIED SEPARATION TECHNIQUE OF BODY AND SURFACE WAVES IN STRONG MOTION ACCELEROGRAMS

3.1 General Remarks

It is a significant subject in earthquake engineering to evaluate ground strain caused by earthquake motion. For estimation of ground strain the multi-reflection theory for shear waves has been often applied for ground motion records. Haskell's model(Ref.3) for surface wave analysis has been also used(Ref.5) for estimation of ground strain caused by surface wave propagation. The strong motion data used for calculation of ground strain should be confirmed whether it consists of body waves or of surface waves. Most of strong motion data, however, consist of body and surface waves, and it is impossible to separate exactly these two types of waves in the data recorded at a single independent site. Dence observation networks for strong ground motion have been recently set up by many research groups(Ref.7) to observe relative ground motion caused by surface and body waves. The arrey data from these network stations have been accumulated little by little, however, the data from strong earthquakes have been scarecely obtained.

In this view of the problem, a simplified separation technique of body and surface waves in strong motion accelerograms is dealt with in this chapter. The evolutionary power spectrum(Ref.4) of strong motion accelerograms have been obtained to specify dispersion characteristic of surface waves. Difference of strain level of surface waves calculated from original data and separated surface waves has been discussed regarding to a relative distance in which relative ground motion are considered.

3.2 Separation of Body and Surface Waves in Strong Motion Accelerograms

Surface waves which propagate in multi-layered media have dispersion characteristic. Evolutionary power spectrum(Ref.4) can make it possible to recognize dispersive wave energy of surface waves in strong motion time histrories(Ref.6). In this study Rayleigh wave, one of the major surface waves, is dealt with as an example of surface wave components. Therefore the evolutionry power spectra for the ground motion in the direction to the

epicenter are examined in the following calculations.

Fig.3.1 shows an example of evolutionary power spectra of strong motion records at Hachinohe-S site from the 1968 Tokachi-oki Earthquake(Ref.9). The filter damping β_0(Ref.4) has been fixed as β_0= 0.05 in calculation of evolutionary spectra. In Fig.3.1, the acceleration time history, which has been corrected(Ref.1) for baseline and instrument, represents ground motion in the direction to the epicenter.

Generally, surface waves can be recognized sometime after the principle motion in recorded accelerograms which contain surface wave components, and surface waves are dominant in relatively low frequency range. Therefore, the peak time $t_*(f)$, which gives a time when the evolutionary spectrum gets its maximum value, can be modeled as shown in Fig.3.2. The point A in Fig.3.2 represents the predominant frequency of surface waves and the energy of waves are concentrated at around this frequency. From these characterictic of surface waves, the ground motion in the shadowed area in Fig.3.2 can be regarded to consists mainly of surface wave components. As shown in Fig.3.2, the lower and upper separation frequencies f_{d_l}, f_{d_u} can be determined at the point B_1 and B_2. the dispersion characteristic cannot be found outside between B_1 and B_2. The separation parameter t_d can be also defined to separate body and surface waves in time domain. The parameter t_d is defined as the time when the evolutionary spectra of low frequency range, in which dispersive wave energy can be observed, start to increase.

Fig.3.3 shows other two typical examples of evolutionary spectra. Fig.3.3(a) shows the example that a depth of fault d_f is quite shallow(less than 10 km), and the dispersive wave energy are recognized clearly. The separation parameters can be determined as f_{d_u}= 0.45 Hz, f_{d_l}= 0.15 Hz, and t_d= 11.6 second. On the other hand, the dispersive wave energy cannot be found in the case of Fig.3.3(b), a fault depth d_f of which is 40 km.

After obtaining the separation parameters f_{d_u}, f_{d_l} and t_d from the evolutionary power spectra of the accelerograms, the separated body wave $x_b(t)$ and surface wave $x_s(t)$ can be represented as follows.

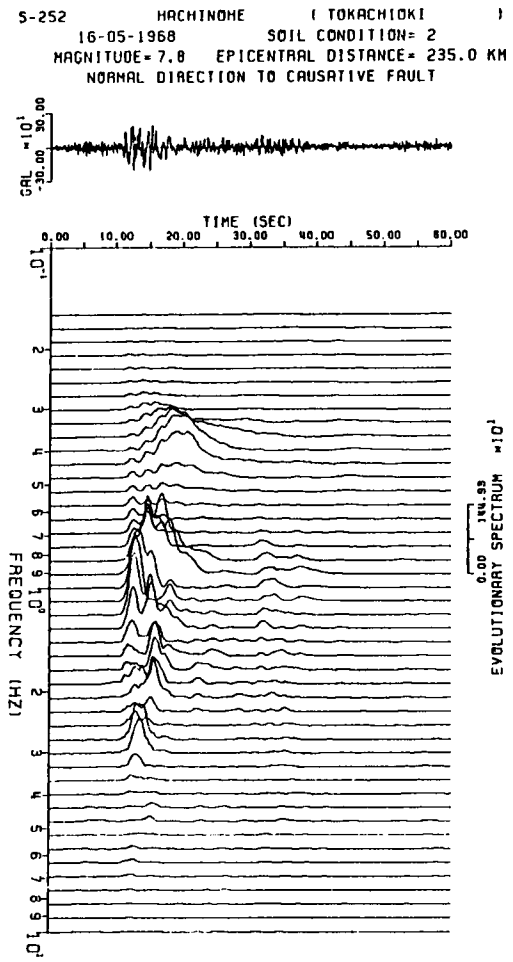

Fig.3.1 Evolutionary Power Spectra with Acceleration Time History (S-252 Hachinohe, Direction to Epicenter, 1968 Tokachi-oki Earthquake).

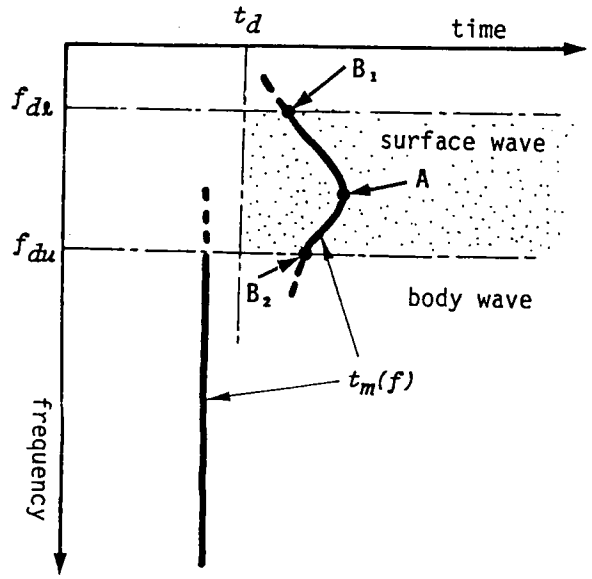

Fig.3.2 Schematic Description for Peak Time $t_m(f)$ of Evolutionary Power Spectra with Separation Parameters.

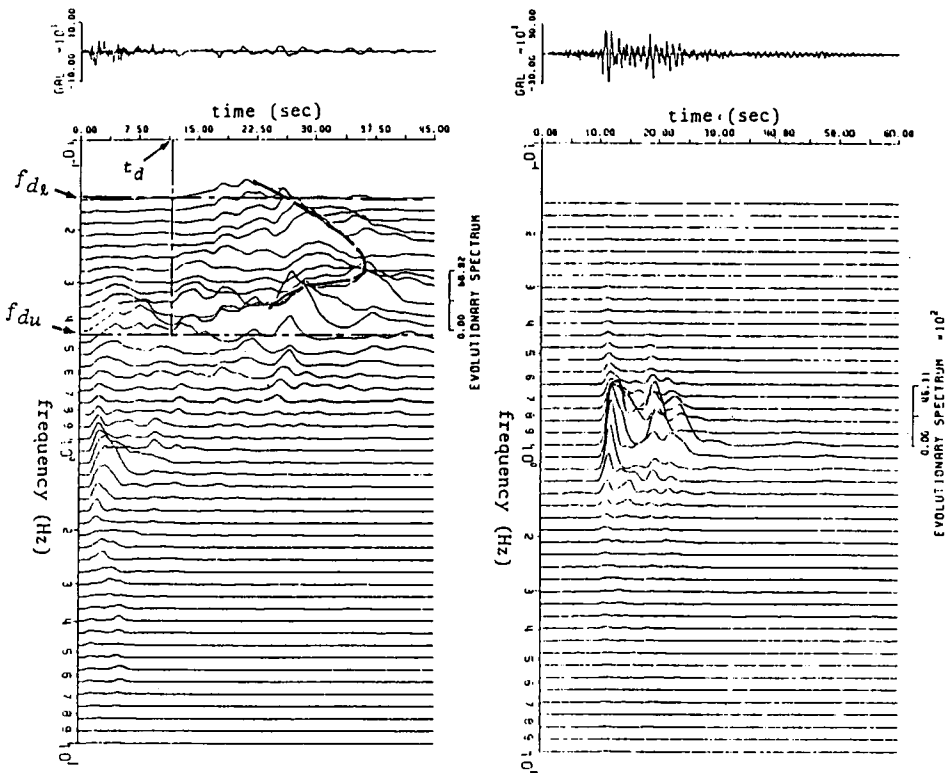

(a) S-1066 Shimizumiho, Direction to Epicenter , Izu-oshima Kinkai Earthq., M=7, Δ=71.4 km d_f<10 km.

(b) S-1202 Shiogama Kojyo, Direction to Epicenter, 1978 Miyagiken-oki Earthq., M=7.4, Δ=100 km, d_f=40 km.

Fig.3.3 Typical Examples of Evolutionary Power Spectra.

(a) $0 \leqq t \leqq t_d$

$$x_b(t) = \int_{-\infty}^{\infty} F(f) e^{2\pi i f t} df,$$

$$x_s(t) = 0 \tag{3.1}$$

(b) $t_d < t$

$$x_b(t) = \int_{-\infty}^{\infty} F_b(f) e^{2\pi i f t} df,$$

$$x_s(t) = \int_{-\infty}^{\infty} F_s(f) e^{2\pi i f t} df \tag{3.2}$$

in which,

$$F_b(f)=0, \qquad F_s(f)=F(f) \quad (f_{d_l} \leqq f \leqq f_{d_u})$$

$$F_b(f)=F(f), \quad F_s(f)=0 \quad (f_l \leqq f < f_{d_l}, \quad f_{d_u} < f \leqq f_u)$$

where $F(f)$= Fourier Transform for accelerogram $x(t)$, and f_l, f_u = lower and upper boundary frequency, respectively. These boundary frequencies are fixed as f_l=0.15 Hz and f_u=10.0 Hz, according to the correction filter(Ref.1) for the accelerograms used in this study.

Fig.3.4 shows examples of separated body and surface waves with its original time histories. The separation parameters for this accelerograms have been given as t_d=10.0 sec and f_{d_u}=0.48, f_{d_l}=0.25 Hz in Fig.3.1. It can be observed that body wave mainly contributes to acceleration of original data and surface wave mainly contributes to displacement in these cases. It may be concluded that the separation procedure descrimbed above can be used for separation of body and surface waves as an approximate estimation in the case that the dispersive wave components are predominant in its evolutionary power spectra.

3.3 Ground Strain Caused by Body and Surface Waves

Ground strain caused by body and surface waves have been discussed using the separated waves and its original data. As a typical example the soil profile data(Ref.8) shown in Table 3.1 and the corrected accelerograms dealt

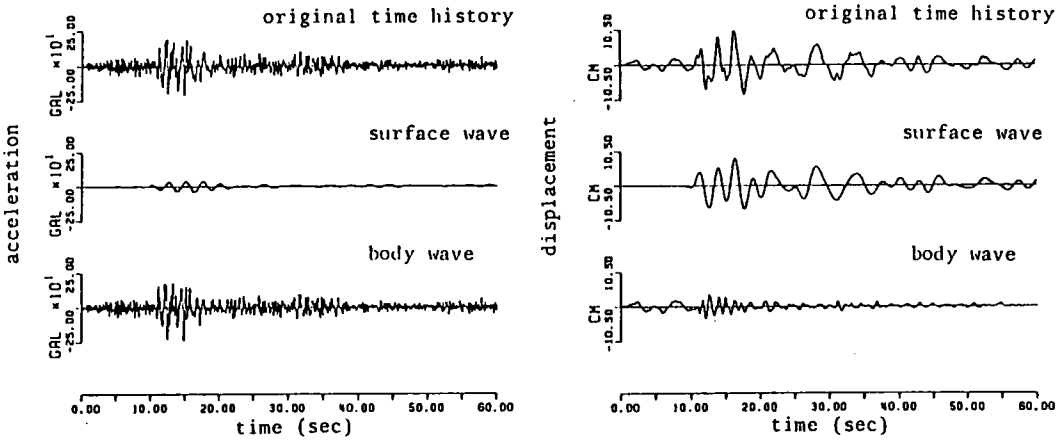

Fig.3.4 Separated Body and Surface Waves with Its Original Time History (S-252 Hachinohe, Direction to Epicenter, 1968 Tokachi-oki Earthquake, t_d=10 sec, $f_{d\ell}$=0.13 Hz, f_{du}=0.48 Hz).

Table 3.1 Velocity Model for Hachinohe-S Site(Ref.8).

layer number	thickness (m)	v_s (m/sec)	v_p (m/sec)	density (gr./cm^3)
1	2.0	100.0	332.0	1.8
2	2.0	160.0	531.0	1.8
3	5.0	200.0	664.0	1.9
4	21.0	275.0	912.0	1.7
5	30.0	320.0	1061.0	1.7
6	15.0	340.0	1128.0	1.8
7	105.0	379.0	1257.0	1.9
8	180.0	690.0	2284.0	2.0
9	20.0	1100.0	3641.0	2.1
10	——	2800.0	5240.0	2.5

in the previous chapter have been used. The P-wave velocity v_p in Table 3.1 is given by use of;

$$v_p = v_s \cdot \frac{2(1-\nu)}{1-2\nu} \tag{3.3}$$

where v_s= shear wave velocity and Poisson's ratio ν is given as ν=0.45 for sand and gravel, ν=0.46 for clay and silt(Ref.2) , and ν=0.3 for rock.

1) Ground Strain Caused by Body Waves

Ground strain caused by body waves have been examined for separated body waves and its original data using the multi-reflection theory for shear waves. The equi-linearized method for shear rigidity and damping has been used for numerical calculations. Table 3.2 shows peak ground strain at the top of each layer of Hachinohe site.

In Table 3.2 peak ground strains for original data and separated body waves do not differ very much specially in the layers near surface ground. The difference of the shear strain between these cases is larger for deeper layers, since the shear strain in the deeper layers is mainly caused by seismic waves of relatively longer period. This result supports the idea that the original data can be used for the approximate estimation of ground strain for body waves for upper soil layers.

2) Ground Strain Caused by Surface Waves

Ground strain caused by surface waves have been examined for original data and separated surface waves. Relative ground motion at two points of relative distance D(Ref.10) along the ground have been dealt with for evaluation of ground strain caused by surface wave motion.

Mean ground strain $\varepsilon(D,t)$ between two points of relative distance D can be represented as

Table 3.2 Maximum Shear Strain at Top of Each Layers obtained from Separated Body Wave and Original Time History (S-252 Hachinohe, 1968 Tokachi-oki Earthquake).

(unit $x10^{-4}$)

layer number	original wave	separated body wave
1	0.	0.
2	3.73	3.70
3	3.31	3.34
4	3.21	2.98
5	4.43	4.01
6	6.27	5.70
7	4.62	4.30
8	1.24	0.63
9	1.01	0.61
10	0.15	0.10

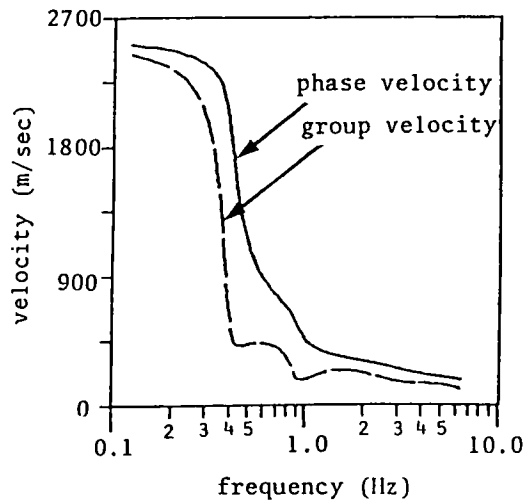

Fig.3.5 Phase and Group Velocity of Principal Mode of Rayleigh Wave for Hachinohe-S Site.

$$\varepsilon(D,t)=\int_{-\infty}^{\infty}F_d(f)\,ik\sin(kD/2)\,(kD/2)e^{2\pi ift}df \tag{3.4}$$

where $F_d(f)$ = Fourier Transform for displacement $d(t)$, k = wave number given as $k=f/c$, and c = phase velocity of surface waves. Ground strain $\varepsilon(t)$ for D=0 is given as

$$\varepsilon(t)=\int_{-\infty}^{\infty}F_d(f)\,ike^{2\pi ift}df \tag{3.5}$$

Fig.3.5 shows phase and group velocities of principal mode of Rayleigh wave for Hachinohe site. The frequency range where dispersive characteristic are predominant is approximately 0.25 $\sim$ 0.45 Hz, and the resonant frequency is around 0.35 $\sim$ 0.4 Hz. These values coincide with those in Fig.3.1.

Assuming that the Rayleigh waves are eminent in the direction to the epicenter, mean ground strain caused by Rayleigh waves have been examined. Fig.3.6 shows examples of mean ground strain obtained from separated surface wave and original data. In case of original data shown in Fig.3.6(b), ground strain strongly depends on relative distance D. The reason for the large value of ground strain for a case of small relative distance is that high frequency componebts of body waves have been regarded as surface waves: these high frequency components, which are regarded to have short wave length, amplify the surface wave strain strongly. Fig.3.7 shows relation between peak values of mean ground strain and relative distance. It can be seen that the peak value of mean ground strain obtained from original data approach that from separated surface waves with increase of relative distance.

From the above numerical results it can be concluded that the separation of surface waves from original data is important specially for a case of estimation of local ground strain.

3.4 Statistical Characteristic of Earthquake Surface Waves Contained in Strong Motion Records

The statistical characteristic of earthquake surface waves contained in

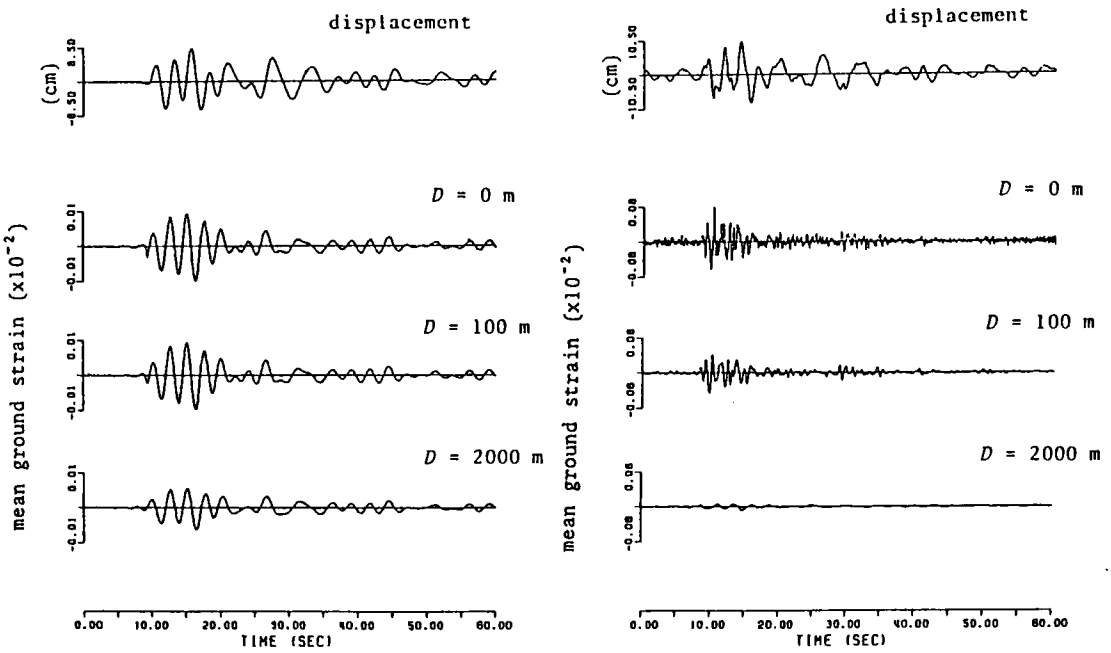

(a) separated surface wave

(b) original time history

Fig.3.6 Mean Ground Strain obtained from Separated Surface Wave and Its Original Time History, and Displacement Time History (S-252 Hachinohe, Direction to Epicenter, 1968 Tokachi-oki Earthquake, t_d=10 sec, $f_{d\ell}$=0.13 Hz, f_{du}=0.48 Hz).

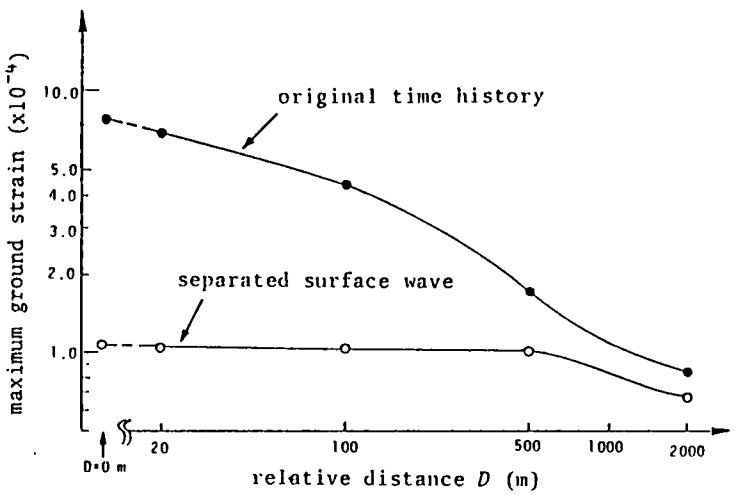

Fig.3.7 Maximum Ground Strain obtained from Separated Surface Wave and Its Original Time History against Relative Distance.

strong motion records have been examined using 367 components of corrected accelerograms stored in the SERM-II Database System. The earthquake surface wave motion have been recognized in 68 components of accelerograms, and the separation parameters for these components have been obtained. The separation parameters and other relevant parameters for these records are listed in Table 3.3.

Table 3.4 shows the occurence ratio of surface wave motion for each earthquakes. Table 3.4(a) shows the list of earthquakes for remarkable occurence of surface wave motion, and Table 3.4(b) for unremarkable occurence of surface wave motion. In the other hand the occurence ratio for each observation sites are shown in Table 3.5(a) and (b). The mean value for the occurence ratio of surface wave motion is 0.18(=68/367). The number of sites, the occurence ratio of which are less than 0.18, is larger than that of earthquakes with the ratio lower than 0.18. It can be supposed that the occurence ratio depends strongly on site condition rather than on earthquake characteristic. In the other words the surface wave motion in the frequency range dealt herein is mainly caused and amplified by local soil condition.

In the following the factor analysis on the occurence of surface wave motion is examined as for several seismic parameters. The strong motion data dealt herein are classified into the following 6 categories.

A : Surface wave motion is clearly recognized and the separation parameters can be obtained(68 comp.)

B_1 : The posibility for containing surface wave motion may be high, and the component for the other direction belongs to the category A(17 comp.)

B_2 : The posibility for containing surface wave motion may be high, however the component for the other direction does not belong to the category A(45 comp.)

C_1 : the several peaks are recognized in the evolutionary power spectra of lower frequency range. Namely, there is some posibility for containing surface wave motion. The component for the other direction belongs to the category A(13 comp.)

C_2 : The same condition as the category C_1 however the component for the other direction dose not belong to the category A(46 comp.)

Table 3.3 Surface Wave-Containing Earthquake Motion Data.

No.	Ref.*1 No.	site	earthquake	t_d (sec)	f_{d_1} (Hz)	f_{d_2} (Hz)	f_0 (Hz)	M	Δ (km)	d_f*2 (km)	comp.
1	1	Shimizukōjyō-S	Shizuoka, off-shore	10.0	0.6	0.85	0.72	6.1	135.0	40.0	N-S
2	2	Shimizukōjyō-S	Shizuoka, off-shore	13.0	0.6	0.85	0.72	6.1	135.0	40.0	E-W
3	4	Kashima-S	Ibaragi, off-shore	13.0	0.37	0.8	0.59	6.0	72.2		E-W
4	11	Aomori-S	1968 Tokachi-oki	47.0	0.2	0.45	0.33	7.9	247.0	20.0	N-S
5	12	Aomori-S	1968 Tokcchi-oki	57.0	0.2	0.45	0.33	7.9	247.0	20.0	E-W
6	18	Hachinohe-S	1968 Tokachi-oki	39.5	0.29	0.48	0.39	7.9	235.0	20.0	N-S
7	19	Hachinohe-S	1968 Tokachi-oki	32.0	0.29	0.48	0.39	7.9	235.0	20.0	E-W
8	21	Aomori-S	1968 Tokachi-oki	68.0	0.33	0.6	0.47	7.4	193.0	20.0	N-S
9	22	Aomori-S	(Aftershock)	44.5	0.33	0.6	0.47	7.4	193.0	20.0	E-W
10	23	Wakayama-ji-S	Wakayama, off-shore	2.5	0.72	1.2	0.96	5.0	6.0		N-S
11	25	Wakayama-ji-S		1.5	0.9	1.4	1.15				N-S
12	26	Wakayama-ji-S		1.5	1.5	2.5	2.00				E-W
13	38	Hososhima-S	Miyazaki, off-shore	12.0	0.85	1.2	1.03	6.7	53.2	10.0	N-S
14	45	Kinuura-S	Aichi, off-shore	10.0	0.41	0.6	0.51	6.1	54.2	40.0	U-D
15	64	Ochiai(B)	Matsushiro	4.5	0.35	0.63	0.49	5.1	8.0	4.3	LG
16	65	Ochiai(B)	Matsushiro	4.5	0.35	0.63	0.49	5.1	8.0	4.3	TR
17	66	Ochiai(A)	Matsushiro	5.5	0.34	0.65	0.50	5.1		4.3	LG
18	67	Ochiai(A)	Matsushiro	3.0	0.41	0.65	0.53	5.1		4.3	U-D
19	68	Ochiai(A)	Matsushiro	4.5	0.38	0.61	2.50	5.1		4.3	TR
20	72	Ochiai(C)	Matsushiro	5.85	1.4	2.5	1.95	4.7		5.6	E-W
21	75	Ochiai(B)	Matsushiro	1.6	0.73	1.2	0.97	5.5			TR
22	88	Ochiai(B)	Matsushiro	3.5	0.72	1.3	1.01	4.6		5.0	LG
23	90	Ochiai(B)	Matsushiro	3.5	0.72	1.3	1.01	4.6		5.0	TR
24	107	Itajima Bridge	Ehime, West coast	2.16	1.1	2.1	1.60	5.3	18.3	40.0	TR
25	112	Ochiai(B)	Matsushiro	4.2	0.45	1.2	0.83	4.5	24.1	0.0	U-D
26	114	Ochiai(B)	Matsushiro	1.8	1.6	2.3	1.95	4.5	15.1	0.0	E-W
27	131	Toyohama Bridge	Aichi, off-shore	8.19	1.1	1.7	1.40	6.1	42.3	40.0	U-D
28	161	Omigawa Bridge	Chiba, off-shore	11.0	1.3	2.5	1.90	6.1	58.2	60.0	U-D
29	172	Tonegawa		9.5	0.6	1.8	1.20				TR
30	183	Chiba-S	1978 Miyagiken-oki	75.0	0.32	0.6	0.46	7.4	340.9	40.0	SOUTH
31	184	Niigata-ji-S	〃	56.0	0.32	0.6	0.46	7.4	272.7	40.0	EAST
32	189	Aomori-S	〃	67.0	0.38	0.72	0.55	7.4	324.2	40.0	EAST
33	200	Koshima-zokan-S	〃	87.0	0.2	0.41	0.31	7.4	281.0	40.0	DOWN
34	207	Ofunado-bochi-S	〃	32.0	0.5	0.8	0.65	7.4	103.0	40.0	DOWN
35	208	Hachinohe-S	〃	27.0	0.36	0.65	0.51	7.4	273.0	40.0	SOUTH
36	210	Hachinohe-S	〃	27.0	0.36	0.65	0.51	7.4	273.0	40.0	WEST
37	216	Shimizu-miho-S	1978 Izu-oshima-kinkai	26.0	0.21	0.53	0.37	7.0	71.4	0.0	EAST
38	218	Shimizu-miho-S		17.0	0.15	0.3	0.23	7.0	71.4	0.0	SOUTH

Table 3.3 Surface Wave-Containing Earthquake Motion Data(Continued).

No.	Ref.*1 No.	site	earthquake	t_d (sec)	f_{d_l} (Hz)	f_{d_u} (Hz)	f_0 (Hz)	M	Δ (km)	d_f*2 (km)	comp.
39	220	Okitsu-S	1978 Izu-oshima-kinkai	27.0	0.21	0.36	0.28	7.0	76.0	0.0	DOWN
40	228	Shimizu-kojyo-S		43.0	0.23	0.45	0.34	7.0	76.0	0.0	S06E
41	235	Tagonoura-S	"(Aftershock)	60.0	0.41	0.53	0.47	5.8	38.0	20.0	W15N
42	238	Shimizu-miho-S	"(Aftershock)	26.0	0.26	0.53	0.39	5.8	41.0	20.0	EAST
43	239	Shimizu-miho-S	"(Aftershock)	36.0	0.26	0.53	0.39	5.8	41.0	20.0	DOWN
44	240	Shimizu-miho-S	"(Aftershock)	24.0	0.26	0.53	0.39	5.8	41.0	20.0	SOUTH
45	241	Shimizu-kojyo-S	"(Aftershock)	14.0	0.28	0.53	0.41	5.4	35.0	10.0	S06E
46	257	Wakayama-S	Wakayama	2.75	1.4	2.2	1.80	3.8	6.0	0.0	S12W
47	265	Onahama-ji-S	Kashimanada	5.64	0.15	0.38	0.27	5.5	57.0	60.0	DOWN
48	268	Tomakomai-S	1982 Urakawa, off-shore	43.0	0.23	0.44	0.34	7.1	102.0	40.0	E08N
49	289	Kashima-zokan-S	Ibaragi, off-shore 2	45.0	0.21	0.42	0.32	7.0	118.0	30.0	DOWN
50	331	Aomori-S	1983 Nihonkai chubu	41.0	0.21	0.38	0.30	7.7	156.0	14.0	EAST
51	332	Aomori-S		60.0	0.21	0.38	0.30	7.7	156.0	14.0	SOUTH
52	336	Akita-S	"(Aftershock)	22.5	0.33	0.72	0.53	6.1	113.0	23.0	NORTH
53	337	Akita-S	"(Aftershock)	22.5	0.31	0.94	0.63	6.1	113.0	23.0	DOWN
54	338	Akita-S	"(Aftershock)	15.0	0.25	0.50	0.38	6.1	113.0	23.0	EAST
55	339	Akita-S	"(Aftershock)	23.0	0.41	0.72	0.57	6.0	115.0	14.0	NORTH
56	340	Akita-S	"(Aftershock)	17.0	0.38	0.65	0.52	6.0	115.0	14.0	DOWN
57	341	Akita-S	"(Aftershock)	19.0	0.41	0.95	0.68	6.0	115.0	14.0	EAST
58	342	Aomori-S	"(Aftershock)	56.0	0.20	0.33	0.27	7.1	160.0	6.0	EAST
59	344	Aomori-S	"(Aftershock)	55.0	0.22	0.41	0.32	7.1	160.0	6.0	SOUTH
60	345	Muroran-S	"(Aftershock)	35.0	0.22	0.41	0.32	7.1	201.0	6.0	WEST
61	354	Hakodate-M	1982 Urakawa, off-shore	29.0	0.20	0.31	0.26	7.1	158.0	40.0	NORTH
62	364	Tokachi-M	Urakawa, off-shore 2	6.67	0.59	1.10	0.85	5.2	59.0	30.0	EAST
63	389	Sendai-M	Fukushima, off-shore	13.0	0.15	0.41	0.28	5.3	77.0	80.0	NORTH
64	395	Hakodate-M	1983 Nihonkai chudu	52.0	0.32	0.70	0.51	7.7	211.0	14.0	N08W
65	397	Hakodate-M		63.0	0.21	0.54	0.38	7.7	211.0	14.0	E08N
66	398	Hakodate-M	"(Aftershock)	52.0	0.20	0.45	0.33	7.1	155.0	6.0	N08W
67	399	Hakodate-M	"(Aftershock)	75.0	0.33	0.54	0.44	7.1	155.0	6.0	UP
68	400	Hakodate-M	"(Aftershock)	50.0	0.20	0.45	0.33	7.1	155.0	6.0	E08N

*1 reference data number arranged in the SERM-II database system(Ref.1)
*2 depth of fault

Table 3.4 Occurence Ratio of Surface Wave Motion for Major Japanese Earthquakes.

(a) earthquakes for remarkable occurence of surface wave motion

earthquake	surface-wave-contained	total number	occurence ratio	M
1983 Nihonkaichubu (Aftershock)	3	3	1.0	6.1
1983 Nihonkaichubu (Aftershock)	3	3	1.0	6.0
1983 Nihonkaichubu (Aftershock)	6	8	0.750	7.1
Matsushiro	5	7	0.714	5.1
Matsushiro	2	3	0.667	5.6
Shizuoka, off-shore	2	4	0.500	6.1
Ibaragi, off-shore	1	2	0.500	6.0
Wakayama, off-shore	1	2	0.500	5.0
Ehime, west coast	1	2	0.500	5.3
Miyazaki, off-shore	1	2	0.500	6.7
Izu-oshima-kinkai, (Aftershock)	4	8	0.500	5.8
Izu-oshma-kinkai, (Aftershock)	1	2	0.500	5.4
1983 Nihonkaichubu	6	17	0.500	7.7
Matsushiro	1	3	0.333	4.7
Matsushiro	2	6	0.333	4.5
Wakayama, off-shore	1	3	0.333	3.8
Urakawa, off-shore 2	1	3	0.333	5.2
1968 Tokachi-oki	4	14	0.286	7.9

(b) earthquakes for unremarkable occurence of surface wave motion

earthquake	surface-wave-contained	total number	occurence ratio	M
Miyagi, off-shore-2	0	18	0.0	6.1
Izu-oshima-kinkai-2	0	12	0.0	5.7
1968 Hyuganada	0	6	0.0	7.5
Matsushiro	0	6	0.0	4.3
Chiba, off-shore	0	6	0.0	6.1
Ibaragi, off-shore-2	1	19	0.053	7.0
1982 Urakawa, off-shore	2	15	0.133	7.1

Table 3.5 Occurence Ratio of Surface Wave Motion for Strong Motion Observation Stations.

(a) sites for remarkable occurence of surface wave motion

site	surface-wave-contained	total number	occurence ratio
Ochiai(A)	3	3	1.0
Shimizu-miho-S	5	6	0.833
Aomori-S	9	13	0.692
Wakayama-ji-S	1	2	0.500
Akita-S	6	12	0.500
Hakodate-M	6	12	0.500
Shimizu-kojyo-S	4	9	0.444
Hachinohe-S	4	12	0.333
Kinuura-S	1	3	0.333
Niigata-ji-S	1	3	0.333
Okitsu-S	1	3	0.333
Tagonoura-S	1	3	0.333
Wakayama-S	1	3	0.333

(b) sites for unremarkable occurence of surface wave motion

site	surface-wave-contained	total number	occurence ratio
Miyako-S	0	13	0.0
Horoman Bridgi	0	6	0.0
Keihin-ji-S	0	6	0.0
Yamashita-hen-S	0	9	0.0
Shiogama-kojyo-S	0	9	0.0
Kawasaki-doi5-ko-M	0	10	0.0
Onahama-ji-S	1	15	0.067
Muroran-S	1	12	0.089
Hososhima-S	1	9	0.111
Ochiai(C)	2	12	0.167
Itajima Bridge	1	6	0.167
Omigawa Bridge	1	6	0.167
Chiba-S	1	6	0.167

D : Judging from the evolutionary power spectra the posibility for containing surface wave motion is very low(159 comp.)

Table 3.6 shows the relation between the occurence ratio of surface wave motion and the seismic parameters, such as earthquake magnitude M, epicentral distance Δ, fault depth d_f, and apparent incident angle θ of earthquake motion defined as $\tan\theta=d_f/\Delta$. The numerals in parenthesis represent the rate in each level of seismic parameters.

As shown in Table 3.6(a) the earthquake magnitude does not have strong correlation on the occurence of surface wave motion. In the other hand the epicentral distance and the fault depth have some correlation on the occurence ratio ; the longer the distance is, the higher the occurence ratio increases, and also, the shallower the fault depth is, the higher it increases. The higher correlation can be recognized in Table 3.6(d) in which the correlation between the apparent incident angle θ and occurence ratio is shown.

From the above investigation on occurence of earthquake surface waves, the following conclusions may be derived.

[1] The earthquake surface wave motion in the frequency range dealt herein is mainly caused and amplified by local site condition. In other words, surface wave motion are caused easily at some sites and, it is not caused easily at some sites.

[2] At the sites where earthquake surface wave motion is caused easily, the apparent incident angle θ effects strongly on the occurence of surface wave motion.

5 Conclusions

Major results derived from this study may be summarized as follows.

[1] A simplified separation technique of body and surface waves in strong motion accelerograms has been proposed. In this technique the

Table 3.6 Relation between Occurence Ratio of Surface Wave Motion and Seismic Parameters.

(a) magnitude and occurence ratio

magnitude \ category	A	B_1	B_2	C_1	C_2	D
~5.0	7 (0.179)	2 (0.051)	5 (0.128)	2 (0.051)	6 (0 154)	17 (0.436)
5.0~5.5	11 (0.245)	1 (0.022)	6 (0.133)	1 (0.022)	0 (0 0)	26 (0.579)
5.5~6.0	8 (0.222)	2 (0.056)	6 (0.167)	0 (0.0)	2 (0 056)	18 (0.500)
6.6~6.5	8 (0.151)	0 (0.0)	6 (0.113)	1 (0 019)	1 (0.019)	37 (0.698)
6.5~7.0	6 (0.122)	4 (0.082)	12 (0.245)	2 (0.041)	5 (0.102)	20 (0.408)
7.0~7.5	18 (0.190)	7 (0.074)	7 (0.074)	5 (0.053)	20 (0 211)	38 (0.400)
7.5~	10 (0.323)	1 (0.032)	3 (0.097)	2 (0.065)	12 (0.097)	3 (0.097)

(b) epicentral distance and occurence ratio

distance Δ(km) \ category	A	B_1	B_2	C_1	C_2	D
~ 20	8 (0.258)	0 (0.0)	8 (0.258)	2 (0.065)	3 (0.097)	10 (0.323)
20~ 50	7 (0.159)	3 (0.068)	3 (0.068)	0 (0.0)	0 (0.0)	31 (0.706)
50~ 80	11 (0.111)	4 (0.044)	13 (0.144)	2 (0.022)	3 (0.033)	57 (0.633)
80~110	2 (0.074)	3 (0.111)	3 (0.111)	1 (0.037)	1 (0.037)	17 (0.630)
110~150	7 (0.234)	0 (0.0)	6 (0 200)	2 (0.067)	1 (0 033)	14 (0 467)
150~200	10 (0.263)	1 (0 0)	4 (0.105)	4 (0.105)	10 (0.263)	9 (0.237)
200~250	7 (0.269)	1 (0.038)	2 (0.077)	2 (0.077)	5 (0.192)	9 (0.346)
250~	6 (0.146)	4 (0.098)	3 (0.073)	3 (0.073)	16 (0.390)	9 (0.220)

Table 3.6 Relation between Occurence Ratio of Surface Wave Motion and Seismic Parameters(Continued).

(c) fault depth and occurence ratio

category / fault depth d_f(km)	A	B_1	B_2	C_1	C_2	D
0～10	21 (0.397)	5 (0.094)	11 (0.208)	3 (0.057)	1 (0.019)	12 (0.226)
10～20	11 (0.315)	2 (0.057)	4 (0.114)	1 (0.029)	11 (0.314)	6 (0 171)
20～30	13 (0.351)	3 (0.081)	4 (0.103)	1 (0.027)	4 (0.108)	12 (0.324)
30～40	2 (0.054)	0 (0.0)	7 (0.189)	2 (0.054)	5 (0.135)	21 (0.568)
40～50	15 (0.123)	7 (0.057)	12 (0.098)	4 (0.033)	21 (0.172)	63 (0.516)
50～	3 (0.070)	0 (0.0)	6 (0.140)	2 (0.047)	0 (0.0)	32 (0.749)

(d) apparent incident angle θ and occurence ratio

category / tan //	A	B_1	B_2	C_1	C_2	D
0.0	7 (0.233)	3 (0.100)	9 (0.300)	2 (0.067)	1 (0.033)	8 (0.267)
0.0～0.1	15 (0.417)	1 (0.028)	1 (0.028)	3 (0.083)	8 (0.222)	8 (0.222)
0.1～0.2	14 (0.203)	4 (0.058)	13 (0.188)	3 (0.043)	21 (0.304)	13 (0.203)
0.2～0.3	6 (0.176)	2 (0.059)	3 (0.088)	3 (0.088)	6 (0.176)	14 (0.412)
0.3～0.5	5 (0.119)	2 (0.048)	6 (0.143)	0 (0.0)	1 (0.024)	28 (0.669)
0.5～0.7	3 (0.086)	2 (0.057)	1 (0.029)	0 (0.0)	1 (0.029)	28 (0.300)
0.7～	8 (0.118)	10 (0.147)	2 (0.029)	4 (0.059)	0 (0.0)	44 (0.647)

evolutionary power spectrum has been used to confirm the dispersion characteristic of surface waves contained in strong motion data. The separation parameters t_d and f_{d_l}, f_{d_u}, in time and frequency domain, respectively, have been proposed.

[2] Ground strains caused by body and surface waves have been analyzed for original data and its separated body and surface waves. It has been pointed out that separation of body and surface waves is important for estimation of local ground strain caused by surface wave propagation.

[3] The statistical characteristic of earthquake surface motion contained in strong motion records have been examined using 367 components of corrected accelerograms. From 68 components of accelerograms the surface wave motion have been separated and the factor analysis has been done as for the occurence of surface wave motion. The significanct characteristic on the occurence of surface wave motion has been derived.

It is an essential subject for earthquake resistant design for buried pipes to evaluate earthquake surface motion rationally. The separation procedure which has been dealt here is anyhow a simplified technique, however, this method can be effective for evaluation of surface wave motion contained in recorded accelerograms, specially under the circumstances that surface wave motion from strong earthquakes have been scarecely recorded independently.

References

1) Design Seismic Load Research Group(SLG)(1984), "Corrected and Integrated Earthquake Motion Accelerograms(Graphical Information)," Revised Edition, Research Report, No.84-ST-03, School of Civil Engineering, Kyoto University.
2) Goto,H., Kameda,H., Takada,S., and Sugito,M.(1981), "Earthquake Motion Estimation for Buried Lifelines," Proc. of the 2nd Specialty Conference of the Technical Council on Lifeline Earthquake Engineering, pp.321-334.
3) Haskell,N.A.(1953), "The Dispersion of Surface Waves on Multilayered Media," BSSA, Vol.43, pp.17-34.

4) Kameda,H.(1980), "Evolutionary Spectra of Seismogram by Multifiltere," Jour. Eng. Mech. Div., ASCE, Vol.101, No.EM6, pp.787-801.

5) Kamiyama, M.(1979), "Stress and Strain in Ground During Earthquake," Proc. JSCE, Vol.250, pp.9-23 (in Japanese).

6) Liang,G.C. and Duke,C.M.(1980), "Evolutionary spectra for Strong Motion Accelerograms," Proc. of 7WCEE, Vol.2, pp.561-568.

7) for example, Okubo,T.,Arakawa,T., and Kawashima,K.(1984), "Dense Instrument Array Observation by the Public Works Research Institute and Analysis of Some Records." Proc. of 8WCEE, Vol.II, pp.151-158.

8) Osawa,Y. et.al.(1972), "Analysis on Accelerograms from 1968 Tokachi-oki Earthquake and Soil Structures at Hachinohe Site," Report of Science Research, Ministry of Education (in Japanese).

9) Tsuchida,H., Kurata,E., and Sudo,K.(1969), "Strong Motion Earthquake Records on the 1968 Tokachi-oki Earthquake and Its Aftershocks," Technical Note of PHRI, Ministry of Transport (in Japanese).

10) Wright,J.P. and Takada,S.(1978),"Earthquake Relative Motion for Lifelines," Proc. 5th Japan Earthq. Eng. Symp., pp.441-448.

4 STATISTICAL PREDICTION MODELS FOR STRONG EARTHQUAKE MOTION ON ROCK SURFACE

4.1 General Remarks

Prediction of earthquake motion at specific sites for given earthquake scale and source-to site distance is a significant subject in earthquake engineering. Theoretical calculation procedure by dynamic faulting model(Ref.2) can simulate ground motion which corresponds to ground motion in relatively low frequency range, such as $f < 0.1$ Hz. However, it is still very hard to simulate theoretical ground motion in high frequency range such as $f > 0.1$ Hz, because it needs detailed information about local soil structures as well as local fault dynamic process.

In the fields of engineering researches where the verification of the model against the real data is indispensable, many statistical models for ground motion have been proposed by using various kinds of strong motion datasets. They mainly dealt with peak acceleration(Ref.12), peak velocity(Ref.12), and acceleration response spectra(Refs.5,11,13), as a function of earthquake magnitude M, and epicentral distance Δ (or hypocentral distance R). Further the earthquake motion prediction models have been also proposed(Refs.3,8,19,21) in which ground motion characteristic such as spectral intensity, duration, nonstationarity, etc. were scaled for magnitude and distance.

In use of these prediction models the following problems may be staying. First, a large statistical uncertainty remains in the models because the strong motion data, which consist of relatively high frequency components as $f > 0.1$ Hz, were strongly affected by the characteristic of local soil conditions. Second, these statistical estimation formulas are mainly based on relatively weak ground motion data recorded on soil overlying sites. Therefore, it is not valid to apply these models for the case of large ground motion, in which the nonlinear response characteristic of overlying soils strongly affect ground motion intensities. As for the former problem, the individual estimation formulas for 4 types of soil conditions prescribed in the design code for bridges(Ref.4) have been proposed to eliminate the local soil effects. The continuous soil parameter S_n(Ref.10) given from SPT

blow-count profiles has been also used in estimation of ground motion intensities to account for the effect of local site conditions on ground motion intensities. However, nonlinear characteristic of soils during great earthquakes, which correspond to the latter problem, can not be solved by using only the relatively weak ground motion data recorded on soil overlying sites.

In this view of the problem, the nonstationary earthquake motion prediction models have been proposed by using rock surface-ground motion dataset(SMD R) developed in Chapter 2. Significance of the prediction model for rock surface is as follows. (1) The model is useful for earthquake motion prediction for soil overlying ground by regarding the given rock surface motion as the input to the bed rock, where the amplification effect and nonlinear characteristic of overlying soils can be considered. (2) The model can be applied for earthquake resistant design of significant structures including nuclear power plants that are built on rock ground.

In the following Chapter 2.2, the prediction model (EMP-IB) for nonstationary earthquake motion on rock surface for given magnitude and distance has been developed. On this basis the near-source earthquake motion prediction model (EMP-IIB) for given fault geometly and typical dynamic fault parameters including rupture velocity and direction of fault rupture has been proposed in Chapter 2.3. In Chapter 2.4, on the basis of the simulated rock surface motion for various combinations of magnitude and distance generated by the EMP-IB model, the estimation formulas have been proposed for peak acceleration, peak velocity, response spectra and strong motion duration.

4.2 Prediction Model for Nonstationary Earthquake Motion on Rock Surface for Given Magnitude and Distance (EMP-IB Model)

4.2.1 Simulation of Nonstationary Earthquake Motion by Evolutionary Process Model

Earthquake acceleration with nonstationary frequency content can be represented by

$$x(t) = \sum_{k=1}^{m} \sqrt{2G_x(t,\omega_k)\Delta\omega} \cdot \cos(\omega_k \cdot t + \varphi_k) \tag{4.1}$$

in which $G_x(t,\omega_k)$ = evolutionary power spectrum of $x(t)$ for time t and anguler frequency ω, $\omega_k = 2\pi + (k-1)\Delta\omega$, $\Delta\omega = 2\pi(f_u - f_l)/(m-1)$, φ_k = independent phase angle distributed randomly over $0 \sim 2\pi$. The upper and lower boundary frequencies f_u and f_l are fixed as f_u=10.03 Hz, and f_l=0.13 Hz regarding to the frequency range of the accelerograms used in this study. The number of superposition m is taken as m=166. The following time-varying function[11] as illustrated in Fig.4.1 is adopted for the model of $G_x(t,\omega)$.

$$\sqrt{G_x(t,\omega)} = \sqrt{G_x(t,2\pi f)} = \begin{cases} 0 & ;0 \leqq t < t_s \\ \alpha_m(f)\dfrac{t-t_s(f)}{t_p(f)}\exp\{1-\dfrac{t-t_s(f)}{t_p(f)}\} & ;t_s \leqq t \end{cases} \tag{4.2}$$

in which $t_s(f)$ and $t_p(f)$, a function of frequency f, are the starting time parameter and the duration parameter of $G_x(t,\omega)$, respectively. $\alpha_m(f)$ is the peak value of $\sqrt{G_x(t,\omega)}$, and is also a function of f.

The parameters $t_s(f)$, $t_p(f)$, and $\alpha_m(f)$ are determined in the following manner so that the model spectrum maintain the basic properties of the evolutionary power spectrum of the recorded accelerogram. The starting time $t_s(f)$ is defined as the time at which the evolutionary spectrum $G_y(t,\omega)$ of the corresponding recorded accelergram $y(t)$ exceeds 0.1 times its peak value for the first time. In determining $t_p(f)$ and $\alpha_m(f)$, equate the areas under $\{G_x(t,\omega)\}^{n/2}$, and $\{G_y(t,\omega)\}^{n/2}$, and also equate their first moment about the time origin; i.e.,

$$\int_0^\infty \{G_x(t,\omega)\}^{n/2} dt = a_0(f) = \int_0^\infty \{G_y(t,\omega)\}^{n/2} dt \tag{4.3}$$

$$\int_0^\infty \{tG_x(t,\omega)\}^{n/2} dt = a_1(f) = \int_0^\infty \{tG_y(t,\omega)\}^{n/2} dt \tag{4.4}$$

in which n is an arbitrary constant that controls the similarity between

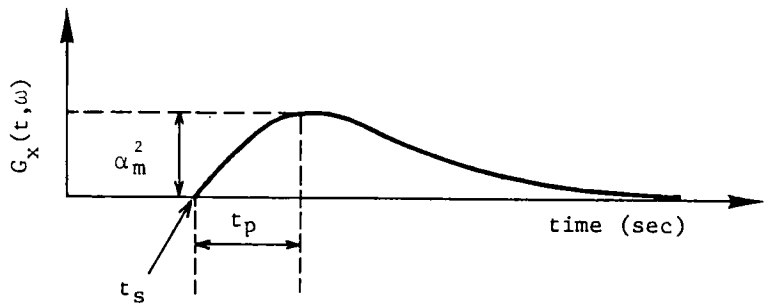

Fig.4.1 Time Varying Function for Modeling of Evolutionary Power Spectrum.

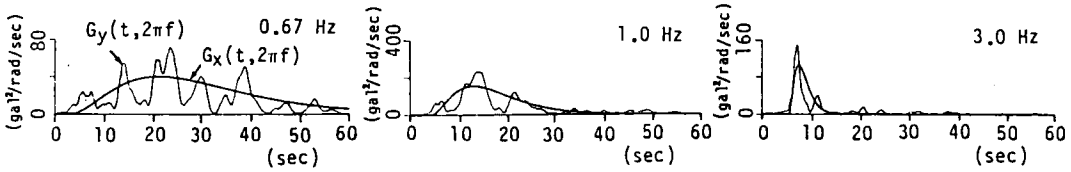

Fig.4.2 Recorded and Simulated Evolutionary Spectra (S-235 Aomori, 1968 Tokachi-oki Earthquake)

$G_x(t,\omega)$ and $G_y(t,\omega)$. In this study n is fixed as $n=4$ with reference to the previous study(Ref.7). Applying Eq.(4.2) to (4.3) and (4.4), and solving for $t_p(f)$ and $\alpha_m(f)$ gives the following expressions:

$$\alpha_m(f) = \frac{n}{e}\left\{\frac{\Gamma(n+2)}{\Gamma^2(n+1)} \cdot \frac{A_0(f)}{A_1(f)/A_0(f)-t_s(f)}\right\}^{1/n} \tag{4.5}$$

$$t_p(f) = n\frac{\Gamma(n+1)}{\Gamma(n+2)}\{A_1(f)/A_0(f)-t_s(f)\} \tag{4.6}$$

Typical example of recorded and simulated evolutionary specta are shown in Fig.4.2. Using these parameters simulated accelerogram is obtained from Eq.(4.1). In Fig.4.3 examples of recorded and simulated accelerograms are shown. It may be observed that the simulated accelerogram reproduces fairy well the nonstationary frequency trend of the corresponding recorded accelerogram.

Simulation Error

The following parameters may be used as a measure of error in this simulation model.

$$r_a=\ln(A_s/A_r) \quad r_p=\ln(P_s/P_r) \quad r_d=\ln(D_s/D_r) \quad r_e=\ln(E_s/E_r) \tag{4.7}$$

in which A_s and A_r are the peak acceleration of simulated and recorded accelerograms, P_s and P_r are their total powers. The yield deformation and the hysteretic energy of elastoplastic systems with 2% viscous damping corresponding to various values of the ductility factor μ for the simulated and the recorded accelerograms are denoted, respectively by D_s, D_r, E_s, and E_r. Fig.4.4 shows the sample deformation spectrum and the hysteretic energy of elasto-plastic systems for recorded and simulated motion. In Fig.4.4(a) the ordinate represents the yield displacement Y_d multiplied by the undamped natural circular frequency o_0, and in Fig.4.4(b) the total hysteretic energy per unit weight of the system multiplied by o_0. As shown in Fig.4.4 the simulated motion include the engineering characteristic of the recorded motion fairly well. Fig.4.5 shows the mean simulation error $\bar{r}_d$ and its

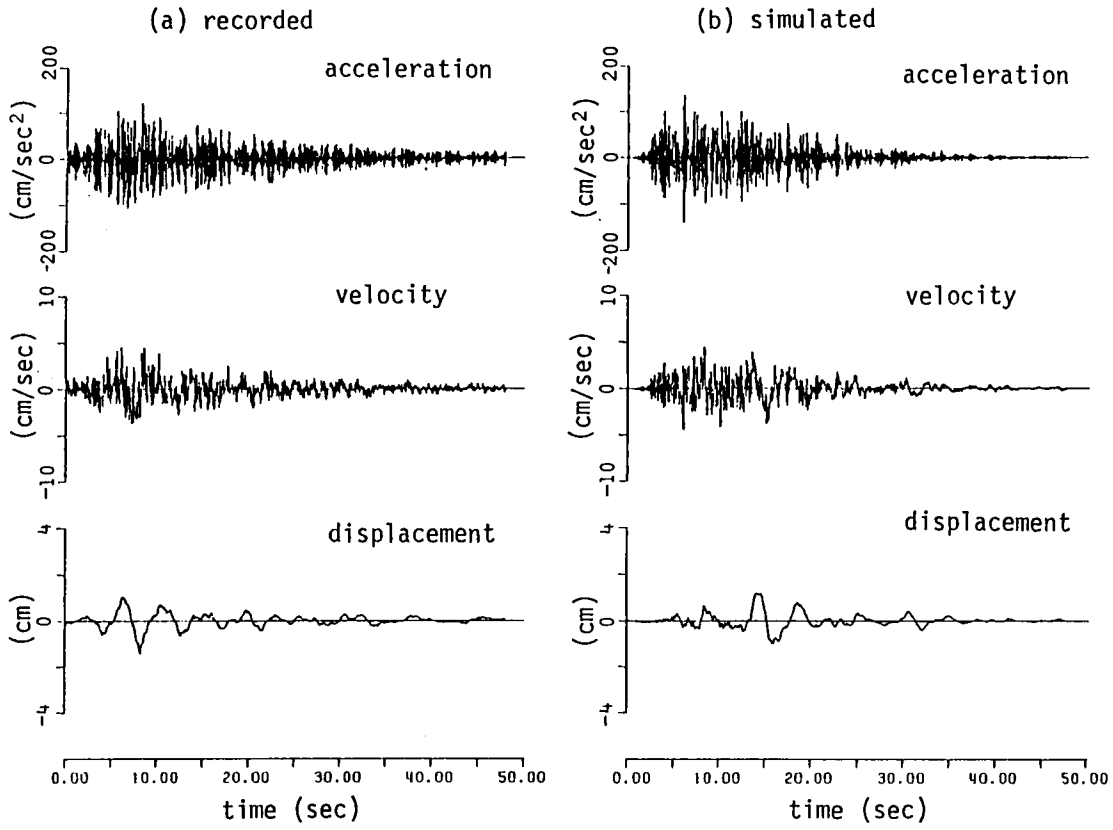

Fig.4.3 Recorded and Simulated Earthquake Motion(S-1204 Sounth, Miyako-S Site, 1978 Miyagiken-oki Earthquake).

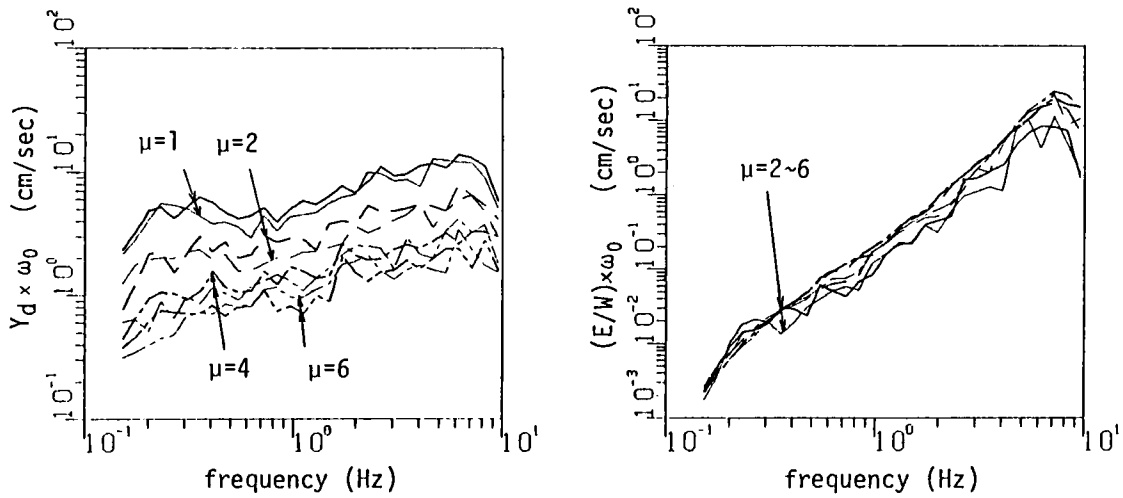

Fig.4.4 Yield Deformation and Hysteretic Energy Spectra(S-1204 South, Miyako-S Site, 1978 Miyagiken-oki Earthquake).

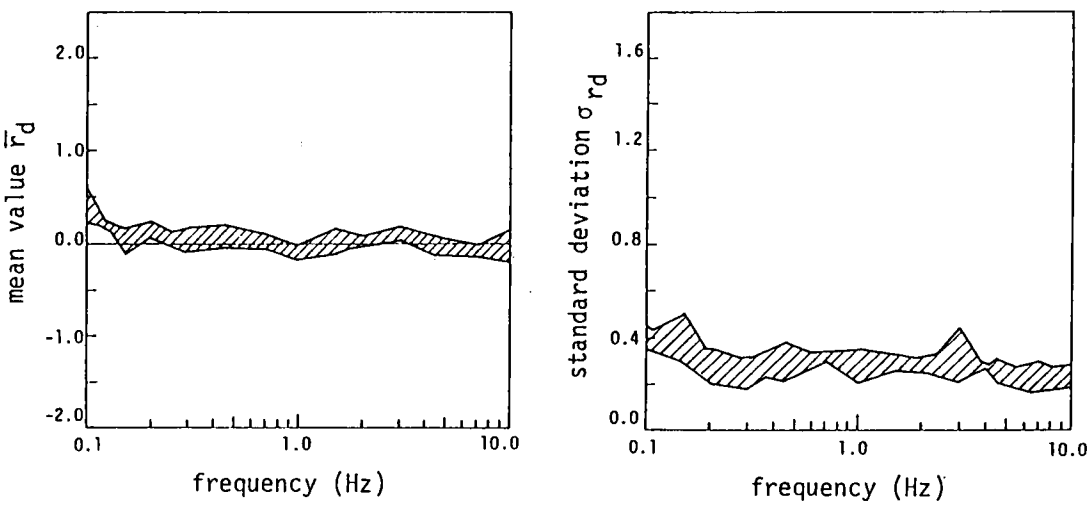

Fig.4.5 Mean of Simulation Error and Standard Deviation of Deformation Spectra.

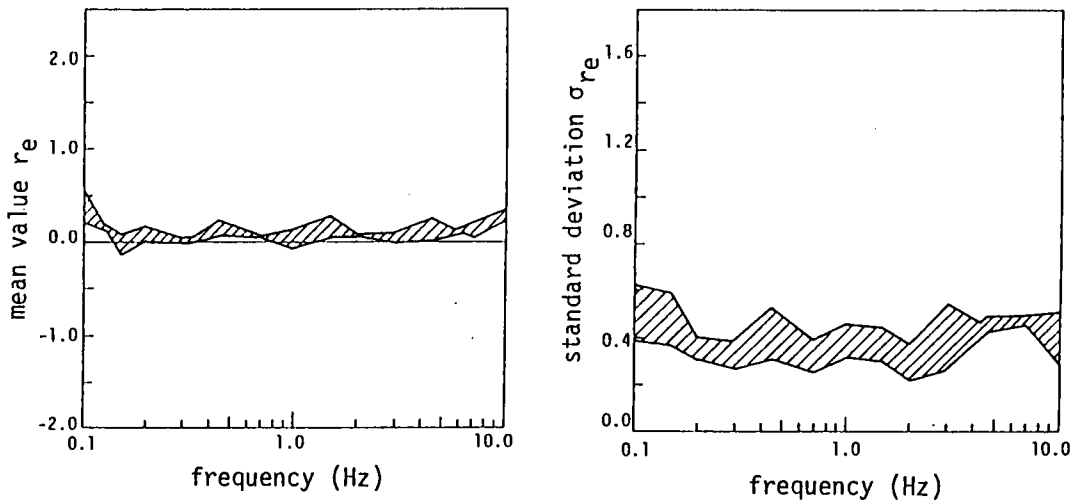

Fig.4.6 Mean of Simulation Error and Standard Deviation of Hysteretic Energy Spectra.

standard deviation σ_{r_d} , and also Fig.4.6 shows $\bar{r}_e$ and σ_{r_e} for 91 components of acceleration time histoties.

It is noticed that the mean simulation error $\bar{r}_d$, $\bar{r}_e$ do not depend very much on the ductility factor μ, and that they are fairy close to zero along the frequency axis; this demonstrate the validity of the simulation model proposed herein. The standard deviations σ_{r_d}, σ_{r_e} also do not depend very much on the ductility factor, and they are nearly constant along the frequency axis.

Mean simulation errors r_a, r_p and their standard deviations σ_{r_a}, σ_{r_e} are as follows:

$$r_a = 0.063, \quad r_p = 0.018, \quad \sigma_{r_a} = 0.333, \quad \sigma_{r_p} = 0.247$$

Note that they are also small enough to verify the usefulness of the proposed simulation model.

4.2.2 Scaling of Model Parameters for Magnitude and Distance, and Modificatin and Modeling of Regression Formulas

Scaling of Model Parameters

In order to develop an earthquake motion prediction model for given magnitude and distance using the simulation model proposed above, the model parameters have been scaled for magnitude M and epicentral distance Δ(in km) on the basis of the multiple regression analysis. The dataset SMD-R introduced in Chapter 2 has been used for this purpose.

The model parameters $t_s(f)$, $t_p(f)$, and $\alpha_m(f)$ have been obtained in the simulation of rock surface earthquake motion including in the SMD-R dataset. The following regression formulas have been used for the estimation of model parameters.

$$\log\hat{\alpha}_m(f) = B_0(f) + B_1(f) \cdot M - B_2(f) \cdot \log(\Delta+c) \tag{4.8}$$

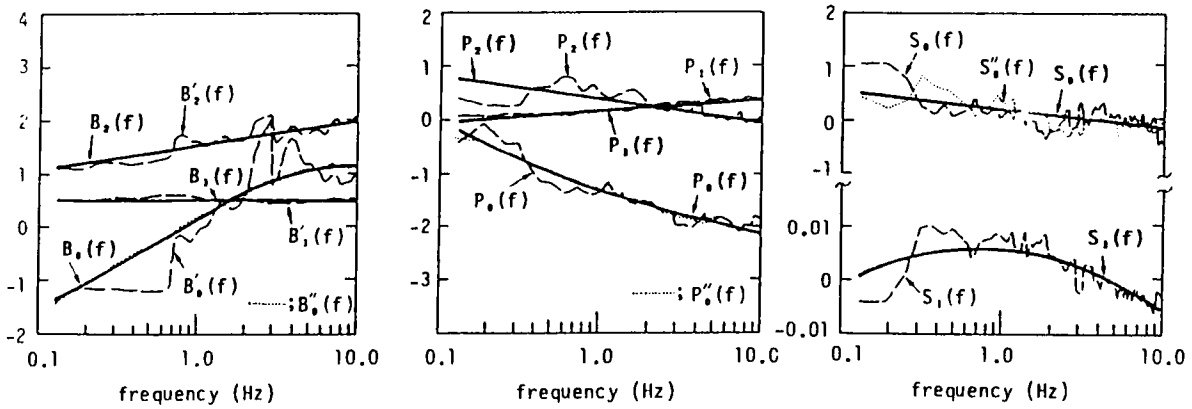

(a) intensity parameter $\alpha_m(f)$ (b) duration parameter $t_p(f)$ (c) starting time parameter $t_s(f)$

Fig.4.7 Regression Coefficients and Its Modeled Functions for Model Parameters.

$$\log\hat{t}_p(f) = P_0(f) + P_1(f)\cdot M - P_2(f)\cdot\log(\Delta+c) \tag{4.9}$$

$$\hat{t}_s'(f) = S_0(f) + S_1(f)\cdot\Delta \tag{4.10}$$

The formulas of Eqs.(4.8) and (4.9) have been commonly used for the estimation of ground motion intensities such as the peak acceleration and the peak velocity. The constant term c in Eqs(4.8) and (4.9) is necessary because the absolute value of logarythmic operation gets quite large when the distance Δ is quite short and the constant term is not incorporated. Herein the constant term c is fixed at c=30 km. In Eq.(4.10), $t_s'(f)=t_s(f)-t_m$, where t_m is the average of $t_s(f)$ over the frequency range considered herein. Consideration of t_m is necessary since the recorded accelerograms used for the statistical analysis have been obtained only on relative reference times. Fig.4.7 shows the results of regression analysis for the three model parameters.

Modification and Modeling of Regression Formulas

A number of free rock surface motion were generated for several combinations of M and Δ by using Eqs.(4.1), (4.2) and (4.8) ~ (4.10). They were converted to soil surface ground motion for a number of sites dealt in this study. The peak ground motion (A_p=peak acceleration, V_p=peak velocity) of them were compared with the estimation formulas (see Appendix A, Eqs.A.-11,12,14,15) which have been obtained using strong motion data recorded on soil sites. Since there were some disagreement specially for the case of the epicentral region(Ref.10), the coefficient $B_0(f)\sim B_2(f)$ in Eq.(4.8), have been modified so that the peak values A_p and V_p of ground motion converted from rock surface motion agree with those given from the estimation formulas for the soil surface motion. These modification procedure are discussed in detail in the Appendix B. The modified coefficients are shown in Fig.4.7(a) by slender broken line ($B_0'(f)$,$B_1'(f)$,$B_2'(f)$).

Since the coefficients for the model parameters have some typical inclination on the frequency axis, they were modeled as a function of the frequency f under the following procedures.

[1] Intensity Parameter $\alpha_m(f)$

As shown in Fig.4.7(a) the modified coefficients $B_1'(f)$ and $B_2'(f)$ can be approximately smoothed by a straight line on the logarythmic frequency axis. Therefore, they were modeled as a function of log$f$ by the least square method. The modeled coefficients $B_1(f)$ and $B_2(f)$ are shown by thick lines. Then, the re-modified constant term $B_0''(f)$ was obtained under the condition that the intensity parameter $\alpha_m(f)$ which is given from the form $\{\log\alpha_m(f) = B_0''(f)+B_1(f)M-B_2(f)\log(\Delta+30)\}$ fit that from the form $\{\log\alpha_m(f) = B_0'(f)+B_1'(f)M-B_2'(f)\log(\Delta+30)\}$ with least square errors. The coefficient $B_0''(f)$ is shown by dotted line. Then, $B_0''(f)$ was modeled as a function of log$f$ of order 3, which is shown by thick line $B_0(f)$ in Fig.4.7(a).

[2] Duration parameter $t_p(f)$

The coefficients $P_0(f)$, $P_1(f)$, $P_2(f)$ obtained from regression analysis are shown by slender broken lines in Fig.4.7(b). The coefficients $P_1(f)$, $P_2(f)$ are modeled as a function of log$f$ by least square error method. The modeled coefficients $P_1(f)$, $P_2(f)$ are shwon by thick lines. Then the modeled constant term $P_0(f)$, a function of log$f$ of order 2, was obtained using the same procedure as used in the case of the intensity parameter.

[3] Starting time parameter $t_s(f)$

The coefficient $S_1(f)$ obtained from regression analysis was modeled as a function of log$f$ of order 2. The re-modified constant term $S_0''(f)$ was modeled as a linear function of log$f$. The modeled coefficients $S_0(f)$, $S_1(f)$ are shown by thick lines in Fig.4.7(c).

The modeled coefficients described above are given in Table 4.1. Fig.4.8 shows values of model parameters given from Eqs.(4.8) $\sim$ (4.10) substituting the modeled coefficients listed in Table 4.1. The simulated rock surface ground motion for several combinations of M and Δ are shwon in Fig.4.9. It can be observed that the typical characteristic of ground motion is clearly

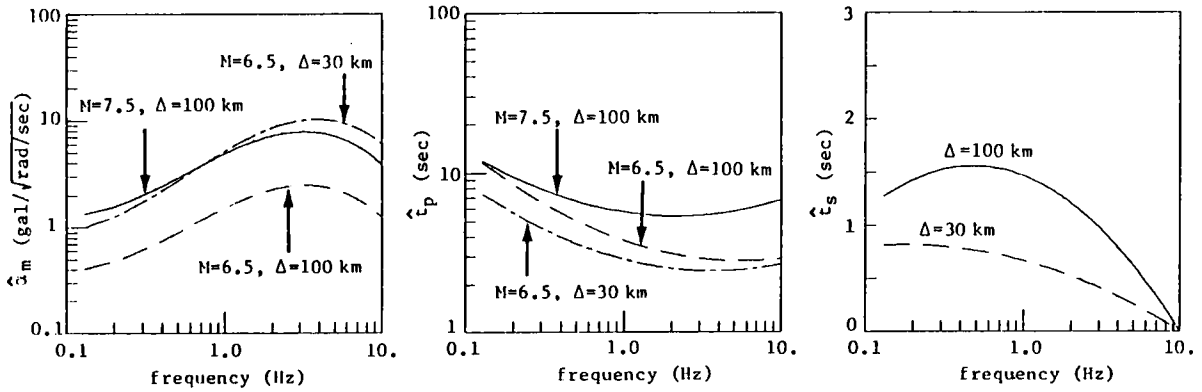

(a) intensity parameter $\alpha_{III}(f)$ (b) duration parameter $t_p(f)$ (c) starting time parameter $t_s(f)$

Fig.4.8 Example of Model Parameters for Combinations of Magnitude and Distance.

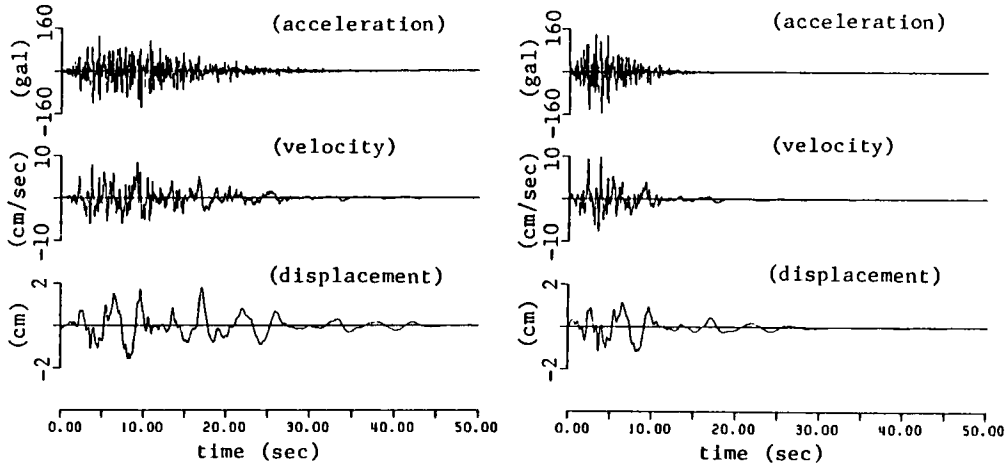

(a) M=7.5, Δ=100 km (b) M=6.5, Δ=30 km

Fig.4.9 Simulated Rock Surface Motion for Combinations of Magnitude and Distance.

Table 4.1 Estimation Formalas for Coefficients appeared in Eqs.(4.8)-(4.10).

$\log\hat{\alpha}_m(f) = B_0(f) + B_1(f)\cdot M - B_2(f)\cdot\log(\Delta+30)$	
$B_0(f)=0.1553+0.175\cdot\log f-0.336(\log f)^2-0.451(\log f)^3$ $B_1(f)=0.506-0.0131\cdot\log f$ $B_2(f)=1.543+0.455\cdot\log f$	(4.11)
$\log\hat{t}_p(f) = P_0(f) + P_1(f)\cdot M + P_2(f)\cdot\log(\Delta+30)$	
$P_0(f)=-1.312-0.1054\cdot\log f+0.227(\log f)^2$ $P_1(f)=0.179+0.188\cdot\log f$ $P_2(f)=0.344-0.240\cdot\log f$	(4.12)
$\hat{t}_s(f) = t_s(f) - t_m = S_0(f) + S_1(f)\cdot\Delta$	
$S_0(f)=0.439-0.978\cdot\log f$ $S_1(f)=\{0.528-0.242\cdot\log f-0.889(\log f)^2\}\times10^{-2}$	(4.13)

represented : the larger ground motion for larger magnitude and shorter distance, the longer duration of motion for larger magnitude, etc.

Since the EMP-IB model has been developed on the basis of the modified ground motion data, the prediction uncertainty cannot be evaluated directly from the result of the regression analysis for the model parameters. In Ref.8, the same procedure has been done to develop the prediction model by using the soil surface records, which were also used to examine the attenuation characteristic of peak ground motions in Appendix A. And the decrease in prediction uncertainty for the intensity parameter $\alpha_m(f)$ with increase in available information on local soil conditions has been characterized. They were classified into three levels as for the available information. The level I represents the condition for given magnitude M and distance Δ, the level II for M, Δ, and the soil parameter S_n defined from blow-count profile for a specific site, and the level III for M, Δ, S_n, and the transfer function of the ground overlying bedrocks. Assuming that the prediction uncertainty for $\alpha_m(f)$ on rock surface level is equivalent to that on soil surface level in which the whole information on local soil condition are available, the coefficient of variation δ_{α_m} for the level III may be substituted for the EMP-IB model. On the basis of the regression analysis developed in Ref.8, the prediction uncertainty for the model parameters of the EMP-IB have been characterized and they are shown in Fig.4.10. They were smoothed on the frequency axis, and the coefficient of variation δ_{α_m} for the intensity parameter $\alpha_m(f)$ and δ_{t_p} for the duration parameter $t_p(f)$ are given as δ_{α_m} = 0.426, δ_{t_p} = 0.650, respectively, for the whole freqyency range of $0.13 \leqq f \leqq 10.03$ Hz.

The nstationary earthquake motion prediction model for given magnitude and distance developed herein is termed EMP-IB which is the abbreviation of Earthquake Motion Prediction Model-I for Bedrock and Rock Surface Level.

4.3 Near-Source Earthquake Strong Prediction Model for Great Earthquake (EMP-IIB Model)

4.3.1 General Idea

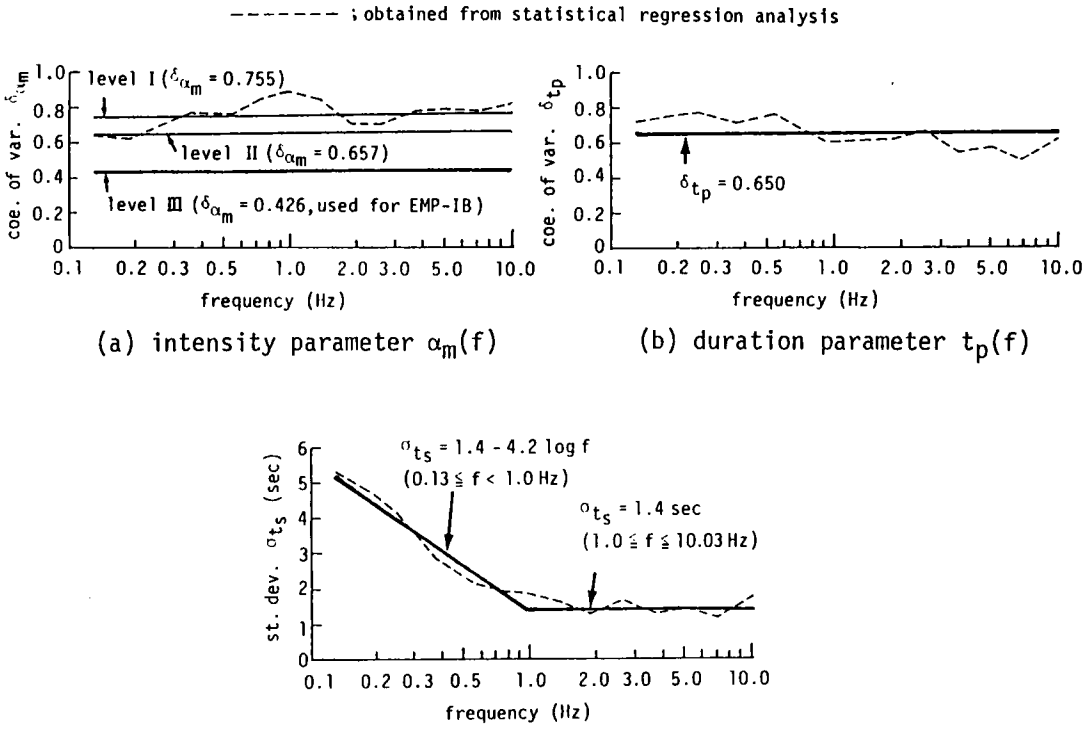

Fig.4.10 Characterization of Prediction Uncertainty for Model Parameters.

Past strong motion data from great earthquakes show that rupture direction relative to sites and geometrical condition between sites and fault make much differences in ground motion intensities and their duration. For prediction of earthquake motion for great earthquakes, therefore, physical parameters about faults and effect of successive faulting should be incorporated(Ref.14). Herein the prediction model (EMP-IIB Model) for large-scale earthquakes is proposed, which incorporates a size of fault, rupture direction and its velocity, and seismic moment as a parameter of earthquake scale. In the EMP-IIB Model, the evolutionary spectra for great earthquakes are given from the superposition of evolutionary spectra which correspond to relatively small earthquake (M=6.0) in the EMP-IB Model.

Fig.4.11 gives general concept of the model. The fault is divided into a number of small events which correspond to the unit event (M=6.0) in the EMP-IB Model. The arriving time lag $t_{a_{ij}}$ resulted from rupture on the fault and difference of propagation distance of ground motion, can be given in the following form.

$$t_{a_{ij}} = d_{ij} / v_r + (\Delta_{ij} - \Delta_s) / v_{pr} \tag{4.14}$$

In case of deep fault, a hypocentral distance r_s in place of Δ_s and direct distance between site and each unit event r_{ij} inplace of Δ_{ij} may be used.

4.3.2 Number of Superposition N_G scaled for Seismic Moment

The number of superposition N_G of evolutionary spectra is defined. The parameter N_G represents the number of small unit events on a specific great fault. The following procedure has been performed to obtain the superposition parameter N_G.

The magnification factor $c(f)$ defined by Eq.(4.15) may be used for amplification value of evolutionary power spectrum.

$$c(f) = \int_0^{t_0} \sqrt{G_x(t,2\pi f)}\, dt \Big/ \int_0^{t_0} \sqrt{G_x^*(t,2\pi f)}\, dt \tag{4.12}$$

where G_x= simulated evolutionary spectrum for the data, G_x^*= evolutionary spectrum given from the EMP-IB Model which corresponds to the earthquake magnitude M=6.0 and the 'same distance' of the specific data, and t_0= duration of the data. The number of superposition N_C, the average of the magnification factor $c(f)$ along the logarithmic frequency axis, is defined as

$$N_C=\int_{\log f_1}^{\log f_2} c(f)d(\log f) \ /(\log f_2- \log f_1) \tag{4.16}$$

where the lower and upper frequencies f_1, f_2 are fixed as f_1=0.13 Hz, and f_2=10.03 Hz. The parameter N_C represents the number of superposition of evolutionary spectra for a standard earthquake of M=6.0 in the EMP-IB Model. The value N_C has been obtained for 53 components obtained from 12 earthquakes listed in Table 4.2, the seismic moment M_0 of which have been given. The parameter N_C has been scaled for M_0, and the following relations has been obtained.

$$\overline{N_C}= 2.317\times 10^{-12}\times M_0^{0.468} \tag{4.17}$$

Fig.4.12 shows the relation between seismic moment M_0 and the number of superposition N_C defined by Eq.(4.16). In Eq.(4.17) the value M_0 which gives N_C=1 is given as M_0=7.24×10^{24}. This value nearly coinside with M_0=7.76×10^{24} which gives M_s=6.0 in the relation between M_0 and the surface magnitude M_s proposed by Geller(Ref.1). Since the JMA magnitude coinside with M_s in case of relatively small magnitude as around M=6.0(Ref.23), the above result supports the validity of the model.

4.3.3 Superposition of Evolutionary Spectra for Great Earthquakes

The superposed evolutionary spectra for great earthquake is given as

$$\sqrt{G_{x_0}(t,2\pi f)}=\frac{N_C}{n_C}\ \beta(f,M_0)\sum_{ij}^{n_C}\sqrt{G_{z_{ij}}(t,2\pi f)} \tag{4.18}$$

where $G_{z_{ij}}$ = evolutionary spectrum for each unit event e_{ij} , which corresponds

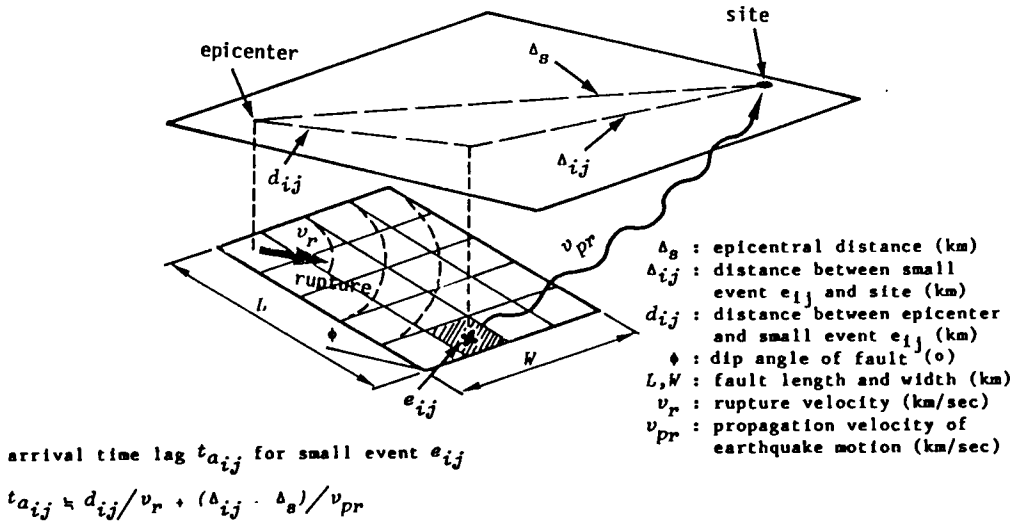

arrival time lag $t_{a_{ij}}$ for small event e_{ij}

$$t_{a_{ij}} \fallingdotseq d_{ij}/v_r + (\Delta_{ij} - \Delta_s)/v_{pr}$$

Fig.4.11 Fault Modeling with Multiple Fault Ruptures.

Table 4.2 Fault Parameters for Major Japanese Earthquakes(Refs.18,22).

event	date	magnitude M	seismic moment M_0 (dyn·cm)
1968 Huganada	April 4, 1968	7.0	1.8×10^{27}*
1968 Tokachi-oki	May 16, 1968	7.9	2.8×10^{28}
Tokachi, Off Shore	May 16, 1968	7.4	1.3×10^{27}*
Saitama, Center	July 1, 1968	6.1	1.9×10^{25}
Ehime, West Coast	August 6, 1968	6.6	2.0×10^{26}
Ibaragi, Off Shore	July 23, 1972	7.0	3.2×10^{26}*
1978 Izuoshima Kinkai	Jan. 14, 1978	7.0	1.0×10^{26}
Miyagi, Off Shore	Feb. 20, 1978	6.7	8.0×10^{25}
1978 Miyagiken-oki	June 14, 1978	7.4	3.1×10^{27}
1982 Urakawa-oki	March 21, 1982	7.1	2.0×10^{26}
1983 Nihonkai-Chubu	May 26, 1983	7.7	5.0×10^{27}
Nihonkai, Center	June 21, 1983	7.1	4.5×10^{26}*

* estimeted from the magnitude as $\log M_0 = 1.5\,M + 16.0$ (Ref.30)

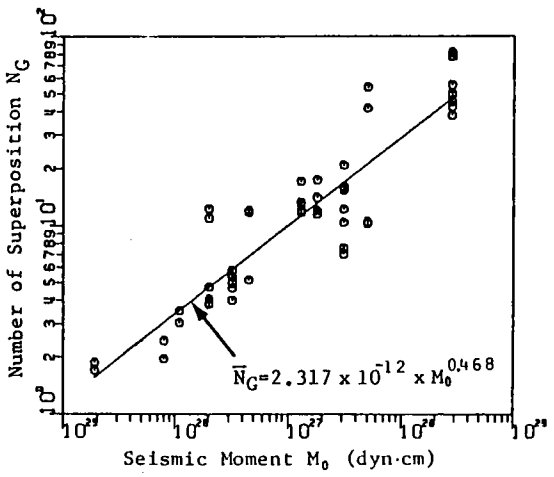

Fig.4.12 Relation between Number of Superposition N_G and Seismic Moment M_0.

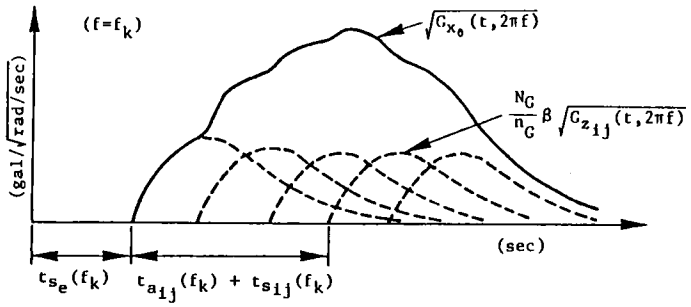

Fig.4.13 Superposed Evolutionary Spectra.

to the earthquake of M=6.0, $\Delta = \Delta_{ij}$ in the EMP-IB Model. The value N_G is generally not an integral number, therefore the numbr n_G which is a similar number for N_G and by which the specific fault can be divided, should be used. Then, the coefficient N_G/n_G is necessary for modification of total power. Further the correction factor $\beta(f,M_0)$ is necessary for superposing of each frequency component, which has been obtained from the regression of the parameter $c(f)$ on seismic moment.

The correction factor $\beta(f,M_0)$ has been also modeled on the frequency axis, and is given

$$\beta(f,M_0)=10^{a_0(f)}M_0^{a_1(f)} \tag{4.19}$$

where

$$\begin{cases} a_0(f)= 0.948-0.460\cdot\log f \\ a_1(f)=-0.388+0.178\cdot\log f \end{cases} \tag{4.20}$$

Fig.4.13 gives a schematic description for the superposed evolutionary spectra.

The prediction uncertainty for the superposed evolutionary spectra in the EMP-IIB model can be characterized by the coefficient of variation δ_N along the regression line shown in Fig.4.12. The value of δ_N has been obtained as δ_N =0.41.

4.3.4 Simulation Procedure in EMP-IIB Model and Simulated Ground Motion for Hypothetical Great Earthquakes

The procedure of earthquake motion prediction in the EMP-IIB Model is as follows.

[1] Calculate the number of superposition N_G for given seismic moment M_0 by Eq.(4.17), and find the integral nimber n_G, by which the given fault can be devided properly according to the fault dimensions.

[2] Calculate the distance Δ_{ij} and the mean arrival time $t_{a_{ij}}$ (Eq.(4.14)) for each unit event by using the given fault dimentions, rupture velocity v_r, and propagation velocity of seismic waves v_{pr}.

[3] Calculate the evolutionary spectra $G_{z_{ij}}$ for each distance Δ_{ij} and M=6.0 in the EMP-IB Model (Eqs.(4.2),(4.8) ~ (4.13)). Then, superpose the evolutionary spectra $G_{z_{ij}}$ considering the arrival time $t_{a_{ij}}$ (Eq.(4.14)).

[4] The ground motion time series is obtained by substituting $G_{x_0}(t,2\pi f)$ for $G_x(t,2\pi f)$ in Eq.(4.1).

The comparison between recorded motion and simulated motion obtained by using the EMP-IIB model is shown in Fig.4.14. Fig.4.14(a) shows the fault geometory and its rupture direction for the 1968 Tokachioki Earthquake (M=7.9), and related two observation sites. Substituting M_0=2.8×10^{28} in Eq.(4.17), the number of superposition N_G is given as N_G=47.7, and the corresponding integral number n_G is given as n_G=45(5×9). In Fig.4.14(b) the simulated rock surface motion for Muroran-S and Hachinohe-S site are shown, and the modified rock surface motion obtained from ground surface records for these two sites are shown in Fig.4.14(c).

Another example for the conparison of recorded and simulated motion is shown in Fig.4.15, in which the fault model for the 1983 Nihonkai-chubu Earthquake (M=7.7) is used. Fig.4.15(a) shows the fault situation and related fault parameters(Ref.17) as well as two observation sites (Akita-S and Muroran-S). As shown in Fig.4.15(a) the fault model consists of two individual events and the second event occured 20 seconds after the first event occured(Ref.17). The seismic moment for this fault is given as M_0=5.8×10^{27}, and the number of superposition is obtained as N_G=22.81 from Eq.(4.17). These two individual events are devided into 16(4×4) unit events. Therefore the integral number n_G for superposition is fixed as n_G=32. Fig.4.15(b) shows the simulated soil surface motion which have been obtained from the simulated rock surface motion by incorporating the nonlinear soil amplification effect of surface layers. Fig.4.15(c) shows the recorded data for these two sites. In the case for Akita-S site, it is observed that the acceleration time history of simulated motion represent the typical

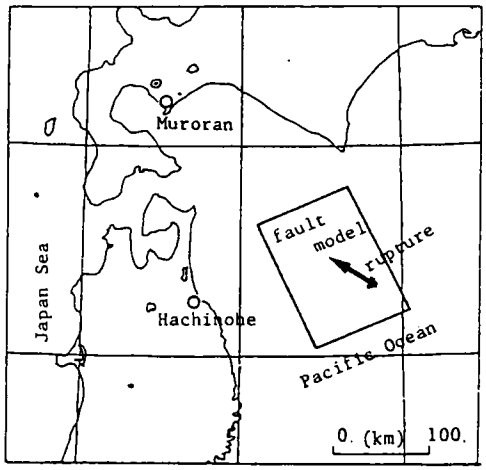

(a) Fault Model for the 1968 Tokachi-oki Earthquake (northeast Japan : M=7.9, $M_0 = 2.8 \times 10^{28}$ dyn·cm)

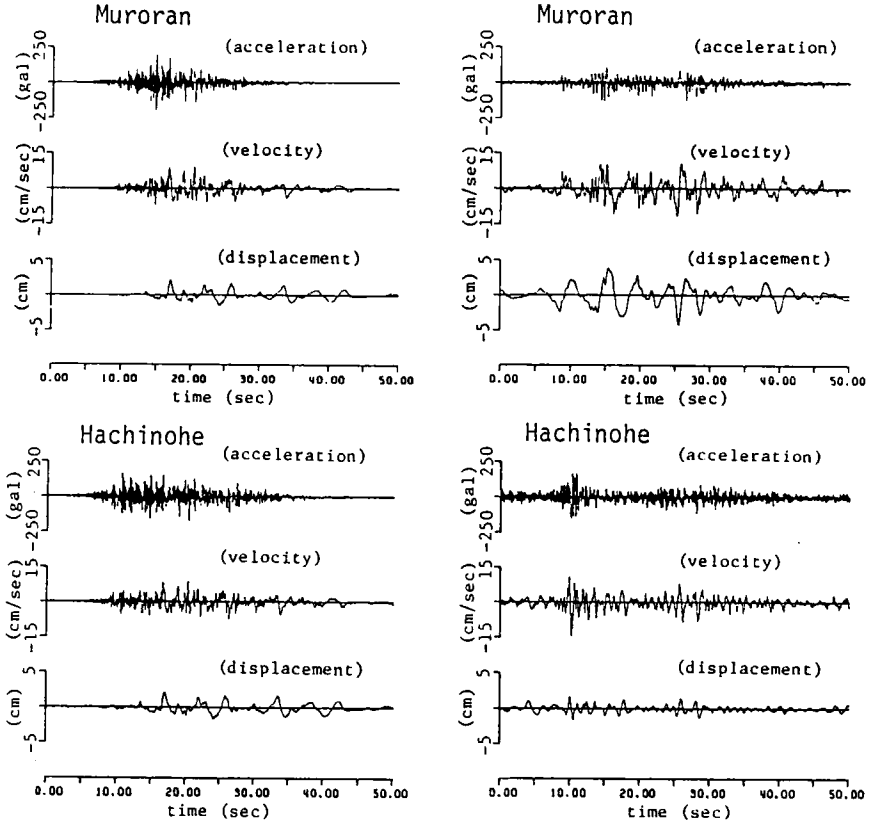

(b) simulated motion

(c) modified from soil surface motion

Fig.4.14 Simulated Rock Surface Motion Compared with Strong Motion Data during the 1968 Tokachi-oki Earthquake.

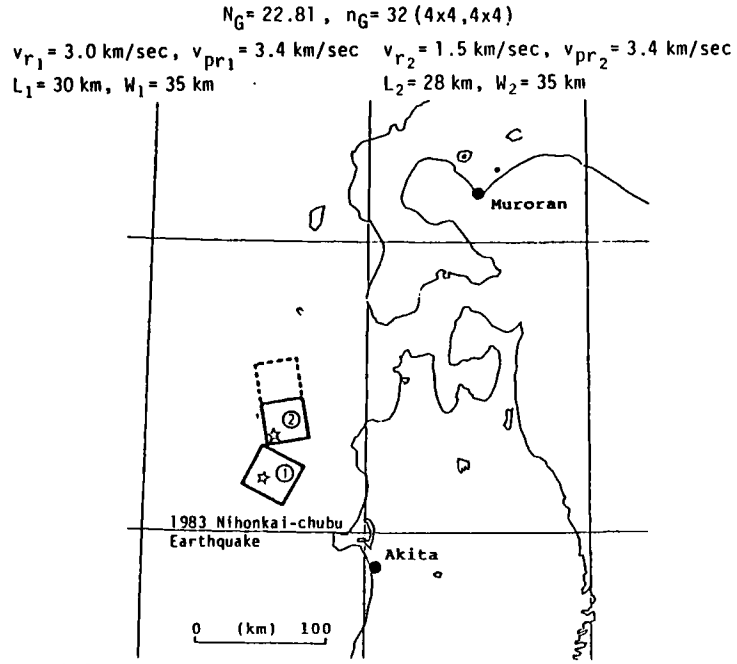

(a) Fault Model for the 1983 Nihonkai-chubu Earthquake (northwest Japan : M=7.7, M_0=5.8 x 10^{27} dyn-cm)

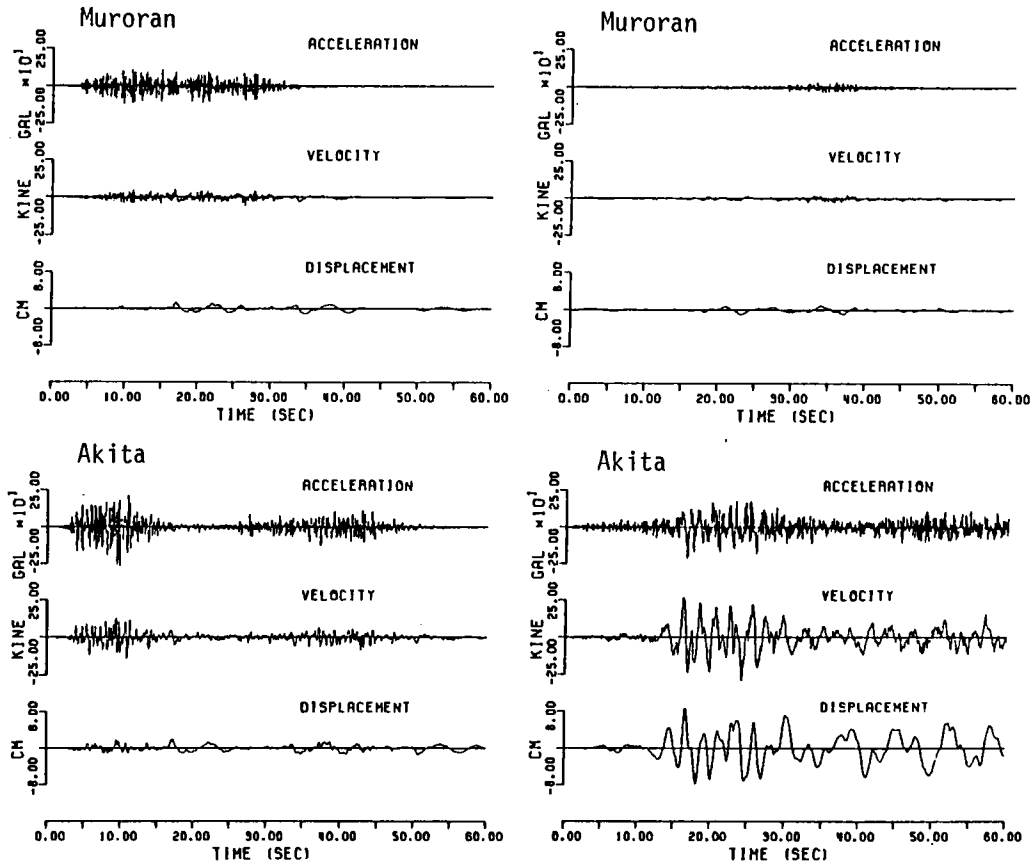

(b) simulated motion

(c) recorded soil surface motion

Fig.4.15 Simulated Soil Surface Motion Compared with Strong Motion Data during the 1983 Nihonkai-chubu Earthquake.

characteristic of the double events earthquake as shown in the recorded data. However the displacement of the simulated motion is much smaller than that for recorded data. The reason for the large difference in the displacemet may be that the surface wave component for around 10 seconds dominant period is included in the recorded data. On the other hand, the acceleration of the simulated motion is much larger than that for the recorded data in the case of Muroran-S site. One of the reason for this result can be derived from the fact that the orogenic belt is located in the middle of Honshu island in the diredtion from north to south which is shown by the shadowed area, and that the earthquake motion are attenuated remarkably when they propagate through these area(Ref.20).

Typical engineering characteristic of strong ground motion derived from the EMP-IIB Model were obtained. A number of sample earthquake motion were generated by the EMP-IIB Model for the hypotherical fault shown in Fig.4.16. Fig.4.17 shows sample earthquake motion for site 1, 7, and 13. Fig.4.18 (a) ~ (d) show the fluctuations of peak ground motion, effective peak acceleration A_e (Ref.9), and ground motion duration T_d (Ref.24) for several values of rupture velocity v_r.

4.4 Estimation Formulas for Peak Ground Motion, Response Spectra, and Ground Motion Duration on Rock Surface

4.4.1 Simulation of Rock Surface Earthquake Motion for Development of Estimation Formulas

The EMP-IB Model developed in the previous chapter has been used for the development of the estimation formulas for the simple hazard parameters including peak rock surface motion, response spectra, and strong motion duration. The estimation formulas for these hazard parameters were obtained on the basis of the simulated rock surface motion generated by the EMP-IB Model. The total of 56 combinations of M and Δ were selected, and 10 sample motion were generated for each combination of M and Δ. Fig.4.19 shows the distribution of M and Δ for generation of sample motion. As shown in Fig.4.19, all combinations were fixed outside the epicentral region defined by Eq.(A-). In the epicentral region it is assumed that the earthquake hazard

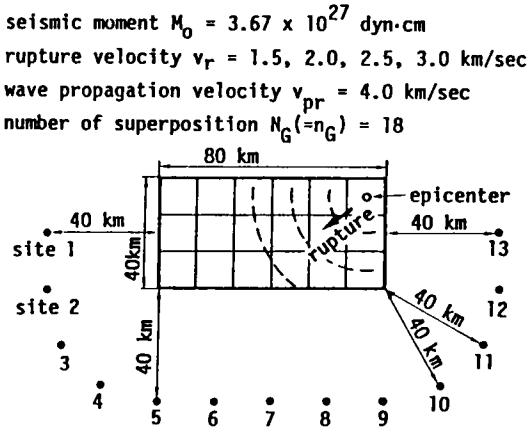

Fig.4.16 Hypothetical Fault Model and Site Locations.

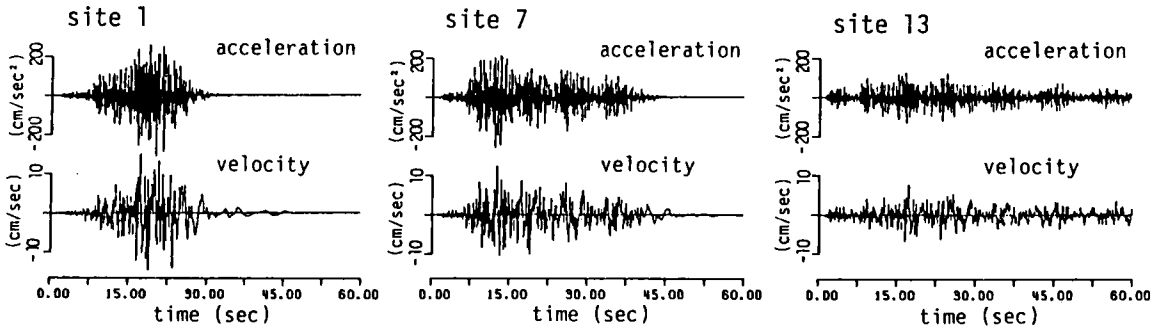

Fig.4.17 Simulated Rock Surface Motion for Sitel, 7, and 13 in Fig.4.16.

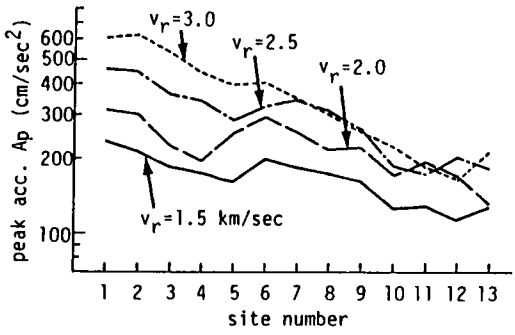

(a) peak acceleration A_p

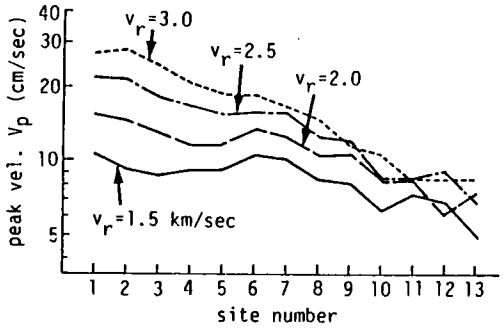

(b) peak velocity V_p

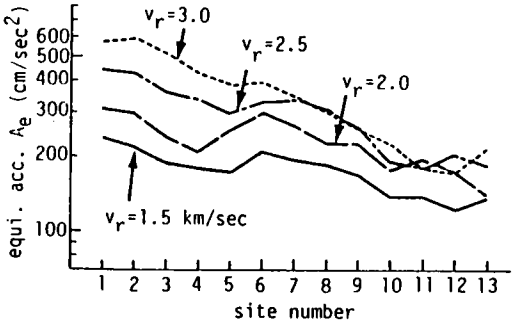

(c) equivalent acceleration A_e

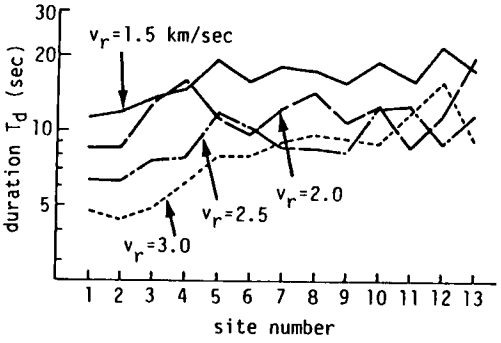

(d) ground motion duration T_d

Fig.4.18 Fluctuation of Ground Motion Intensities and Ground Motion Duration.

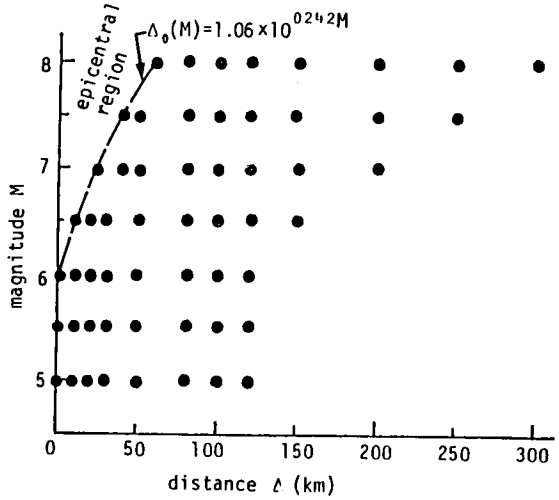

Fig.4.19 Combinations of Magnitude and Distance for Simulation of Rock Surface Motion by EMP-IB Model.

parameters dealt here do no depend on the epicentral distance and are relatively constant. In total 560 sample motion were generated and the simple hazard parameters described above were obtained from each sample motion.

It is expected that the estimation formulas developed on the basis of the dataset obtained in a way described above are consistent with the EMP-IB Model.

4.4.2 Estimation Formulas for Peak Earthquake Motion on Rock Surface

The following estimation formulas for peak earthquake motion have been obtained on the basis of the rock surface strong motion dataset described in the previous chapter.

Peak Acceleration (cm/sec^2)

$$\overline{A}(B,\Delta) = \begin{cases} 111 \times 10^{0.534M}/(\Delta+30)^{1.857} & ;\Delta \geqq \Delta_0(M) \\ 99.6 \times 10^{0.0846M} & ;\Delta < \Delta_0(M) \end{cases} \tag{4.21}$$

Peak Velocity (cm/sec)

$$\overline{V}(M,\Delta) = \begin{cases} 2.21 \times 10^{0.545M}/(\Delta+30)^{1.636} & ;\ \Delta \geqq \Delta_0(M) \\ 2.01 \times 10^{0.149M} & ;\ \Delta < \Delta_0(M) \end{cases} \tag{4.22}$$

In Fig.4.20 the attenuation characteristic of Eqs.(4.21) and (4.22) are shown by solid lines. The broken lines in Fig.4.20 represent the attenuation curves given from the estimation formulas for the soil surface earthquake motion(see Appendix A.1).

It is clear that the peak motion on rock surface depend more strongly on M and Δ than those for soil surface motion. This result may be derived from the nonlinear amplification effects of the ground overlying bedrock. The amplification ratio of the soil surface motion to rock surface motion decrease with increase in the rock surface motion.

The effect of nonlinear amplification characteristic of soil overlying ground argued above were examined using the simulated soil surface motion which were converted from the rock surface motion. The soil surface motion for 12 Japanese strong motion stations at alluvial and diluvial sites were computed by using generated rock surface motion; the input motion from bedrock were given by scaling their amplitudes by 0.5. The peak acceleration and peak velocity of them were averaged for each set of M and Δ, and the results were shown by the dotted lines in Fig.4.20. They agree satisfactory with the broken lines specially for the region of large earthquake motion.

4.4.3 Estimation Formula for Acceleration Response Spectra

The estimation formula for pseud-acceleration response spectra of rock surface motion with 5% critical damping have been obtained as follows.

$$\log\bar{S}_M(T,5) = \begin{cases} b_o(T) + b_1(T)M - b_2(T)\log(\Delta + 30) & ; \Delta \geqq \Delta_o(M) \\ b_o'(T) + b_1'(T)M & ; \Delta < \Delta_o(M) \end{cases} \tag{4.23}$$

where

$$\begin{cases} b_0(T) = 1.05 - 2.29\log T - 0.644(\log T)^2 \\ b_1(T) = 0.547 \\ b_2(T) = 1.469 - 0.492\log T \\ b_0'(T) = 0.978 - 2.27\log T - 0.644(\log T)^2 \\ b_1'(T) = 0.192 + 0.1192\log T \end{cases} \tag{4.24}$$

Using the multiple regression analysis on M and Δ, the coefficients in Eq.(4.23) were obtained independently for each period T in the range of $0.1 \leqq T \leqq 7.7$ seconds. Then they were smoothed on the log-period axis and represented as a function of the period T. Fig.4.21 shows the modeled coefficients represented by Eq.(4.24).

Estimation formulas given by Eq.(4.23) have been obtained for 5% critical damping. For the estimation of the response spectra for other damping values, it is convenient to use a scaling factor versus the response

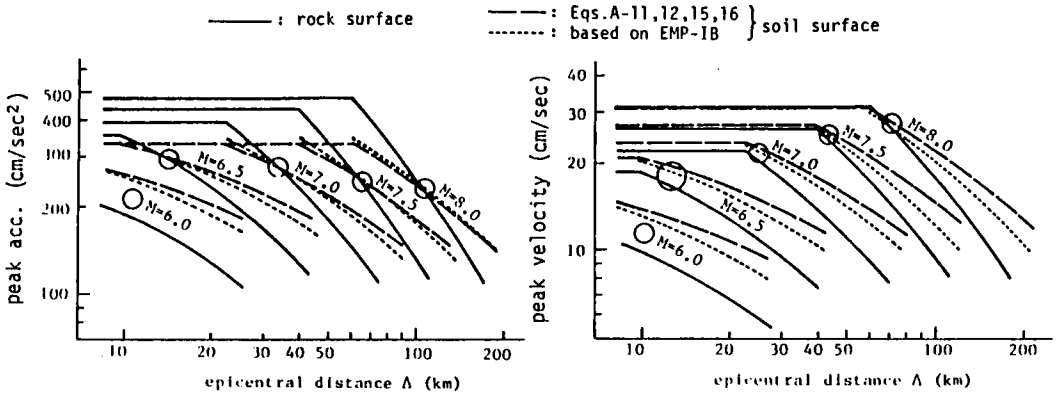

Fig.4.20 Attenuation Characteristic of Peak Acceleration and Peak Velocity.

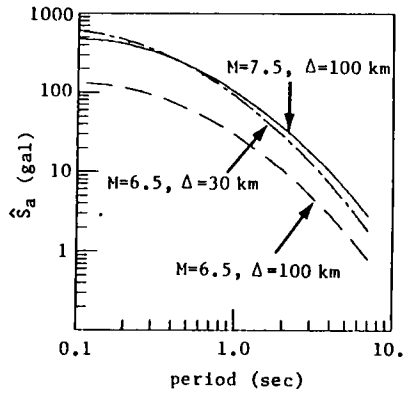

Fig.4.21 Modeled Acceleration Response Spectra for Combinations of Magnitude and Distance.

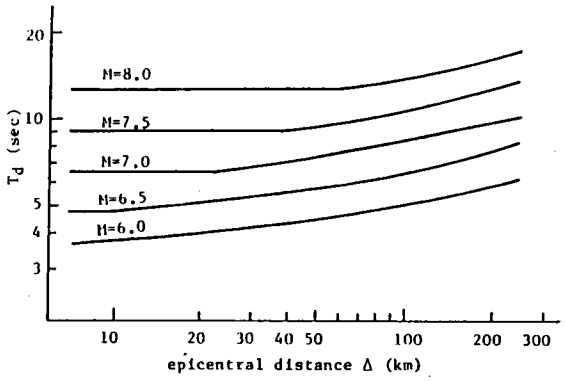

Fig.4.22 Modeled Strong Motion Duration.

spectra for 5% critical damping. The conversion factor for the acceleration response spectra have been proposed(Refs.13,15).

4.4.4. Estimation Formula for Earthquake Motion Duration

It has been pointed out that the earthquake motion duration contribute strongly to nonlinear response characteristic of structures. In the relation between dynamic ground accelerations and equivalent static, seismic loads, the earthquake motion duration also performs an important part. Herein, the strong motion duration T_d defined by Vanmarke and Lai(Ref.24) has been scaled for M and Δ and given in the following form.

$$T_d = \begin{cases} 0.0706 \times 10^{0.218M}(\Delta+30)^{0.257} & ; \Delta \geqq \Delta_0(M) \\ 0.0717 \times 10^{0.280M} & ; \Delta < \Delta_0(M) \end{cases} \tag{4.25}$$

where $T_d=7.5P_t/A_p^2$ in sec, P_t = acceleration total power in cm^2/sec^3, and A_p= peak acceleration in cm/sec^2. Fig.4.22 shows their plots.

4.5 Conclusions

The major conclusions derived from this Chapter may be summarized as follows.

[1] The simulation technique of nonstationary earthquake motion prediction has been demonstrated on the basis of the modeling of evolutionary power spectrum with typical three model parameters. Validity of the simulation method has been examined not only for peak acceleration and acceleration total power but for inelastic structural response including deformation spectra and total hysteretic energy for elasto-plastic systems.

[2] The simulation technique developed herein has been applied for the strong motion dataset arranged in Chapter 2. On this basis the the nonstationary earthquake motion prediction model on free rock surface (EMP-IB Model) for given magnitude and distance has been developed. The model is also applicable for esrthquake motion prediction on soil sites by incorporating the amplification effects of the soil layers overlying

bedrocks.

[3] The EMP-IB Model has been extended to the prediction model for great earthquakes (EMP-IIB Model) which incorporates the effect of fault size, successive fault rupture, and rupture direction, on characteristic of ground motion. The EMP-IIB Model is based on the superposition technique of evolutionary spectra of small events that corresponds to the earthquake of M=6.0 in the EMP-IB Model. For the scaling of the number of superposition N_G, the seismic moment has been incorporated.

[4] The comparison between recorded motion and the simulated motion obtained by the EMP-IIB model have been discussed for the Japanese two typical great earthquakes. Typical engineering characteristic of strong ground motion derived from the EMP-IIB Model have been demonstrated using the hypothetical fault model with several rupture velocities of faulting.

[5] Simulated rock surface motion have been generated for for several combinations of magnitude and distance by using the EMP-IB model. On this basis, the estimation formulas for peak ground motion, acceleration response spectra, and ground motion duration on rock surface have been proposed.

REFERENCES

1) Geller,R.J.(1976), "Scaling Relations for Earthquake Source Parameters and Magnitudes," BSSA, Vol.66, pp.1501-1523.
2) Haskell,N.A.(1969), "Elastic Displacements in the Near-field of a Propagating Fault," BSSA, Vol.59, pp.865-908.
3) Izutani,Y.(1981), "A Statistical Model for Prediction of Quasi-realistic Strong Ground Motion," J.Phys. Earth, 29, pp.537-557.
4) Japan Road Association(1980), Design Code for Bridges, -Earthquake Registant Design-, Vol.V (in Japanese).
5) Katayama,T., Iwasaki,T. and Saeki,T.(1978), "Statistical Analysis of Earthquake Acceleration Response Spectra," Proc., JSCE, No. 275, pp.2940 (in Japanese).
6) Kameda,H.(1977), "Stochastic Process Models of Strong Earthquake Motions

for Ineastic Structural Response," U.S.-Southeast Asia Symposium on Engineering for Natural Hazards Protection, Manila.

7) Kameda,H. and Ang,A.H-S.(1977), "Simulation of Strong Earthquake Motions for Ineastic Structural Response," Proc. of 6WCEE, Vol.I.

8) Kameda,H., Sugito,M., and Asamura,T.(1980), "Simulated Earthquake Motions Scaled for Magnitude, Distance, and Local Soil Conditions," Proc., 7WCEE, Vol.2, pp.295-302.

9) Kameda,H. and Kohno,K.(1983), "Effect of Ground Motion Duration on Seismic Design Load for Civil Engineering Structures," Memoirs of the Faculty of Engineering, Kyoto University, Vol.XLV, Part 2, pp.140-184.

10) Kameda,H., Sugito,M., and Goto,H.(1982), "Microzonaiotion and Simulation of Spatially Correlated Earthquake Motions," Proc. of the 3rd International Earthquake Microzonation Conference, Vol.III, pp.1463-1474.

11) Kameda,H. and Ieiri,R.(1982), "Attenuation and Microzonation of Acceleration Response Spectra," Proc. of the 37th Annual Conference of the JSCE, No.1, pp.667-668 (in Japanese).

12) Kanai,K.(1966), "Empirical equations for earthquake motion intensity," 5th Japan Earthquake Engineering Symposium, pp.1-4. (in Japanese).

13) Kawashima,K., Aizawa,M., and Takahashi,k.(1983), "Estimation of Peak Ground Motions and Response Spectra," Reports of Public Work Research Institute, No.1993. (in Japanese).

14) Midorikawa,S. and Kobayashi,H.(1978), "On Estimation of Strong Motion with Regard to Fault Rupture, 2nd International Earthquake Microzonation Conference, Vol.II, pp.825-836.

15) Milutinovic,Z. and Kameda,H.(1984), "Statistical Model for Estimation of Inelastic Response Spectra," Proc. of JSCE, Structural Eng./Earthquake eng. Vol.1, No.2, pp.105-114.

16) Mori,J. and Shimazaki,K.(1983), "Source Process of the May 26, 1983 Japan Sea Earthquake," Proc. of the Seismological Society of Japan, No.2, p.16.

17) Osawa,I, Kameda,H. and Sugito,M.(1980), "Predicti Model for Near-Source Ground Motions for Great Earthquakes by Fault Division Model," Proc. of the 35th Annual Conference of the JSCE, No.1, pp.376-377(in Japanese).

18) Seno.T., Shimazaki,K., Somerville,P., and Eguchi,T.(1979), "Rupture Process of the Miyahiken-oki Earthquake of June 12, 1978," Submitted to

Phys. Earth. Planet. Inter.

19) Sugito,M. and Kameda,H.(1984), "Prediction of Near-Source Ground Motions for Great Earthquakes from Superposed Evolutionary Process Models," Proc.8WCEE, Vol.II, pp.509-516.

20) Takemura,M, Ohta,T. and Ikeura,T.(1984), "Attenuation Process of Short-Period Seismic Waves in Northeast Japan," Research Report, No.32, Technical Research Institute of Kajima Construction, pp.135-140.

21) Toki,K. and Sato,T.(1980), "Simulation of Strong Motion Seismograms by Autoregressive Moving Average Process," Disaster Prevention Research Institute, Annuals, No.23B-2, pp.1-12(in Japanese).

22) Usami,T.(1975), "Catalogue of Japanese Disastrous Earthquakes," University of Tokyo Press (in Japanese).

23) Utsu,T.(1982), "Relationship between Earthquake Magnitude Scales," Bull. Earthq. Res. Inst., Vol.57, pp.465-497(in Japanese).

24) Vanmarke,E.H. and Lai,S-S.P.(1980), "Strong Motion Duration and RMS Amplitude of Earthquake Records," BSSA, Vol.70, No.4, pp.1293-1307.

5. CONVERSION FACTOR BETWEEN EARTHQUAKE MOTION ON SOIL SURFACE AND ROCK SURFACE WITH CONSIDERATION ON NONLINEARITY OF SOIL LAYERS

5.1 Introduction

The earthquake motion prediction model (EMP-IB,IIB) developed in the previous chapter can be applied for estimation of ground motion on soil surface in the case that the soil formation over the bedrock is given. This method is useful in an engineering sense because the frequency characteristic and the effect of nonlinearity of soil layers can be included in the estimated ground motion. However, in the case that the distribution of the ground motion intensity is necessary for many sites in some wide area, detailed site conditions for the area and a lot of numerical calculations are necessary to obtain corresponding soil surface motion from bedrock motion for many sites. For this purpose it is useful to develop the method to convert the ground motion from rock surface or bedrock level to soil surface level without nonlinear response analysis of soil layers over bedrocks.

The amplification effect of soil layers over bedrock have been observed in the earthquake records(Refs.1,2,5,7). They have dealt with peak ground motion and response spectra on bedrock and soil surface. Since most of the recorded data were those for relatively weak earthquakes, their discussions have been mainly focused on the constant amplification ratio due to the soil conditions. However, in an engineering point of view, the nonlinear amplification effect of soil layers for stronger ground motion is of special importance.

In this chapter the simple conversion technique is developed, which convert the peak ground motion, response spectra, and the intensity parameter used in EMP-IB model from rock surface level to soil surface level. The nonlinear amplification/deamplification effect of soil layers over bedrocks is significant and this characteristic depend on the level of ground motion intensity as well as site conditions. Therefore, the conversion factor β is defined as the function of simple soil parameters and the value of ground motion intensity on rock surface level.

5.2 Simulation of Rock Surface Motion and Corresponding Soil Surface Motion

The multi-observation systems for earthquake motion on soil surface and bedrock have been completed in last 15 years(Refs.3,4,6). However, the data obtained from these obsevation systems are not enough to develop statisticaly the general conversion technique of earthquake motion.

Herein the simulated motion both for rock surface and soil surface are used for development of conversion technique. The simulated rock surface motion have been generated for various combinations of magnitude and distance using the EMP-IB model developed in Chapter 4. Fig.5.1 shows distributions of magnitude and distance used for simulation of rock surface motion. They consist of 56 combinations, and 7 sample motion for different random phase angles have been obtained for each combination. As shown in Fig.5.1, the combinations inside the epicentral region(see Appendix A.1) are excluded for generation. The corresponding soil surface motion have been calculated for the typical Japanese strong motion observation stations where the soil profile data to the bedrock are available. In this calculation the input motion to the bedrock are obtained from the rock surface motion by multiplying them by 1/2, and the equi-linearized method argued in Chapter 2 have been used.

Fig.5.2 shows the example of simulated earthquake motion on rock surface and soil surface. Fig.5.2(a) is the example for relatively weak earthquake motion (M=7.0, Δ=80 km) and Fig.5.2(b) for stronger motion (M=7.0, Δ=22.4 km). The effect of the soil layers over the bedrock can be recognized clearly in the comparison of the acceleration Fourier spectra. In the higher frequency region (f>3.0Hz) the nonlinear amplification/deamplification effect is predominant, specially in the case of larger ground motion (Fig.5.2(b)). In the middle frequancy region (0.8<f<3.0 Hz) the spectrum intensity is amplified remarkably because of the resonance of the surface layers. In the lower frequency region (f<0.7Hz) the Fourier spectra for soil surface motion are not amplified very much. These amplification characteristic as shown above are commonly observed in other cases. The total number of simulated earthquake motion is 392 components for rock surface motion, and 3920 components for soil surface motion, respectively.

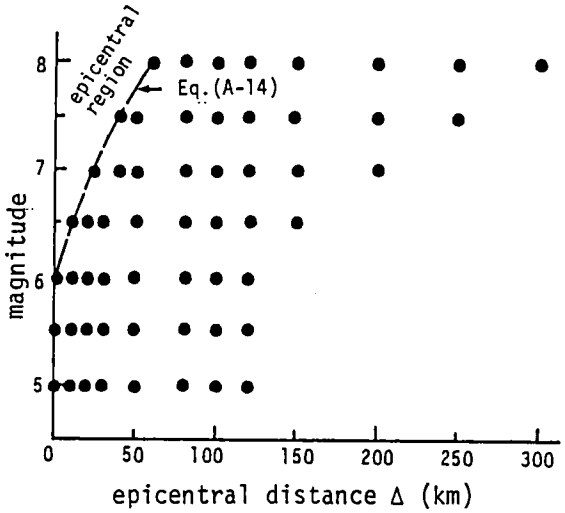

Fig.5.1 Combination of Magnitude and Distance for Simulation of Rock Surface Eartnquake Motion.

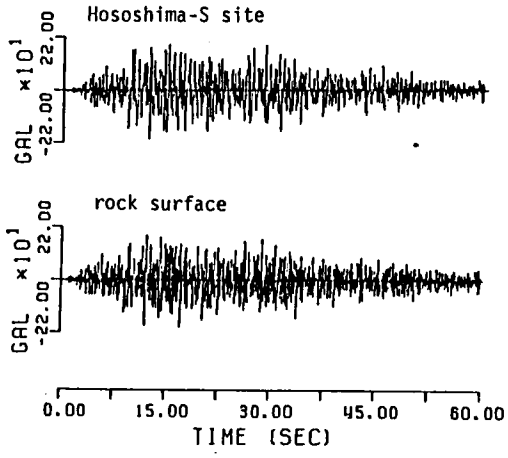

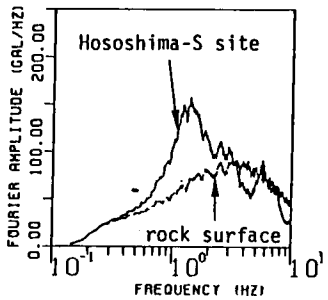

(acc. Fourier spectrum)

(a) M=8.0, Δ=120 km

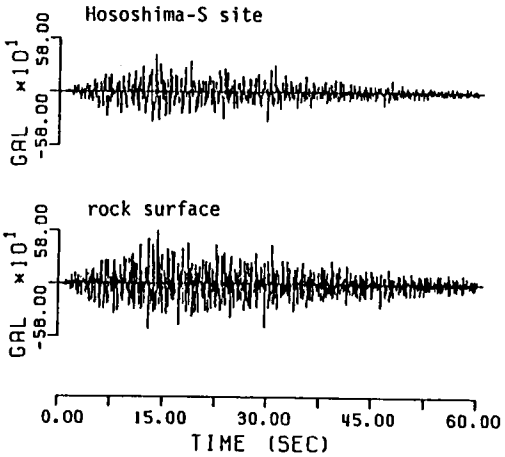

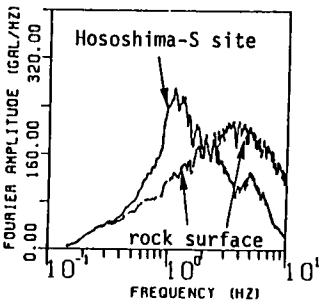

(acc. Fourier spectrum)

(b) M=8.0, Δ=61 km

Fig.5.2 Simulated Earthquake Motion on Rock Surface and Soil Surface.

5.3 Site Model and Soil Parameters S_n and d_p

The typical 10 soil profiles of the Japanese strong motion observation stations have been selected for calculation of soil surface motion. They are listed in Table 2.1(a) ~ (i), and (m). The corresponding soil surface motion for these sites were obtained for 392 components of generated rock surface motion as mentioned before.

Table 5.1 shows the soil parameters for these sites. The soil parameter S_n is calculated from the blow-count profile obtained from the standard penetration test, and is given by

$$S_n=0.264\int_0^{d_s}\exp\{-0.04\cdot N(x)\}\exp\{-0.14x\}\,dx - 0.885 \qquad (5.1)$$

where $N(x)$= blow-count at depth x meters and d_s= depth of the blow count profile. The numerals in Eq.(5.1) have been obtained statistically under the condition that the parameter S_n represents the effect of the softness of surface layers on peak ground motion (see Appendix A.1). Because of the coefficient $\exp\{-0.14x\}$ in Eq.(5.1), the parameter S_n represents the softness of surface layers within the depth 15 ~ 20 meters.

The parameter d_p gives the depth to the bedrock where the shear velocity is approximately 600 ~ 700 m/sec. The two soil parameters S_n and d_p are generally easy to obtain at specific sites. Although these parameters are simple in their defenition, they include generous significant characteristic of surface layers; the soil parameter S_n includes relatively higher frequency characteristic and d_p does relatively lower frequency characteristic of sites over bedrocks.

5.4 Conversion Factor between Rock Surface and Soil Surface Peak Motion

On the basis of the simulated earthquake motion both on rock surface and soil surface, a simple conversion factor β between rock surface and soil surface peak motion is defined.

Table 5.1 Soil Parameters S_n and d_p for Japanese Strong Motion Observation Stations.

site	S_n	d_p (m)
Muroran-S	0.03	14.5
Hachinohe-S	-0.01	180.0
Hososhima-S	-0.06	51.0
Aomori-S	0.37	115.1
Shinagawa-S	0.71	28.9
Itajima brg.	0.48	18.5
Shiogama-kojyo-S	0.52	16.8
Onahama-ji-S	-0.22	8.3
Yamashita-hen-S	0.39	35.0
Sendai-M	-0.07	11.6

Let A_s, V_s, A_r, V_r represent the peak acceleration, velocity on soil surface and those on rock surface, respectively. These peak motion are related by the conversion factor as follows.

$$\begin{cases} A_s = \beta_a \cdot A_r \\ V_s = \beta_v \cdot V_r \end{cases} \tag{5.2}$$

where β_a, β_v are conversion factors for peak acceleration and peak velocity, respectively. The factors β_a, β_v are defined as the function of the soil parameters S_n, d_p and the peak ground motion on rock surface level. The peak ground motion on rock surface level is necessary to incorporate the nonlinear amplification characteristic depending on the level of input motion. The conversion factor for peak motion has been obtained in the following procedure.

[1] The amplification ratio between soil surface and rock surface peak motion have been obtained for the modeling of the conversion factor. Fig.5. shows the typical examples for the amplification ratio of the peak acceleration, and Fig.5.4 for peak velocity. The abscissa represents the peak motion on rock surface. These simulation data were plotted for 10 sites listed in Table.5.1

[2] In Figs.5.3 and 5.4, the relation between the conversion factor and rock surface peak motion can be devided into two typical regions: one for relatively constant (linear response) region and another for nonlinear amplification/deamplification region. The specific rock surface peak motion A_r^l and V_r^l, by which the inclination of the conversion factors can be devided into two regions, have been identified for each sites. Fig.5.5 shows the relation between these specific peak motion and the soil parameter S_n and d_p. As shown in Fig.5.5, the specific peak motion depend strongly on the soil parameter S_n, therefore, the estimation formulas for A_r^l and V_r^l have been obtained as the function of S_n using the least square method and they are shown by the solid lines in Fig.5.5. These estimation formulas are given by

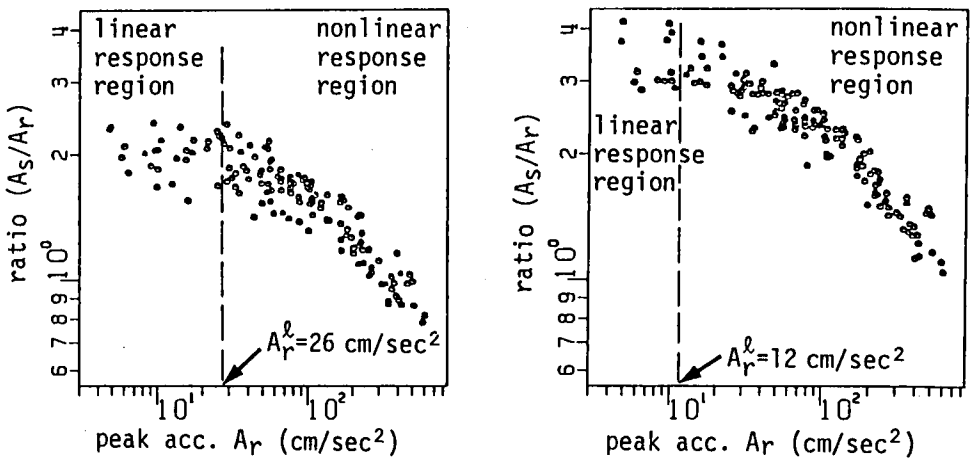

(a) Hososhima-S site (S_n=-0.06, d_p=51 m)

(b) Shinagawa-S site (S_n=0.71, d_p=28.9m)

Fig.5.3 Relation between Amplification Ratio A_s/A_r and Corresponding Peak Acceleration on Rock Surface.

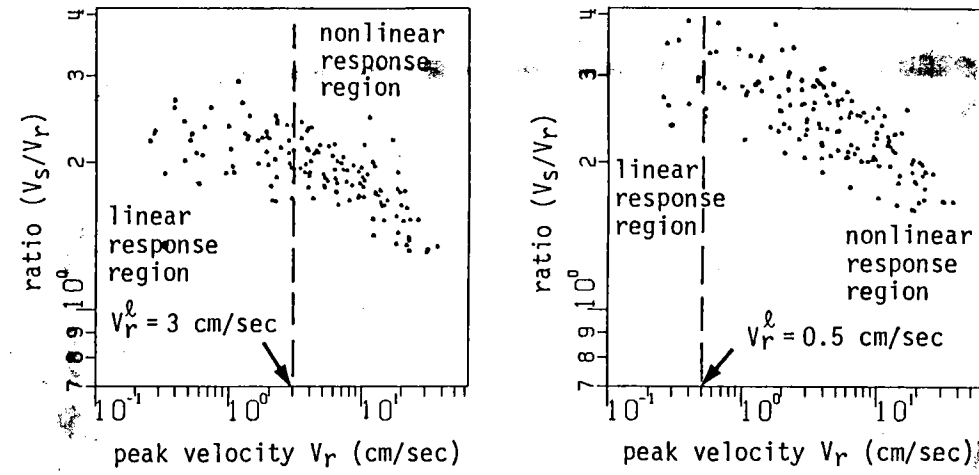

(a) Hososhima-S site (S_n=-0.06, d_p=51 m)

(b) Shinagawa-S site (S_n=0.71, d_p=28.9 m)

Fig.5.4 Relation between Amplification Ratio V_s/V_r and Corresponding Peak Velocity on Rock Surface.

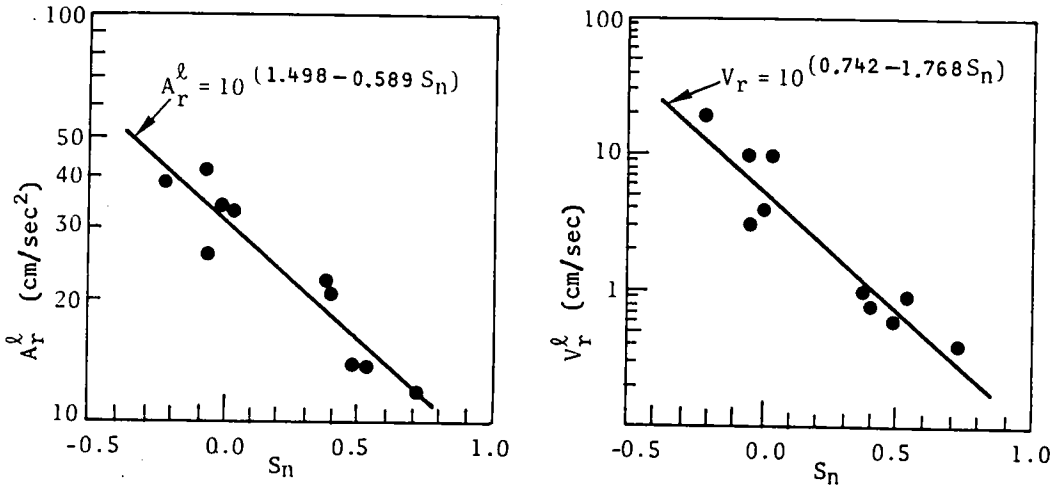

(a) peak acceleration

(b) peak velocity

Fig.5.5 Relation between Specific Peak Value A_r^{ℓ}, V_r^{ℓ} and Soil Parameter S_n.

Table 5.2 Formulas for Estimation of Conversion Factors β_a and β_v.

definition of conversion factor β_a and β_v	$\beta_a = 10^{r_{oa}} \cdot A_r^{r_{ia}}$; $A_r \geqq A_r^{\natural}$	(5.5)
	$\beta_v = 10^{r_{ov}} \cdot V_r^{r_{iv}}$; $V_r \geqq V_r^{\natural}$	(5.6)
	$\beta_a = 10^{r_{oa}} \cdot (A_r^{\natural})^{r_{ia}}$; $A_r < A_r^{\natural}$	(5.7)
	$\beta_v = 10^{r_{ov}} \cdot (V_r^{\natural})^{r_{iv}}$; $V_r < V_r^{\natural}$	(5.8)
definition of specific value A_r^{ℓ} and V_r^{ℓ}	$A_r^{\natural} = 10^{(1.498-0.589 \cdot S_n)}$	(5.3)
	$V_r^{\natural} = 10^{(0.742-1.768 \cdot S_n)}$	(5.4)
coefficients appearing in Eqs.(5.5)-(5.8)	$r_{oa} = 0.705 + 0.187 \cdot S_n + 0.0513 \cdot \log dp$ $r_{ia} = -0.193 - 0.157 \cdot S_n - 0.066 \cdot \log dp$	(5.9)
	$r_{ov} = 0.454 - 0.020 \cdot S_n - 0.038 \cdot \log dp$ $r_{iv} = -0.400 + 0.120 \cdot S_n + 0.108 \cdot \log dp$	(5.10)

$$\log A_r^l = 1.498 - 0.589 \cdot S_n \tag{5.3}$$

$$\log V_r^l = 0.742 - 1.768 \cdot S_n \tag{5.4}$$

[3] Using the least square method, the relation between $\beta_{a,v}$ and peak motion on rock surface have been obtained for the data larger than the given specific peak motion A_r^l and V_r^l. They have been obtained for each site model by using the following formula.

$$\beta_a = 10^{r0_a} \cdot A_r^{r1_a} \quad : A_r \geqq A_r^l \tag{5.5}$$

$$\beta_v = 10^{r0_v} \cdot V_r^{r1_v} \quad : V_r \geqq V_r^l \tag{5.6}$$

Then, the relation between the coefficients appearing in Eqs.(5.5), (5.6) and the soil parameters S_n and d_p have been obtained by using the multiple regression analysis. The results are shown in Table.5.2(Eqs.(5.9) and (5.10)).

[4] The conversion factors β_a, β_v for the region in $A_r < A_r^l$ and $V_r < V_r^l$ are evaluated as the values for the case of the specific peak motion. Namely β_a and β_v are constant in the case of $A_r < A_r^l$ and $V_r < V_r^l$. They are given by Eqs.(5.7) and (5.8) as listed in Table 5.2.

Fig.5.6 shows the examples of the modeled conversion factors and simulated data for two typical sites. It can be observed that the modeled conversion factor represents the nonlinear amplification/deamplification characteristic of surface layers clearly even the conversion factor is estimated from the two simple soil parameters such as S_n and d_p.

Fig.5.7 gives the variation of the conversion factor for three combinations of S_n and d_p. As shown in Fig.5.7, the conversion factor β_a is larger for softer ground in the case of the smaller input motion and is smaller in the case of the larger input motion: on the other hand the conversion factor β_v is larger for softer ground for the whole level of input motion. This phenomena is derived from that the nonlinearity of surface layers is dominant for higher frequency motion. The result is consistent with

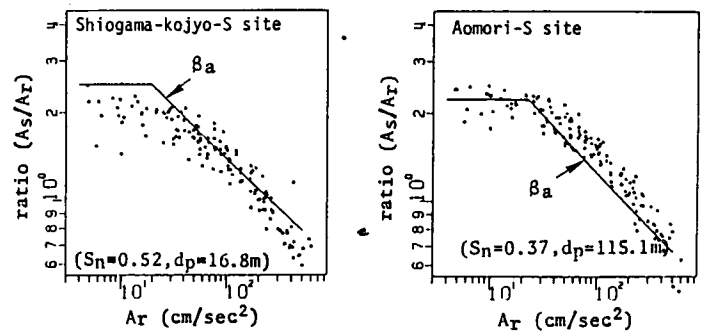

(a) peak acceleration

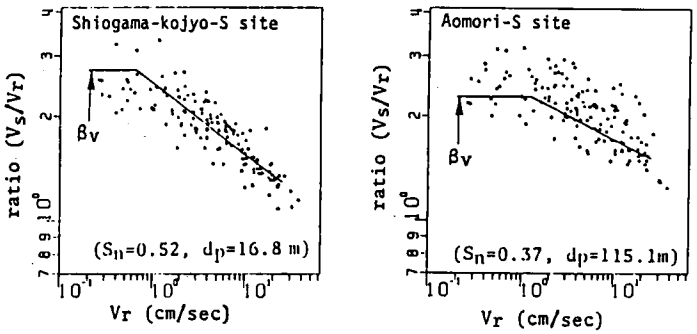

(b) peak velocity

Fig.5.6 Relation between Amplification Ratio and Corresponding Peak Values on Rock Surface with Values of Conversion Factors β_a and β_v.

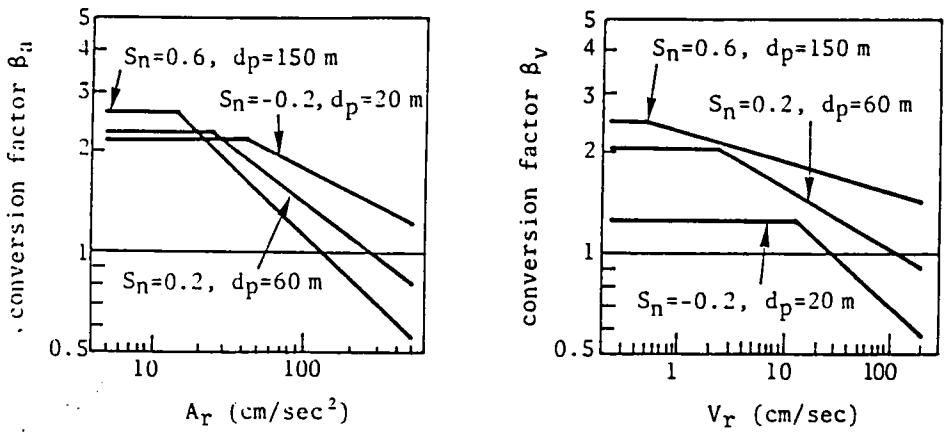

Fig.5.7 Values of Conversion Factors β_a, β_v for Typical Combinations of Soil Parameters.

the significant aspects on ground motion intensities: the peak acceleration does not depend strongly on softness of surface layers, however, the peak velocity is effected by softness of surface layers. It has been pointed out in the past data on earthquake disasters that the earthquake damage depends on softness of ground and has strong correlation with the peak velocity rather than the peak acceleration. The results developed herein coincides with this actual phenomena.

Table 5.2 gives the summary for the estimation formula for the conversion factors β_a and β_v.

5.5 Conversion Factor for Acceleration Response Spectrum

Herein the conversion factor for acceleration response spectra is defined on the basis of the simulated motion developed in Chapter 5.2. The pseudo-acceleration resonse spectrum is dealt with, which is given from the displacement response spectrum in the following form.

$$S(T)=(\frac{2\pi}{T})^2 \cdot S_d(T) \tag{5.11}$$

where $S_d(T)$ is the maximum relative displacement for a period T, and $S(T)$ is the pseudo-acceleration response. The conversion factor β_s proposed here relates both the response spectra on rock surface and soil surface in the following formula.

$$S_s(T)=\beta_s(T) \cdot S_r(T) \tag{5.12}$$

where $S_r(T)$, $S_s(T)$ = acceleration response spectrum for rock surface and soil surface, respectively, and $\beta_s(T)$ = conversion factor for a period T.

Fig.5.8 shows the examples of the acceleration response spectra for Aomori-S site with the corresponding response spectra on rock surface. The solid lines in Fig.5.8 represent the smoothed response spectra as the function of log$T$ with the order of three by using the least square method. Herein the ratio of the smoothed response spectra are used.

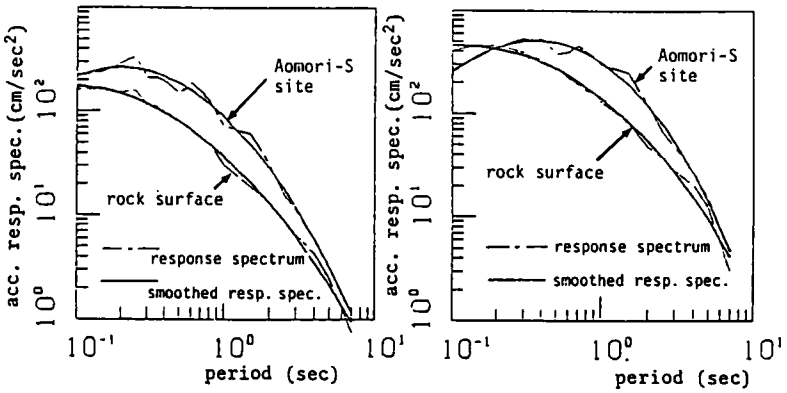

Fig.5.8 Example for Acceleration Response Spectra and Their Smoothed Curves.

The reason to deal with the smoothed response spectra is as follows. In the original response spectra the frequency-characteristic of the ground are usually remarkable. For the estimation of these frequency-dependent characteristic, the transfer function of the ground, calculated from the detailed information for a specific site, is indespensable. However the objectives of the analysis here is to propose the simple conversion factor of response spectra which are obtained from the simple soil parameters. For this purpose it is considered to be better to deal with the smoothed values to grasp the general inclination of the response spectra.

The conversion factor β_s for response spectra is obtained in the following procedure, which is nearly the same as that in the peak ground motion.

[1] The amplification/deamplification ratio between soil surface and rock surface response spectra have been obtained. Fig.5.9 shows the typical examples for the amplification/deamplification ratio of reponse spectra on rock surface level. This kind of figures have been obtained for 10 sites for 20 periods which are distributed in the period range between 0.1 to 7.0 second.

[2] The specific value $S_r^!$, by which the inclination of the conversion factor may be devided, have been identified for each site. They have been obtained generally for the period shorter than 1 second. The estimation formula of the specific value $S_r^!$ for given value of S_n has been obtained using the following formula.

$$\log S_r^!(T) = l_{0s}(T) + l_{1s}(T) \cdot S_n \qquad (5.13)$$

on the period T. Fig.5.10 shows the values of $l_{0s}(T)$ and $l_{1s}(T)$ in Eq.(5.13), which have been obtained for 13 individual points in the period range for $0.1 \leqq T \leqq 1.0$. The solid line in Fig.5.10 represents the smoothed coefficients for $l_{0s}(T)$, $l_{1s}(T)$, and they are given as:

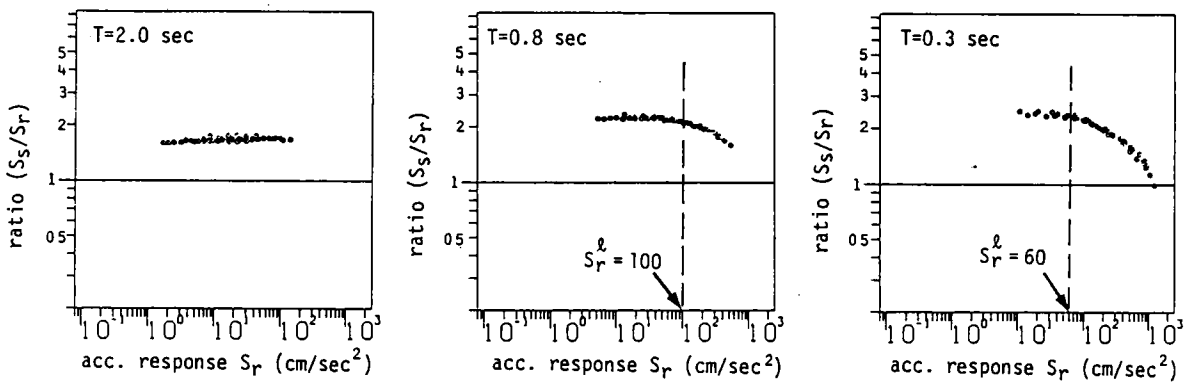

Fig.5.9 Relation between Magnification Ratio S_S/S_r and Corresponding Response Spectra on Rock Surface with Specific values S_r^{ℓ}.

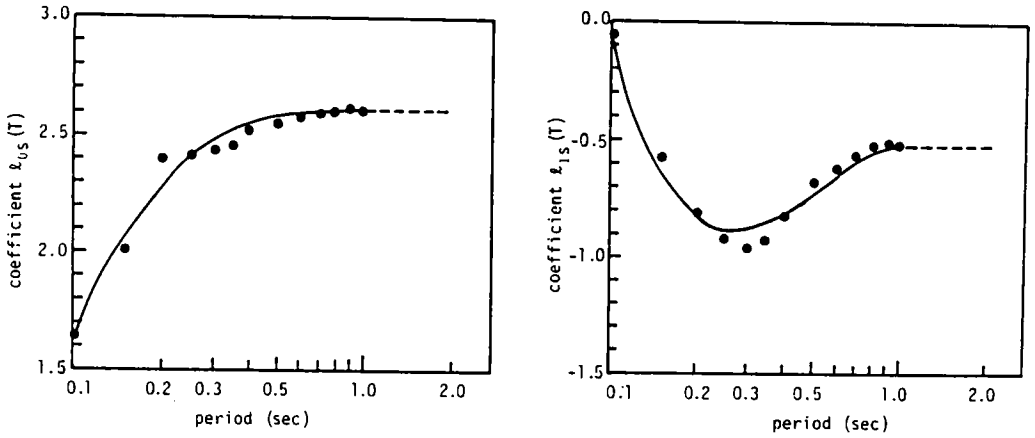

Fig.5.10 Values of Coefficients ℓ_{0S}, ℓ_{1S} with Their Modeled Functions.

$$\begin{cases} l_{0s}(T) = 2.618+0.219\cdot(\log T)+0.732\cdot(\log T)^2+1.505\cdot(\log T)^3 \\ l_{1s}(T) = -0.499+0.369\cdot(\log T)-2.268\cdot(\log T)^2-3.050\cdot(\log T)^3 \end{cases} \quad (5.14)$$

[3] The relation between β_s and the acceleration response spectra S_r on rock surface for the data larger than the given specific value S_r^l have been obtained for each site. The estimation formula for the conversion factor β_s is as follows.

$$\log\beta_s(T) = r_{0s}(T) + r_{1s}(T)\cdot\log S_r(T), \quad S_r(T)\geqq S_r^l(T) \quad (5.15)$$

where $r_{0s}(T)$, $r_{1s}(T)$ = coeficients obtained for the each site. The relation between the coefficients in Eq.(5.15) and the soil parameters S_n, d_p have been obtained using the following formulas.

$$\begin{cases} r_{0s}(T) = r_{00}(T) + r_{01}(T)\cdot S_n + r_{02}(T)\cdot\log d_p \\ r_{1s}(T) = r_{10}(T) + r_{11}(T)\cdot S_n + r_{12}(T)\cdot\log d_p \end{cases} \quad (5.16)$$

The conversion foctor β_s for the region $S_r<S_r^l$ is regarded as constant, and is given by the value for $S_r=S_r^l$ as follows.

$$\log\beta_s(T)=r_{0s}(T) + r_{1s}(T)\log S_r^l(T) \quad (5.17)$$

[4] For the longer period as $T\geqq 1$ sec, where the nonlinear amplification characteristic is not identified, the average of $\beta_s(T)$ for each site has been obtained. These average value were regarded to be the constant term $r_{0s}(T)$ in Eq.(5.15), and the relation between $r_{0s}(T)$ and the soil parameters S_n, d_p has been also evaluated as in the same formula in Eq.(5.16). Namely the conversion factor β_s for $T>1.0$ sec is given by

$$\log\beta_s(T) = r_{0s}(T) \quad (5.18)$$

The values of the coefficients in Eq.(5.16) are shown in Fig.5.11, which were smoothed on the period axis. Table 5.3 gives these values. In Fig.5.11 the typical amplification/deamplification characteristic of soil layers is

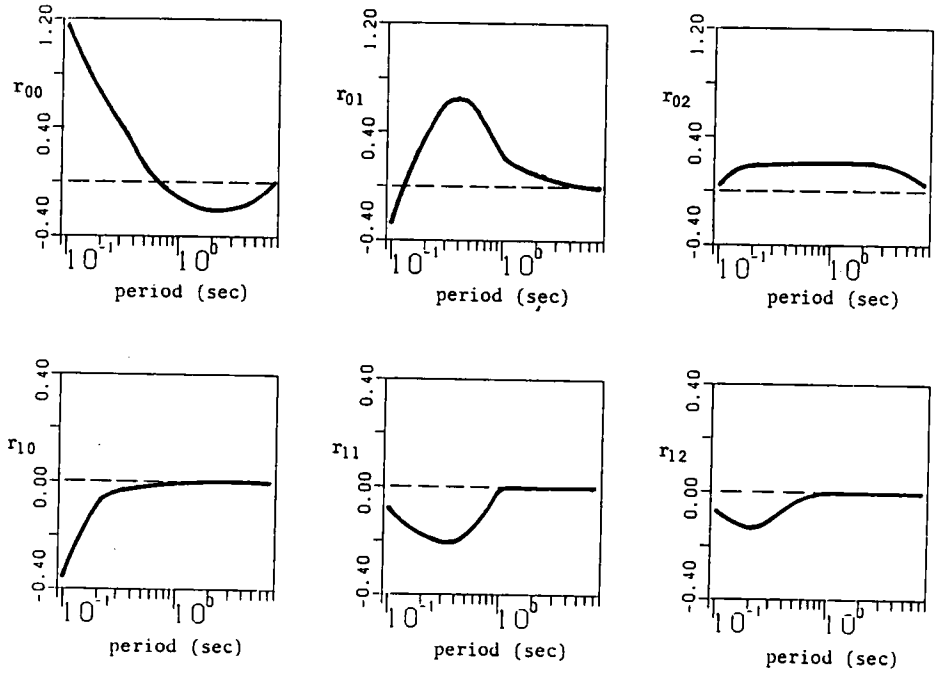

Fig.5.11 Values of Coefficients $r_{00} \sim r_{12}$ Appeared in Eq.(5.16).

Table 5.3 Values of Coefficients $r_{00} \sim r_{12}$ Appeared in Eq.(5.16).

period(sec)	r_{0_0}	r_{0_1}	r_{0_2}	r_{1_0}	r_{1_1}	r_{1_2}
7.00	-0.020	0.002	0.045	0.0	0.0	0.0
5.00	-0.135	0.005	0.131	0.0	0.0	0.0
4.00	-0.171	0.010	0.163	0.0	0.0	0.0
3.00	-0.193	0.035	0.193	0.0	0.0	0.0
2.50	-0.202	0.059	0.208	0.0	0.0	0.0
2.00	-0.203	0.099	0.217	0.0	0.0	0.0
1.50	-0.184	0.138	0.218	0.0	0.0	0.0
1.00	-0.120	0.198	0.213	0.0	0.0	0.0
0.90	-0.075	0.280	0.213	-0.003	-0.038	-0.004
0.80	-0.040	0.370	0.212	-0.005	-0.079	-0.009
0.70	-0.005	0.453	0.212	-0.007	-0.115	-0.014
0.60	0.050	0.550	0.211	-0.013	-0.151	-0.024
0.50	0.120	0.615	0.210	-0.017	-0.180	-0.038
0.40	0.260	0.660	0.208	-0.020	-0.201	-0.070
0.35	0.358	0.645	0.206	-0.028	-0.210	-0.090
0.30	0.441	0.615	0.203	-0.040	-0.210	-0.105
0.25	0.544	0.540	0.196	-0.052	-0.200	-0.123
0.20	0.655	0.388	0.180	-0.076	-0.180	-0.133
0.15	0.835	0.164	0.168	-0.184	-0.150	-0.119
0.10	1.163	-0.270	0.043	-0.339	-0.080	-0.073

shown clesrly. The coefficient r_{01} of the soil parameter S_n is predominant in the range 0.2~1.0 sec, namely, the ground motion in this period range is amplified mainly because of the softness of surface layers. Since the coefficient r_{01} takes negative values for the period such as T<0.15 sec, ground motion in this shorter period is amplified on hard ground for the case S_n<0. The coefficient r_{02} of the depth to bedrock d_p is relatively constant on the period axis. The coefficient r_{11} of S_n and r_{12} of d_p, which represent the nonlinear characteristic of soil layers, take negative value for the period such as T<1.0 sec. On the other hand the coefficients r_{10}, r_{11}, r_{12} are equal to zero for T>1.0 sec. From the result on these coefficients it is concluded that the nonlinear characteristic of soil layers is predominant for the period range, T<1.0 sec, and the ground motion for longer period is not effected by nonlinear characteristic of surface layers.

Table 5.4 gives the summary of the estimation formulas for the conversion factor β_s. Fig.5.12 shows the examples for the comparison between the conversion factor β_s and simulation data. The abscissa represents the values of the acceleration response spectra on rock surface and the ordinate represents the amplification/deamplification coefficients obtained from the simulated earthquake motion. The broken lines represent the modeled conversion factor β_s given by Eqs.(5.15), (5.17) and (5.18). Fig.5.12(a) is the example for relatively hard ground (Hachinohe-S Site, S_n=-0.01, d_p=180m), and Fig.5.12(b) for very soft ground (Shinagawa-S Site, S_n=0.71, d_p=28.9 m). It can be observed that the conversion factor β_s discribed by broken lines coincide with the simulation data and represent the nonlinear amplification/deamplification characteristic of soil layers fairly well.

Fig.5.13 shows the comparison of response spetra between (a) S_r for rock surface motion, (b) S_s, represented by circles, for soil surface motion given by use of β_s as $S_s(T)=\beta_s(T)\cdot S_r(T)$, and (c) S_s' obtained from simulated soil surface motion. It is observed that the estimated value S_s by use of β_s represent fairly well the general characteristic of response spectra for simulated soil surface motion.

Fig.5.14 shows the dependence of β_s on the level of the ground motion intensities for typical two site conditions. It is easy to recognize the

Table 5.4 Formulas for Estimation of Conversion Factor β_S.

conversion formula	$S^{10} = \beta_s \cdot S_r(M, \Delta, T, h)$ --(5.12)
definition of conversion factor β_S	$T < 1.0$(sec) ; $\beta_s = 10^{r_{os}} \cdot S_r^{r_{is}}$; $S_r \geqq S_r^{\ell}$ --(5.15) $\beta_s = 10^{r_{os}} \cdot (S_r^{\ell})^{r_{is}}$; $S_r < S_r^{\ell}$ --(5.17) $T \geqq 1.0$(sec) ; $\beta_s = 10^{r_{os}}$ --(5.18)
definition of specific value S_r^{ℓ} .(T 1.0 sec)	$S_r^{\ell} = 10^{(\ell_{os} + \ell_{is} \cdot S_n)}$ --(5.13) $\begin{cases} \ell_{os} = 2.618 + 0.219 \cdot \log T + 0.732 \cdot (\log T)^2 + 1.505 \cdot (\log T)^3 \\ \ell_{is} = -0.499 + 0.369 \cdot \log T - 2.268 \cdot (\log T)^2 - 3.050 \cdot (\log T)^3 \end{cases}$ --(5.14)
coefficients appearing in Eqs.(5.15)-(5.18)	$\begin{cases} r_{os}(T) = r_{o0}(T) + r_{o1}(T) \cdot S_n + r_{o2}(T) \cdot \log dp \\ r_{is}(T) = r_{i0}(T) + r_{i1}(T) \cdot S_n + r_{i2}(T) \cdot \log dp \end{cases}$ --(5.16)

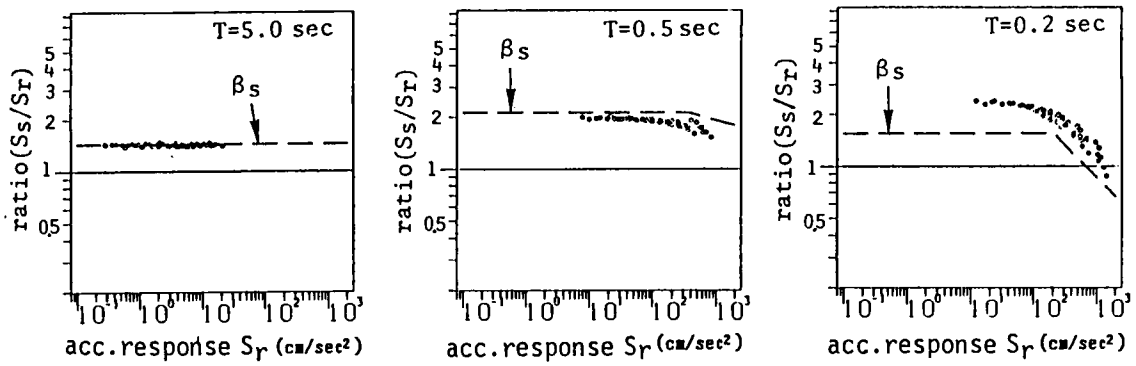

(a) Hachinohe-S site (S_n=-0.01, d_p=180 m)

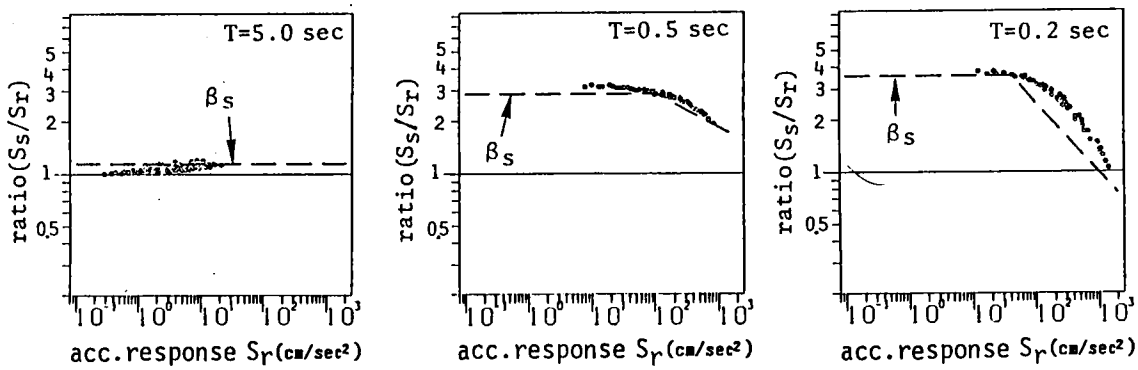

(b) Shinagawa-S site (S_n=0.71, d_p=28.9 m)

Fig.5.12 Relation between Magnification Ratio S_S/S_r and Corresponding Response Spectra on Rock Surface with Values of Conversion Factor β_S.

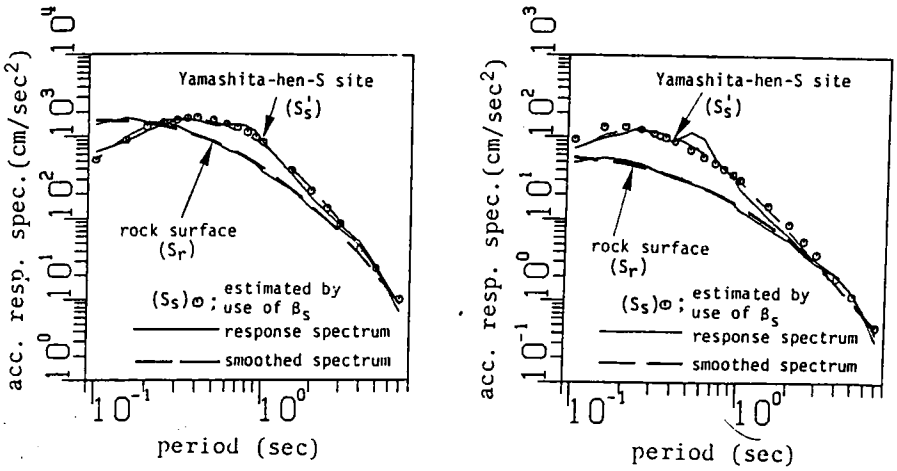

(a) M=8.0, Δ=61 km (b) M=6.0, Δ=120 km

Fig.5.13 Comparison of Response Spectra for Rock Surface and Soil Surface Motion with Values of $S_S(T)$ estimated by Use of $\beta_S(T)$.

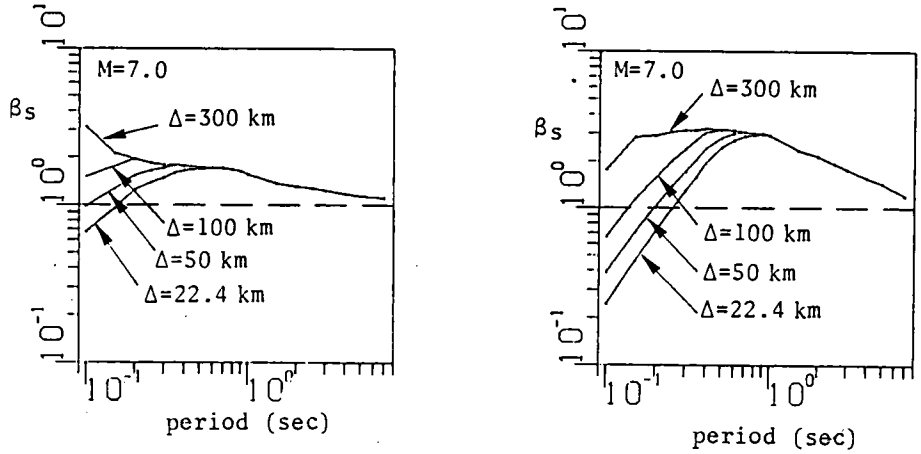

(a) S_n=0.0, d_p=30 m (b) S_n=0.6, d_p=150 m

Fig.5.14 Values of Conversion Factor β_S for Typical Combinations of Soil Parameters.

effect of the predominant nonlinear characteristic in the case of soft ground. It is also observed and very important aspect in a sense of the earthquake engineering that the conversion factor β_s is larger for softer ground without depending on the level of the input motion in the period region $T \geqq 0.5$ sec, in which the spectrum intensity of the ground motion is generally strong.

5.6 Conversion Factor for Evolutionary Power Spectrum

The conversion technique of ground motion intensities can be also useful for the nonstationary earthquake motion prediction model on rock surface (EMP-IB) developed in Chapter 4. It is very useful to convert the evolutionary power spectrum estimated on rock surface level into those for soil surface level without response analysis of soil layers over bedrocks. The procedure dealt in Chapter 5.5 has been applied for the development of the conversion factor for evolutionary power spectrum.

Fig.5.15 shows the example for simulated rock surface motion and corresponding soil surface motion. The soil surface motion were obtained on the basis of the multi-reflection theory with equi-linearized method, which was explained in Chapter 2.2. The simulated ground motion time history is ahown, in Fig.5.15(a) and (b). In Fig.5.15(c) the evolutionary spectra and their model function developed in Chapter 4.2 are shown. In Fig.5.15(c), the model parameters $t_{p_s}(f)$ and $t_{s_s}(f)$ for soil surface motion are fixed as the same values as those for rock surface motion. Accordingly the intensity parameter $\alpha_{m_s}(f)$ for soil surface motion is given as follows.

$$\alpha_{m_s}(f)=\frac{n}{e}\left\{\frac{n}{\Gamma(n+1)}\cdot\frac{A_{0s}(f)}{t_{p_r}(f)}\right\}^{1/n} \tag{5.19}$$

In Fig.5.15(d) the intensity parameters both for rock surface and soil surface motion are shown. The shin solid line in Fig.5.15(d) represents the intensity parameter $\alpha_{m_s}'(f)$ calculated under the same condition described by Eqs.(4.3) $\sim$ (4.5). Since the intensity parameter $\alpha_{m_s}(f)$ does not differ very much from $\alpha_{m_s}'(f)$, it is regarded that the surface layers over bedrocks effect mainly on the intensity parameter, and that the duration parameter

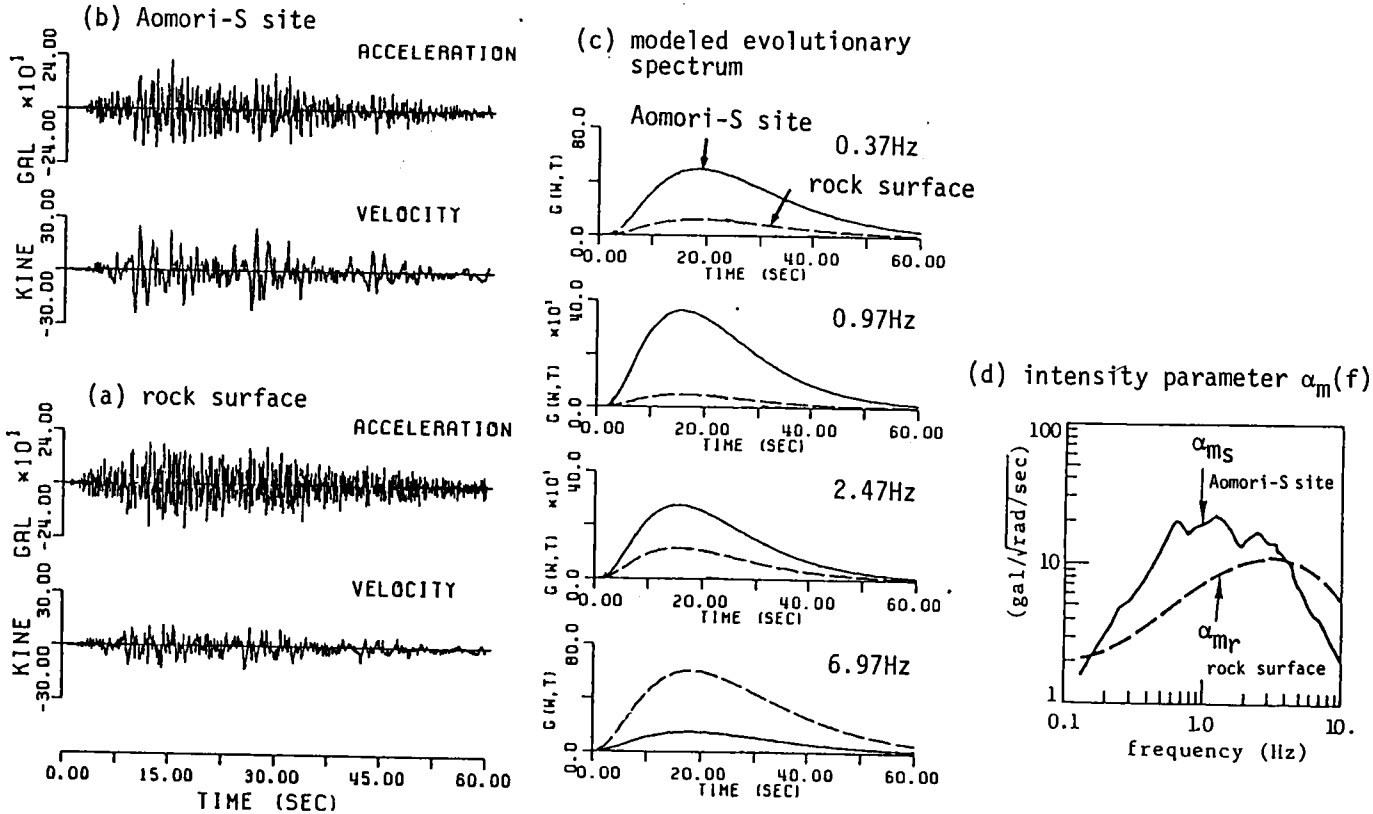

Fig.5.15 Simulated Rock Surface and Soil Surface Motions with Modeled Evolutionary Spectra and Intensity Parameters.

$t_{p_r}(f)$ and starting time parameter $t_{s_r}(f)$ for rock motion can be substituted those for soil surface motion.

Under this assumptions the conversion factor $\beta_\alpha(f)$ for the intensity parameter $\alpha_m(f)$ can be defined as follows.

$$\alpha_{m_s}(f)=\beta_\alpha(f)\cdot\alpha_{m_r}(f) \tag{5.20}$$

Fig.5.16 shows the example for the intensity parameter both for rock surface and soil surface motion. The broken line in Fig.5.16 represents the smoothed curve which were given as the function of log$f$ with the order of three. These smoothed values were dealt with to incorporate the general inclination of the parameters. The conversion factor $\beta_\alpha(f)$ has been obtained by using the same procedure as that for the response spectra.

Fig.5.17 shows the relation between the intensity parameter α_{m_r} on rock surface and the ratio $\alpha_{m_s}/\alpha_{m_r}$ for typical three frequencies. In Fig.5.17, the specific value $\alpha^l_{m_r}(f)$ devides the line nonlinear amplification characteristc of the intensity parameter $\alpha_m(f)$: in the case $\alpha_{m_r}(f)<\alpha^l_{m_r}(f)$ the ratio $\alpha_{m_s}(f)/\alpha_{m_r}(f)$ is relatively constant, and in the case $\alpha_{m_r}(f)\geqq\alpha^l_{m_r}(f)$ the ratio decreases with increase in $\alpha_{m_r}(f)$, i.e. the nonlinearity of surface layers is predominant.

The estimation formula of the specific value $\alpha^l_{m_r}(f)$ for given value of S_n has been obtained using the following formula.

$$\log\alpha^l_{m_r}(f)=l_{0\alpha}(f)+l_{1\alpha}(f)\cdot S_n \tag{5.21}$$

where $l_{0\alpha}(f), l_{1\alpha}(f)$ = coefficients depending on the frequency f. Fig.5.18 shows the value of $l_{0\alpha}(f)$ and $l_{1\alpha}(f)$ by circles, which were obtained for 16 individual points for the range $f\geqq 1.0$ Hz. The solid lines in Fig.5.18 represents the smoothed coefficients for $l_{0\alpha}(f)$, $l_{1\alpha}(f)$, and they are given as,

$$\begin{cases} l_{0\alpha}(f)= 1.135-0.643\cdot\log f+2.256\cdot(\log f)^2-2.913\cdot(\log f)^3 \\ l_{1\alpha}(f)=-0.350+0.286\cdot\log f-4.960\cdot(\log f)^2+4.888\cdot(\log f)^3 \end{cases} \tag{5.22}$$

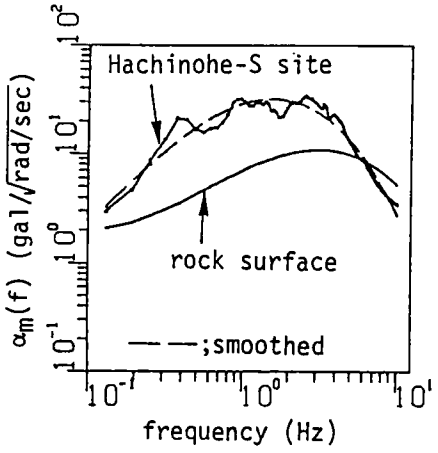

Fig.5.16 Example for Intensity Parameter on Rock Surface and Soil Surface with Their Smoothed Curve.

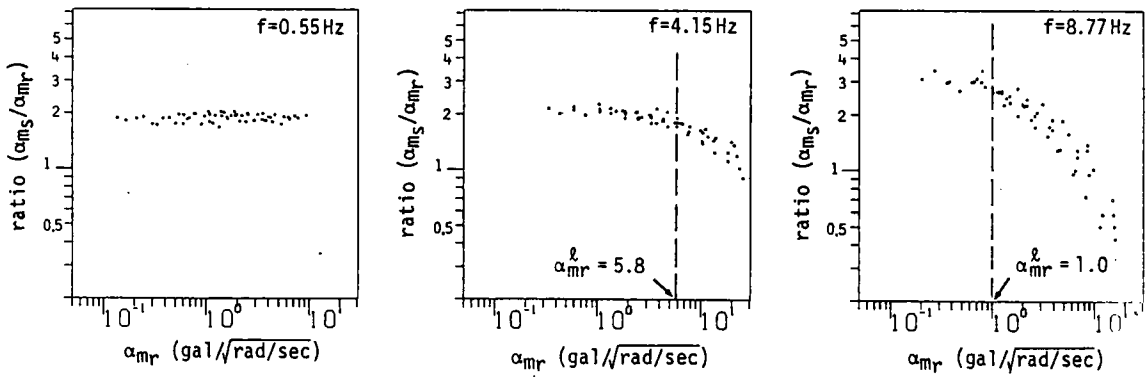

Fig.5.17 Relation between Magnification Ratio α_{ms}/α_{mr} and Corresponding Intensity Parameter on Rock Surface with Specific Values α_{mr}^{ℓ}.

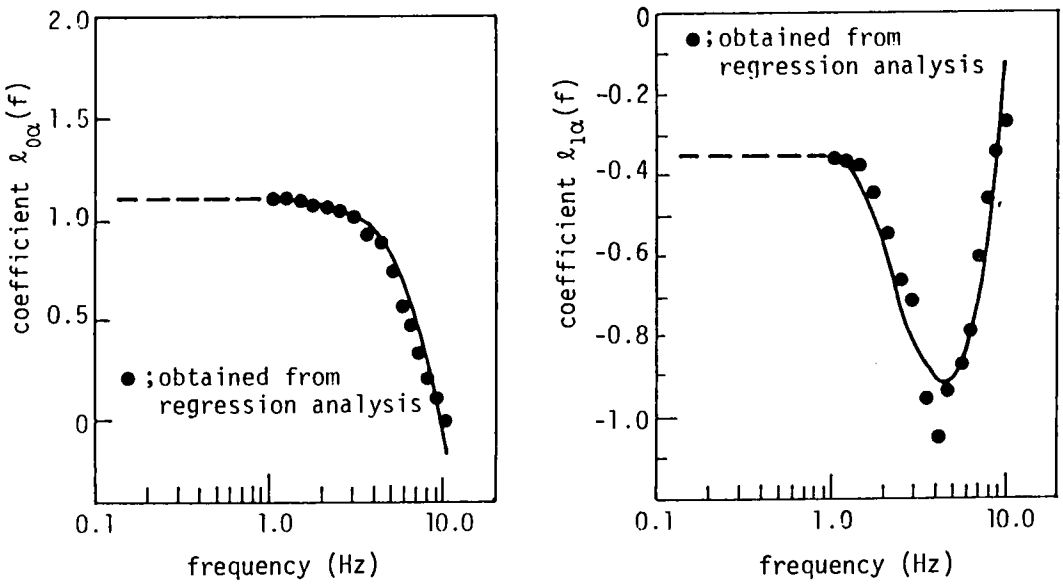

Fig.5.18 Values of Coefficients $\ell_{0\alpha}$, $\ell_{1\alpha}$ with Their Modeled Functions.

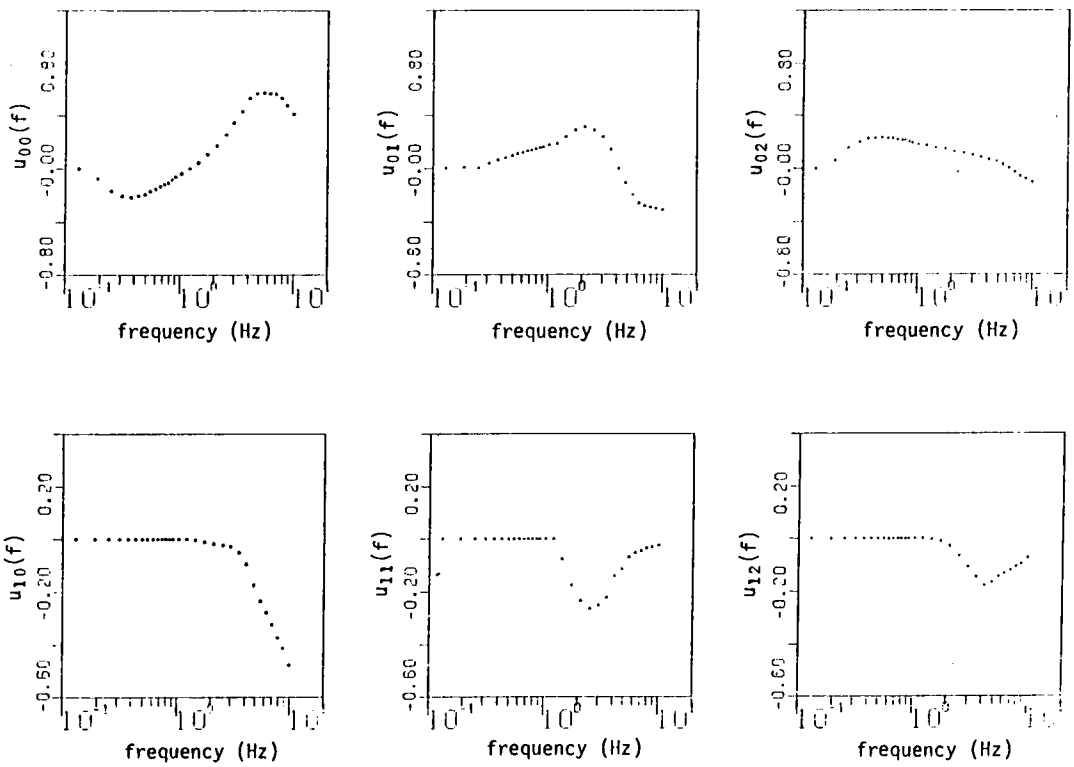

Fig.5.19 Values of Coefficients $u_{00} \sim u_{12}$ Appeared in Eq.(5.24).

For the simulation data for each site, the following relation has been obtained using only the data larger than the given specific value $\alpha^{l}_{m_r}(f)$.

$$\log\beta_\alpha(f)=r_{0\alpha}(f)+r_{1\alpha}(f)\cdot\log\alpha_{m_r}(f), \qquad \alpha_{m_r}(f)\geqq\alpha^{l}_{m_r}(f) \tag{5.23}$$

where $r_{0\alpha}(f), r_{1\alpha}(f)$ = coefficients obtained for each site. Then the relation between the coefficients in Eq.(5.23) and the soil parameters S_n, d_p have been obtained in the following formulas.

$$\begin{cases} r_{0\alpha}(f)=u_{00}(f)+u_{01}(f)\cdot S_n+u_{02}(f)\cdot\log d_p \\ r_{1\alpha}(f)=u_{10}(f)+u_{11}(f)\cdot S_n+u_{12}(f)\cdot\log d_p \end{cases} \tag{5.24}$$

The conversion factor β_α for the region $\alpha_{m_r}<\alpha^{l}_{m_r}$ is regarded to be constant, amd is given by the value for $\alpha_{m_r}=\alpha^{l}_{m_r}$ and follows.

$$\log\beta_\alpha(f) = r_{0\alpha}(f) + r_{1\alpha}(f)\log\alpha^{l}_{m_r}(f), \qquad \alpha_{m_r}(f)<\alpha^{l}_{m_r}(f) \tag{5.25}$$

For the lower frequency as $f<1.0$Hz, in which the nonlinear amplification characteristic is not identified, the average ratio $\alpha_{m_s}/\alpha_{m_r}$ for each site was obtained, and they were used as the constant term $r_{0\alpha}(f)$ in Eq.(5.23). Namely, the coefficient $r_{1\alpha}(f)$ in Eq.(5.23) was evaluated as $r_{1\alpha}(f)\equiv 0$ for the region $f<1.0$Hz, and given by

$$\log\beta_\alpha(f) = r_{0\alpha}(f), \qquad f\leqq 1.0Hz \tag{5.26}$$

Fig.5.19 shows the values of the coefficients appearing in Eq.(5.22), and Table 5.5 gives their values for 30 individual frequency points. The coefficients shown in Fig.5.19 and Table 5.5 were slightly smoothed on the frequency axis.

Fig.5.20 shows the values of the conversion factor $\beta_\alpha(f)$ given by Eq.(5.21) for typical site conditions and several sets of magnitude and distance. It can be observed that the conversion factor $\beta_\alpha(f)$ for higher

Table 5.5 Values of Coefficients $u_{00} \sim u_{12}$ Appeared in Eq.(5.24).

f (Hz)	u_{00}	u_{01}	u_{02}	u_{10}	u_{11}	u_{12}
0.13	0.0	0.006	0.0	0.0	0.0	0.0
0.19	-0.073	0.007	0.071	0.0	0.0	0.0
0.25	-0.169	0.008	0.156	0.0	0.0	0.0
0.31	-0.201	0.040	0.198	0.0	0.0	0.0
0.37	-0.212	0.069	0.222	0.0	0.0	0.0
0.43	-0.202	0.083	0.231	0.0	0.0	0.0
0.49	-0.192	0.098	0.236	0.0	0.0	0.0
0.55	-0.168	0.110	0.230	0.0	0.0	0.0
0.61	-0.151	0.121	0.227	0.0	0.0	0.0
0.67	-0.130	0.135	0.218	0.0	0.0	0.0
0.73	-0.115	0.139	0.216	0.0	0.0	0.0
0.79	-0.104	0.149	0.212	0.0	0.0	0.0
0.85	-0.083	0.156	0.203	0.0	0.0	0.0
0.91	-0.061	0.162	0.194	0.0	0.0	0.0
1.03	-0.035	0.178	0.184	0.0	0.0	0.0
1.21	0.0	0.195	0.171	-0.002	-0.010	-0.002
1.45	0.032	0.256	0.160	-0.004	-0.103	-0.004
1.75	0.087	0.322	0.148	-0.010	-0.206	-0.019
2.11	0.158	0.348	0.130	-0.015	-0.262	-0.048
2.53	0.236	0.330	0.118	-0.023	-0.283	-0.086
3.01	0.318	0.254	0.104	-0.035	-0.266	-0.125
3.55	0.389	0.150	0.087	-0.055	-0.228	-0.155
4.15	0.452	0.0	0.067	-0.089	-0.152	-0.176
4.81	0.482	-0.128	0.054	-0.155	-0.114	-0.164
5.53	0.507	-0.218	0.031	-0.239	-0.072	-0.144
6.25	0.527	-0.284	0.002	-0.295	-0.053	-0.130
7.03	0.540	-0.342	-0.026	-0.350	-0.040	-0.119
7.87	0.559	-0.401	-0.054	-0.401	-0.030	-0.105
8.77	0.560	-0.468	-0.075	-0.441	-0.024	-0.095
10.03	0.552	-0.555	-0.100	-0.500	-0.020	-0.072

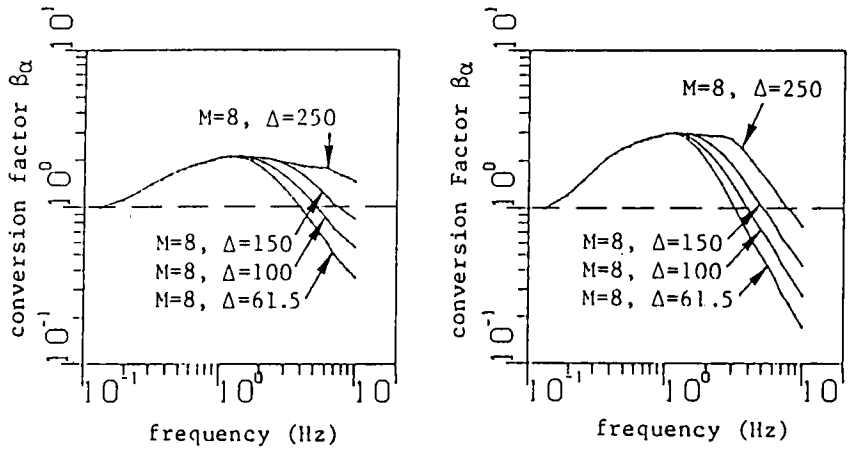

Fig.5.20 Values of Conversion Factor β_α for Typical Combinations of Soil Parameters.

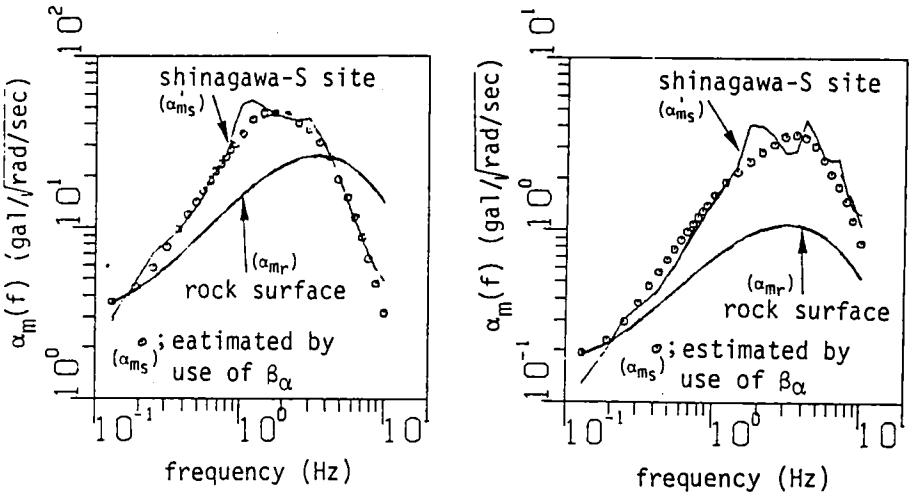

Fig.5.21 Comparison of Intensity Parameters for Rock Surface and Soil Surface Motion with Values of $\alpha_{ms}(f)$ estimated by Use of $\beta_\alpha(f)$.

Table 5.6 Formulas for Estimation of Conversion Factor β_α.

conversion formula	$\alpha_{ms}(f)=\beta_\alpha(f)\ \alpha_{mr}(f)$	--(5.20))
definition of conversion factor β_α	$f>1.0$(Hz);	
	$\beta_\alpha=10^{\Gamma_{0\alpha}}\cdot\alpha_{mr}{}^{\Gamma_{1\alpha}}$ $\quad \alpha_{mr}\geqq\alpha_{mr}^{s}$	--(5.23)
	$\beta_\alpha=10^{\Gamma_{0\alpha}}\cdot(\alpha_{mr}^{s})^{\Gamma_{1\alpha}}$ $\quad \alpha_{mr}<\alpha_{mr}^{s}$	--(5.25)
	$f\leqq 1.0$(Hz);	
	$\beta_\alpha=10^{\Gamma_{0\alpha}}$	--(5.26)
definition of specific value α_m^{ℓ} (f 1.0 Hz)	$\alpha_{mr}^{s}=10^{(\ell_{0\alpha}+\ell_{1\alpha}Sn)}$	--(5.21)
	$\begin{cases}\ell_{0\alpha}=1.135-0.643\log f+2.256(\log f)^2-2.913(\log f)^3\\ \ell_{1\alpha}=-0.350+0.286\log f-4.960(\log f)^2+4.888(\log f)^3\end{cases}$	--(5.22)
coefficients appearing in Eqs.(5.23)-(5.26)	$\begin{cases}\Gamma_{0\alpha}(f)=u_{00}(f)+u_{01}(f)Sn+u_{02}(f)\log dp\\ \Gamma_{1\alpha}(f)=u_{10}(f)+u_{11}(f)Sn+u_{12}(f)\log dp\end{cases}$	--(5.24)

frequency region such as $f \geqq 3.0$Hz strongly depend on the level of input motion intensity, and $\beta_\alpha(f)$ is smaller for softer ground in the case of relatively larger input motion. On the other hand the conversion factor $\beta_\alpha(f)$ is generally larger for middle and lower frequency region such as $f<3.0$Hz for softer ground. The conversion factor $\beta_\alpha(f)$ depends strongly on the soil parameters for middle frequency region in which earthquake motion intensity is generally predominant. These phenomena was also pointed out in the case of the conversion factor β_s for response spectra in Chapter 5.5.

Fig.5.21 shows the comparison of the intensity parameters : (a) $\alpha_{m_r}(f)$ for rock surface motion, (b) $\alpha_{m_s}(f)$ for soil surface motion given by use of the conversion factor β_α as $\alpha_{m_s}(f)=\beta_\alpha(f)\cdot\alpha_{m_r}(f)$., and (c) $\alpha'_{m_s}(f)$ obtained from simulated soil surface motion. It can be observed that the intensity parameter $\alpha_{m_s}(f)$, which is converted from that on rock surface $\alpha_{m_r}(f)$ by $\beta_\alpha(f)$, includes the general characteristic of $\alpha_{m_s}'(f)$ on the frequency axis even though $\beta_\alpha(f)$ is defined by only the simple soil parameters.

The usefulness of the conversion factor $\beta_\alpha, \beta_v, \beta_s(T)$, and $\beta_\alpha(f)$ developed herein may be summarized as follows.

[1] To obtained the conversion factor, only the simple soil parameters such as S_n and d_p are necessary as for site conditions.

[2] The nonlinear amplification effect of soil layers over bedrocks can be incorporated into the earthquake motion prediction without the nonlinear response analysis of surface layers.

[3] As for the factor $\beta_\alpha(f)$ the technique is specially effective for the case that the ground motion time series on many soil sites are necessary for given common input bedrock motion.

5.7 Conclusions

In this Chapter a simple conversion factor between earthquake motion on soil surface and rock surface has been developed. The major results derived here may be summarized as follows.

[1] The dataset of the simulated earthquake motion on rock surface for several combinations of magnitude and distance have been generated by using the nonstationary earthquake motion prediction model (EMP-IB) developed in Chapter 4. The corresponding soil surface motion for these rock surface motion have been calculated for typical earthquake motion observation stations on the basis of the multi-layer reflection theory with the equi-linearized method.

[2] Based on this simulated ground motion dataset the conversion factor β_a,β_v for peak acceleration and peak velocity, respectively, have been developed focussing on the nonlinear amplification characteristic of surface layers over bedrocks. The conversion factor β_a, β_v are defined by the simple soil parameters S_n, d_p which are generally available at a specfic construction sites, and the peak earthquake motion on rock surface. The peak ground motion on soil surface are simply converted from those on rock surface as in the form $A_s=\beta_a \cdot A_r$ and $V_s=\beta_v \cdot V_r$.

[3] The technique has been applied for acceleration response spectra and the intensity parameter of evolutionary power spectra used in the nonstationary earthquake motion prediction model on rock surface (EMP-IB). In the development of the conversion factor for these spectrum intensities the significant characteristic of the nonlinear amplification/deamplification effect of surface layers has been derived.

To verify the validity of the conversion factor proposed in this Chapter by actual data, several sets of ground motion data recorded both on soil surface and bedrock for several type of sites are indispensable. Since the multi-observation system for ground motion have been completed by many research groups and the simultaneous records both on soil surface and bedrock or rock surface have been accumulated gradually, the verification and the further development of the conversion technique will be possible.

The development of the database for simultaneous earthquake motion on bedrock and soil surface has been started through the good offices of the concerning research groups including the staffs in private companies (See

Appendix C.). This kind of database is of special importance not only for verification of the conversion technique developed herein, but for general analysis on uncertainty factors in earthquake ground motion.

REFERENCES

1) Abe,Y. et al.(1984), "Dynamic Behavior of Pile Foundation During Earthquake," Proc. of 8th World Conference on Earthquake Engineering, Vol.III, pp.585-592.
2) Arakawa,T., Kawashima,K., Aizawa,T., and Takahashi,K.(1982), "Analysis on Underground Earthquake Motion at Tokyo Bay Area," Research Report, No.1852, Public Works Research Institute, Ministry of Construction (in Japanese).
3) Katayama,T. and Sato,N.(1982), "Ground Strain Measurements by a Densely Located Seismometer Array," Proc of the 5th Japan Earthquake Engineering Symposium, pp.241-248.
4) Noda,S., Kurata,E., Iai,S., and Tsuchida,H., "Observation of Earthquake Motions by Instrument Arrays in Port Area and Preliminary Analysis," Proc. of the 5th Japan Earthquake Engineering Symposium, pp.289-296.
5) Ohta,T. and Niwa,M(1977), "Amplification Ratio and Spectral Characteristic of Surface Soil," Annuals Kajima Construction Research Institute, No.26(in Japanese).
6) Okubo,T. and Kawashima,K.(1982), "Dense Instrument Array Observation by the Public Works Research Institute and Analysis of Some Records," Proc. of the 5th Japan Earthquake Engineering Symposium, pp.297-304(in Japanese).
7) Sawada,Y. et al.(1983), "Soil-Structure Interaction of JPDR Reactor -Investigation of Dynamic Characteristic based on Earthquake Observation," Research Report, Electric Power Research Institute, No.383029(in Japanese).

6. EARTHQUAKE RESPONSE ANALYSIS AND DAMAGE ESTIMATION FOR JOINT-CONNECTED BURIED PIPES

6.1 General Remarks

It is an indispensable subject for a seismic risk assessment of underground lifeline systems to make clear the response behaviors of buried pipes during earthquakes. In the response analysis of buried pipes, the effect of propagating seismic waves, one of the major causes of structural damage to buried pipes, has been studied (Refs.7,13,18,20,21,23,24,41). Their results are generally summarized as follows.

(1)The behavior of buried pipes is subjected to the relative displacement of the ground, and the mass effect of pipes is negligible.

(2)The axial strain is predominant in pipes compared with the bending strain.

(3)The slippage between pipes and surrounding soils makes the pipe strain smaller than in the case of no slippage.

(4)At bent and crossing sections of pipes, a relatively large stress occurs in comparison with the straight part of pipes.

(5)In the case of joint-connected pipes, the joint absorbs the the relative ground displacement and the axial pipe stress scarcelly occurs in the expansion side where the joint is movable.

Table 6.1 gives the historical review for the study on earthquake response of buried pipelines and system reliability of lifeline systems. The field observation has been started as the first step in lifeline earthquake engineering. Then, the response behavior of buried pipes have been studied analitically, and the experimental work have been also performed to evaluate the mechanizm of pipe slippage and response behavior of pipes in liquefied sand as well as in dislocated ground. The methodology for system reliability of lifeline netwoek systems started to be discussed after the above

Table 6.1 Historical Review for Study on Earthquake Response and System Reliability of Buried Pipeline System.

year	response behavior of buried pipes			system reliability	occurence of major earth-quake*
	field observasion	experimental study	response analysis		
1964					1964 Niigata Earthquake(M=7.5)
65					
66					
67					
68					1968 Tokachi-oki Earthquake(M=7.9)
69	Sakurai, Takahashi(31)				
1970					
71					1971 San Fernand Earthquake(M_L=6.3)
72					
73		Bouwkamp, Stephen(3)			
74				Panoussis(28)	
75			Miyajima, Miyauchi(20) Permelee, Ludtke(29)	Taleb-Agha(39)	
76		Miyamoto, Hojyo, Furusho(21)	Takada, Nagao(38)		
77		Kuribayashi, Iwasaki, Kawashima, Miyata(18)		Shinozuka, Takada, Kawakami (34)	
78			Saionji, et.al.(30) Ukai, Yamaguchi(41)		1978 Miyagiken-oki Earthquake(M=7.4)
79			Muleski, Ariman(23) Shinozuka, Koike(33) Takada, Takahashi(36)		1979 Imperial Valley Earthquake (M_L=6.6)
1980			Hindy, Novak (6) Wang (42)	Toki, Sato (40)	
81		Katada, Hakuno(15)		Kameda, Goto, Sugito, Asaoka (13) Isoyama, Katayama(18) Noda, Yamada, Iemura(25) O'Rourke, Wang(27) Tamura, Kawakami(35)	
82	Iwamoto, Sakurai, Wakai, Hojyo, Furusawa(9)	Kitaura, Miyajima(16) Takada (37)	Kameda, Shinozuka(14) Akiyoshi, Fuchida(1) Goto, Sugito, Kameda, Ishikawa(4)	Moghtaderizadeh, Kiureghian(22)	1982 Urakawa-oki Earthquake(M=7.1)
83				Hoshiya, Miyazaki(7)	1983 Nihonkai-Chubu Earthquake (M=7.7)
84	Oishi, Sekiguchi(26)			Kameda, Goto, Kasuga (12) Sato (32)	
85					1985 Mexico Earthquake(M_S=8.1)

* M : JMA magnitude, M_L : local magnitude, M_S : surface wave magnitude

fundamental works started. Several earthquakes both in Japan and U.S.A. have motivated the development of the research in this field.

Most of the analytical works have dealt with the response behavior of straight pipes. Some works have been extended to the curved pipes or junctions (Refs.13,20,23,24), however, most of works have dealt with some simplified models and they do not correspond to the actual cases where some complex structural forms as mentioned later have been used.

In this chapter, focussing on the joint-connected pipes which have been commonly used for water supply systems, earthquake response analysis is carried out for their typical forms used in the actual systems. In chapter 6.2 the structural characteristic of joint connected buried pipes are discussed on the basis of the data from the Kyoto City Water Supply System. In Chapter 6.3 the earthquake response analysis of joint-connected buried pipes is carried out for the two typical forms; the model I for a straight part of pipelines, and the model II for a typical section where pipes are reinforced and fixed. Then, in Chapter 6.4, for the simplified estimation for earthquake damage of joint-connected pipes, the formulas to estimate the axial and bending strain, and the joint displacement of pipes are proposed as functions of input ground strain amplitude and apparent wave length in longitudinal direction. Based on the response characteristic of joint-connected buried pipes, the simple method for the mitigation of bending stress at the concrete-fixed section is demonstrated.

6.2 Structural Characteristic of Joint-Connected Buried Pipelines

The details on the structures and materials along the aqueducts and trunk routes of the Kyoto City Water Supply Districts have been examined to establish the analytical models, types of which are commonly used in the actual systems. Fig.6.1 shows the aqueducts and the water supply districts in Kyoto City.

In Fig.6.1, the aqueducts and the trunk routes in zones[5] and [11] have been surveyed, focusing on the materials and the diameters of pipes, the angle of the bent pipes, the structural forms at the bent and crossing

Water supply district

(1) Matsugasaki S.HE.D.
(2) Matsugasaki HE.D.
(3) Matsugasaki H.D.
(4) Yamanouchi H.D.
(5) Keage H.D.
(6) Keage HE.D.
(7) Yamanouchi L.D.
(8) Keage L.D.
(9) Kujyoyama HE.D.
(10) Shinyamashina H.D.
(11) Shinyamashina L.D.
(12) Rakusai N.T.

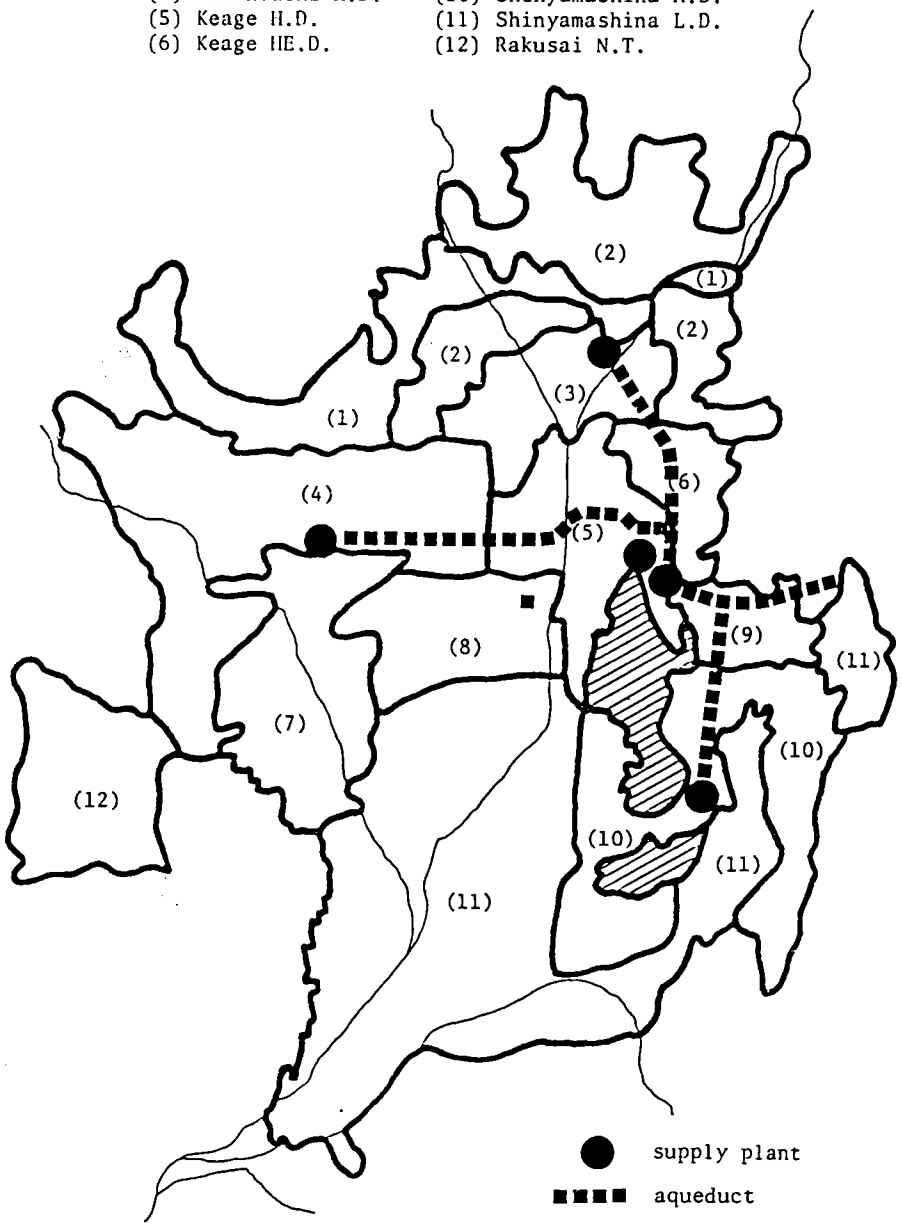

Fig.6.1 Kyoto City Water Supply District.

sections, and the types of joints, etc. Fig.6.2 shows the percentage of pipe materials in the total length of construction and that of bent angles in horizontal and vertical bent pipes.

In the survey for the trunk routes of the Kyoto City Water Suplly System, the following articles of their structural and material characteristic have been summarized.

(1) The trunk routes consist mostly of ductile iron pipes(DIP), and partly of steel pipes(SP), concrete pipes(RC), and cast iron pipes(CIP).

(2) The bent pipes are used mainly in horizontal and vertical directions, and the bent angles, in the case of ductile iron pipes, are of 5 types, namely 90°, 45°, $22^{1}/_{2}$°, $11^{1}/_{4}$°, and $5^{5}/_{8}$° . In these five kinds of bent pipes, the angles for $22^{1}/_{2}$° is used most frequently, and that for 90°, which has been often applied in the analytical models of pipelines including bent sections (Refs.14,19,21,23), is very few.

(3) A couple of bent pipes are commonly used for bent sectios such as two 45° bent pipes for a 90° bent section(Fig.6.3)

(4) Most of the bent sections are protected by concrete, and at these sections a special type of joint, which is superior in capacity of displacement and of resistance to pulling out, is used frequently.

(5) At the intersection of the pipelines, a special structural form called "L-junction" is commonly employed using bent pipes and T-junction pipes(Fig.6.3)

(6) The pipe-bridges, the pipes attached to bridges, and the provisionally distributed pipes on some structures exist at sections where pipelins are exposed on the ground.

Judging from a standpoint of earthquake responses of buried pipes, they may be classified into two typical forms; one for the straight part of pipes and another for the concrete-fixed sections where bent pipes are used. In the

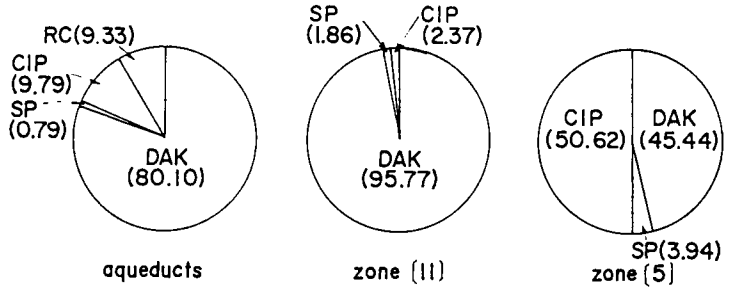

(a) percentage of pipe materials in total length of construction

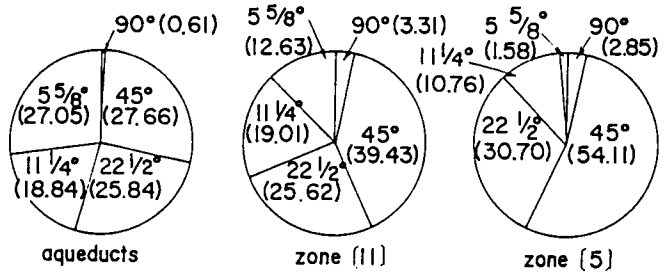

(b) percentage of bent angles in horizontal bent pipes

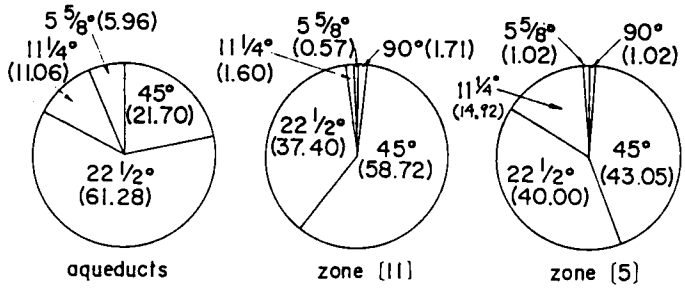

(c) percentage of bent angles in vertical bent pipes

Fig.6.2 Percentage of Pipe Materials and Angles of Bent Pipes in Kyoto City Water Supply System(aqueducts, zone[5], zone[11]).

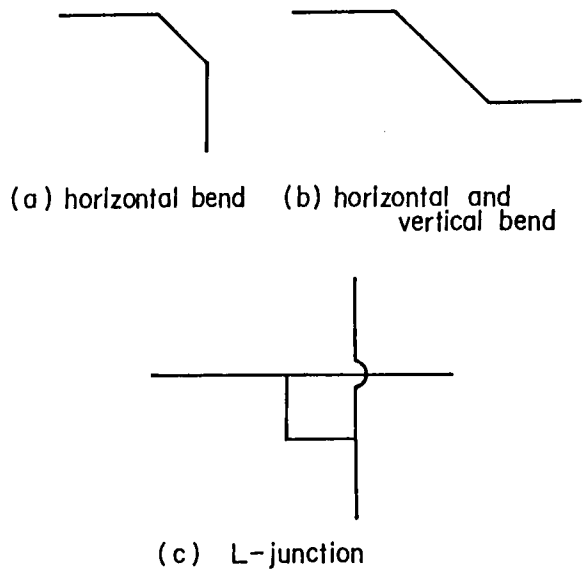

Fig.6.3 Typical Structural Forms at Bent and Crossing Sections.

following Chapter 6.3, therefore, the earthquake response analysis of buried pipes are carried out for these two typical pipes forms.

6.3 Earthquake Response Analysis of Joint-Connected Buried Pipes Including Concrete-Fixed Sections

6.3.1 Analytical Technique by Transfer Matrix Method(Ref.24)

Herein, the analytical technique for response analysis of buried pipes is mentioned. The computer program used in the following response analysis has been modified from the basic program termed 'ERAUL(1)' coded by Takada(Ref.36).

Analytical models are constructed under the following condision:

1) Quasi-static analysis can be applied, i.e. the effect of the inertia forces and damping are assumed to be negligible.

2) Buried pipelines are treated as a series of segmented elastic beams, connected longitudically with joints which have a non-linear spring behavior for both axial and bending motion. Each beam is supported by soil springs with sliding characteristic.

3) Seismic forces, generated by soil deformation relative to pipe motion, act on the pipe body through the soil spring.

4) The pipe motion is analyzed within a two dimensional horizontal plane, and a perfect elastic behavior is assumed for the pipe material.

Fig.6.4 shows the analytical model of buried pipes. Differential equations can be established with respect to the internal force within the pipe, and the force proportinal to the displacement of the pipe relative to those of the free field:

1) longitudinal motion

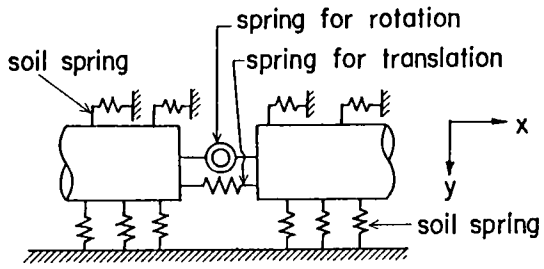

Fig.6.4 Analytical Model for Buried Pipes.

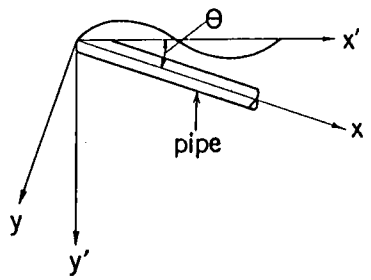

Fig.6.5 Buried Pipe and Horizontally Propagating Seismic Wave.

$$-EA\frac{d^2u}{dx^2}+k_{s_x}\cdot u=k_{s_x}\cdot u_{s_x} \tag{6.1}$$

2) tramnsverse motion

$$EI\frac{d^4v}{dx^4}+k_{s_y}\cdot v=k_{s_y}\cdot u_{s_y} \tag{6.2}$$

where u, v=the longitudinal and transverse displacements of the pipe, u_{s_x}, u_{s_y}=the logitudinal and transverse displacements of the free fields, respectively, E=Young's modulus of the pipe material, A, I=the cross sectional area and geometrical moment of inertia of the pipe, respectively, k_{s_x}, k_{s_y} =the equivalent spring constants for the longitudinal and transverse motion, respectively , to reflect the soil-structure interaction.

Fig.6.5 shows the relation between the pipe and horizontally propagating seismic waves. Eqs.(6.1) and (6.2) are rewrittten as follows, using the free field displacement represented by a sinusoidal wave with an arbitrary incident angle θ to the longitudinal axsis(x-axsis) of the pipeline:

1) longitudinal motion

$$-EA\frac{d^2u}{dx^2}+k_{s_x}u=k_{s_x}\cdot u_{s_{x0}}\sin\left[\omega\cdot\left\{t-\frac{(x+\xi)\cos\theta}{c}\right\}\right] \tag{6.3}$$

2) transverse motion

$$EI\frac{d^4v}{dx^4}+k_{s_y}v=k_{s_y}\cdot u_{s_{y0}}\sin\left[\omega\cdot\left\{t-\frac{(x+\xi)\cos\theta}{c}\right\}\right] \tag{6.4}$$

where $u_{s_{x0}}$ and $u_{s_{y0}}$ =the longitudinal and transverse displacement amplitudes of the free field, ω=angular frequency, c= apparent wave speed, ξ=distance which results from a phase delay at the origin of x-axsis. In Eqs.(6.3) and (6.4), the displasement amplitudes $u_{s_{x0}}$ and $u_{s_{y0}}$ are represented by the free field displacement amplitude u_m:

$$u_{s_{x0}}=u_{in}\cdot\cos\theta$$

$$u_{s_{y0}}=-u_{in}\cdot\sin\theta \tag{6.5}$$

The general solution $u(x)$ and $v(x)$ in Eqs. (6.3) and (6.4) are obtained as follows:

$$v(x)=e^{\beta_1 x}(C_1\cos\beta_1 x+C_2\sin\beta_1 x)+e^{\beta_1 x}(C_3\cos\beta_1 x+C_4\sin\beta_1 x)+v_0(x) \tag{6.6}$$

$$u(x)=C_5\cosh\beta_2 x+C_6\sinh\beta_2 x+u_0(x) \tag{6.7}$$

where

$$\beta_1=(k_{s_y}/4EI)^{1/4} \tag{6.8}$$

$$\beta_2=(k_{s_x}/EA)^{1/2} \tag{6.9}$$

$$v_0(x)=\frac{u_{s_{y0}}}{1+(\omega\cos\theta/c)^4 EI/k_{s_y}}\sin\left[\omega\cdot\left\{t-\frac{(x+\xi)\cos\theta}{c}\right\}\right] \tag{6.10}$$

$$u_0(x)=\frac{u_{s_{x0}}}{1+(\omega\cos\theta/c)^2 EA/k_{s_y}}\sin\left[\omega\cdot\left\{t-\frac{(x+\xi)\cos\theta}{c}\right\}\right] \tag{6.11}$$

In Eqs.(6.6) and (6.7), $C_1\sim C_6$ are the constants of integration to be determined by the boundary conditions.

Then, the physical quantities such as the deflections u and v, the deflection angle φ, the axial force N, the moment M, and the shear force Q at an arbitrary point x are obtained, using the boundary condisions u^L, v^L, φ^L, N^L, M^L, and Q^L.

$$u(x)=u^L\beta_5(x)-N^L\frac{B_6(x)}{EA\beta_2}+D_5(x) \tag{6.12}$$

$$v(x)=v^L B_1(x)-\frac{\varphi^L}{2\beta_1}B_3(x)+\frac{M^L}{2\beta_1^2 EI}B_2(x)-\frac{Q^L}{4\beta_1^3 EI}B_4(x)+D_1(x) \tag{6.13}$$

$$\varphi(x)=-v^L\beta_1 B_4(x)+\varphi^L B_1(x)-\frac{M^L}{2\beta_1 EI}B_3(x)-\frac{Q^L}{2\beta_1^2 EI}B_2(x)+D_2(x) \tag{6.14}$$

$$N(x)=-u^L EA\beta_2 B_6(x)+N^L B_5(x)+D_6(x) \tag{6.15}$$

$$M(x)=-2v^L EI\beta_1^2 B(x)-\varphi^L\beta_1 EIB_4(x)+M^L B_1(x)+\frac{Q^L}{2\beta_1}B_3(x)+D_3(x) \tag{6.16}$$

$$Q(x)=-2v^L EI\beta_1^3 B_3(x)+2\varphi^L B_1^2 EIB_2(x)+M^L\beta_1 B_4(x)+Q^L B_1(x)+D_4(x) \tag{6.17}$$

In Eqs.(6.12)$\sim$ (6.17), the functions $B_1(x)\sim B_6(x)$ and $D_1(x)\sim D_6(x)$, which are called load terms, are represented in Appendix D. The positive directions of the forces N^L, Q^L, M^L, etc. in i-the beam are shown in Fig.6.6.

Transfer Matrix Method

Substituting $x=l$, which is the length of the unit pipe, into Eqs(6.12)$\sim$ (6.17) the relationship between the physical quantity V^R on the right side of the i-th beam and V^L on the left side is given as:

$$V^R = F\ V^L \tag{6.18}$$

where V^R and V^L, called state vectors, are the column vectors of physical quantities such as the deflections u and v, the deflection angle φ, the axial force N, the moment M, and the shear force Q at the ends of the right and left side of i-th beam, and F is the field matrix which has the function of transferring the state vector from one end to other of the beam.

Next, the equilibrium equations at the joints are given by

$$\begin{bmatrix} u \\ v \\ \varphi \end{bmatrix}^L_{k+1} = \begin{bmatrix} u \\ v \\ \varphi \end{bmatrix}^R_k + \begin{bmatrix} -N/k_T \\ -M/k_R \\ 0 \end{bmatrix}^R_k, \qquad \begin{bmatrix} N \\ M \\ Q \end{bmatrix}^L_{k+1} = \begin{bmatrix} N \\ M \\ Q \end{bmatrix}^R_k \tag{6.19}$$

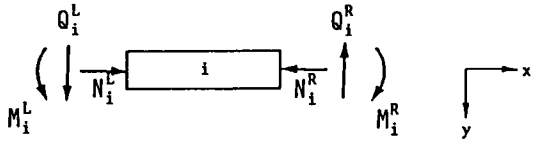

Fig.6.6 Positive Direction of Forces.

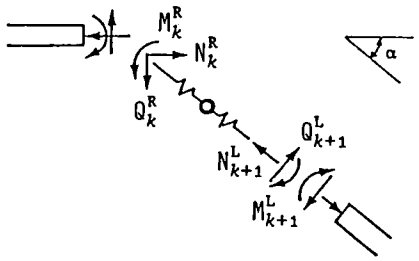

Fig.6.7 Equilibrium State of Forces at Bent Section.

where k_T and k_R are translational (longitudinal) and rotational springs representing the mechanical features of the joints. Eq.(6.19) is rewriten as follows:

$$V^L_{k+1} = P_k \; V^R_k \tag{6.20}$$

where P_k is the point matrix which relates V^L_{k+1} with V^R_k. (See Appendix C)

The equilibrium state of the deformations and forces at the bent sections are shown in Fig.6.7. The following relations for the deformations and forces at the bent sections of the pipes are obtained using the bent angle α of the pipelines.

$$\begin{cases} N^L_{k+1} = N^R_k\cos\alpha + Q^R_k\sin\alpha \\ Q^L_{k+1} = -N^R_k\sin\alpha + Q^R_k\cos\alpha \\ M^L_{k+1} = M^R_k \end{cases} \tag{6.21}$$

$$\begin{cases} u^L_{k+1} = -N^R_k\cos\alpha/k_T - Q^R_k\sin\alpha/k_T + u^R_k\cos\alpha + v^R_k\sin\alpha \\ v^L_{k+1} = v^R_k\cos\alpha - n^R_k\sin\alpha \\ \varphi^L_{k+1} = \varphi^R_k - M^R_k/k_R \end{cases} \tag{6.22}$$

The point matrix P at the bent sections is given from Eqs.(6.21) and (6.22). (See Appendix D.) The boundary condition at the left hand side of the pipeline is represented by the boundary matrix R and the initial matrix A^L_1 as

$$V^L_1 = R \; A^L_1 \tag{6.23}$$

In Eq.(6.23), the menbers of the initial vector A^L_1 represent the degree of freedom. In the response analysis , the hinged condition is used at the ends of both sides to neglect the infleunce of the boundary conditions on the computational results of the analysis. Then, R, A^L_1, and the boundary matrix R', at the right nand side, are represented as follows.

$$R^T=\begin{bmatrix} 0 & 0 & 0\ 1\ 0\ 0\ 0 \\ 0 & 0 & 1\ 0\ 0\ 0\ 0 \\ 0 & 0 & 0\ 0\ 0\ 1\ 0 \\ u_{s_x}(0,t) & u_{s_y}(0,t) & 0\ 0\ 0\ 0\ 1 \end{bmatrix}, \qquad A_1^l=\begin{bmatrix} N \\ \varphi \\ Q \\ 1 \end{bmatrix}_l^L,$$

$$R'=\begin{bmatrix} 1\ 0\ 0\ 0\ 0\ 0 & -u_{s_x}(nl,t) \\ 0\ 1\ 0\ 0\ 0\ 0 & -u_{s_y}(nl,t) \\ 0\ 0\ 0\ 0\ 1\ 0 & 0 \end{bmatrix} \tag{6.24}$$

The boundary condition at the right hand side of the pipeline is represented by using the boundary matrix R' as:

$$R'V_N=0 \tag{6.25}$$

Substituting the boundary conditions of Eqs. (6.23) and (6.25) into the relations of Eqs. (6.18) and (6.20), the following linear equation can be obtained.

$$R'\cdot F_N\cdot P_{N-1}\cdot F_{N-1}\cdot\cdot\cdot P_1\cdot R\cdot A_1^l=0 \tag{6.26}$$

In Eq. (6.26), the solution for A_1^l is given, and then all unknown variables can be obtained with the aid of the field and point matrices.

Then, the transfer matrix and the soil spring constant for a concrete-fixed section are given as follows.

The transfer matrix for a concrete-fixed section

The following two conditions are asseumed for simplification of numerical analysis.

a) The ground displacement arround the concrete-fixed section is constant as shown in Fig.6.8(b) instead of the actual distributions (Fig.6.8(a)),

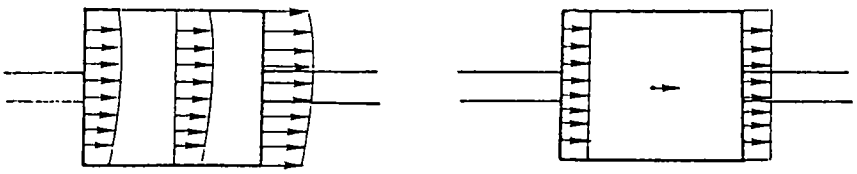

(a) displacement distribution

(b) simplifierd displacement distribution

Fig.6.8 Distribution of Displacement at Concrete-Fixed Section.

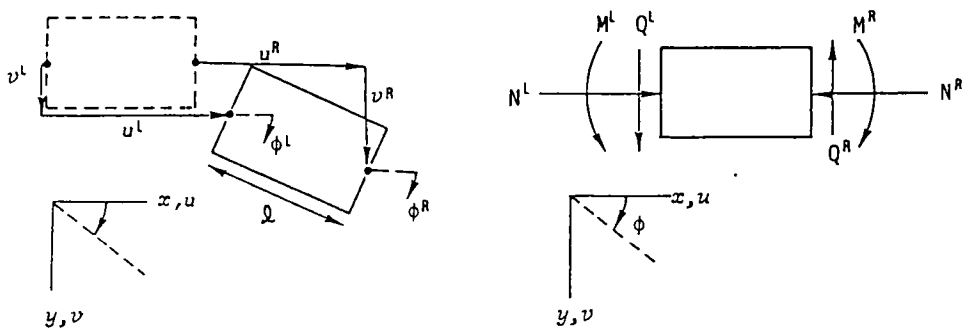

Fig.6.9 Equilibrium of Displacement and Force at Concrete-Fixed Section.

since the length of each side of the concrete-fixed section is relatively very short comparing with the wave length of input ground motion.

b) The body of the concrete-fixed section is treated to be rigid.

The equilibrium of the physical quantities at both side of the concrete-fixed section are given as follows (See Fig.6.9).

· displacement in longitudinal direction (x-axis)

$$u^R = u^L - l(1-\cos\Phi^L) \fallingdotseq u^l \tag{6.27}$$

· displacement in transverse direction (y-axis)

$$v^R = v^l + l\sin\varphi^L \fallingdotseq v^L + l\varphi^L \tag{6.28}$$

· rotation

$$\varphi^R = \varphi^L \tag{6.29}$$

· axial force

$$N^R = N^L + k_x \cdot (u_{s_x} - u^L) \tag{6.30}$$

· bending moment

$$M^R = M^L + k_\theta \cdot \varphi^L \tag{6.31}$$

· shear force

$$Q^R = Q^L + k_x (u_{s_y} - v^L) \tag{6.32}$$

where,

u^L, u^R ; displacement at left and right sides in the logitudinal direction,

v^L, v^R ; displacement at left and right sides in the transverse direction,

Φ^L, Φ^R ; rotational angle in rad,

l ; length of the concrete-fixed section in the longitudinal direction

N^L, N^R ; axial force at left and right sides

M^L, M^R ; bending moment at left and right sides

u_{s_x}, u_{s_y} ; ground displacement in longitudinal and transverse direction

k_x, k_θ ; soil spring

Summarizeing the Eqs.(6.27)~ (6.32), the relation of the physical quantities at left and right hand side of the concrete-fixed section is given as follows.

$$\begin{bmatrix} u \\ v \\ \varphi \\ N \\ M \\ Q \\ 1 \end{bmatrix}^R = \begin{bmatrix} 1 & 0 & 0 & 0 & 0 & 0 & 0 \\ 0 & 1 & l & 0 & 0 & 0 & 0 \\ 0 & 0 & 1 & 0 & 0 & 0 & 0 \\ -k_x & 0 & 0 & 1 & 0 & 0 & k_x \cdot u_{s_x} \\ 0 & 0 & k_\theta & 0 & 1 & 0 & 0 \\ 0 & -k_x & 0 & 0 & 0 & 1 & k_x \cdot u_{s_y} \\ 0 & 0 & 0 & 0 & 0 & 0 & 1 \end{bmatrix} \cdot \begin{bmatrix} u \\ v \\ \varphi \\ N \\ M \\ Q \\ 1 \end{bmatrix}^L \tag{6.33}$$

Evaluation of the soil spring of the concrete-fixed section

Barkan(Ref.2) examined the characteristic of the soil spring for bases and foundations and the following simple formulas have been proposed.

· horizontal movement

$$k_x = 0.5\ k\ A \quad \text{in} \quad \text{kg/cm} \tag{6.34}$$

· rotational movement

$$k_\theta = 1.5\ k\ I_\theta \quad \text{in} \quad \text{kg} \cdot \text{cm/rad} \tag{6.35}$$

where A= the area of foundation in contact with soil (cm^2), I_θ= the

geometrical moment of inertia for rotation (cm^4), and k= the coefficient of subgrade reaction (kg/cm^3). In this analysis the coefficient k is fixed as k=4.41(kg/cm^3), which is the mean value for the soil of the moderate stiffness(Ref.10).

6.3.2 Typical Models for Response Analysis

Based on the survey of the structural characteristic of buried pipes in the actual water supply system, the two representative pipe models are examined as for response behavoir caused by earthquake ground motion. Fig.6.10(a) shows a pipe model for a straight part(model I) and Fig.6.10(b) for a concrete-fixed section(model II). The soil spring for the concrete-fixed section is much larger than that for the pipes, therefore it can be regarded that the axial and the bending force of the pipe at each side are not transfered to the pipe at other side. Under this assumtion the model II is selected as the representative model for the concrete-fixed ection where the pipe route generally change its direction.

Following computational parameter in response analysis are adopted.

(1) input ground motion

The propagating sinusoidal waves are dealt with in the response analysis. A number of works have dealt with a longitudinal waves for the response analusis of buried pipes. However, Kameda and Shinozuka(Ref.14) pointed out that in some cases in which the slippage between pipes and soils occurs, the response values of pipes are larger for the transverse waves than that for the longitudinal waves. Therefore these two typical types of waves are equaly dealt with in this analysis. The wave length L is fixed as L= 120 m and various cases as for an angle of incidence in the range 0°$\sim$ 75° are examined. The maximum ground strain amplitude used in the analysis is ε= 4.19×10^{-3}, the value of which is considerably large as those for surface waves.

(2) soil spring

(a) straight pipes

(b) straight pipes with fixed section

Fig.6.10 Analytical Models.

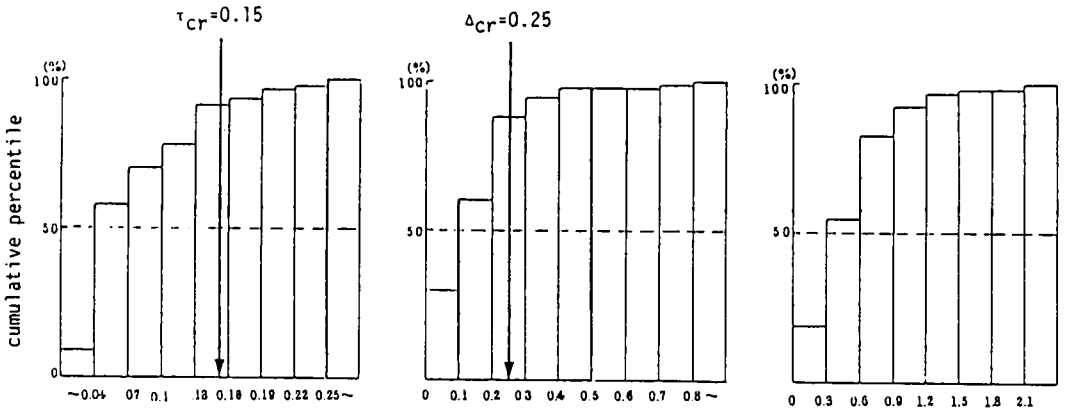

Fig.6.11 Experimental Statistics of Soil Spring Characteristic(Ref.10).

The two kinds of soil springs for the longitudinal (axial) and the transverse directions have been determined as follows.

soil-spring characteristic for longitudinal directions

Fig.6.11 shows the experimental statistics of soil-spring characteristic for (a) critical shear stress τ_{cr} , (b) relative displacement Δ_{cr} at critical shear point, and (c) soil-spring coefficint k_l in longitudinal direction(Ref.10). As the representative values for the following analysis, the standard values for the critical shear stress, which strongly effects the maximum stress of pipes, is fixed as τ_{cr}=0.15kg/cm^2 . The soil spring coefficient k_l in longitudinal direction is fixed as k_l=0.6kg/cm^3 , and accordingly the critical relative displacement Δ_{cr} between pipe and soil is given as Δ_{cr}=0.25 cm.

According to the report on the design code for the equipments of gas-supply systems(Ref.11), the restriction force F (kg) caused by the extruded section of joint pipe is given as,

$$F = 3.49 \times A \times \sqrt{\delta} \quad \text{in kg} \tag{6.36}$$

where A denotes the area of the extruded section in cm^2 and δ denotes the joint displacement in cm. The Eq.(6.36) can be rewritten as

$$\frac{F}{\pi D l} = 3.49 \frac{A}{\pi D l} \sqrt{\delta} \tag{6.37}$$

where D= the diameter of pipe in cm and l= the length of pipe. The left side of the Eq.(6.37) represents the additional value for the critical shear atress for a unit area of pipes. In the following response analysis the effect of the extruded part of pipes on the soil-spring characteristic is considered. The additional value of the critical shear stress Δ_τ caused by the extruded part of pipes is simply represented by two linear functions of δ.

$$\Delta_\tau = \begin{cases} 3.49\dfrac{A}{\pi D l}\dfrac{\delta}{\sqrt{\delta_0}} & ;\delta \leqq \delta_0 \\ 3.49\dfrac{A}{\pi D l}\dfrac{\sqrt{\delta_1}-\sqrt{\delta_0}}{\delta_1-\delta_0}(\delta-\delta_0) & ;\delta > \delta_0 \end{cases} \tag{6.38}$$

where δ_0 = the critical relative displacement for the slippage of pipes, and δ_1 = the relative displacement which controls the stiffness of soil spring after slippage occurs.

soil spring characteristic for transverse direction

According to the experimental result on the soil spring characteristic performed by Miyazima, Miyauchi, and Aono(Ref.20), the soil spring k_{s_y} per unit area for transverse direction can be given from the soil spring k_1 for longitudinal direction.

$$k_{sy} = \pi D k_1 \quad \text{in kg/cm}^2 \tag{6.39}$$

The critical relative displacement $\Delta_{y,cr}$ for the transverse direction has been examined by Takada and Takahashi(Ref.36), and given as

$$\Delta_{y,cr}=1.0 \quad \text{in cm} \tag{6.40}$$

Table 6.2 shows the soil-spring characteristic for the four types of pipe diameters.

6.3.3 Numerical Results and Discussions

The following assumption and numerical technique are introduced in the response analysis.

(1) The response values are calculated for each 1 m point of pipes.

(2) The load increment method is used to characterize the non-linear

Table 6.2 Soil Spring Characteristic for Buried Pipes.

(a) soil-spring characteristic in longitudinal direction

diameter (mm)	ϕ 200	ϕ 400	ϕ 800	ϕ 1650
area of joint (cm^2)	2026	4021	9334	24431
τ_{cr} (kg/cm^2)	0.201	0.194	0.202	0.250
k_2 (kg/cm^3)	0.0120	0.0103	0.0122	0.0235

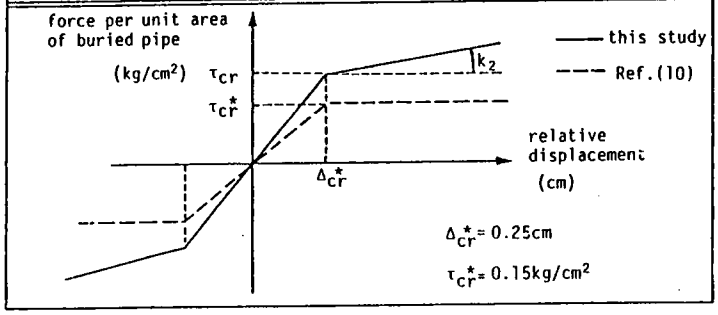

(b) soil-spring characteristic in transverse direction

diameter (mm)	ϕ 200	ϕ 400	ϕ 800	ϕ 1650
k_{sy} (kg/cm^2)	41.47	80.22	157.58	320.63

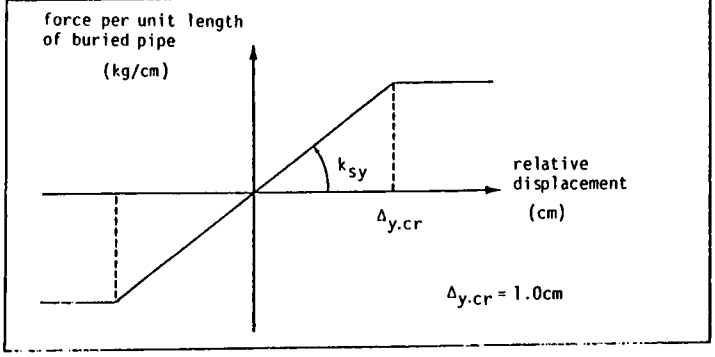

behavior of the soil and joint springs. The maximum value for the increment of displacement amplitude has been fixed as 0.1 cm.

(3) At both the ends of pipe models, the pipe is regarded to move as same as the surrounding soil and not to be restricted for the rotation. Accordingly the hinge is used for the boundary condition of the pipe models.

The analytical results are as follows.

[1] Model I (straight pipes)

Fig.6.12 shows the examples of the distribution of the response values for the pipes of Φ800. The abscissa represents a length in the axial component. It can be observed that the axial stress is relatively larged on the compression side of the ground strain where the joints can not be pushed in easily. In contrast with this the relative joint displacement is large on the tensile side where the axial stress is rather small. This tendency is predominant particularly for the ductile iron pipelines with K and A joints. Fig.6.13 shows these typical pipe joints. In the case of large displacement amplitude (Fig.6.12(b)) the slippage between pipes and surrounding soils occurs. The slippage part is shown by the shadow area. It can be also recognized that the bending stress scarecely occurs in pipes because each joint of pipes release the bending motion.

In the following the discussions are forcussed on the two typical response values: one the maximum joint displacement and another the maximum totale fiber stress of pipes. Figs.6.14 and 6.15 show the maximum joint displacement and the total fiber stress for the longitudinal and transverse waves for Φ200 and Φ400 pipes, respectively. The response values are plotted for 16 steps of the input displacement amplitude from 0.5 to 8 cm. The abcissa in these figures represents the incident angle of seismic waves. It is observed that the joint displacement is proportional to the amplitude of input motion and the maximum value is given for the incident angle of 0° for the longitudinal waves and 45° for the transverse waves. On the other hand the response characteristic of the total fiber stress is not so simple as

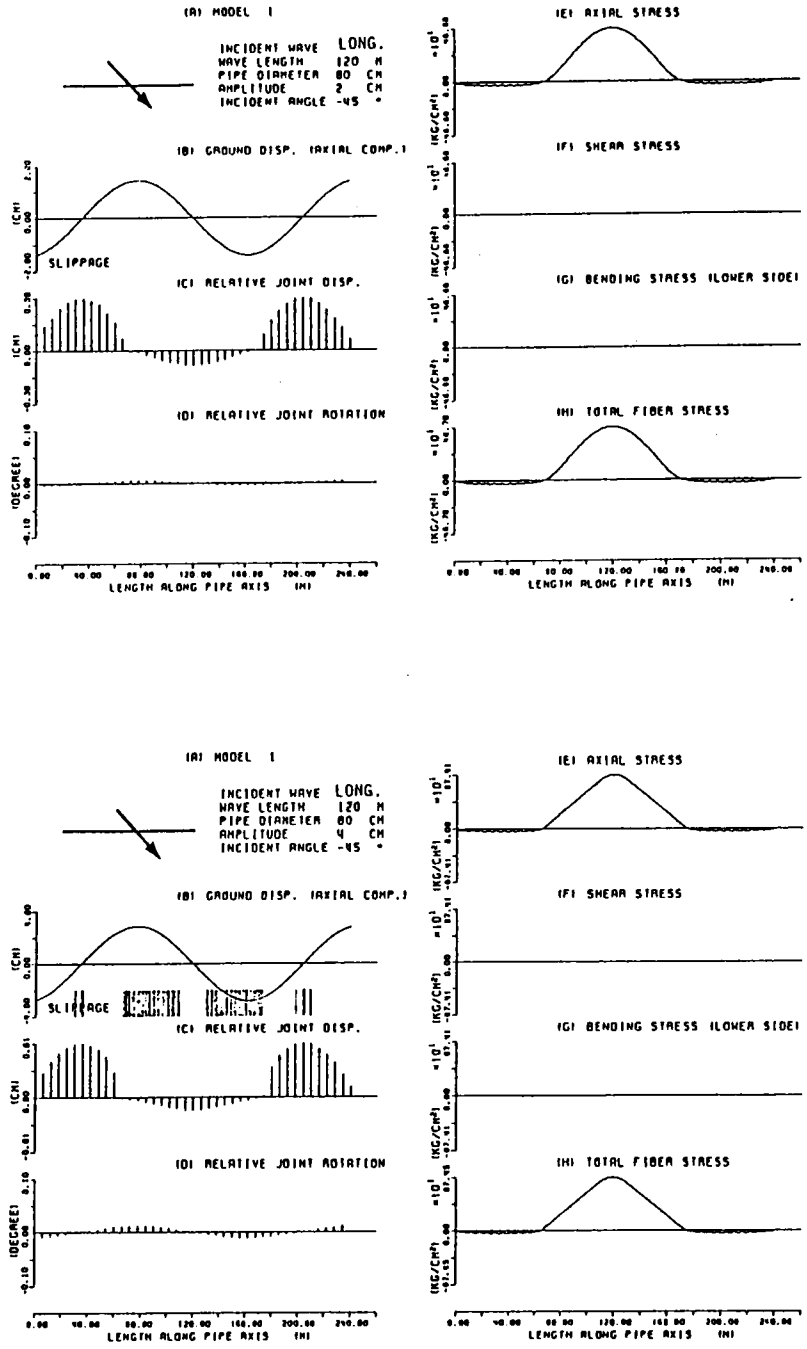

Fig.6.12 Distribution of Response Values(Φ800).

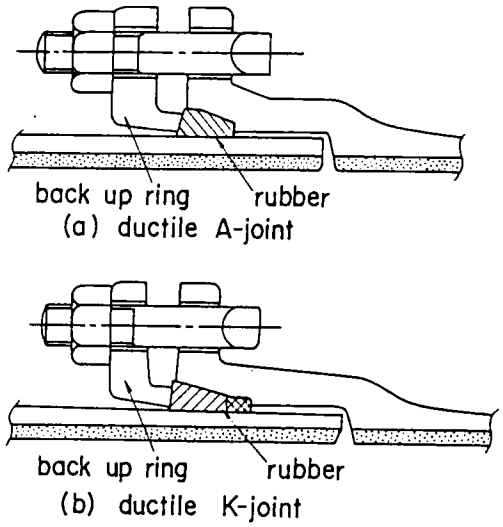

Fig.6.13 Typical Pipe Joints.

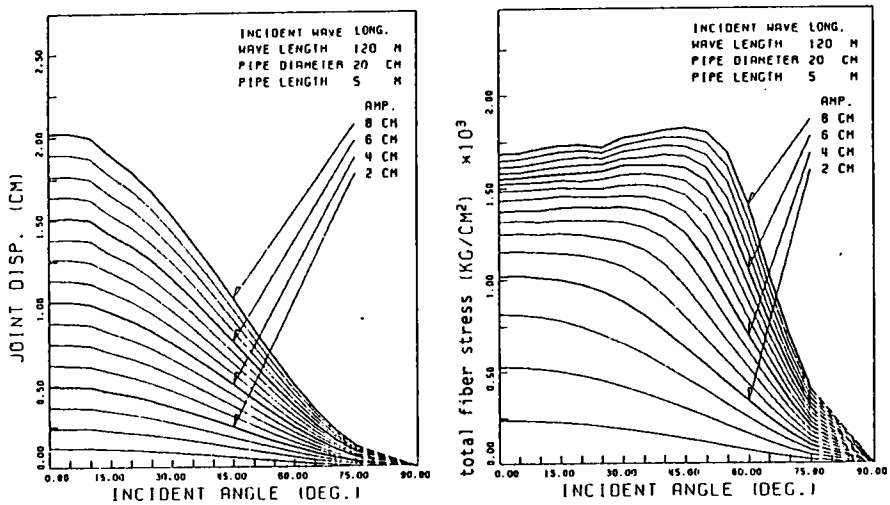

(1) longitudinal wave

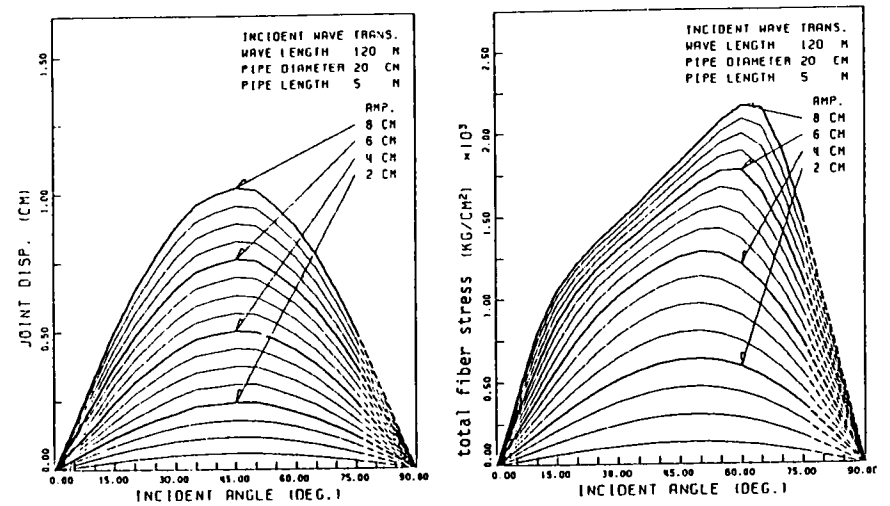

(2) transverse wave

Fig.6.14 Joint Displacement and Total Fiber Stress versus Incident Angle(Φ200).

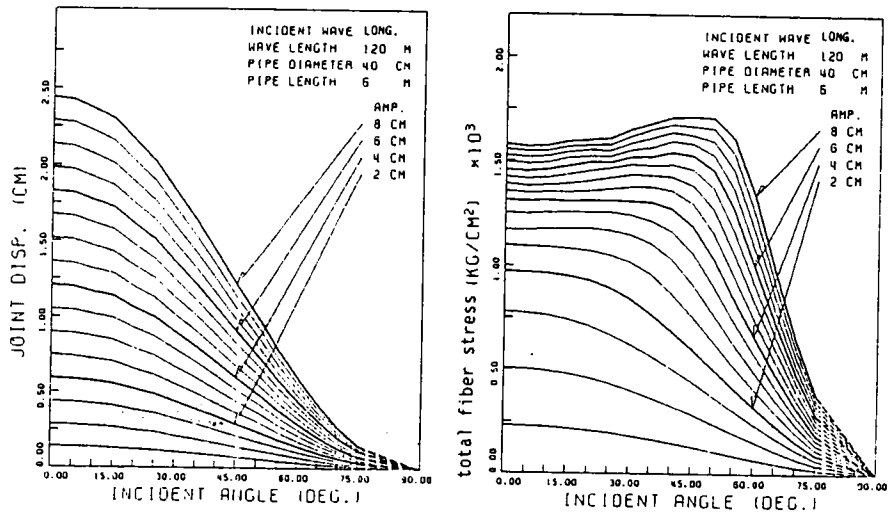

(1) longitudinal wave

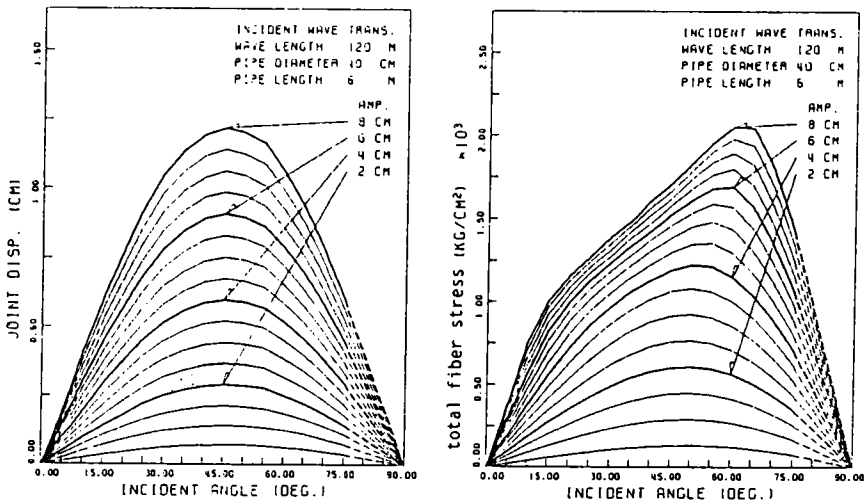

(2) transverse wave

Fig.6.15 Joint Displacement and Total Fiber Stress versus Incident Angle(Φ400).

that of joint displacement since the slippage between pipes and soils effect the distribution of the axial stress.

Let α_p denote the incident angle which gives the maximum total fiber stress for given input displacement amplitude. In the case of smaller displacement amplitude (linear response region), the value of α_p is constant as α_p = 0.0 for longitudinal waves and α_p = 45.0 for transverse waves. For larger displacement amplitudes, α_p increases with increase in the input displacement amplitude. It is also observed that the total fiber stress is proportional to the displacement amplitude a_l until $a_l \fallingdotseq$ 2 cm. However, for the larger displacement amplitude, it does not increase proportionally.

Fig.6.16 shows the relation between the total fiber stress and the ground displacement amplitude for the longitudinal and transverse waves. In the case of the smaller displacement amplitude the maximum total fiber stress for the longitudinal waves is larger than that for the transverse waves. However, the maximum total fiber stress for the transverse wave is larger than that for the longitudinal wave when the ground displacement amplitude is considerably large. These response characteristic of buried pipes have been also pointed out in the theoretical analysis developed by Kameda and Shinozuka(Ref.7).

[2] Model II (straight pipes with concrete-fixed section)

Figs.6.17 and 6.18 show the maximum joint displacement and the total fiber stress for Φ200 and Φ400 pipes, respectively. The maximum joint displacement is proportinal to the input displacement amplitude, however it is larger than that for the model I. The reason for the larger joint displacement for the model II is that the distance between two joints at the concrete-fixed section is longer than the unit length of pipes. The maximum total fiber stress for the model II is also larger than that for the model I, and the value of incident angle α_p is different from that for the model I. The larger response values for the model II are caused by the bending stress which occurs at the pipe fixed to the concrete-fixed section. Fig.6.19 shows the contribution ratio of the axial and bending stress for the total fiber stress. It can be observed that the contribution ratio of the benging stress

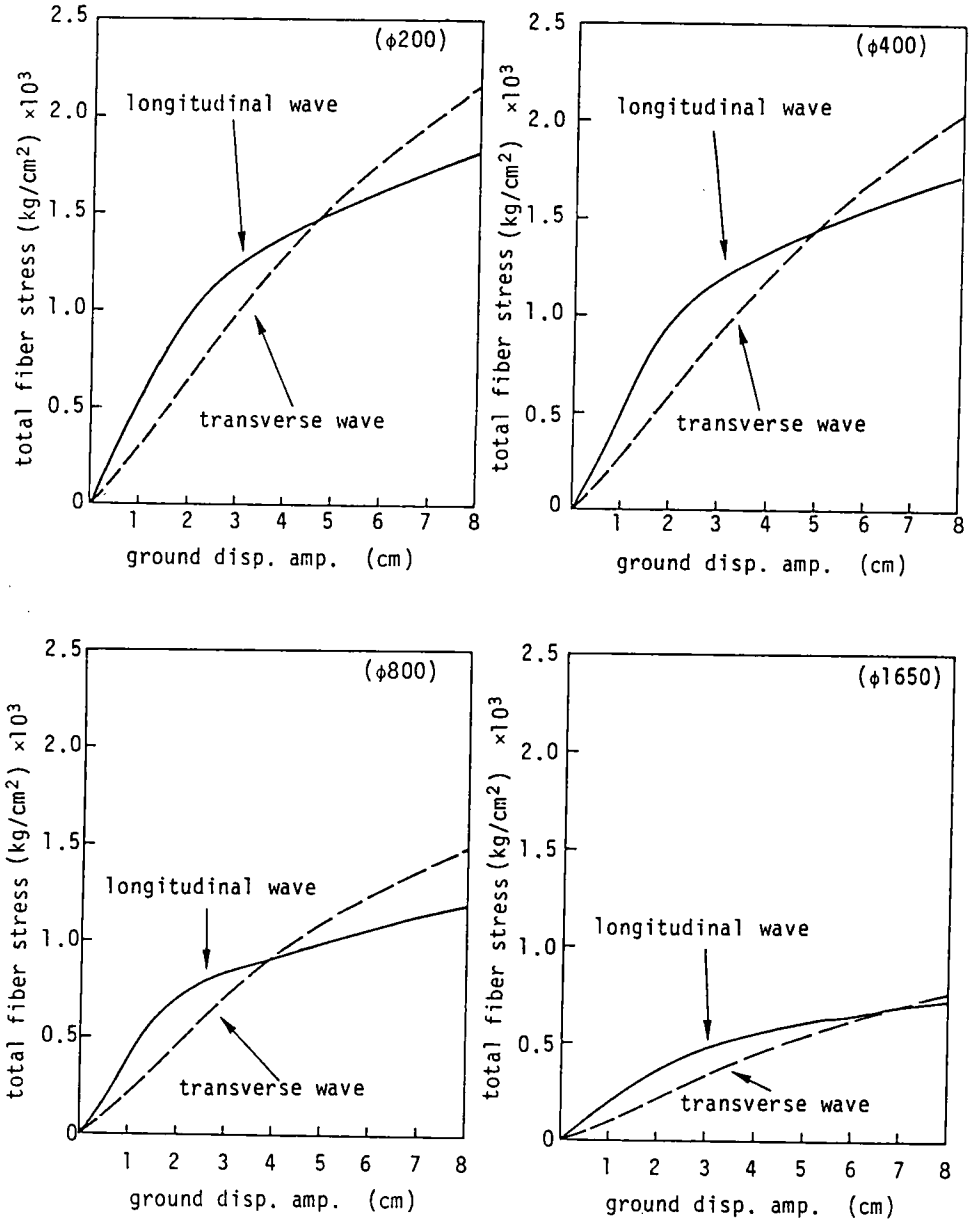

Fig.6.16 Total Fiber Stress versus Displacement Amplitude(straight pipes).

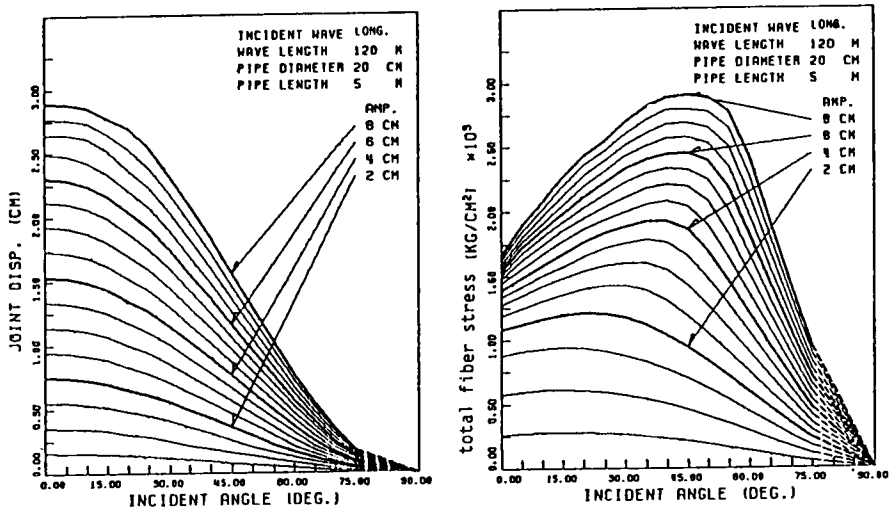

(1) longitudinal wave

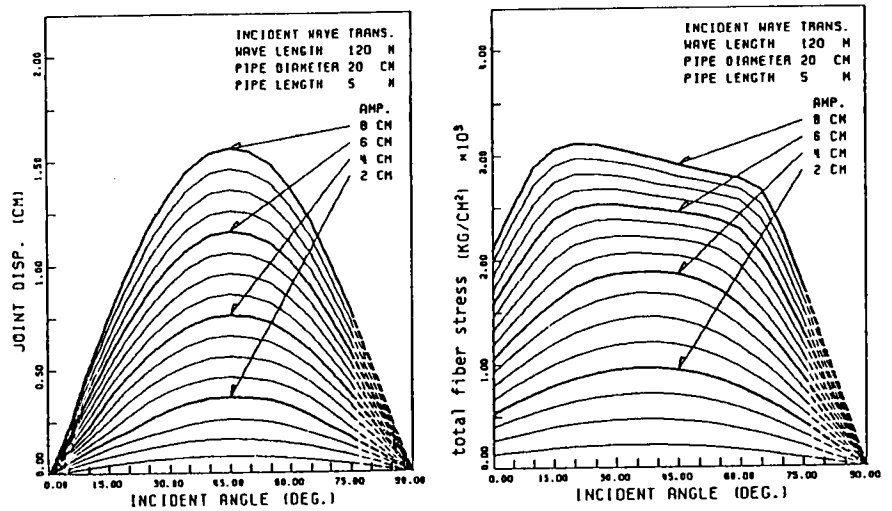

(2) transverse wave

Fig.6.17 Joint Displacement and Total Fiber Stress versus Incident Angle (concrete-fixed section, Φ200).

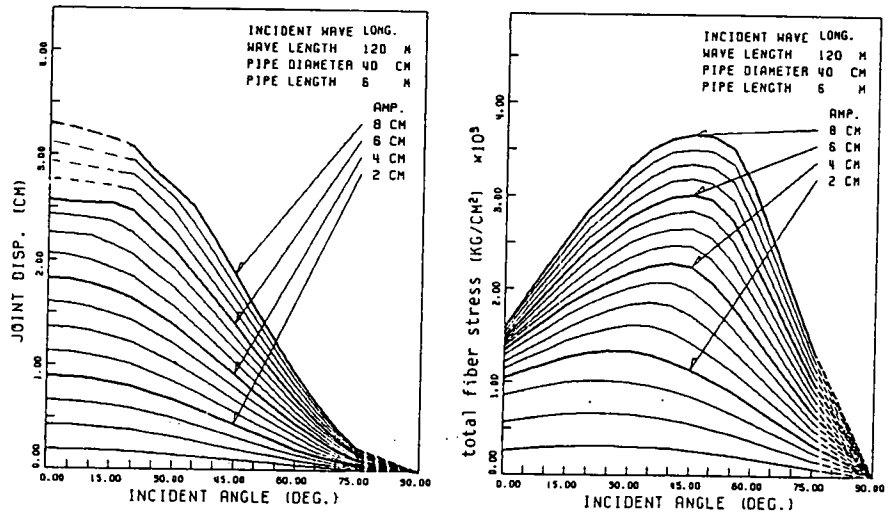

(1) longitudinal wave

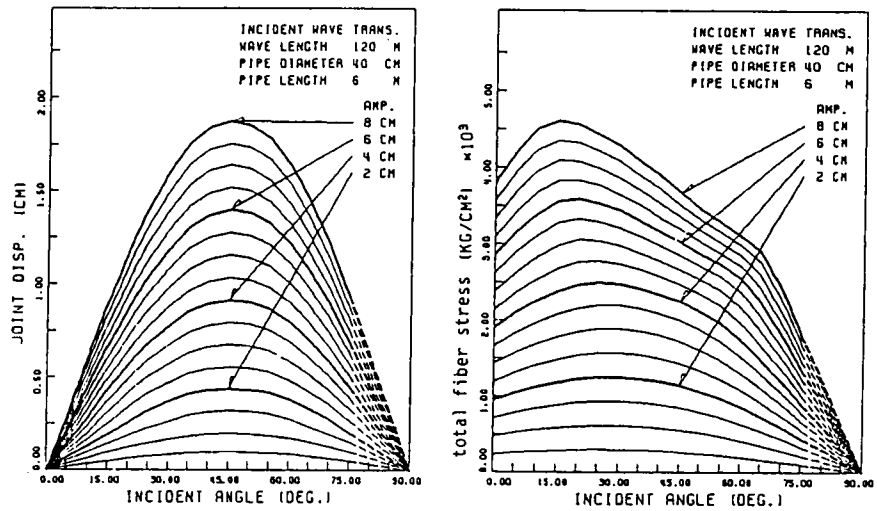

(2) transverse wave

Fig.6.18 Joint Displacement and Total Fiber Stress versus Incident Angle (concrete-fixed section, φ400).

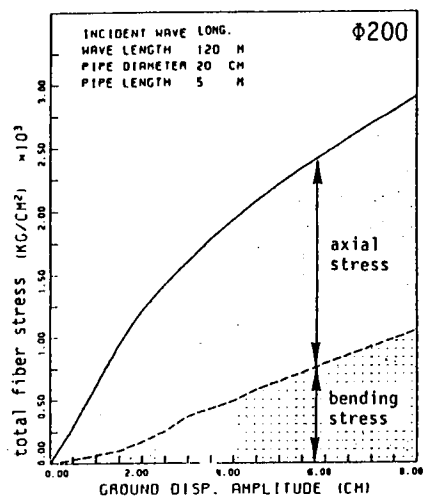

(1) longitudinal wave

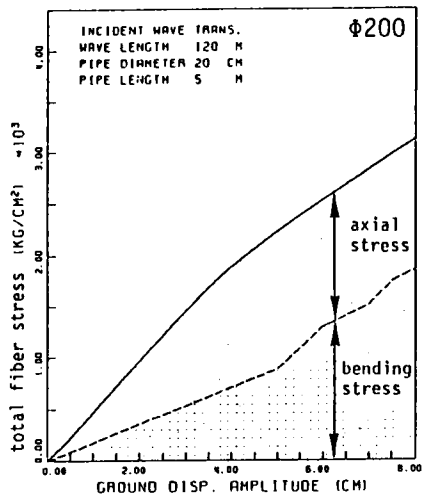

(2) transverse wave

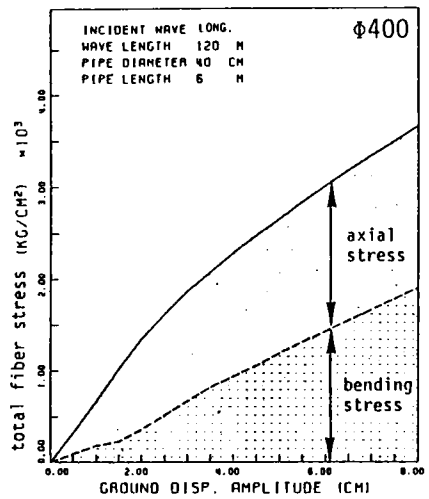

(3) longitudinal wave

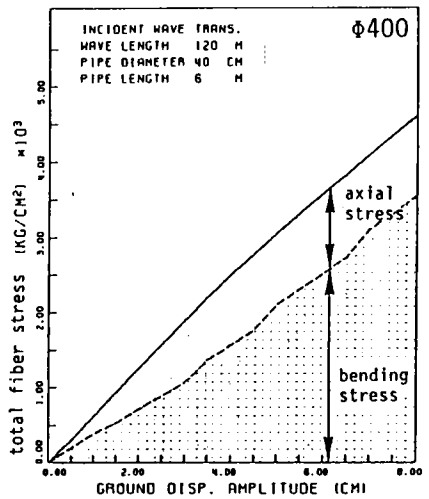

(4) transverse wave

Fig.6.19 Axial and Bending Stress versus Displacement Amplitude at Concrete-Fixed Section.

for the transverse waves is larger than that for the longitudinal waves.

The following items on the response characteristic of the joint connected buried pipes may be summarized from the above discussions.

[1] The joint displacement strongly depends on the unit length of pipes. In the case of the concrete-fixed section the joint displacement is larger than that for the atraight part, since the distance between two joints around the concrete-fixed part is longer than that for the ordinary part.

[2] In the case of smaller displacement amplitudes, the incident angle α_p, at which the total fiber stress gets its maximum value for a given displacement amplitude, is 0° for the longitudinal waves and 45° for the transverse waves. In the case of larger displacement amplitude the incident angle for the maximum total fiber stress changes because of the slippage between pipes and soils. In the comparison between the normal straight pipes (model I) and the concrete-fixed pipes(model II), the total fiber stress is larger for the model II than that for the model I, since the bending stress occurs at around the concrete-fixed section. The incident angle for the maximum total fiber stress is also different between these two models.

Judging from the numerical results it can be concluded that the concrete-fixed section is a weak point in the sence of earthquake resistant of buried pipes.

6.4 Simplified Estimation Model for Earthquake Damage of Joint-Connected Buried Pipes

6.4.1 Dependence of Strain and Joint Displacement of Pipes on Ground Strain

Herein the analytical results discussed in the previous chapter is summarized as for the dependence of strain and joint displacement of pipes on the ground strain amplitude of input motion. Under the same condition of input ground motion, it is clear that the maximum axial stress for the

concrete-fixed section(model II) is nearly the same as that for the model I and the bending stress, which occurs only at the concrete-fixed section, makes the total fiber stress larger for the model II. Therefore, the four response values such as [1] joint displavcement for the ordinary straight pipes, [2] joint displacement at concrete-fixed section, [3] axial strain for the ordinary straight pipes, and [4] bending strain at the concrete-fixed section, are examined to represent them as the function of the maximum ground strain of input motion in the longitudinal and transverse directions of pipe formations. These four response values can be easily estimated without distinction of longitudinal and transverse waves.

Figs.6.20 and 6.21 show the relation between the above four response values and the ground strain amplitude in longitudinal direction for Φ200 and Φ400, respectively. It can be seen that the apparent wave length in the longitudinal direction of pipes does not effect on the joint displacement and the bending stress but on the axial stress. Even for the same ground strain amplitude in the longitudinal direction, the axial stress is larger for longer apparent wave length. This difference of response values against apparent wave length is much clear for the case of larger strain amplitude. These response characteristic can be also recognized for other pipe diameters as Φ800 and Φ1650. According to these results the conversion factor β can be obtained to relate the response values with the ground strain amplitude in the longitudinal direction.

[1] joint displacement Δ_J

The joint displacement Δ_J(cm) can be represented as follows.

$$\Delta_J=\begin{cases}\beta_J \cdot \varepsilon_{sl} \cdot l(\Phi) & \text{for ordinary straight pipe} \\ \beta_{JR} \cdot \varepsilon_{sl} \cdot l(\Phi) & \text{for concrete-fixed section}\end{cases} \tag{6.41}$$

where ε_{sl} = ground strain amplitude in longitudinal direction, $l(\Phi)$= unit length of pipe, and β_J, β_{JR} =conversion factors for ordinary and concrete-fixed section, respectively. Table 6.3 gives the values for β_J and β_{JR} .

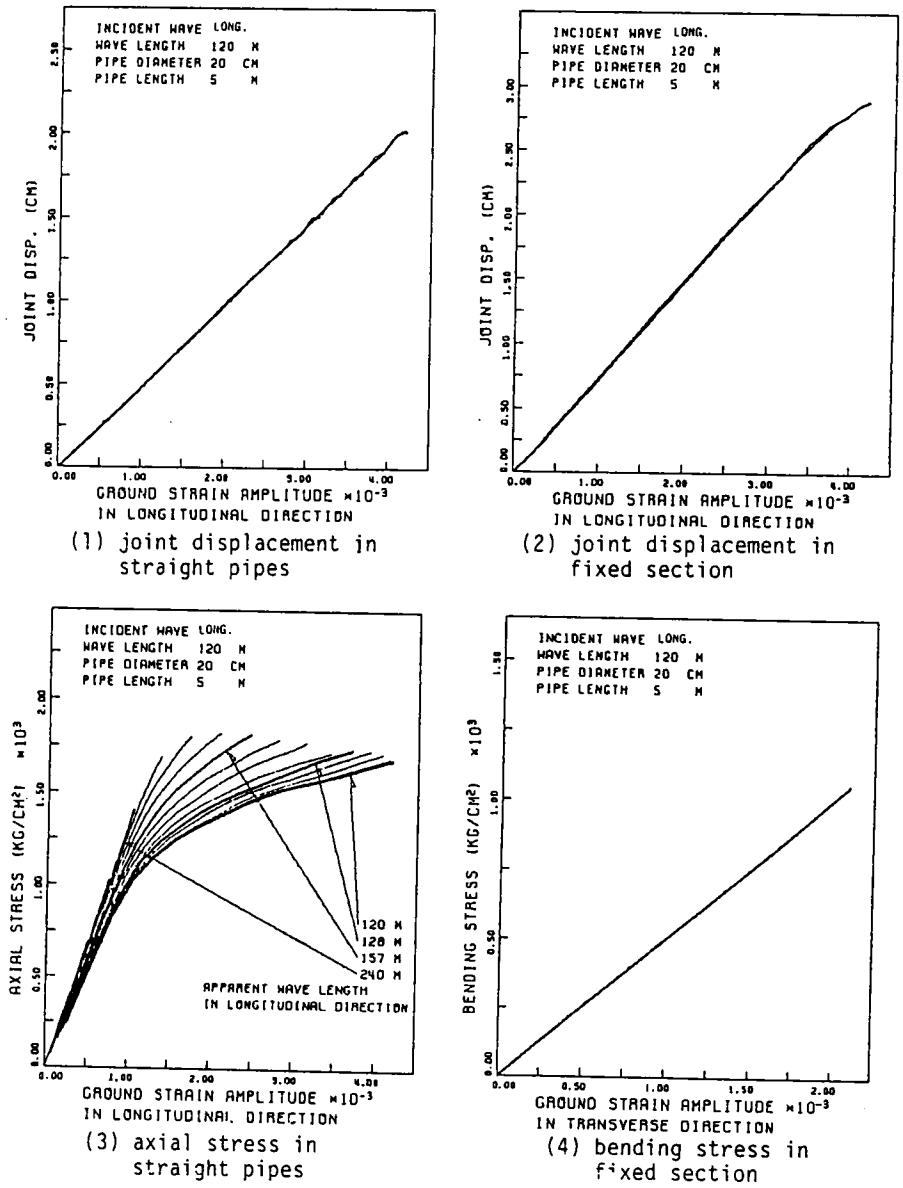

Fig.6.20 Peak Response Values versus Ground Strain Amplitude in Longitudinal and Transverse Directions(Φ200).

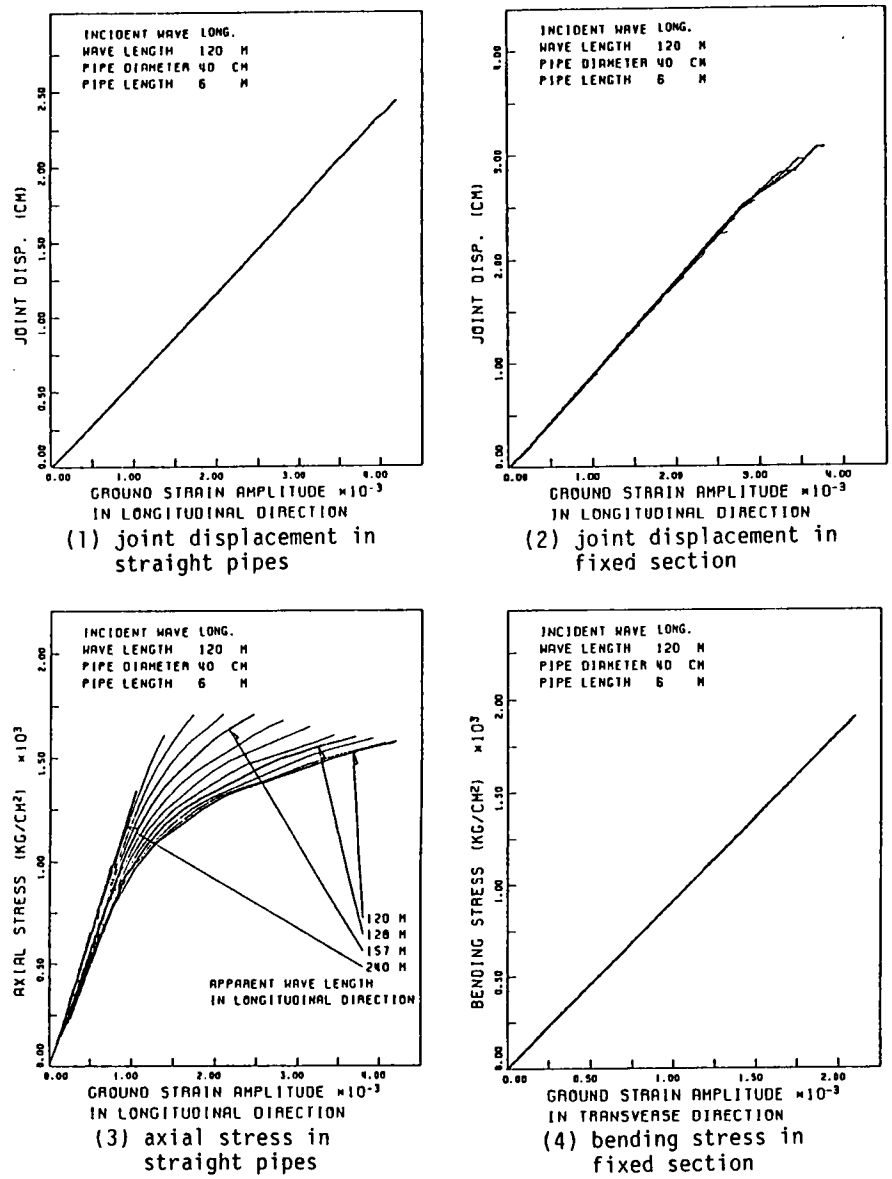

Fig.6.21 Peak Response Values versus Ground Strain Amplitude in Longitudinal and Transverse Directions(Φ400).

Table 6.3 Values for Conversion Factor β_J and β_{JR}.

diameter	β_J	β_{JR}
ϕ200	1.0	1.5
ϕ400		1.5
ϕ800		1.6
ϕ1650		1.7

[2] axial strain ε_N

As shown in Figs.6.20 and 6.21, the axial strain ε_N depends on the apparent wave length in longitudinal direction and, ε_N does not increase proportionary with increase in ground strain amplitude in longitudinal direction. The axial strain ε_N of pipes, therefore, can be approximately represented by three straight lines (for the three regions of ground strain level) as a function of the apparent wave length L_l in the longitudinal direction, the pipe diameter Φ, and ε_{sl} . The axial strain ε_N is given by

$$\varepsilon_N = \beta_N(L_l, \varepsilon_{sl}, \Phi) \cdot \varepsilon_{sl} + c(L_l, \varepsilon_{sl}, \Phi) \tag{6.42}$$

where β_N= conversion factor for the axial strain and $c(L_l, \varepsilon_{sl}, \Phi)$ = constant term for the three lines. Table 6.4 gives the values for $\beta_N(L_l, \varepsilon_{sl}, \Phi)$ and $c(L_l, \varepsilon_{sl}, \Phi)$.

[3] bending strain ε_B

As shown in Figs.6.20 and 6.21, the bending strain ε_B of pipes is proportional to the ground strain amplitude ε_{st} in transverse direction. Therefore, the bending strain ε_B of pipes at the concrete-fixed section is represented in the following form.

$$\varepsilon_B = \beta_B(\Phi) \cdot \varepsilon_{st} \tag{6.43}$$

where $\beta_B(\Phi)$= conversion factor for the bending strain. Table 6.5 gives the values of β_B.

Using the Eqs.(6.41)~ (6.43), the response values of the joint-connected buried pipes are easily estimated for given ground strain amplitude and the wave length. The total fiber stress at the concrete-fixed section may be given as the sum of the axial stress and the bending stress. This is the most conservative value since the incident angle which give the maximum axial strain, does not generally coinside with that for the bending strain.

Table 6.4 Values for Conversion Factor β_N and Constant c.

wave length L_l (m)	ground strain amplitude in longitudinal direction ε_{sl} ($\times 10^{-3}$) 1.0	1.3	1.7	2.0	2.5
120	$\beta_N=0.63$ $c=0.0$	$\beta_N=0.187$ $c=0.443$			$\beta_N=0.087$ $c=0.693$
140	$\beta_N=0.68$ $c=0.0$	$\beta_N=0.260$ $c=0.420$		$\beta_N=0.130$ $c=0.680$	
160	$\beta_N=0.72$ $c=0.0$	$\beta_N=0.400$ $c=0.320$		$\beta_N=0.162$ $c=0.725$	
190	$\beta_N=0.78$ $c=0.0$	$\beta_N=0.733$ $c=0.047$	$\beta_N=0.286$ $c=0.629$		
240	$\beta_N=0.86$ $c=0.0$				

Table 3.2 Conversion Factor β_N and Constant c (ϕ400).

wave length L_l (m)	ground strain amplitude in longitudinal direction ε_{sl} ($\times 10^{-3}$) 1.0	1.3	1.7	2.0	2.5
120	$\beta_N=0.6$ $c=0.0$	$\beta_N=0.173$ $c=0.427$			$\beta_N=0.08$ $c=0.66$
140	$\beta_N=0.65$ $c=0.0$	$\beta_N=0.26$ $c=0.39$		$\beta_N=0.105$ $c=0.7$	
160	$\beta_N=0.68$ $c=0.0$	$\beta_N=0.357$ $c=0.323$		$\beta_N=0.192$ $c=0.603$	
190	$\beta_N=0.75$ $c=0.0$	$\beta_N=0.633$ $c=0.117$	$\beta_N=0.314$ $c=0.531$		
240	$\beta_N=0.78$ $c=0.0$				

Table 3.3 Conversion Factor β_N and Constant c (ϕ800).

wave length L_l (m)	ground strain amplitude in longitudinal direction ε_{sl} ($\times 10^{-3}$) 1.0	1.3	1.7	2.0	2.5
120	$\beta_N=0.41$ $c=0.0$	$\beta_N=0.107$ $c=0.303$			$\beta_N=0.06$ $c=0.42$
140	$\beta_N=0.47$ $c=0.0$	$\beta_N=0.12$ $c=0.38$		$\beta_N=0.08$ $c=0.46$	
160	$\beta_N=0.50$ $c=0.0$	$\beta_N=0.22$ $c=0.279$		$\beta_N=0.107$ $c=0.474$	
190	$\beta_N=0.58$ $c=0.0$	$\beta_N=0.317$ $c=0.263$	$\beta_N=0.185$ $c=0.434$		
240	$\beta_N=0.61$ $c=0.0$				

wave length L_l (m)	ground strain amplitude in longitudinal direction ε_{sl} ($\times 10^{-3}$) 1.0	1.3	1.7	2.0	2.5
120	$\beta_N=0.22$ $c=0.0$	$\beta_N=0.10$ $c=0.12$			$\beta_N=0.043$ $c=0.262$
140	$\beta_N=0.235$ $c=0.0$	$\beta_N=0.135$ $c=0.10$		$\beta_N=0.07$ $c=0.23$	
160	$\beta_N=0.245$ $c=0.0$	$\beta_N=0.164$ $c=0.018$		$\beta_N=0.098$ $c=0.194$	
190	$\beta_N=0.26$ $c=0.0$	$\beta_N=0.25$ $c=0.01$	$\beta_N=0.164$ $c=0.121$		
240	$\beta_N=0.275$ $c=0.0$				

Table 6.5 Values for Conversion Factor β_M.

diameter	β_M
ϕ200	0.4
ϕ400	0.6
ϕ800	1.8
ϕ1650	1.0

6.4.2 A Comment on Mitigation of Bending Stress at Concrete-Fixed Section

As shown in the previous section, the bending stress occurs at both sides of concrete-fixed section and it makes the total fiber stress larger than that for non-fixed section. Therefore it can be concluded that the occurence of bending stress at concrete-fixed sections decreases the system reliability of water supply systems against for earthquakes. Herein the discussion is forcussed on the mitigation of the bending stress at concrete-fixed sections.

It is the typical characteristic of joint connected buried pipes that the joint can absorb the tensile stress of pipes by sliding, and it can also release the bending stress to a certain degree. It is clear in the results of response analysis that bending stress occurs only in the pipes which come out from the concrete-fixed part, and the bending stres is not transfered to the next pipe through the joint. Judging from this characteristic it may be an effective method for decrease in the bending stress of pipes to set up the joint near the concrete-fixed part.

Let l_u denote the uncovered length between the concrete-fixed part and the nearest joint. Fig.6.22 shows the dependence of the axial stress and the bending stress at concrete-fixed section on the ground displacement amplitude for 5 typical uncovered length. The abscissa represents the ground displacement amplitude of input waves, and the incident angle of which is fixed at 45°.

The uncovered length (1) l_u=5.7m is the ordinary type for Φ400, Φ800 pipes. The axial stress does not depend on l_u, however, the bending stress strongly depends on l_u. It is clear that the bending stress can be decreased by setting up the pipe jont near the concrete-fixed part, such as l_u<1.0 m. Even in the case of (3) l_u=1.0m, the bending stress is nearly 1/20 of that for the o l_u=5.7m. To set up the pipe joint near the concrete-fixed part is also effecteive to decrease the joint displacement at concrete-fixed section.

6.5 Conclusions

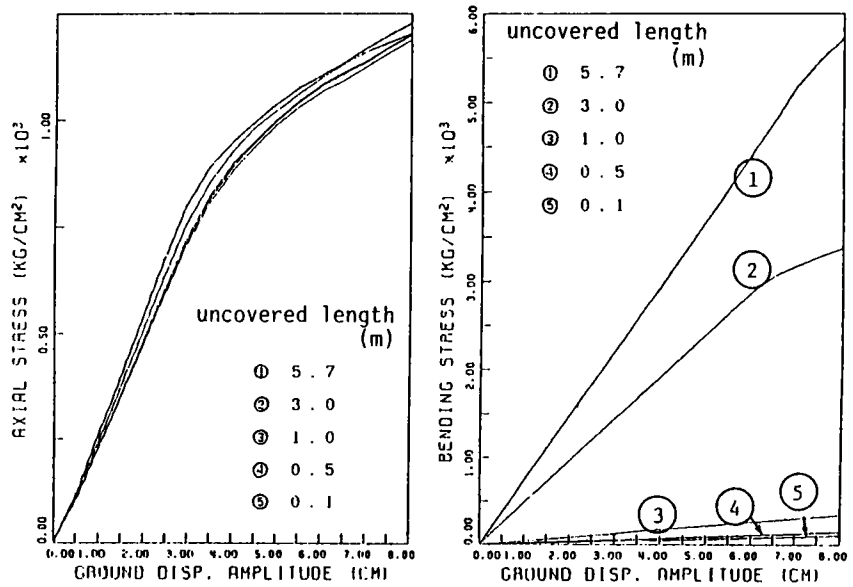

(1) axial stress

(2) bending stress

Fig.6.22 Effect of Uncovered Length of Pipe on Response Values(Φ800).

The major results derived from the discussions in this chapter may be summarized as follows.

[1] The details of the structures and materials along the trunk routes of the Kyoto City Water Supply System have been thoroughly examined to establish analytical models of pipes which are commonly used in the actual lifeline systems. From this examination, the two typical analytical models have been proposed for the joint-connected buried pipes: model I for the straight part without any additional structure, model II for the straight part with concrete-fixed section.

[2] The analytical procedure for the non-linear response analysis of joint-connected buried pipes including the modeling of the concrete-fixed section has been explained. Based on the experimental data for pipes and soils, the physical parameters including the non-linear soil spring and the joint spring have been examined for the response analysis.

[3] The reponse analysis of joint-connected buried pipes have been carried out for the two typical models. It has been demonstrated that the joint displacement and the total fiber stress are generally larger at the concrete-fixed section (model II) than those for the straight part (model I). The reason for the larger value of the joint displacement at the concrete-fixed section is that the distance between the two joints is larger than that for the ordinary pipes. The bending stress, which occurs at the concrete-fixed section, makes the total fiber stress much larger. On this basis the simplified estimation formulas have been proposed for the joint displacement, axial strain of pipes, and the bending strain of pipes at concrete-fixed section, as the functions of ground strain amplitude in longitudinal and transverse directions and the apparent wave length in longitudinal direction.

[4] In the view point of earthquake resistant design of joint-connected buried pipes, the method for the mitigation of the bending stress at the concrete-fixed section has been demonstrated by setting up the pipe joint near the concrete-fixed part. The effectiveness of the method has

been clearly shown as the remarkable decrease in the bending stress in the case of the shorter uncovered pipe length.

References

1) Akiyoshi, T. and Fuchida, K.(1982), "Effect of Slippage on Seismic Response of Buried Pipeline Systems," Proc. of the 6th Japan Earthquake Engineering Symposium, pp.1913-1920.
2) Barkan,D.D.(1948), "Dynamics of Bases and Foundations," (translated from the Russian by L. Drashevska, and translation edited by G.P.Tschebotarioff), McGrawHill Book Co. (New York), p.434.
3) Bouwkamp,J.G. and Stephen,R.M. (1973), "Large Diameter Pipe Under Combined Loading," Proc. ASCE, TE3, pp.521-536.
4) Goto,H.,Sugito,M.,Kameda,H., and Ishikawa,Y.(1982), "Seismic Response Analysis of Joint-Connected Buried Pipelines Including Bent Sections," Memoirs of the Faculty of Engineering, Kyoto University, Vol.XLIV, Part 1, pp.182-221.
5) Hall,W.J. and Newmark,N.M.(1977), "Seismic Design Criteria for Pipelines and Facilities," Current State of Knowledge of Lifeline Earthquake Engineering, ASCE, pp.18-34.
6) Hindy,A. and Novak,M.(1980), "Pipeline Response to Random Ground Motion," Proc. ASCE, EM2, pp.339-360.
7) Hoshiya,M. and Miyazaki,M.(1983), "Strategy and Prediction of Water Pipeline Restoration from Earthquake," Proc. JSCE, No.331, pp.45-54 (in Japanese).
8) Isoyama,R. and Katayama, T.(1981), "Practical Performance Evaluation of Water Supply Networks During Seismic Disaster," Lifeline Earthquake Engineering, The Current State of Knowledge, ASCE, pp.111-126.
9) Iwamoto,T., Sakurai,Y., Wakai,N., Hoojyo,S., and Furusho,K.(1982), "Observation of Dynamic Behavior of Earthquake proof Ductile Pipelines during Earthquakes," Technical Report, Kubota Corporation, Vol.7, No.1, pp.34-53.
10) Japan Gas Association(1982), Earthquake Resistant Design Code for Gas Supply Pipes for Trunk Route.
11) Japan Gas Corporation(1981), Survey on Design Code for Equipments of Gas Supply System, pp.91-93.
12) Kameda,H., Goto,H., and Kasuga,T.(1984), "System Reliability and Serviceability of Water Supply Pipelines under Seismic Environment," Proc. of 8WCEE, Vol.VII, pp.491-498.
13) Kameda,H., Goto,H., Sugito,M., and Asaoka, K.(1981), "Seismic Risk and Performance of Water Lifelines," Probabilistic Methods in Structural Engineering, American Society of Civil Engineers, pp.179-195.

14) Kameda,K. and Shinozuka,M.(1982), "Simplified Formula for Axial Strains of Buried Pipes Induces by Propagating Seismic Waves," Memoirs of the Faculty of Engineering, Kyoto University, Vol.XLIV,Part 2, pp.287-308.

15) Katada,T. and Hakuno,M.(1981), "Experimantal Analysis of Dynamic Behavior of Underground Structures in the Liquefaction Process," Proc. JSCE, No.306, pp.1-10.

16) Kitaura,M. and Miyajima,M.(1982), "Experimantal Study on Reduction of Damage to Pipes Buried Near Structure Due to Soil Liquefaction," Proc. of the 6th Japan Earthquake Engineering Symposium, pp.1937-1944.

17) Kubota,LTD.(1976), "Handbook of Ductile Iron Pipe," (in Japanese).

18) Kuribayashi,E., Iwasaki, T., Kawashima,K., and Miyata,T.(1977), "Experimental Study on Dynamic Relative Displacement and Resistant Strength between Buried Pipes and Soil," Transactions of Public Works Research Institute, Ministry of Construction, No.1266, (in Japanese).

19) Kyoto City(General Affairs Bureau) (1979), "Boring Data in Kyoto City"

20) Miyajima,N. and Miyauchi,J.(1975), "Stresses in Buried Pipes during Earthquake Based on Static Friction," Proc. of Symposium on Buried Pipelines, Japan Society of Soil Mechanics and Foundation Engineering, pp.57-60, (in Japanese).

21) Miyamoto,H., Hojyo,S., and Kosho,K.(1976), "Bibration Tests of Buried Pipes for Estimation of Its Behavior during Earthquakes," Kubota Technical Report, Vol.1, No. 2, pp. 126-153, (in Japanese).

22) Moghtaderizadeh,M. and Kiureghian,A.d.(1982), "Reliability Upgrading of Lifeline Networks for Post-Earthquake Serviceability," Proc. of the 5th European Conference on Earthquake Engineering, Athens, pp.130-139.

23) Muleski,G.E., Ariman, T., and Aumen., C.P.(1979), "A Shell Model of a Buried Pipe in a Seismic Environmet," Journal of Pressure Vessel Technoloy, Vol. 101, pp.44-50.

24) Naruoka,M.(1970), "Transfer Matrix Method," Baifu-kan (in Japanese).

25) Noda,S., Yamada,Y., and Iemura,H.(1981), "Restoration of Serviceability of a Pipeline System," Lifeline Earthquake Engineering, The Current State of Knowledge, ASCE, pp.225-240.

26) Ohishi,H. and Sekiguchi,K.(1984), "Earthquake Observation of an Underground Pipeline and Seismic Response Analysis," Roc. of 8WCEE, Vol.V, pp.295-301.

27) O'Rourke,M. and Wang,L.R.(1981), "Seismic Vulnerability, Behavior and

Design of Underground Piping Systems II," Technical Report (SVBDUPS Project) No.12. Department of Civil Engineering, Rensselaer Polytechnic Institute.

28) Panoussis,G.(1974), "Reliability of Lifeline Networks," SDDA Report No.15, Department of Civil Engineering, MIT.

29) Parmelee,R. and Ludtke,C.(1975), "Seismic Soil-Structure Interaction of Buried Pipelines," Proc. of the U.S. National Conference on Earthquake Engineering, Ann Arbor, pp.406-417.

30) Saionji,S., Taguchi,M., Tsuzuki,K., and Tabata,H.(1978), "Stress at Bent Section of Buried Pipes during Earthquakes." Proc. of the 5th Japan Earthquake Eagineering, pp.929-936, (in Japanese).

31) Sakurai,A., and Takahashi,T.(1969), "Dynamic Stresses of Underground Pipelines during Earthquakes" Proc. of the 4th World Conference on Earthquake Engineering, Santiago, Vol.II, pp.81-95.

32) Sato,T.(1984), "Seismic Reliability Analysis of Lifeline Networks Taking Into Account Fault Extent and Local Ground Conditions," Journal of Natural Disaster Science, Vol.6, No.2, pp.51-72.

33) Shinozuka, M., and Koike,T.(1979), "Estimation of Structural Strains in Underground Lifeline Pipes." Lifeline Earthquake Engineering-Buried Pipelines, Seismic Risk and Instrumentation, ASME, pp.31-48.

34) Shinozuka,M., Takada,S., and Kawakami,H.(1977), "Risk Analysis of Underground Lifeline Network Systems," Technical Report No.CU-3, Columbia University, Department of Civil Engineering.

35) Tamura,C. and Kawakami,H.(1981), "Seismic Risk Analysis of Underground Lifeline Systems by use of Monte Carlo Method," Proc. of JACE, No.311, pp.37-48.

36) Takada,S., and Takahashi,S.(1979), "On the Estimation for Relative Displacement at Joint of Buried Pipes Convension JSCE, pp.352-353, (in Japanese).

37) Takada,S. and Yamabe,Y.(1982), "An Experiment on a Seismic Behavior of Buried Pipelines Subjected to Large Ground Defoemations Using the Sinking-Soil-Box," Proc. of JSCE, No.323, pp.55-65.

38) Takada,S., and Nagao,S.(1976), "Dynamic Frictional Forces and Efficiency of Joint Parts for Aseismic Strength of Buried Pipelines," Proc. of the U.S.-Japan Seminar on Earthquake Engineering with Emphasis on Lifeline Systems, Tokyo, pp.211-222.

39) Taleb-Agha,G.(1975), "Seismic Risk Analysis of Networks, SDDA Report, No.22, Department of Civil Engineering, MIT.

40) Toki,K., and Sato,T.(1980), "Estimation of Damage of Water Distribution Systems by Earthqyakes," Recent Advances in Lifeline Earthquake Engineering in Japan, pp.89-96.

41) Ukai,K. and Yamaguchi,H.(1978), "Theorectical Research for Behavior of Buried Pipes during Earthquakes," Proc. of the 5th Japan Earthquake Engineering, pp.433-436, (in Japanese).

42) Wang,L.R.-L(1980), "Seismic Analysis and Design of Buried Pipelines," Proc. of International Conference on Engineering for Protection from Natural Disasters, Bangkok, pp.71-83.

7. CONCLUDING REMARKS

The main concern of this thesis were as follows

[1] To develop the earthquake ground motion prediction model on rock surface by using the strong motion records.

[2] To propose sinple conversion technique between earthquake motions on rock surface and soil surface for use of earthquake microzonation.

[3] To analyse the nonlinear response behavior of joint connected buried pipelines by using the two typical models which have been used in ordinary water supply systems.

Besides briefly summarizing the important conclusions obtained in each chapter, the general synopsis of the work presented in the preceding chapter and recommendation for future work are given in the present chapter.

In Chapter 1, the general scope of this thesis and, the remarks and the history of earthquake motion prediction and response behavior of buried pipelines were noted.

In Chapter 2, the selection and modification of rock surface earthquake motion were performed for the development of statisical prediction models. The significance of the numerical database for earthquake engineerig was noted and the outline of the SERM-II Database was introduced. On this basis the modified acceleration dataset of rock surface motion were created. They classified into these types : (1) rock surface ground motion estimated from the accelerograms recorded on alluvial and diluvial sites, (2) rock surface ground motion modified from bedrock ground motion, and (3) ground motion recorded on rock surface. As mentioned in Chpter 2, the rock surface strong motion records are of special importance in the engineering point of view, however the available records are not enough at present stage. The accumlation of these data and their arrangement for the database system are important in the future study.

In Chapter 3 a simple method was proposed for separation of body and surface waves in strong motion accelerograms. In this method the evolutionary power spectrum was used to confirm the dispersion characteristic of surface waves contained in strong motion records. The significance of evaluation of surface waves in strong motion records was demonstrated in caluculation of ground strain caused by surface wave propagations. Then the statistical characterisic of earthquake surface motion contained in strong motion records were examined using 367 components of corrected acclerograms. For the verification of the separation technique proposed in Chapter 2, the surface wave-containing records obtained from the array observation system can be used, and the prediction model for earthquake surface waves, which are mainly caused by local site conditions, should be propsed in the future study.

In Chapter 4 the statistical prediction models for strong earthquake motion on rock surface were proposed on the basis of the modified rock surface motion dataset prepared in Chapter 2. The two nonstatonary earthquake motion prediction models were developed : one, the model for given earthquake magunitude and epicentral distance(EMP-IB) and, the other, the model for given fault geometry including fault size, the seismic moment, rupture pattern and rupture velocity. On the basis of simulated motion by the EMP-IB model, the estimation formulas for peak acceleration, peak velocity, acceleration response spectra, and ground motion duration were proposed. The prediction models developed in Chapter 4 deal with ground motion in the frequency range between 0.15 and 10.0 Hz. As for the extension of the models for lower frequency range the theoretical caluculation procedure can be incorporated, since it is generally recognized that the simulated motion, obtained theoretically by use of fault parameters, represent the recorded motion satisfactory for the frequency range of $f<0.1$ Hz. The extension of the model for higher frequency region is also important for earthquake registant design of secondary-equiped structures such as those in nuclear power plants. These extension work should be performed in the future study.

In Chapter 5 a conversion technique between eartquake motions on rock surface and soil surface was proposed. The simulated rock surface motion for various combinations of magunitude and distance were generated by EMP-IB model, and the corresponding soil surface motion for these rock surface

motion were caluculated for typical strong motion observation stations by using the multi-layer reflection theory with equi-linearized method. On this basis the simple conversion factor β was defined for peak acceleration, peak velocity, acceleration response spectra, and the intencity parameter of evolusionary power spectra. The conversion factor β was modeled as the functions of the soil parameters S_n, d_p and the intensity of earthquake motion so that the nonlinear amplification/deamplification effect of soil layers can be incorporated into the conversion factor.

Because of the lack of the data for simultaneous strong motion both on soil surface and bedrock or corersponding rock surface, the simulated earthquake motion were used in Chapter 4. In the engineering point of view, however, the verification of the model is of special important. The development of the database for these strong motion records is necessary for this objectives and should be performed in future study. The author have started the work for this.

In Chapter 6 the earthquake response analysis of joint-connected buried pipelines were carried out and, the estimation formulas for axial and bending strain of pipes and joint displacement were proposed. After the detailed survey on structural characteristic of buried pipelines in the actual water supply system, the two representative models were selected for the response analysis : model I for straight part of pipelines and model II for the straight part with concrete-fixed section. In the response analysis the nonlinear soil spring characteristic, which is caused by the slippage between pipes and soils, was incorporated. On the basis of the results of response analysis the simplified estimation formulas were proposed for joint displacement, axial strain of pipes, and bending strain of pipes at concrete-fixed section, as the function of input ground strain amplitude in longitudinal and transverse directions and the apparent wave length in longitudinal direction.

The propagating seismic waves were dealt with as the input ground motion in Chapter 6, however, it is known in the past earthquakes that the buried pipes, specially pipes of relatively small diameters, were damaged by the local parmanent dislocation and liquefaction of soils rather than propagating

seismic waves. Further studies on these phenomenon should be performed in the future.

Appendix A General Characteristic of Soil Surface Strong Motion, and Definition of Soil Parameters S_n and d_p for Application of Earthquake Microzonations

General Remarks

In Japan, most of strong motion accelerograms have been recorded on alluvial and diluvial sites. In these soil surface motion the strong effect of local soil conditions and nonlinear response characteristic over bedrocks are generally included. In Chapter 2, the rock surface strong motion dataset(SMD-R) has been arranged for development of earthquake motion prediction model on rock surface level. Most of acceleration time histories in the SMD-R dataset have been obtained from the modification of soil surface records including elimination of surface wave motion. The objective of the development of the earthquake motion prediction model on rock surface level is as follows.

(1) The frequency characteristic and nonlinear amplification/deamplification effect of surface layers can be incorporated into the earthquake motion prediction on soil surface: the soil surface motion are easily obtained from the response analysis of surface layers for given bedrock motion. The input bedrock motion are given from rock surface motion by multiplying by 1/2.

(2) Critical engineering structures including nuclear power plants are generally constructed on stiff ground such as rock surface as dealt with here. For the earthquake resistant design for these significant structures the evaluation of design earthquake motion time history is of special importance. The prediction model on rock surface level is applicable for this purpose.

Since the prediction model developed in Chapter 4 is based on the modified rock surface motion, it is necessary to verify that the simulated soil surface earthquake motion obtained from the EMP-IB,IIB model are consistant with the recorded soil surface motion. For this objective the general characteristic of soil surface earthquake motion have been evaluated.

In this procedure the soil parameters S_n and d_p used in Chapter 5 have been proposed. In the following the attenuation characteristic of peak ground motion on soil surface is examined using 346 components of Japanese strong motion records. The two simple soil parameters S_n and d_p are defined, which are incorporated into the conversion factor of ground motion between rock surface and soil surface in Chapter 5.

Dependence of Attenuation Characteristics on M-Δ Regions

The attenuation characteristic of peak ground acceleration in M-Δ regions are examined using 346 components of accelerograms recorded in Japan. They include the data for alluvial and diluvial sites as well ae rock and very soft grounds. Fig.A-1 shows the scattergram for magnitude and distance for major Japanese recods, as well as the frequency distribution for peak acceleration which is the largest value of two horizontal peak accelerations recorded by the same accelerograph. These data were divided into two groups according to magnitude, distance, and the expected value of peak acceleration, to investigate the attenuation characteristic of peak acceleration in each region. The following estimation formula was used for this purpose.

$$\overline{A} = b_0\ 10^{b_1 M}/(\Delta+c)^{b_2} \qquad (A\text{-}1)$$

where $\overline{A}$ is the expected value of peak acceleration (cm/sec^2), c is a constant term (km), and b_0, b_1, b_2 are regression coefficients. The constant term c is considered so that the estimation formula can be applicable for the case Δ=0, and is fixed as c=30 in this analysis according to the region for distance and focal depth of the data. For the evaluation of the variation of the data, uncertainty U of peak acceleration is used and is given by,

$$U = A\ /\ \overline{A} \qquad (A\text{-}2)$$

where A is the recorded peak acceleration and $\overline{A}$ is the expected peak acceleration for given magnitude and distance. The sample peak acceleration in recorded accelerograms, A, is then represented by,

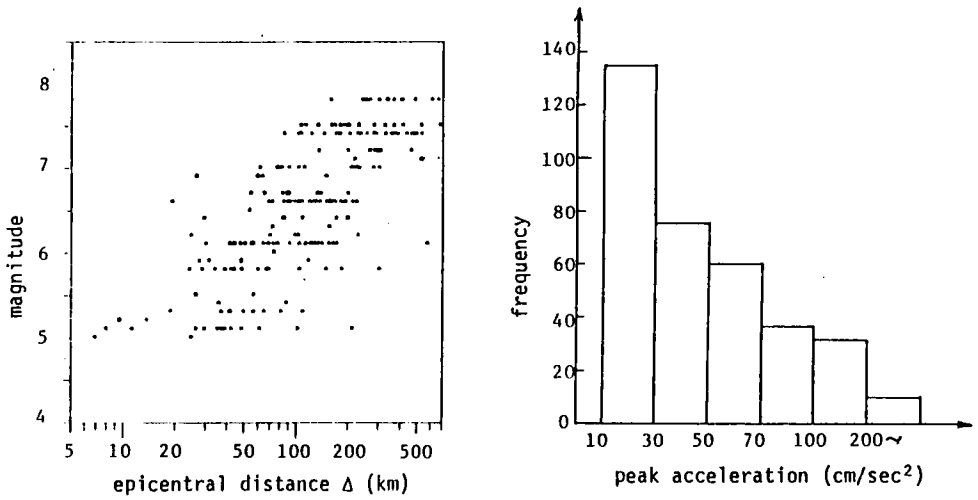

Fig.A-1 Scattergram for Magnitude and Epicentral Distance, and Histogram for Peak Acceleration.

$$A = U\,\overline{A} = U\,\{b_0\ 10^{b_1 M}/(\Delta+c)^{b_2}\} \qquad (A\text{-}3)$$

The acceleration data are devided into two groups using the following specific values for magnitude and distance so that the number of data falling into each group are equal.

Region M_1 · · · · · $M \geqq 6.6$
Region M_2 · · · · · $M < 6.6$
Region D_1 · · · · · $\Delta \leqq 119$ km
Region D_2 · · · · · $\Delta > 119$ km
Region Y_1 · · · · · M-Δ region for $\overline{A}^* \geqq 39$ (cm/sec^2)
Region Y_2 · · · · · M-Δ region for $\overline{A}^* < 39$ (cm/sec^2)

where $\overline{A}^*$ is the expected value of acceleration given from the estimation formula obtained using all of the data (region T). Table A-1 shows the estimation formulas for each of the M-Δ regions, and Fig.A-2 shows the scattergrams for magnitude and distance for each M-Δ region. The relations between $\overline{A}$ (expected peak acceleration), M, and Δ for each M-Δ region are shown in Figs.A-3, A-4, and A-5.

The following conclusions can be derived from the above results.

[1] Comparing the estimation formuala for region M_1 with that for region M_2 ,the coefficient b_1 for the magnitude and the coefficient of variation δ_{M_1} are larger for region M_1 than that for region M_2. This is partially due to the fact that the magnitude M determined from relatively long-period displacement amplitude does not represent the size of an earthquake precisely, especially in the case of large earthquakes(Ref.15). Fig.A-6 relates the fault area S and the seismic moment M_0 to surface wave magnitude M_s (Ref.3). In this figure, S and M_0 increase with M_s remarkably in regions of larger values for M_s. It can be said that physical quantities such as the fault area S and the seismic moment M_0 increase exponentially with the surface wave magnitude M_s and that the amounts of variation increases with increase in M_s as well. Even the magnitude M in Fig.A-1 is not exactly the same as the

Table A-1 Estimation Formulas for Peak Acceleration Depending on M-Δ Regions.

region	estimation formula	coefficient of variation	number of data
T (total)	$\bar{A}= 78.0\times10^{0.316M}/(\Delta+30)^{1.087}$ --(A-4)	0.696	346
$M_1(M\geq6.6)$	$\bar{A}= 10.0\times10^{0.439M}/(\Delta+30)^{1.083}$ --(A-5)	0.758	173
$M_2(M<6.6)$	$\bar{A}=375.0\times10^{0.217M}/(\Delta+30)^{1.138}$ --(A-6)	0.603	173
$D_1(\Delta\leq119$ km)	$\bar{A}=175.4\times10^{0.283M}/(\Delta+30)^{1.166}$ --(A-7)	0.713	173
$D_2(\Delta>119$ km)	$\bar{A}= 41.5\times10^{0.360M}/(\Delta+30)^{1.098}$ --(A-8)	0.671	173
Y_1 { $M-\Delta$ region where $\bar{A}^*\geq39$ gals }	$\bar{A}= 61.0\times10^{0.275M}/(\Delta+30)^{0.891}$ --(A-9)	0.773	173
Y_2 { $M-\Delta$ region where $\bar{A}^*<39$ gals }	$\bar{A}= 67.9\times10^{0.216M}/(\Delta+30)^{0.789}$ --(A-10)	0.601	173

A* ; expected value of peak acceleration given by the estimation formula based on the all data

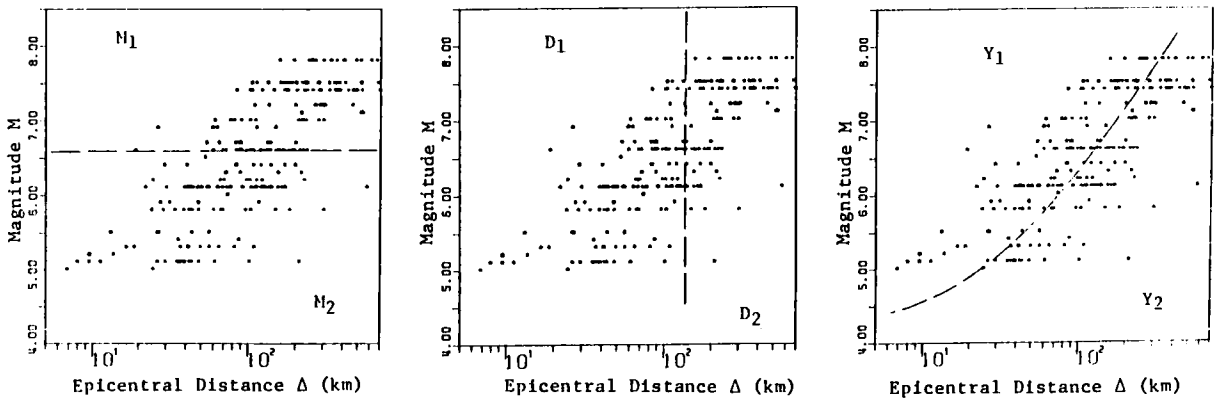

Fig.A-2 Data Separation for Statistical Regression Analysis.

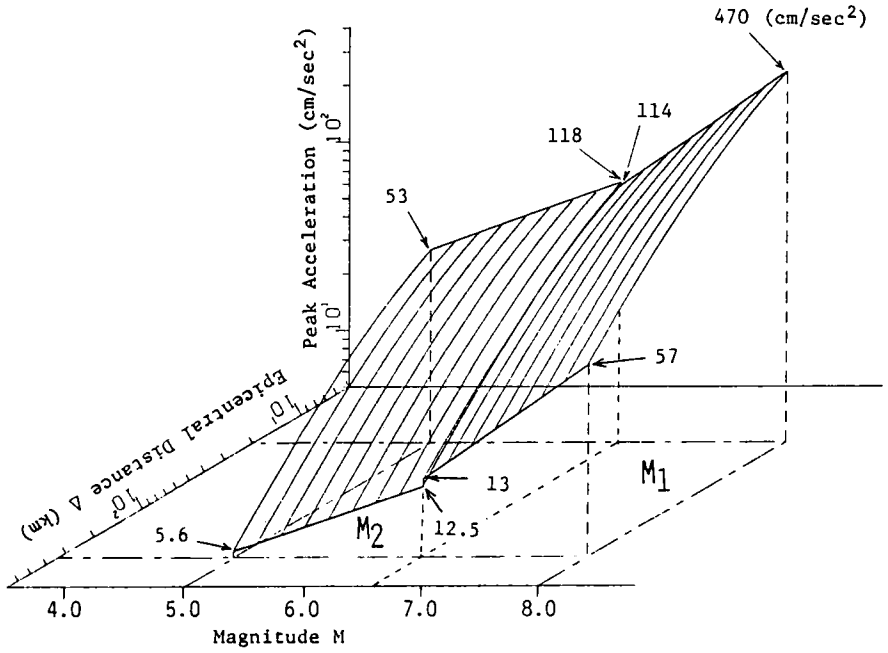

Fig.A-3 Attenuation Characteristic of Peak Acceleration in Regions M_1 and M_2.

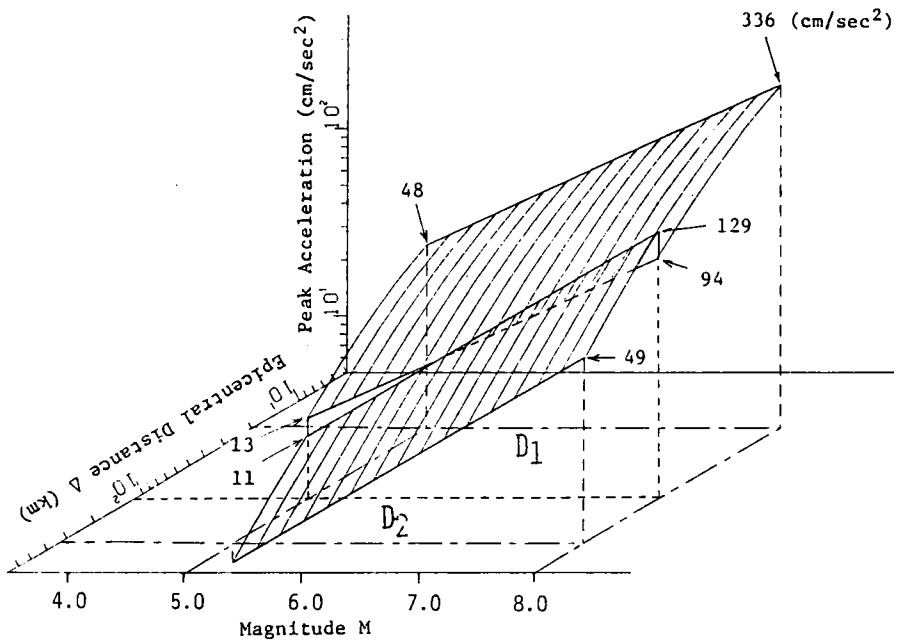

Fig.A-4 Attenuation Characteristic of Peak Acceleration in Regions D_1 and D_2.

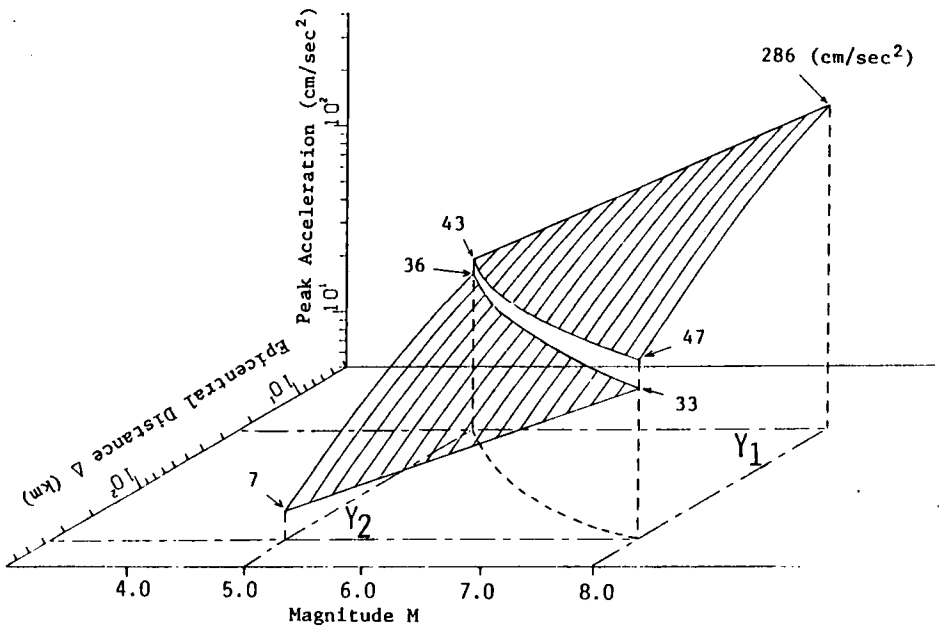

Fig.A-5 Attenuation Characteristic of Peak Acceleration in Regions Y_1 and Y_2.

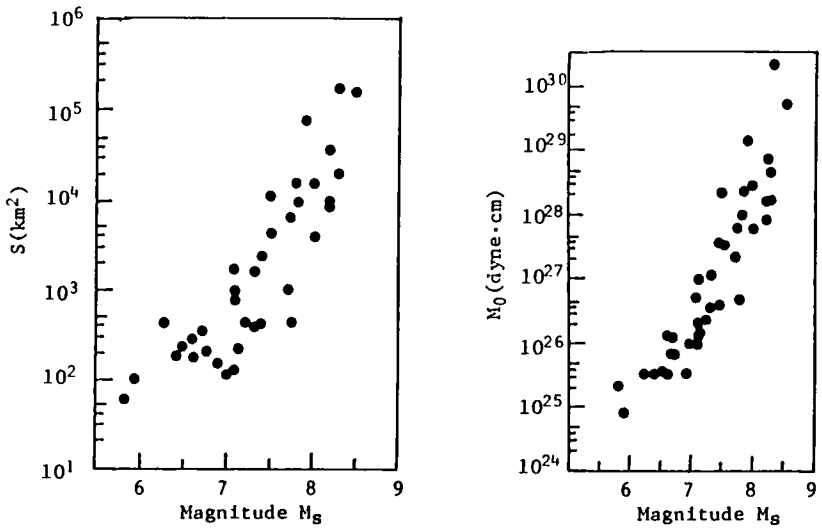

Fig.A-6 Relation between Surface Magnitude M_S, Fault Area S, and Seismic Moment M_0(Ref.3).

surface wave magnitude M_s in Fig.A-6, M is determined on the basis of M_s (Ref.15), therefore the reason for the relatively large values of b_1 and δ_{M_1} for region M_1 can be easily understood. The dependence of estimation formulas on magnitude levels also has been pointed out by Boore(Ref.1) using strong motion data recorded in the U.S.A., and those results agree with the above discussions qualitatively.

[2] As for the attenuation characteristic of regions D_1 and D_2 the coefficient b_2 does not differ very much in these two regions, and it can be said that the attenuation of peak acceleration versus the value of $\log(\Delta+c)$ is relatively constant. On the other hand, the coefficient b_1 is larger for region D_2 than that for D_1. Region D_2 includes many data for larger magnitude, and therefore, the value of coefficient b_1 tends to be larger as mentioned above.

[3] The data in region Y_1 have large peak accelerations, such as larger than some 40 cm/sec^2, and those in region Y_2 have smaller peak accelerations. The coefficients b_1 and b_2 for region Y_1 are larger than those for region Y_2, and coefficient of variation δ_{Y_1} for region Y_1 is also larger than δ_{Y_2} for region Y_2

Table A-2 gives examples of estimation formulas for peak ground acceleration using accelerograms recorded in Japan. The estimation formula by Katayama(Ref.7) and that by Saeki, Katayama, and Iwasaki (Ref.11) are similar to that for region T and D_2 ($\Delta>119$ km). On the other hand, the value of the coefficients b_1, b_2 of the estimation formula by Goto, Kameda, Imanishi, and Hashimoto (Ref.4) are equivalent to those for region Y_1. The above results on the attenuation characteristic of peak acceleration are qualitatively the same as in other studies.

From the above discussion, it may be concluded that the attenuation characteristic of peak acceleration depends on M-Δ regions and that variations in data are larger for region of large earthquakes. The value of peak acceleration, which is mainly concerned about in earthquake engineering, will be more than some ten cm/sec^2 and the estimation formula for engineering purpose should be determined using data corresponding to region Y_1 because of

Table A-2 Estimation Formulas for Peak Acceleration in Previous Studies.

author	dataset	estimation formula	coefficient of variation
(1) Katayama (Ref.7)	330 components from 46 earthquakes recorded in Japan. Mean value of two horizontal components. $M=5.1$ 7.8	$\bar{A}=9.59\times10^{0.466M}/\Delta^{0.129}$ $\bar{A}=203\times10^{0.411M}/(R+30)^{1.637}$	0.877 0.942
(2) Saeki Katayama Iwasaki (Ref.11)	298 components for 4 types of soil conditions class-I site--29 comp. class-II site--74 comp. class-III site--127 comp. class-IV site--68 comp.	class-I site $\bar{A}=28.5\times10^{0.207M}/\Delta^{0.598}$ class-II site $\bar{A}=13.2\times10^{0.330M}/\Delta^{0.806}$ class-III site $\bar{A}=32.1\times10^{0.254M}/\Delta^{0.757}$ class-IV site $A=6.47\times10^{0.430M}/\Delta^{0.977}$ all data $\bar{A}=18.4\times10^{0.302M}/\Delta^{0.800}$	
(3) Goto Kameda Imanishi Hashimoto (Ref.4)	45 components of corrected accelerograms recorded on Japanese alluvial sites. All of data are more than 50 gals.	$\bar{A}=407\times10^{0.160M}/(\Delta+30)^{0.752}$	0.443

A;peak acceleration in cm/sec^2, M;magnitude, Δ;epicentral distance in km, R;hypocentral distance in km.

the different dependence of peak ground motion on M-Δ regions.

Estimation Formulas for Peak Ground Motion on Soil Surface by using Larger Ground Motion Data

On the basis of the previous discussions the estimation formulas for peak ground motion on soil surface are proposed to grasp the general characteristic of soil surface ground motion for relatively larger earthquake conditions. As mentioned above, the estimation formula for peak ground motion should be developed using relatively larger records since the engineering interest is mainly setteled on the large ground motion.

The ninety-one components of accelerograms have been selected for the development of estimation formulas for soil surface peak ground motion. Fig.A-7 shows the scattergram of magnitude and epicentral distance, and the histogram for peak acceleration for the dataset. The broken line in Fig.A-7 represents the value of magnitude and distance by which the estimated mean values from Eq.(A-4) gives as $\bar{A}$=30 cm/sec^2. The dotted line represents the boundary for epicentral region, which is given by Eq.(A-14). These data were corrected for baseline and instrument characteristic of the accelerograph (Ref.2).

The estimation formulas for peak acceleration and peak velocity obtained from this dataset are listed in Table A-3. Comparing the estimation formula for peak acceleration in Table A-3 to that based on the data in region Y_1 (Table A-1), it may be noted that the coefficients b_1 and b_2 for Eq.(A-11) are similar, since the condition of the data selection for Y_1 is nearly the same as that for this dataset. However, the estimation formula Eq.(A-11) gives a larger value of acceleration than that by Eq.(A-9). This result may comes from the fact that the peak value of corrected accelerograms is commonly takes as 1.1 $\sim$ 1.3 times the original data in the case of the SMAC-type accelerograph (Ref.2), and most of data used for this estimation equation were recorded by this type of accelerograph. The coefficient of variation δ_U of the estimation formula Eq.(A-11) in Table A-3 is smaller than that for region Y_1 listed in Table A-1. The reason for the small coefficient of variation may be a consequence of the site conditions used herein which

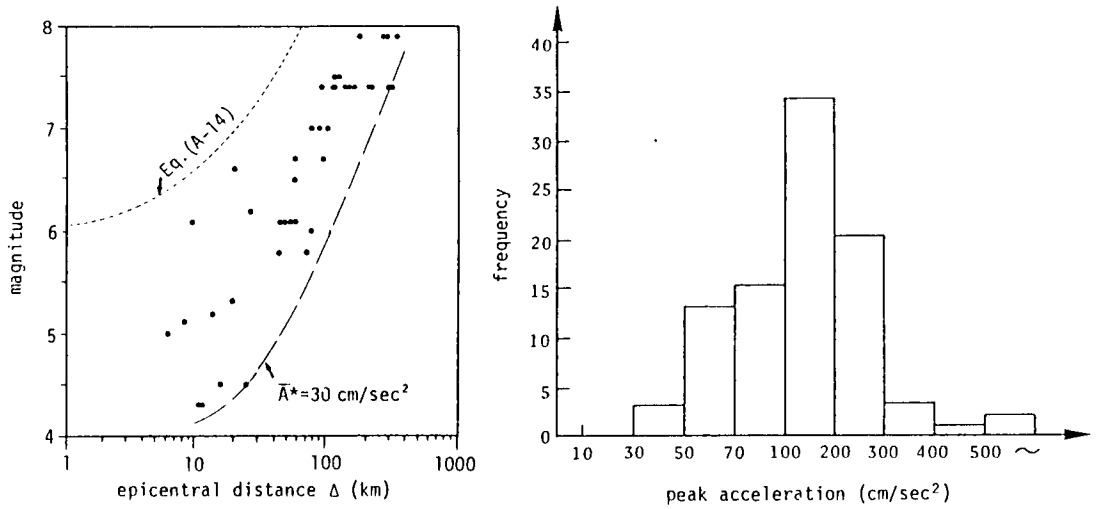

Fig.A-7 Scattergram for Magnitude and Epicentral Distance, and Histogram for Peak Acceleration.

Table A-3 Estimation Formulas for Peak Acceleration and Peak Velocity (obtained from the selected ground motion data).

	(a) $\Delta \geq \Delta_0(M)$	(b) $\Delta < \Delta_0(M)$, $M \geq 6$
peak acc. $\bar{A}(M,\Delta)$, in cm/sec	$349 \times 10^{0.232M}/(\Delta+30)^{0.959}$ --(A-11)	330 --(A-15)
peak vel. $\bar{V}(M,\Delta)$, in cm/sec	$2.65 \times 10^{0.360M}/(\Delta+30)^{0.893}$ --(A-12)	$2.52 \times 10^{0.144M}$ --(A-16)

are limited to alluvial and diluvial sites.

Extension of Estimation Formulas for Near Source Region(Ref.6)

The estimation formulas represented by Eqs.(A-11), (A-12) cannot be applied directly for the case of the near-source region such as large magnitude and short distance, the combination of which is not included in the used data. It is empirically known that the ground motion intensity does not depend strongly on the epicentral distance in near source region and it is rather constant(Ref.8). Herein, the estimation formulas are modified for the near source region by using other empirical imformation on near source ground motion.

Muramatsu(Ref.8) proposed the following empirical relation between earthquake magnitude M and radius r of an equivalent circle within which the seismic intensity is at least VI in JMA scale (IX in MM intensity).

$$r_0 = 10^{0.68M-3.58} \quad , \quad \text{in km} \tag{A-13}$$

It can be assumed that the parameter r_0 defines the limit of near source region within which the ground motion intensity does not depend on the epicentral distance and is relatively uniform. The value of acceleration obtained from Eq.(A-11) with $\Delta=r_0$ does not depend very much on M as shown in Fig.A-8, and the approximate mean value 330 cm/sec^2 may be used for an average value in the near-source region. The distance Δ_0 obtained from $\overline{A}(M,\Delta)$ =330 in Eq.(A-11) may be used for near-source region, and as represented by

$$\Delta_0(M) = 1.06\times 10^{0.242M} - 30 \quad (M\geqq 6.0) \quad , \text{in km} \tag{A-14}$$

Substituting $\Delta_0(M)$ in Eqs.(A-11) and (A-12), the peak acceleration and peak velocity in the near-source region are given as follows.

$$\overline{A} = 330 \quad , \text{ in cm/sec}^2 \tag{A-15}$$

$$\overline{V} = 2.52\cdot 10^{0.144M} \quad (M\geqq 6.0) \quad , \text{ in cm/sec} \tag{A-16}$$

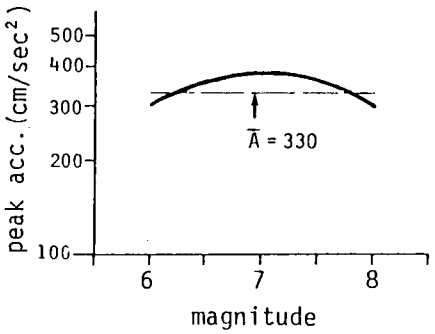

Fig.A-8 Estimation of Median Value for Peak Acceleration in Epicentral Regions.

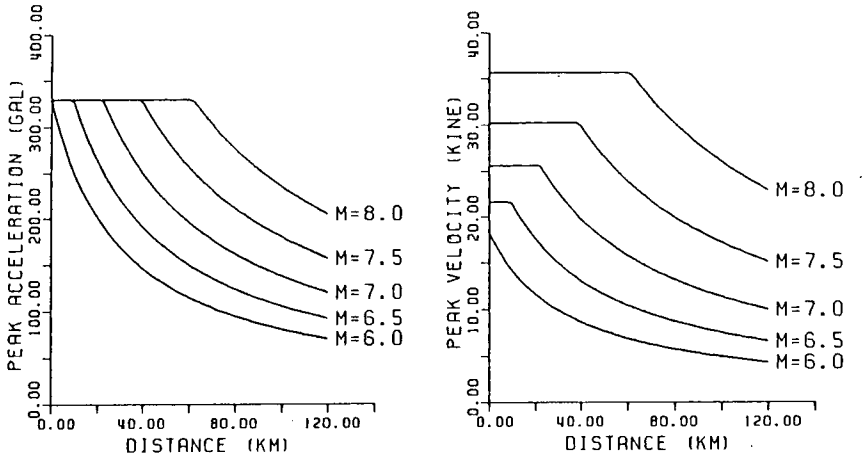

(a) acceleration (b) velocity

Fig.A-9 Attenuation Characteristic of Peak Ground Motion on Soil Surface.

Fig.A-9 shows attenuation characteristic of peak ground motion given by Eqs.(A-11), (A-12), (A-15), and (A-16).

Definition of Soil Parameters for Earthquake Microzonation(Refs.5,6)

(1) soil parameter S_n

It has been pointed out that ground motion intensities depend heavily on the softness of surface layers, and this can be seen in the spatial distribution of damage in past earthquakes. Here the softness of a site is defined in the following form by using blow-count profiles which are commomly available at construction sites.

$$S_l = \int_0^{d_s} \exp\{-\gamma_1 N(x)\} \exp\{-\gamma_2 x\} \, dx \qquad (A\text{-}17)$$

where $N(x)$=blow-count at a depth of x meters, d_p is total depth in which blow-count is available, and γ_1 and γ_2 constants. In Eq.(A-17), γ_1 is defined as a positive constant so as to make the parameter S_l larger in case blow-count is smaller. The second term, $\exp\{-\gamma_2 x\}$, is used because it makes the correlation between S_l and peak ground motion notably larger. The constant γ_2 also takes a positive value, as shown in the following, and this implies that site conditions close to the surface strongly affect earthquake motion intensities.

It has been pointed out that the blow-count has different meanings for different soil types (Ref.12): for example, it is used to express the consistency of clay and the index of relative density for sand. The relation between shear wave velocity and blow-count has been obtained for various types of soil(Refs.10,13,14). Fig.A-10 show the relation between the shear wave velocity and blow-count for clay and sand (Refs.10,14). It is clear that the shear wave velocity is generally higher for clay than that for sand for the same value of the blow-count. In the case of gravel, it has been pointed out that the blow-count is sometimes overestimated because of the resistance of small rubbles agaist the edge of samplers(Ref.9). From these investigations the correction factor ζ_N for blow-count for each type of soil

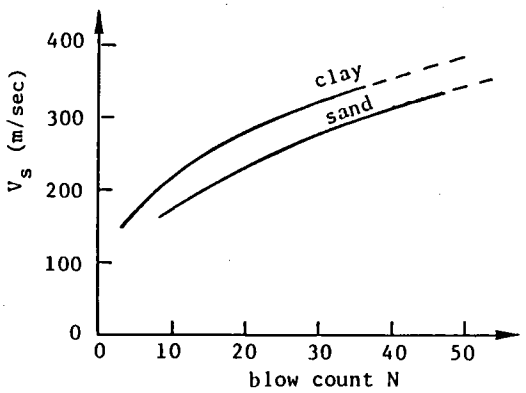

(a) Okubo & Ogawa(Ref.10)

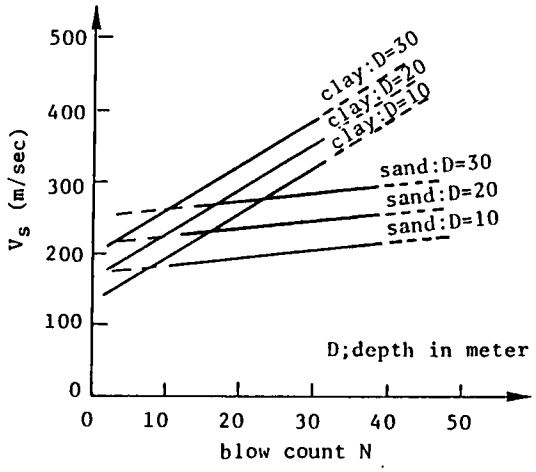

(b) Tajime(Ref.14)

Fig.A-10 Relation between Shear Wave Velocity and Blow-count.

Table A-4 Correction Factor ζ_N for Blow-count.

Geomaterial	Sand	Clay, Loam, Silt	Gravel
ζ_N	1.0	1.2	0.8

can be defined by obtaining S_I from Eq.(A-17). Table A-4 shows the correction factor ζ_N for blow-count for each type of soil.

In the following the continuous soil parameter S_n is proposed on the basis of statistical analysis on peak ground motion including the parametr S_I defined by Eq.(A-17). The soil parameter S_n is defined as the function of the blow-count profile, and is developed under the condition that the parameter S_n has the strongest correlation with the site-dependent peak ground motion.

Uncertainty U of peak ground motion can be separated into two terms as follows.

$$Y=U\cdot\overline{Y}(M,\Delta)=U_1\cdot C(S_n)\cdot\overline{Y}(M,\Delta) \qquad (A\text{-}18)$$

where $\overline{Y}$ is the estimation formulas giving a mean value for peak motion Y for given values of magnitude M and distance Δ, and S_n is a site parameter which is difined as a function of S_I defined by Eq.(A-17). $C(S\_n\&)$ is a correction factor for peak ground motion associated with local site conditions, and U_1 is the remaining uncertainty after considering site conditions. The following relation is assumed between the correction factor $C(S_n)$ in Eq.(A-18) and S_I in Eq.(A-17).

$$\log C=a_0+a_1\cdot S_I \qquad (A\text{-}19)$$

The constants γ_1,γ_2 in Eq.(A-17) and a_0,a_1 in Eq.(A-19) are obtained under the condition that the scatter of data about Eq.(A-19) takes the minimum value. The parameter S_I, which is defined both for peak acceleration and velocity can be normalized for more convenient use. Namely the site parameter S_n is defined as

$S_n=1.0$ .... where $N(x) = 0$ for all x

$S_n=0.0$ .... where $C(S_n) = 1.0$

Using the site parameter S_n defined above, the correction factor $C(S_n)$ in Eq.(A-19) is represented by

$$C(S_n)=10^{(\alpha_1/\gamma_2+\alpha_0)S_n}=C_m^{S_n} \tag{A-20}$$

where

$$S_n=(S_I-\beta)/(1/\gamma_2-\beta) \tag{A-21}$$

where β is a value of S_n giving $C=1$ ($\beta=-\alpha_0/\alpha_1$), and C_m is the maximum value for C represented by $C_m=10^{(\alpha_1/\gamma_2+\alpha_2)}$.

After a number of trial chalculations to minimize the coefficients of variation of U_I in Eq(A-18), the soil parameter S_n and the correction factors for peak acceleration C_a and for peck velocity C_v have been obtained as follows.

$$S_n=0.264\int_0^{ds}\exp\{-0.04N(x)\}\exp(-0.14x)dx-0.885 \tag{A-22}$$

$$C_a(S_n)=\begin{cases}2.09^{S_n}, & S_n\leqq 0.6\\ 1.56, & 0.6<S_n\leqq 1.0\end{cases} \tag{A-23}$$

$$C_v(S_n)=2.23^{S_n} \tag{A-24}$$

Fig.A-11 shows the values of log U_a for peak acceleration and log U_v for peak velocity plotted against S_n. The circles represent the data recorded on ordinary sites, which have been used to obtaine the estimation formulas for peak acceleration and velocity. They include 58 data points associated with 16 sites. The asterisks represent the data for very soft ground which have been excluded from the regression analysis. In the case of the peak acceleration the value of log U_a does not increase with increase in S_n for $S_n>0.6$. Therefore the correction factor C_a is modeled as $C_a=1.56$ for $S_n>0.6$, the value of which is equal to $C_a(0.6)$ in Eq.(A-23). The brokene lines in Figs.A-12, 13 represent the correction factor C_a and C_v defined by Eqs.(A-23) and (A-24).

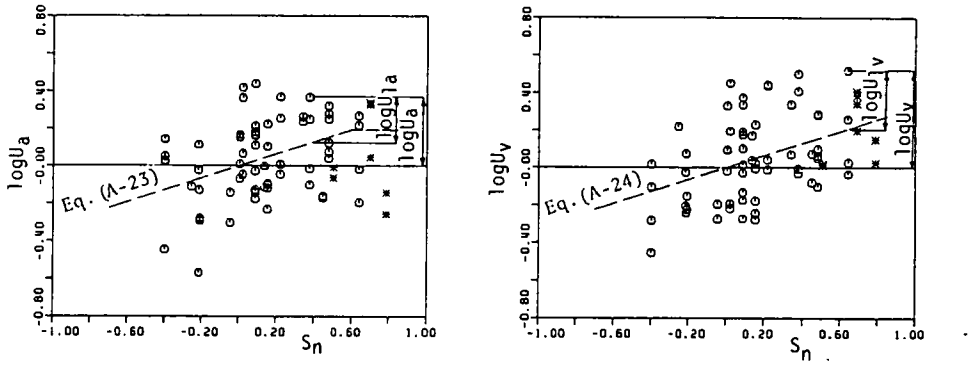

(a) peak acceleration (b) peak velocity

Fig.A-11 Effect of Soil Patameter S_n in Reduction of Estimation Uncertainty.

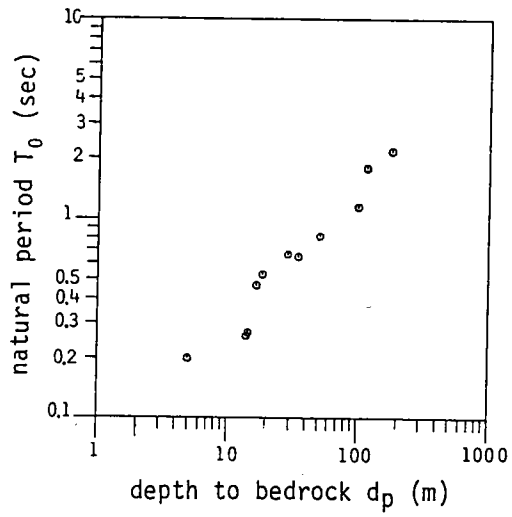

Fig.A-12 Relation between Depth to Bedrock d_p and Natural Period of Ground T_0.

From these results, it may be concluded that the scatter of peak acceleration and velocity are affected strongly by local site conditions, and that the parameters S_n is effective in the estimation of site-dependent earthquake motion such as peak acceleration and velocity. This effectiveness can be observed in the decrease in the coefficient of variations attained by considering S_n. Comparing δ_U, in Table A-5 to that in Table A-3, the decrease in the coefficient of variation are 14% for peak acceleration and 18% for peak velocity.

(2) depth to bedrock d_p

In general a depth d_p to bedrock is easily obtained and it can be also an effective soil parameter as well as the soil parameter S_n. The soil parameter S_n represents the softness of surface layers for approximately 15 to 20 meters depth. On the other hand the depth to bedrock d_p represents the deeper characteristic of surface layers.

Fig.A-12 shows the relation between the depth to bedrock d_p and the natural period T_0 of the first mode for Japanese strong motion observation stations. As shown in Fig.A-12, the depth d_p can be an significant soil parameter for evaluation of site-dependent earthquake motion.

REFERENCES

1) Boore,D.M., Joyner,W.B., Oliver,A.A., and Page,R.A.(1980), "Peak Acceleration, Velocity, and Displacement from Strong Motion Record," BSSA, Vol.70, No.1, pp.305-321.
2) Design Seismic Load Research Group(SLG)(1984), "Corrected and Integrated Earthquake Motion Accelerograms(Graphical Information)," Revised Edition, Research Report, No.84-ST-03, School of Civil Engineering, Kyoto University.
3) Geller,R.J.(1976), "Scaling Relations for Earthquake Source Parameters and Magnitudes," BSSA, Vol.66, pp.1501-1523.
4) Goto,H., Kameda,H., Imanishi,N., and Hashimoto,O.(1978), "Statistical Analysis of Earthquake Ground Motion with the Effect of Frequency-content Correction," 5th Japan Earthquake Engineering Symposium, pp.49-56(in

Japanese).

5) Goto,H., Sugito,M., Kameda,H., and Isoda,A.(1982), "Microzonation of Ground Strain for Estimation of Earthquake Damage to Buried Pipelines," Proc. of 3rd International Microzonation Conference, Vol.III, pp.1653-1664.

6) Kameda,H., Sugito,M., and Goto,H.(1982), "Microzonaiotion and Simulation of Spatially Correlated Earthquake Motions," Proc. of the 3rd International Earthquake Microzonation Conference, Vol.III, pp.1463-1474.

7) Katayama,T.(1974), "Statistical Analysis of Peak Accelerations of Recorded Earthquake Motions," Research Report, Vol.26, No.1, Institute of Industrial Science, Univ. of Tokyo, pp.18-21.

8) Muramatsu,I.(1969), "Relation between the Distribution of Seismic Intensity and the Earthquake Magnitude," Research Report of the Faculty of Education, Gifu Univ., Natural Science Series, Vol.4, No.3, pp.168-176.

9) Nishigaki,T.(1974), "Mechanism of Standard Penetration Test," Soils and Foundation, Vol.193, pp.77-84. (in Japanese).

10) Okubo,T and Ogawa,M.(1974), "S-wave Velocity in the Osaka Area," 9th Annual Convension on Geotechnical Engineering, pp.725-728. (in Japanese).

11) Saeki,M., Katayama,T., and Iwasaki,T.(1977), "Statistical Characteristics of Accelerograms Recorded in Japan," 32th Annual Convension, JSCE, Part I, pp.304-305(in Japanese).

12) Sakaguchi,O.(1974), "Problems in use of N-value," Soils and Foundations, Vol.196, pp.83-89. (in Japanese).

13) Shibata,T.(1969), "Relation between S-wave Velocity and N-value obtained from Standard Penetration Test," 5th Annual Convension on Geotechnical Engineering, pp.101-106. (in Japanese).

14) Tajime,T., Mochizuki,T., and Matsuda,I.(1979), Sites and Earthquake Damage, Maki Shoten. (in Japanese).

15) Utsu,T.(1977), Seismology, Kyoritsu Shuppan. (in Japanese).

Appendix B. Modification of Coefficients in Eq.(4.8) for Application of the EMP-IB Model for Epicentral Region

Herein a modification is performed for the coefficients of estimation formula for the intensity parameter $\alpha_m(f)$ [Eq.(4.8)], which have been obtained from regression analysis, so that the general characteristic of peak ground motion on soil surface, which are obtained from simulated rock surface motion by use of the nonlinear response analysis of surface layers over bedrocks, is consistent with those estimated on the basis of the soil surface strong motion records.

Let A_r and V_r denote the peak acceleration and peak velocity obtained from simulated rock surface motion, respectively. And also, let A_s and V_s denote those obtained from corresponding soil surface motion by use of the nonlinear soil surface response analysis. Fig.B-1 shows the attenuation characteristic of A_r and the variation of A_s for the alluvial and diluvial sites listed in Table 2.1. The values of A_s are obtained only for the combinations of magnitude and distance for the boundary of epicentral region, which is represented by Eq.(A-14). The broken line $\overline{A}$=330 (cm/sec^2) represents the avarage value for soil surface ground inside the epicentral region[Eq.(A-15)]. As shown in Fig.B-1, the average value of A_s slightly higher than the value $\overline{A}$=330 in the case of larger magnitude.

Fig.B-2 shows the attenuation characteristic of V_r and the variation of vs. The broken line in Fig.B-2 represents the values of peak velocity for the epicentral region[Eq.(A-16)] and, the dotted line represents those obtained on the basis of the soil furface strong motion records, the surface wave motion of which are eliminated using the separation technique proposed in Chapter 2. The values of V_s should be compared with those represented by the dotted line represented as follows, since the surface wave motion are not included in the simulated soil surface motion.

$$\overline{V}_s=3.61\times 10^{0.117M} \qquad (B\text{-}1)$$

It is observed that the average values of V_s are consistent with those represented by the dotted line in the case of larger magnitude, however, the

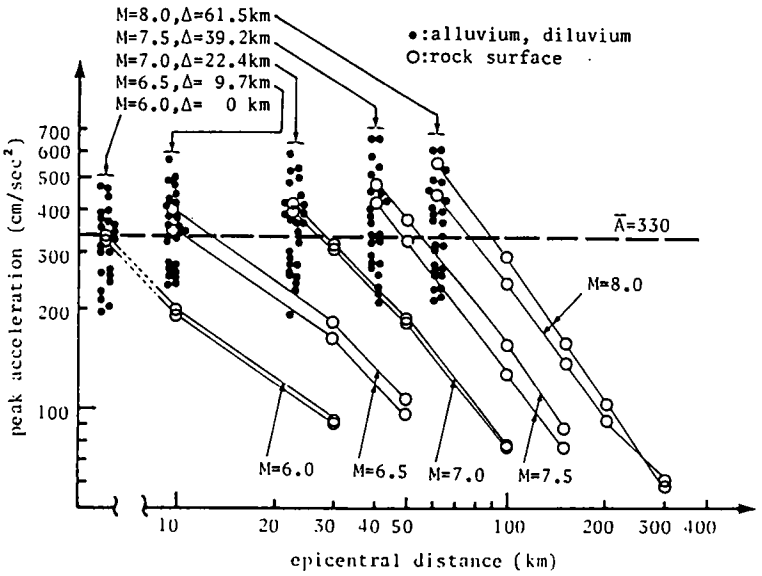

Fig. B-1 Variation of Peak Acceleration for Simulated Soil Surface Motion Compared with Values of Eq.(A-15)

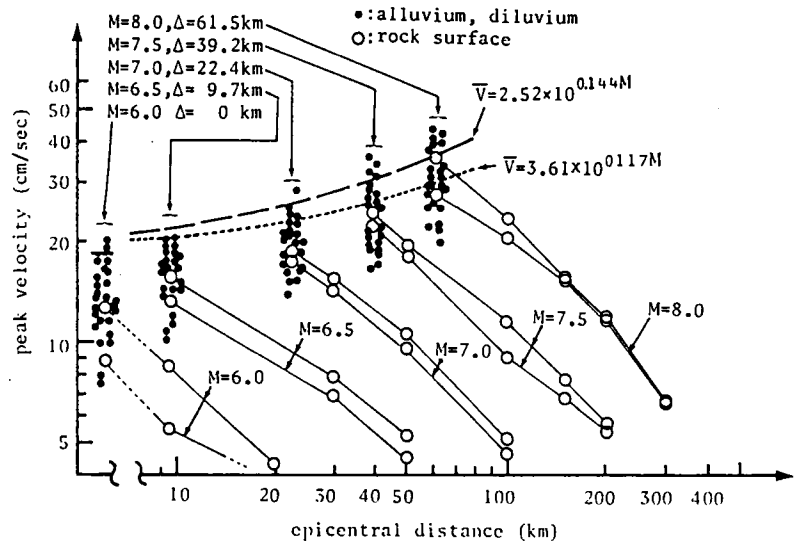

Fig.B-2 Variation of Peak Velocity for Simulated Soil Surface Motion Compared with Values of Eqs.(A-16) and (B-1).

values of V_s are smaller in the case of smaller magnitude.

To eliminate the disagreement on peak ground motion as shown above, the following modification on the coefficients for the intensity parameter $\alpha_m(f)$ has been performed. Fig.B-3 shows the control points for modification of coefficients. The point α_1 gives the combination for M=8.0 and Δ= 61.5 at which the avarage values of A_s is slightly higher than $\overline{A}$=330 which is the value for epicentral region. The point α_2 gives the combination for M=6.0 and Δ=0 at which the average values of V_s is smaller than the expected value obtained from soil surface records. The point α_0 gives the combination for M=6.59 and Δ=96.3 which are the mean values of magnitude and distance for the SMD-R dataset.

Under the following conditions the coefficients $B_0(f)$,$B_1(f)$,and $B_2(f)$ obtained from the regression analysis are modified.

[1] high frequency region, control of a peak acceleration ($f_a<f\leqq 10.03$)

At the point α_0 and α_2, the estimated values of $\alpha_m(f)$ are equal to those obtained from regression analysis. And the values of $\alpha_m(f)$ are to be slightly smaller at the point α_1 by using the coefficient α_a as $\alpha_a<1.0$.

[2] middle frequency region, control of a peak velocity ($f_v\leqq f\leqq f_a$)

At the point α_0 and α_1, the estimated values of $\alpha_m(f)$ are equal to those obtained from regression analysis. At the point α_2 the values of $\alpha_m(f)$ are to be larger.

These two conditions are equivalent to solve the simultaneous simple equations on the coefficients $B_0(f)$,$B_1(f)$,and$B_2(f)$ for each frequency. After the iterative calculations these parameters for the modification of the coefficients have been obtained as follows.

f_a=2.0Hz, f_v=0.7Hz, α_a=1.35, υ_a=0.95

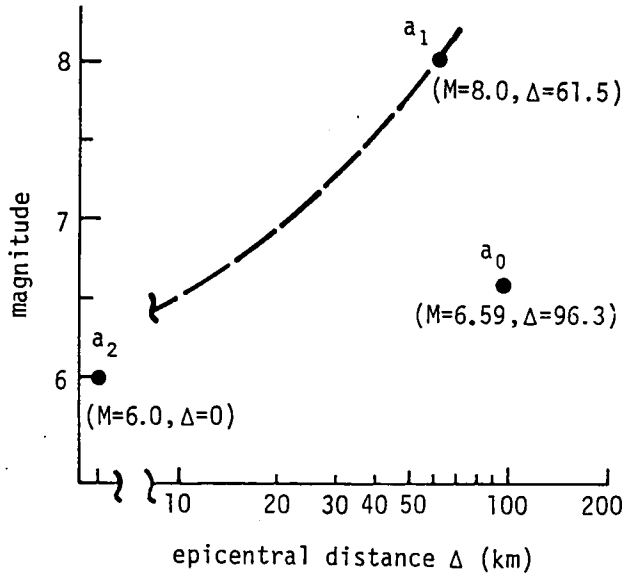

Fig.B-3 Control Points for Modification of Coefficients for Intensity Parameter $\alpha_m(f)$.

Table B-1 Comparison between Expected Values of Peak Ground Motions by Estimation Formulas and Geometric Average Obtained from Simulated Earthquake Motion.

	(a) estimation formula		(b) basic model		(c) modified model	
	Eq.(A-15)	Eq.(B-1)				
	peak acc. (cm/sec²)	peak vel. (cm/sec)	peak acc. (cm/sec²)	peak vel. (cm/sec)	peak acc. (cm/sec²)	peak vel. (cm/sec)
$M=8.0$ $\Delta=61.48$	330	30.8	359	31.8	340	29.6
$M=7.5$ $\Delta=39.23$	330	26.9	357	24.1	338	25.2
$M=7.0$ $\Delta=22.40$	330	23.5	340	19.6	341	23.0
$M=6.5$ $\Delta=9.66$	330	20.6	340	16.5	331	20.8
$M=6.0$ $\Delta=0.01$	330	18.0	333	13.8	320	18.2

Table B-1 shows the combination of the geometric average of peak ground motion for the basic model based on the regression analysis and the modified model. It is observed that the germetric average of peak ground motion for the modified model are equivalent to those given from the estimation formulas which have been obtained on the basis of the soil surface records. The modified coefficients $B_0(f)$,$B_1(f)$, and $B_2(f)$ obtained herein are further modeled as a function of log$f$ in Chapter 4.

Appendix C. Development of bedrock and soil surface Simultaneous Earthquake Motion

The simultaneous records from soil surface and corresponding bedrock motion are of special importance in earthquake engineering, since ground motion are effected strongly by local site conditions over bedrock. They can be used for analysis on uncertainty factors in earthquake ground motion including the verification of the conversion factors developed in this thesis.

The database for simultaneous earthquake motion on bedrock and soil surface has been developing through the good offices of the concerning research groups including research institutes in private companies.

Table C-1 shows the summary of the simultaneous earthquake motion data which have been stored in the Data Processing Center, Kyoto University. This database is aimed to be used cooperatively by the research groups who supplied the strong motion data.

Table C-1 List of Simultaneous Strong Motion Data (data : September, 1986).

Company, Research Inst.	site number	number of seismograph	number of earthquake	number of components	depth to bottom seismograph(m)	S wave velocity of bedrock (m/sec)	maximum value of peak acc. (cm/sec)	
							soil surface	bedrock
Tokyo Elec. Pow. & T E P Service	No.1	3	3	2 1	-160.0	800	434.8	416.7
Ohbayashi Research Inst.	No.2	2	6	2 4	-22.0	460	97.6	21.0
Takenaka Const. Research Inst.	No.3	6	3	4 2	-153.0	480	77.2	22.1
Ohsaki Research Inst.	No.4	2	9	5 4	-30.0	400	113.5	38.5
Tobishima Const.	No.5	2	3	1 8	-50.0	330	8.6	2.0
Kajima Const. Civil Eng. Design Div.	No.6	6	6	7 6	-100.0	500	57.0	10.7
	No.7	2	2	1 0	-27.0	360	69.8	21.1
Nippon Kokan Tech. Research Center	No.8	6	4	5 4	-50.0	300	80.2	33.3
	No.9	2	2	1 2	-60.0	480	25.0	15.0
Okumuragumi Tsukuba Research Inst.	No.10	2	1	1 5	-50.0	460	11.0	5.7
	No.11	5	1	1 5	-150.0	460	21.5	6.8
Tokyo Prefect. Office, Div. of Minami-tama	No.12	2	28	168	-21.5	680	60.0	19.5
	No.13	2	28	420	-31.5	350	70.8	35.6
Taisei Const. Civil Eng. Design Div.	No.14	2	2	1 2	-36.0	285	37.9	17.1
	No.15	2	2	8	-14.1	400	64.3	23.6
Inst. of Indust. Science, Univ. of Tokyo	No.16	2	2	1 2	-56.0	660	23.8	17.7
	No.17	5	26	390	-40.0	420	82.0	17.8

Appendix D. Representation of Functions and Matrices Appearing in Chapter 6.

The functions $B_1(x)\sim B_6(x)$ and $D_1(x)\sim D_6(x)$ in Eqs.(6.12) $\sim$ (6.17) are represented as follows.

$$B_1(x) = \cos\beta_1 x \cosh\beta_1 x \tag{D-1}$$

$$B_2(x) = \sin\beta_1 x \sinh\beta_1 x \tag{D-2}$$

$$B_3(x) = \cos\beta_1 x \sinh\beta_1 x + \sin\beta_1 x \cosh\beta_1 x \tag{D-3}$$

$$B_4(x) = \cos\beta_1 x \sinh\beta_1 x - \sin\beta_1 x \cosh\beta_1 x \tag{D-4}$$

$$B_5(x) = \cosh\beta_2 x \tag{D-5}$$

$$B_6(x) = \sinh\beta_2 x \tag{D-6}$$

$$D_1(x) = -v_0(0)B_1(x) - \frac{v_0'(0)}{2\beta_1}B_3(x) - \frac{v_0''(0)}{2\beta_1^2}B_2(x) + \frac{v_0'''(0)}{4\beta_1^3}B_4(x) + v_0(x) \tag{D-7}$$

$$D_2(x) = v_0(0)\beta_1 \cdot B_4(x) + v_0'(0)B_1(x) + \frac{v_0''(0)}{2\beta_1}B_3(x) + \frac{v_0'''(0)}{2\beta_1^2}B_2(x) - v_0'(x) \tag{D-8}$$

$$D_3(x) = 2v_0(0)EI\beta_1^2 \cdot B_2(x) - v_0'(0)EI\beta_1 \cdot B_4(x) - v_0''(0)EIB_1(x) - \frac{v_0'''(0)EI}{2\beta_1}B_3(x) + EIv_0''''(x) \tag{D-9}$$

$$D_4(x) = 2v_0(0)EI\beta_1^3 \cdot B_3(x) + 2v_0'(0)EI\beta_1^2 \cdot B_2(x) - v_0''(0)EI\beta_1 \cdot B_1(x) - v_0'''(0)EIB_1(x) + EIv_0''''(x) \tag{D-10}$$

$$D_5(x) = -u_0(0)B_5(x) - \frac{u_0'(0)B_6(x)}{\beta_2} + u_0(x) \tag{D-11}$$

$$D_6(x) = u_0(0)EA\beta_2 \cdot B_6(x) + u_0'(0)EAB_5(x) - EAu_0'(x) \tag{D-12}$$

The field matrix F in Eq.(6.18) and the point matrix P in Eq.(6.20) at the joints of straight and bent sections are represented as follows.

$$\mathbf{F}=\begin{pmatrix} B_5(l) & 0 & 0 & -\frac{B_6(l)}{EA\beta_2} & 0 & 0 & D_5(l) \\ 0 & B_1(l) & -\frac{B_3(l)}{2\beta_1} & 0 & \frac{B_2(l)}{2\beta_1^2EI} & -\frac{B_4(l)}{4\beta_1^3EI} & D_1(l) \\ 0 & -\beta_1B_4(l) & B_1(l) & 0 & -\frac{B_3(l)}{2\beta_1EI} & -\frac{B_2(l)}{2\beta_1^2EI} & D_2(l) \\ -EA\beta_2B_6(l) & 0 & 0 & B_5(l) & 0 & 0 & D_6(l) \\ 0 & -2EI\beta_1^2B_2(l) & -\beta_1EIB_4(l) & 0 & B_1(l) & \frac{B_3(l)}{2\beta_1} & D_3(l) \\ 0 & -2EI\beta_1^3B_3(l) & 2\beta_1^2EIB_2(l) & 0 & \beta_1B_4(l) & B_1(l) & D_4(l) \\ 0 & 0 & 0 & 0 & 0 & 0 & 1 \end{pmatrix} \tag{D-13}$$

for the straight section:

$$\mathbf{P}=\begin{pmatrix} 1 & 0 & 0 & -\frac{1}{k_T} & 0 & 0 & 0 \\ 0 & 1 & 0 & 0 & 0 & 0 & 0 \\ 0 & 0 & 1 & 0 & -\frac{1}{k_R} & 0 & 0 \\ 0 & 0 & 0 & 1 & 0 & 0 & 0 \\ 0 & 0 & 0 & 0 & 1 & 0 & 0 \\ 0 & 0 & 0 & 0 & 0 & 1 & 0 \\ 0 & 0 & 0 & 0 & 0 & 0 & 1 \end{pmatrix} \tag{D-14}$$

for the bent section:

$$\mathbf{P}=\begin{pmatrix} \cos\alpha & \sin\alpha & 0 & -\frac{\cos\alpha}{k_T} & 0 & \frac{\sin\alpha}{k_T} & 0 \\ -\sin\alpha & \cos\alpha & 0 & 0 & 0 & 0 & 0 \\ 0 & 0 & 1 & 0 & -\frac{1}{k_R} & 0 & 0 \\ 0 & 0 & 0 & \cos\alpha & 0 & \sin\alpha & 0 \\ 0 & 0 & 0 & 0 & 1 & 0 & 0 \\ 0 & 0 & 0 & -\sin\alpha & 0 & \cos\alpha & 0 \\ 0 & 0 & 0 & 0 & 0 & 0 & 1 \end{pmatrix} \tag{D-15}$$